Mathematical Modeling of *C elegans* L1 aggregation

by

Leon Avery

A thesis
presented to the University of Waterloo
in fulfillment of the
thesis requirement for the degree of
Doctor of Philosophy
in
Applied Mathematics

Waterloo, Ontario, Canada, 2019

Examining Committee Membership

The following served on the Examining Committee for this thesis. The decision of the Examining Committee is by majority vote.

External Examiner:	Thomas Hillen Professor and Associate Chair of Research, Department of Mathematical and Statis
Supervisor:	Brian Ingalls Professor, Dept. of Applied Mathematics, University of Waterloo
Internal-External Member:	Justin W.L. Wan Professor, David R. Cheriton School of Computer Science, University of Waterloo
Other Members:	Matthew Scott Professor, Dept. of Applied Mathematics, University of Waterloo Sander Rhebergen Assistant Professor, Dept. of Applied Mathematics, University of Waterloo

I hereby declare that I am the sole author of this thesis. This is a true copy of the thesis, including any required final revisions, as accepted by my examiners.

I understand that my thesis may be made electronically available to the public.

Abstract

First-stage larvae (L1s) of the nematode *Caenorhabditis elegans* aggregate after starvation. I develop a mathematical model of this behavior based on the classic Keller-Segel model. In the Keller-Segel model, organisms emit a diffusible signal, to which they are attracted. The model is embodied in two partial differential equations (PDEs): an advection-diffusion equation for density of organisms, and a reaction-diffusion equation for the concentration of chemical signal. The PDE system has an equilibrium in which organisms and signal are uniformly distributed, but this equilibrium becomes unstable when the density of organisms exceeds a threshold, resulting in formation of aggregates.

To model *C elegans* L1 aggregation, I develop versions of the Keller-Segel model. The Keller-Segel partial differential equations (PDEs) are solved numerically, and the results compared to observed *C elegans* behavior. I find that I cannot reproduce observed behavior with a single attractive signal. In particular, aggregates become very large in an attractant-only model, while aggregates of *C elegans* L1s are fairly uniform in size (typically ca. $500\,\mu\mathrm{m}$ diameter) and limited to a few hundred animals each. To reproduce this behavior, it is necessary to introduce a second chemical signal, a repellent, with longer diffusional range than the attractant. In addition, the model is designed to prevent density within aggregates from rising above that density at which the worms are tightly packed. With this design, two other features of actual L1 behavior are reproduced. First, the worms form disk-shaped aggregates. Second, even after long times, the density of worms outside aggregates remains low but positive.

To better understand the behavior of the PDE system—its equilibria, in particular—I describe a general method for developing exact or approximate energy functionals that are stationary at equilibrium. (Some but not all of these energy functionals are Lyapunov functionals.) I use these energy functionals to analyze aggregation behavior. I also describe their use to determine the properties of equilibria, e.g. the expected geometry and arrangement of aggregates.

Acknowledgements

This work depended on help from three people more than any others: Alex Artyukhin, Young-jai You, and Brian Ingalls.

Alex, of course, started the project by discovering the phenomenon: L1 aggregation. This was quite a surprise, since it was generally believed among *C elegans* researchers that hermaphrodites don't pay much attention to each other. Alex has been generous with data and ideas. Indeed, the model I analyze here is based on the "active walker" model he first proposed to explain aggregation.

Young is a long-time colleague and good friend. She has helped to keep my time as a grad student interesting by inviting me repeatedly to Nagoya University to work and explore Japan.

Brian, of course, is my PhD mentor. He has given me a lot of good advice. While I may have been too slow to follow some of it, it has always proved helpful when I finally threw off procrastination. He also gave me a extraordinary amount of freedom to determine my own research direction.

I also thank my defense committee, particularly Sander Rhebergen, for pointing out some grave defects in the thesis, which I will attempt to correct, and David Hillen for doing likewise and also suggesting approaches to certain problems I had found intractable.

I also want to express my thanks to the Applied Mathematics Department (and to Brian especially) for making an unusual student welcome.

Dedication

This is dedicated to my colleagues and friends Youngjai You and Alex Artyukhin, who started the trouble.

Table of Contents

List of Tables

List of Figures

Acronyms

BC Bimodality Coefficient 131

cAMP cyclic adenosine monophosphate 15

CAS Computer Algebra System 91

CDF Cumulative Distribution Function 124

CFL Courant–Friedrichs–Lewy 85

CT Convolution Theorem 61

DAE Differential Algebraic Equation 92

DG Discontinuous Galerkin 86

FFT Fast Fourier Transform 137

IBP integration by parts 22, 47

KDF Kernel Density Function 124

KS Kolmogorov-Smirnov 124

MCMC Markov Chain Monte Carlo 150

MDS Multidimensional Scaling 122

MPI Message Passing Interface 92

ND Negative Definite 36

NGM Nematode Growth Medium 7

NSD Negative Semidefinite 36

ODE Ordinary Differential Equation 92

PD Positive Definite 36

PDE partial differential equation iv, 15

PSD Positive Semidefinite 36

SSA Stochastic Simulation Algorithm 150

Nomenclature

ASE A *C elegans* sensory neuron type 11

ASK A *C elegans* sensory neuron type 11

Conditioned Medium Solution in which organisms have previously been maintained 4

L1 First-stage larva 2

N2 The usual base laboratory strain of *C elegans*, from which most of the strains used for genetic studies derive 14

wild type Genetically normal 6

Chapter 1

Introduction

1.1 The importance of purpose

The first question to be asked on beginning a new research project is "Is this interesting?" In biology, this question has a dimension not present in mathematics or physics: purpose. (To be clear: although it is evident that the question of purpose arises in mathematics and physics, this is because mathematics and physics are endeavours conducted by mathematicians and physicists, who are living things. Permutation groups and electrons do not have intrinsic purpose, although they may serve the purposes of mathematicians and physicists. This contrasts with the objects biologists study.)

In almost every cell of almost every living thing, there are hundreds of copies of a molecular mill, called ATP synthase (Yoshida et al. 2001). This mill is powered not by a flow of water or air, but of protons, which in flowing through it cause part of it to spin. The motion of this spinning rotor against a stator does chemical work, forcing molecules of adenosine diphosphate (ADP) to combine with phosphate ions to produce adenosine triphosphate (ATP). It is a beautiful, elegant little machine, whose workings are now known in atomic detail. (You can easily find video animations on the Internet.) It has every right to be considered interesting for this reason alone.

Yet, if you ask a biologist why ATP synthase is interesting, you will almost certainly get a different answer. She will tell you that ATP is the currency of chemical energy in living things, and that ATP synthase is the machine that makes ATP and thus allows you to move and stay alive. The burning of sugars and fats and even alcohol in your food and drink pumps protons uphill (i.e., to locations where their energy is higher), so that they can then flow down through

ATP synthase to capture energy. It is by this means that the food you eat and the air you breathe give you energy.

The previous two paragraphs answer the question "Why does ATP synthase make ATP?" in two distinct but accurate ways. The first describes in physical terms how the operation of the mechanism makes ATP—the second describes the purpose of making ATP. (These were called "proximate" and "ultimate" causes by Nikolaas Tinbergen——philosopher Daniel Dennett calls them "How come?" and "What for?" questions (Dennett 1996).) The sciences in general and biology in particular have a historical shyness about teleology: ascribing of purposes to things. Yet no biologist I know would seriously dispute the statement "The purpose of ATP synthase is to make ATP", although they might prefer to replace the word "purpose" with less loaded code phrases. It is no more controversial than the idea that eyes are for seeing, or that lungs are for breathing.

That we can ascribe purpose to biological machines is, of course, a consequence of evolution by natural selection (Dennett, (1996), see also Dennett's lecture "The Evolution of Purpose"). But evolution is more complicated than the simple "adaptation by natural selection" picture taught in high school biology. There are important evolutionary mechanisms that can produce maladaptive traits, i.e. mechanisms that harm the organism they inhabit, or that result in the appearance of intricate side effects that in themselves have no adaptive significance. These are sometimes called "spandrels" after a famous and still controversial paper by Gould and Lewontin (1979).

The point I want to make is that, in deciding whether a biological phenomenon is interesting, one must ask "What is its purpose?". ("What selective advantage does it confer?' or "Why would such a mechanism persist in the population?" are versions of the question.) And, if no purpose is obvious, one must ask whether there is one.

In describing the details of *C elegans* L1 social behavior, my goal is to present it as a set of intricate processes with many moving parts, in order to argue that there must be an evolutionary mechanism to maintain it. Because they are specified by a genome that can't be copied with 100% accuracy, complicated biological mechanisms can't persist without a purifying mechanism that eliminates the errors.

1.2 Starved *C elegans* L1 larvae aggregate

While working with *C elegans*, we noticed aggregation of starved L1s on old agar plates after the worms had exhausted the food. (In the lab, the food is typically *E. coli* bacteria.) One of my colleagues suggested that larvae aggregated around worm corpses in their search for food,

being attracted by the smell of decomposing worm bodies. If this were true, one would predict that starved (but living) larvae transferred to a fresh plate should not aggregate. Contrary to this expectation, Alex Artyukhin found that after brief initial dispersal starved L1 larvae aggregated on fresh agar plates as efficiently as they did on old, exhausted plates. (The following description of L1 aggregation is based on Artyukhin et al (2015).) This result rules out any necessity for worm corpses in L1 aggregation and suggests a more interesting mechanism, by which L1s attract each other. It is this mechanism that I seek to explore and understand in this dissertation.

To avoid ambiguity in age, composition, and potential contamination of exhausted plates, Alex performed all aggregation experiments on clean, foodless plates onto which he pipetted a defined number of L1 larvae prestarved in a buffered salt solution for a specific amount of time. He washed worms before pipetting on the plate to remove any soluble substances that worms might have released up to this point. (We know there are many such substances, e.g. Ludewig and Schroeder (2013).) He observed three distinct stages of worm behavior after L1 larvae were pipetted on a clean plate (Figure 1.1). During the first 2-3 hours worms disperse from the starting point and gradually fill the entire plate. There is no sign of any order or correlation among worms during this time; local density fluctuations quickly appear and disappear. After 2-3 hours small fluctuations in worm density suddenly amplify and give rise to an array of circular aggregates, which is then metastable for at least $24\,\mathrm{h}$. By "metastable", I mean that once formed the aggregates do not dissociate, but neighboring aggregates may occasionally merge. After 1–4 days circular aggregates start to lose their shape and aggregate morphology transitions to stripes. The timing of this transition depends on worm density on the plate—the more worms, the faster it happens. For low enough densities it may never happen. (We now know that this transition occurs because of the depletion of ethanol in the agar.) In this dissertation, I will mostly focus on the second stage of L1 aggregation—formation of circular aggregates.

As expected for many-body interactions, L1 aggregation depends critically on worm density. A threshold density (about $1500\,\mathrm{cm}^{-2}$) is required for aggregation, which suggests that L1 aggregation is a fairly weak interaction (e.g. compared to sexual attraction). There is no visible interaction between two L1s crawling on a plate, even when they run into each other. They part and continue their ways. Yet, at large numbers random fluctuations can bring enough worms together to nucleate an aggregate. We observed aggregation only after L1 larvae had been prestarved for at least 3 days. L1s within $24\,\mathrm{h}$ of hatching disperse on the plate and do not aggregate. L1s adjust their gene expression program quickly after hatching without food (Baugh et al. 2009). Apparently, just the fact that the worms are starved and their development is arrested is not sufficient to cause their aggregation. It requires that they be starved for 2–3 days. Since aggregation most likely relies on diffusible signals (see below), this result may mean that the repertoire of signals that L1s release changes after 2–3 days of starvation (com-

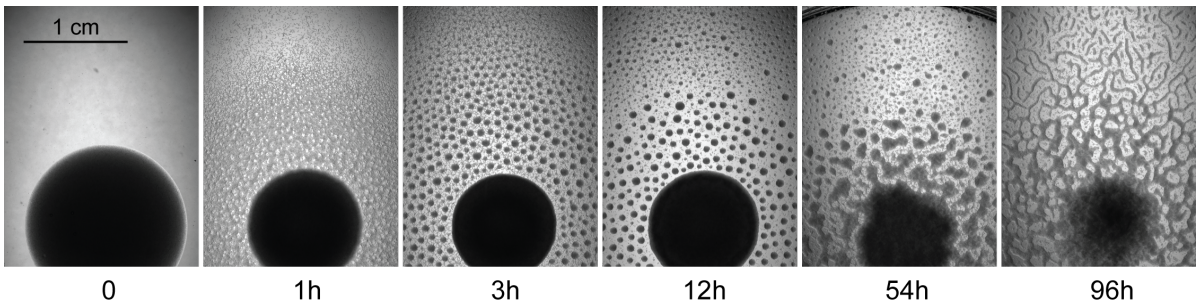

Figure 1.1: Time-course of *C elegans* L1 aggregation
One million 3-day starved L1 worms were thoroughly washed, dispersed in 100 µL of buffer, and pipetted into the center of a clean 6 cm NGM plate at time zero (dark circular area in the lower half of the images).
This figure is copied from Artyukhin et al (2015) with permission.

pared to day 1) or that worms change their response to existing cues, or both. Alex has found that L1s release the most metabolites during hatching or within a few hours after hatching. The best understood worm chemical signals are the ascaroside pheromones (Choe et al. 2012; Ludewig and Schroeder 2013). Among the chemicals released shortly after hatching are several ascarosides responsible for avoidance and dispersal (A B Artyukhin et al. 2013), though ascaroside-independent avoidance signals also exist (A. Artyukhin, unpublished). Medium conditioned with starved L1s for one day is a strong worm deterrent (A B Artyukhin et al. 2013). (Conditioned Medium means solution in which organisms have been soaked for long enough to collect chemicals they release, then separated from the organisms. Thus, for instance, beer is yeast conditioned medium.) This deterrence is consistent with the observed dispersal behavior during the first day of starvation. Far less is known about molecules released by L1 larvae after 48h of arrest. We hypothesize that this late conditioned medium contains an attractant responsible for L1 aggregation at later stages of starvation.

Comparing *C elegans* with its close relative, *C briggsae* (Félix et al. 2012; Stein et al. 2003), we were surprised to find that *C briggsae* L1s do not aggregate. Furthermore, when we mixed starved L1s of *C elegans* and *C briggsae* expressing different fluorescent proteins, *C briggsae* were effectively excluded from *C elegans* clumps (Figure 1.2). We observed a mixed population on the plate——some worms were in aggregates, while many were individually dispersed (Figure 1.2, left). From two-color imaging we determined that aggregates were composed primarily of *C elegans*, whereas worms that did not participate in clumps were mostly *C briggsae* (Figure 1.2, right). This result excludes the possibility that L1 aggregation is governed

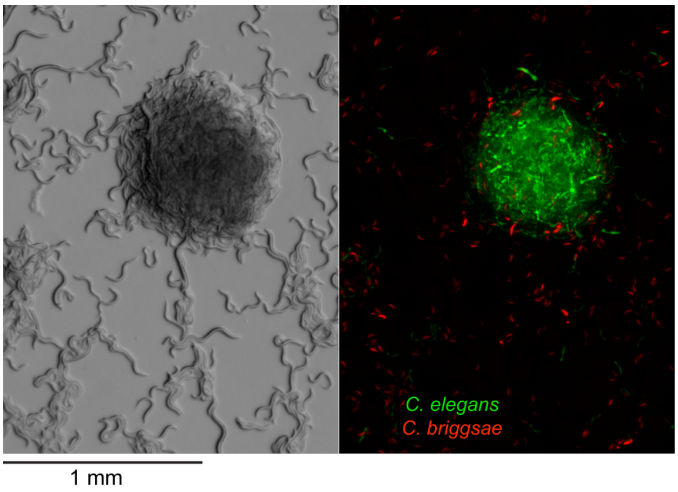

Figure 1.2: *C briggsae* do not participate in *C elegans* aggregation
Bright field image (left) and overlay of green and red channels (right) from the same area on the plate with a mixture of GFP-expressing *C elegans* (green) and dsRed-expressing *C briggsae* L1 larvae (red).
This figure is copied from Artyukhin et al (2015) with permission.

by a simple physical mechanism, such as surface tension. When crawling on the agar surface, worms are surrounded by a thin layer of water. Due to their small size (ca. $150\,\mu\mathrm{m} \times 25\,\mu\mathrm{m}$) surface tension may significantly affect the behavior of L1 larvae and thus has to be taken into account (Gart et al. 2010). However, *C elegans* and *C briggsae* L1 larvae are physically almost indistinguishable. The difference between *C elegans* and *C briggsae* behavior and the lack of aggregation in certain *C elegans* mutants (see below) strongly suggest that surface tension is not the determining factor in L1 aggregation.

Several examples of *C elegans* aggregation have been described before. One of them is mediated by indole-containing ascarosides (Reuss et al. 2012). Alex examined the behavior of starved *daf–22* mutant L1s. (A quick note on nomenclature: the names of *C elegans* genes are three or four lower case letters, followed by a hyphen, followed by a number, e.g. *daf–22*. Gene names are always italicized. The expression of a gene produces a product (almost always a protein), which is denoted by uppercase roman type. For instance, the product of *daf-22* is the protein DAF–22. A *daf–22* mutant is a worm both of whose *daf-22* genes are abnormal. In this document, it will always refer to a genetic knockout, i.e., a *daf-22* mutant means a worm that lacks functional *daf-22* genes, and therefore has no DAF–22 protein.) *daf–22* mutants lack all ascarosides commonly released by wild type (Srinivasan et al. 2012). The product of *daf–22*, DAF–22, is the enzyme peroxisomal 3-keto-acyl-CoA thiolase. DAF–22 is necessary for β-oxidation of fatty acids and ascaroside biosynthesis (Butcher et al. 2009; Golden and Riddle 1985; Joo et al. 2009). L1s of *daf–22* mutants aggregated similarly to wild type. This demonstrates that ascarosides are not necessary for L1 aggregation. Another aggregation behavior is modulated by the signaling molecule NPR–1 (product of the *npr–1* gene) and ambient oxygen (Bono and Bargmann 1998; Bono, Tobin, et al. 2002; Chang et al. 2006). Aggregation results from the worm's preference for lower than normal oxygen levels and the effect disappears at $[O_2] < 10\%$. Alex tested L1 aggregation in low oxygen conditions and found little effect of oxygen concentration on aggregation down to 1%. From these results he infers that the mechanism of starved L1 aggregation is different from known examples of social behavior in *C elegans*.

1.2.1 Evidence that L1 aggregation is mediated by chemical signal(s)

We hypothesize that L1 aggregation is mediated by diffusible signal(s) that L1 worms release. For communication, *C elegans* relies extensively on chemical signals, which are sensed by 11 pairs of chemosensory amphid neurons (Bargmann 2006). (The paired amphids, located in the worm's nose, are the main chemosensory organs.) To test this hypothesis Alex examined L1 aggregation behavior in mutants that lack the function of one or more chemosensory neuron types. The results of these experiments were inconclusive. In some experiments, mutant worms

lacking the function of the main attractive neuron type, ASE, or the main repulsive neuron type, ASH, showed weak or no aggregation. But the results were variable. Alex and I have a small difference of opinion on the meaning of these results. Because of the variability, Alex thinks they cannot be relied on. I think the weight of evidence is in favor of there being some weakening of aggregation in mutants with chemotactic defects, and that the results might be more clear if we had a way of quantifying the strength of aggregation. (This is one of the problems I hope to address by mathematical modeling.)

1.2.2 L1 aggregation requires acetate

Alex performed his initial experiments on Nematode Growth Medium (NGM) plates, an agar-based gel mixture commonly used by researchers to maintain *C elegans* in the lab. Besides agar it contains peptone (a crude protein mix), cholesterol, antibiotics, and some inorganic salts. To determine if the aggregation is triggered by any of these components, he prepared a set of plates where he excluded the components one by one. Quite surprisingly, he found that the two-carbon alcohol ethanol, the solvent used for making a stock solution of cholesterol, was necessary and sufficient for L1 aggregation. 0.1% (17 mmol/L) ethanol in water was enough to support aggregation. (In these experiments the medium was solidified with agarose, a purified form of agar.)

Carbon and energy metabolism in cells generally operates on two-carbon units. The main energy storage molecules are carbohydrates and fats. Carbohydrates are composed of six-carbon monosaccharides with the formula $C_6H_{12}O_6$. To exploit them for energy, the cell breaks each monosaccharide into two molecules of acetate (CH_3-COO^-, the two-carbon acid——the other two carbons are lost as carbon dioxide). Acetate is then transported into mitochondria, where it is burned to water and carbon dioxide in a process that pumps protons out of the mitochondrion. These protons then power the ATP synthase to produce usable energy. In the absence of oxygen, acetate may instead be released into the environment in the form of ethanol. (This process, called fermentation, is how beer and wine are made.) Fats contain fatty acids. Each fatty acid is a long (typically 12–22 carbons) unbranched hydrocarbon chain with an acid group at one end. Natural fatty acids have an even number of carbons——they are made by joining acetate units end-to-end, and broken down by sequentially removing acetate units from one end. In the presence of oxygen, even-chain alcohols such as ethanol and butanol (four carbons) are oxidized to the corresponding acids (acetate and butyrate) by the enzyme alcohol dehydrogenase, and burned for energy, or used to make longer acids. The cell is unable to make use of odd-chain alcohols such as methanol (one carbon) or propanol (three).

On learning that ethanol was necessary for aggregation, Alex tested other alcohols. Butanol,

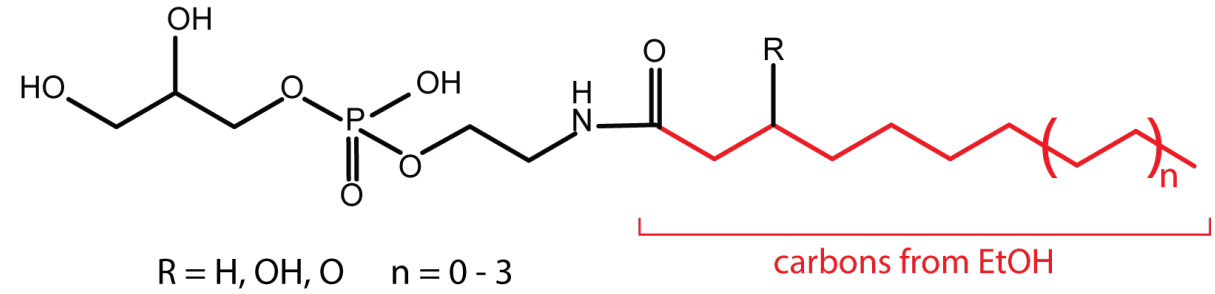

Figure 1.3: Glycerophosphoethanolamides are ethanol metabolites in L1 *C elegans*
Molecules with longer acyl chains are additionally glycosylated on one of the free glycerol hydroxyls, which suggests that these metabolites are tagged to be removed from the worm body.
This figure is copied from Artyukhin et al (2015) with permission.

but not methanol or n-propanol, could substitute for ethanol. The striking difference between even- and odd-chain alcohols suggested that it is not the alcohol molecule itself but rather its metabolites that may play a role in the process. To explore this possibility he examined aggregation behavior of worms with mutated alcohol dehydrogenase gene *sodh–1* (Alaimo et al. 2012; Williamson et al. 1991). He found that mutant L1s with a nonfunctional *sodh-1* gene did not aggregate on ethanol-containing plates. Furthermore, acetate can substitute for ethanol in the plates and support L1 aggregation. In fact, not only wild-type but also *sodh-1* mutant L1s were able to aggregate on acetate plates, clearly demonstrating that the requirement for ethanol can be bypassed by supplementation with its metabolite. (Butyrate, which is metabolized to two molecules of acetate, also works.) Thus, the aggregation signal appears to be downstream of acetate.

As a first step toward establishing how starved L1 worms respond to low doses of ethanol or acetate Alex performed differential LC/MS (liquid chromatography/mass spectroscopy—a method for identifying the components of complex chemical mixtures) analysis of the chemicals released by starving L1s in the absence or presence of 0.1% ethanol or butanol. He also compared results from wild-type worms with *sodh-1* mutants. He found dozens of compounds that were produced only in the presence of ethanol or were significantly increased compared to the control. Many of these required functional *sodh-1*. Subsequent MS/MS analysis led to structure elucidation of a large family of related metabolites, glycerophosphoethanolamides (Figure 1.3). By comparing fragmentation spectra of these molecules produced in the presence of normal vs. ^{13}C–labeled ethanol, he found that their acyl chains are built exclusively

from ethanol-derived carbons (shown in red in Figure 1.3). Most likely, acetate resulting from ethanol oxidation is used in *de novo* fatty acid biosynthesis to build C8–C14 fatty acids, which are then conjugated to phosphatidylethanolamine. Derivatives with β–hydroxy, β–keto as well as unsaturated chains appear to be intermediates from the fatty acid biosynthetic pathway, which further supports this hypothesis. These metabolites are also present in the medium when worms are exposed to acetate, butyrate, or n-butanol instead of ethanol. The two most abundant members of this series in *C elegans* L1 extracts are glycerophosphoethanolamides of decanoic and β–hydroxydecanoic acids (R = H, n = 1 and R = OH, n = 1 in Figure 1.3).

That the acyl chain carbons derive exclusively from ethanol was surprising. As described above, acetate is central to cellular metabolism. There is no cell in the body that lacks acetate, whether or not ethanol is present in the surroundings. Why doesn't some of that acetate show up in the acyl chains? Deepening the mystery, Alex found that on plates containing glucose or peptone (a protein source) but no ethanol, L1 larvae do not aggregate, even though glucose, a monosaccharide, can certainly be metabolized to produce acetate. He has also found recently that *C briggsae* will aggregate very slowly and loosely on acetate plates but not at all on plates containing only ethanol (as described above). They do not make glycerophosphoethanolamides from ethanol.

Together, these results suggest that the acetate produced from alcohol in the environment under conditions that promote L1 starvation is kept in a separate pool from other acetate in the worm's body, and that this pool is exclusively used to synthesize glycerophosphoethanolamides. Together these results suggest that aggregation is a specific response to the presence of ethanol/acetate in the environment. *C elegans* is a free-living nematode. In the wild, it forages for blooms of bacteria that arise in rotting fruit and other decomposing material (Felix and Braendle 2010). These environments often contain ethanol from fermentation of sugar.

What is the significance, if any, of glycerophosphoethanolamides for L1 aggregation? We of course made the obvious guess——that they might themselves be aggregation signals. This does not seem to be the case. glycerophosphoethanolamides added to the plates do not attract worms, nor do they interfere with aggregation when added at a uniform high concentration. Although frustrating, this result is not terribly surprising. Dozens, possibly hundreds of new chemicals are released by L1s in the presence of ethanol. Most of them are unidentified. The glycerophosphoethanolamides prove the existence theorem——the worms do indeed make and release into the environment specific chemicals under the very specific genetic and chemical conditions required for L1 aggregation. But the glycerophosphoethanolamides themselves play no direct role in aggregation, as far as we can detect. Simple calculations (described below) suggest that the hypothetical aggregation signal might be unstable, with a lifetime of at most hours, and therefore difficult to isolate.

In subsequent experiments, Alex found that many molecules with primary amino or SH groups (e.g. amino acids) are acetylated in the L1 conditioned medium in the presence of ethanol (Alex Artyukhin, personal communication, quoted by permission). This probably happens through acetyl-coenzyme A as it is quite reactive. It is also safe to assume, although Alex has not himself tested this, that under these conditions many lysine residues on proteins would be acetylated as well. Thus, buildup of acetate (and/or acetyl-coenzyme A) results in widespread acetylation of many small molecules and macromolecules in the cell.

1.2.3 L1 aggregation leads to longer starvation survival

While observing starved L1s on plates Alex noticed that larvae in aggregates survived starvation longer than individually dispersed worms. He hypothesized that longer survival in aggregates is mediated by higher local worm density. To examine the effect of worm density on L1 starvation survival quantitatively he carried out these experiments in liquid, where worm density can be easily controlled and adjusted and survival rates quantified (A B Artyukhin et al. 2013). He found that L1-arrested *C elegans* survived starvation in buffer significantly longer when they were starved at higher worm density (Figure 1.4a), referred to as density dependence hereafter. To check if this density dependence is mediated by chemical cues, he collected the medium from high density L1s starved for 24h (conditioned medium) and studied its effect on starvation survival of L1 larvae at low density. Conditioned medium extended L1 survival indicating that the density effect is mediated at least in part by released chemical(s) (1.4c). Several simple tests with size cut-off filters and lyophilization (freeze-drying) of conditioned medium led him to conclude that the active component was composed of nonvolatile small molecule(s) ($<3\,\mathrm{kDa}$). Alex tested the effect of *daf-22* conditioned medium in L1 survival of wild type (i.e., genetically normal) worms and found that it had an effect similar to wild-type conditioned medium. This result rules out ascarosides as necessary active ingredients of conditioned medium. So far, his attempts to isolate and identify the conditioned medium signal responsible for the density dependence using activity-guided fractionation and HPLC-MS analysis have failed. The only conclusion that we can state with reasonable confidence is that the activity results from a synergistic effect of several components.

Similar experiments with *C briggsae*, which, as described above, has no L1 aggregation, revealed that worm density has no effect on survival of *C briggsae* L1 larvae (Figure 1.4b) (Alexander B. Artyukhin et al. 2013). The apparent correlation between L1 aggregation and density dependence in *C elegans* and *C briggsae* suggests that these phenomena are related. Alex repeated the experiments with several wild isolates of *C elegans* and *C briggsae* and found consistent results——all *C elegans* strains that he tested had strong density dependence whereas survival of all *C briggsae* strains was independent of the density (Alexander B. Artyukhin et al.

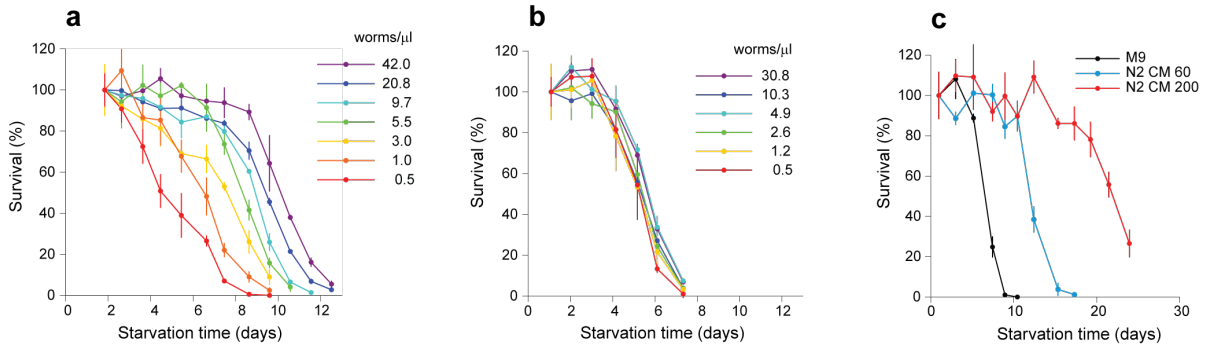

Figure 1.4: *C elegans* survives L1 starvation longer when starved at high density
Survival curves of *C elegans* (a) and *C briggsae* (b) in L1 starvation at different worm densities. (c) Conditioned medium from high density *C elegans* L1s extends survival at low density in a dose dependent manner. Black—survival curve in M9 buffer, blue and red—survival curves in conditioned medium prepared at 60 and 100 worms per µL respectively.
This figure is copied from Artyukhin et al (2013), with permission.

2013). Experiments with two other Caenorhabditis species (*C remanei*, *C. sp. 11*) revealed that L1s of the species that aggregate also have a strong density dependence and *vice versa* (Figure 1.5).

Alex then studied survival of *C elegans* L1s in conditioned medium from *C briggsae*. Although *C briggsae* did not have the density dependence, *C briggsae* conditioned medium extended survival of *C elegans* L1s. Combined with the lack of an effect in the opposite experiment, i.e. *C elegans* conditioned medium does not extend *C briggsae* L1 survival, this result suggests that *C briggsae* produces the signal responsible for longer survival at higher densities but does not respond to it. Conditioned medium from two other nematode species (*C sp. 11* and *Oscheius myriophila*) also extended *C elegans* L1 survival, confirming that the signals responsible for longer survival are quite general and not species-specific. Since the density effect in *C elegans* involves small-molecule signals, Alex hypothesized that the response pathway may start with sensory neurons, where these signals are first detected. In keeping with this model, he found that several chemosensory mutants had no or greatly diminished density dependence. Among these were *che-2*, *daf-6*, *osm-1*, *osm-3*, *osm-6*, and *tax-4* (Alexander B. Artyukhin et al. 2013). (Unlike the sensory mutant effects on aggregation, these effects on density dependence are completely clear.) These results confirm the hypothesis that the density dependence relies on diffusible, soluble signal(s). He also tested a *che-1* mutant (lacking functional ASE neurons) and worms with genetically ablated ASK neurons. Both had near normal density dependence,

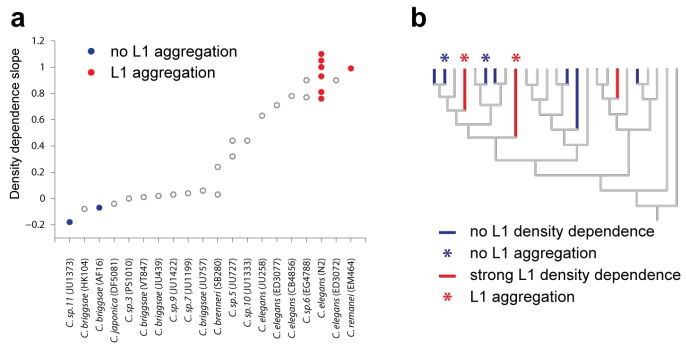

Figure 1.5: L1 aggregation and density dependence correlate across Caenorhabditis species.
(a) L1s of the species that show strong density dependence of starvation survival aggregate and *vice versa*. Density dependence slopes were obtained from linear regression of 50% survival times as a function of $\log_2$(worm density). (b) L1 aggregation and density dependence appeared independently several times during evolution of Caenorhabditis genus, which suggests that these traits are under positive selection.
This figure is copied from Artyukhin et al (2013), with permission.

indicating that neither of these two neuron types is individually necessary for the density effect.

Despite apparent mechanistic differences between L1 aggregation and density dependence, we think they are likely to be related phenomena. We believe that in species where survival through long starvation benefits from high worm density, aggregation is the natural way to concentrate worms and obtain locally high density. It is the first step in coping with long starvation.

1.2.4 Why does survival depend on density?

Density dependence would be easy to understand if the worms released into the medium something that was physically necessary for long survival: an energy source, for instance. This does not seem to be the case——the quantity of nutrient in conditioned medium is not sufficient to prolong survival (Alexander B. Artyukhin et al. 2013). That the density effect requires sensory neurons (see above) suggests that what the conditioned medium provides is information. There is additional evidence to make this plausible——mutant worms with reduced insulin signaling also survive L1 starvation longer (Baugh 2013; Lee et al. 2012).

It is worth taking a moment to appreciate that this is surprising. The hypothesis is that, unless

they receive certain information, the physiology of starving L1s changes in a way that causes them to die. This implies that dying early at low density is a choice——there is no physical reason why those worms that die could not have lived. How can it possibly be to the advantage of an animal, no matter what information it receives or fails to receive, to die earlier than it is forced to? This question is especially acute so early in the worm's life, before it has had an opportunity to contribute to its own or others' reproductive success. (One obvious answer, that in dying worms release nutrients that allow their sisters to survive, is implausible because of the same experiments that show that the survival factors in conditioned medium are not nutrients.)

This paradox is easier to resolve with the help of the word "risk": perhaps there is a benefit that accrues to worms that risk early death. Here, for example, is a possibility: Suppose that, to survive, a worm must keep its metabolism running at some positive rate. If it runs out of energy, it dies. Metabolic rate can be lowered almost to zero. A worm that maintains a fairly high metabolic rate while starving risks early death, but if food appears soon enough, it can immediately start growing again. A worm that slows its metabolism down must take some time to get everything running again when food appears, so it will resume growth with a delay. A worm population can double in about 11 hours (Leon Avery 2014), so a worm whose development is delayed 11 hours has only half the reproductive value of a worm that is able to start growing immediately.

This idea has the advantage of being consistent with observation. L1s fed after one or two days of starvation recover and grow immediately, while those fed after two weeks of starvation recover with a variable delay, on the rough order of one day. Furthermore, the mutants with reduced insulin signaling that survive longer than normal worms have reduced metabolic rate (Lee et al. 2012) and their recovery is variably delayed compared to normal worms, even after brief starvation (Youngjai You, personal communication).

Thus, we propose that if worm density is low, the best strategy for an individual hungry worm may be to explore the surroundings and search for food. Absence of outside starvation signals tells the worms that there are not many competitors around, so chances for finding something eatable may be reasonable. But when population density is high, worms receive starvation signals from each other, which tell them that the famine is widespread and/or has been around for some time. In this situation the chance of finding food is low, which suggests that one would be better off minimizing unnecessary energy expenditure and preparing for a long battle for survival——worms aggregate.

Based on this hypothesis we would predict that lack of aggregation and density dependence in *C briggsae* and some other Caenorhabditis species implies that their starved L1s seldom find themselves at high density in nature, so their optimal strategy is to disperse and actively look for food. In variable and unpredictable environments genotypic fitness can be maximized either

by reducing individual-level variance in fitness or by reducing between-individual correlations in fitness (or some combination of the two) (Starrfelt and Kokko 2012). Aggregating species may choose to minimize individual-level variance by having a mechanism that helps them to acquire more accurate information about their environment. Non-aggregating species may use dispersal as a strategy to minimize between-individual correlations.

1.2.5 Other examples of *C elegans* aggregation behavior

As mentioned above, it has been known for many years that in the presence of food (bacteria), most true wild isolates of *C elegans* aggregate, a behavior known as social feeding (Bono and Bargmann 1998; Bono, Tobin, et al. 2002). (To my knowledge, it was first reported informally by Randy Cassada in 1987.) Wild strains of *C elegans* prefer low concentrations of oxygen, and we have speculated that the consumption of oxygen in an aggregate of worms lowers oxygen concentration and thereby attracts more worms, although this explanation is disputed (Ding et al. 2019). The usual *C elegans* laboratory strain, N2, has sustained a gain-of-function mutation in the neuropeptide receptor gene *npr–1* and is, as a result, less sensitive to oxygen than wild strains (Bono and Bargmann 1998)——it therefore does not display social feeding at ordinary oxygen levels. (Confusingly, N2 is generally referred to as the "wild type"—even though it has many genetic differences from any true wild strain of *C elegans*——"Wild type" is the usual geneticist's term for the base laboratory strain of an organism.) A mathematical model of social feeding has recently been published (Ding et al. 2019).

Observations of a different type of aggregation have recently been published, together with a model (Sugi et al. 2019). This form occurs in the long-term survival form of the worm—the dauer larva— and is probably mediated largely by a simple physical mechanism, surface tension.

1.3 Goals of mathematical modeling

In this dissertation I develop a model for L1 aggregation based on the famous Keller-Segel model (Keller and Segel 1970). My goal is to use it for numerical experiments whose results can be compared to those of past and future real experiments to be carried out on living animals. Some of the specific goals are:

1. **Reproducing the phenomenon of *C elegans* L1 aggregation.**

2. **Understanding how the pattern of aggregates forms.**

3. **Estimating behavioral and chemical parameters.** These parameters are numerical constants that describe such things as how rapidly chemical signals decay and how strongly worms respond to them.

4. **Working out how to quantify aggregation.**

5. **Simulating individual worm movements.**

Goals 1 – 3 are addressed in subsequent chapters — 4 – 5 are left for future work.

1.4 The Keller-Segel Model

The model that I employ for *C elegans* aggregation is similar to one published by Evelyn Keller and Lee Segel (1970) to explain the aggregation of cellular slime molds. This model has since become one of two principal models for pattern formation in mathematical biology. (The other is Turing (1952) instability.) Of the Keller-Segel model Gurusamy and Balanchandran (2018) remark, "Chemotaxis . . . can be modelled by [a] system of partial differential equations and this system of equations is one of the favorite playgrounds of theoretical and numerical analysis." The literature on the Keller-Segel system is therefore large and has been well-reviewed. Sections 11.1 – 11.3 of Edelstein-Keshet's textbook *Mathematical Models in Biology* (2005) are an accessible introduction. Horstmann (2003; 2004) presents a comprehensive overview of the mathematics of the Keller-Segel system, while Hillen and Painter's (2009) review focuses on biologically plausible variations of the model. Since these excellent reviews exist, I will not here attempt a comprehensive survey. I will merely discuss the results of past work that will be most helpful in understanding subsequent chapters.

Cellular slime molds such as *Dictyostelium discoideum* are single-celled amoebae that feed on bacteria. When the food runs out, they stream together into aggregates that erect an elevated spore-filled structure called a fruiting body. It was proposed that to aggregate they secrete an attractant called acrasin (later identified as cyclic adenosine monophosphate (cAMP)). It was thought that any local fluctuation towards increased cell density would become a local source of acrasin and thereby lead to spontaneous aggregate formation. Evelyn Keller and Lee Segel (1970) published a simple model that demonstrated that this mechanism could work. The model comprises two PDEs, one for the acrasin, and one for the cells, represented by twice-differentiable positive functions $U(t, x)$ and $\rho(t, x)$ respectively. Although they first develop the

model in a quite general form, Keller and Segel (1970) focus their attention on a simple variation. Most subsequent analysis has focused on an even simpler variation, the "minimal system" of Childress and Percus (1981). This is the minimal system:

$$\begin{aligned} \rho_t(t,\mathbf{x}) &= -\nabla_{\mathbf{x}} \cdot (\beta\rho(t,\mathbf{x})\nabla_{\mathbf{x}} U(t,\mathbf{x})) + \sigma\nabla^2_{\mathbf{x}}\rho(t,\mathbf{x}), \quad t>0, \mathbf{x}\in\Omega\subseteq\mathbb{R}^d \\ U_t(t,\mathbf{x}) &= -\gamma U(t,\mathbf{x}) + D\nabla^2_{\mathbf{x}} U(t,\mathbf{x}) + s\rho(t,\mathbf{x}), \qquad t>0, \mathbf{x}\in\Omega\subseteq\mathbb{R}^d \end{aligned} \tag{1.1}$$

$\rho(t,\mathbf{x})$ is the local density of cells
$U(t,\mathbf{x})$ is the local concentration of acrasin
$d\in\mathbb{Z}_{>0}$ is the spatial dimension
$\beta>0$ is the chemotactic sensitivity of the cells to acrasin
$\sigma>0$ quantifies the random movement of the cells
$\gamma>0$ is the spontaneous decay rate of acrasin
$D>0$ is the diffusion constant of acrasin
$s>0$ is the rate of secretion of acrasin per cell

The ρ PDE is an advection-diffusion equation. The diffusion term $\sigma\nabla^2\rho$ results from random movement of the cells. The advection term $\nabla\cdot(\beta\rho\nabla U)$ represents movement with mean velocity $v = \beta\nabla U$ in the direction in which acrasin concentration most rapidly increases. It may seem surprising that chemotaxis is modeled as cells responding to the gradient of attractant, rather than the concentration itself. This is, however, a characteristic of real chemotactic responses, at least approximately. Single cells can do calculus. Even bacteria!

Our hypothesis is that worms aggregate by a mechanism similar to that used by *Dictyostelium discoideum*. We therefore propose to model *C elegans* L1 aggregation by a similar pair of PDEs. In this case ρ (in worms/cm^{d}) will represent the local density of worms and U the concentration of an unknown chemical attractant released by the worms.

Most analysis has focused on the case with reflecting boundaries,

$$\frac{\partial\rho}{\partial n} = \frac{\partial U}{\partial n} = 0, \qquad t>0, \mathbf{x}\in\partial\Omega, \tag{1.2}$$

where $\partial/\partial n$ represents the derivative along the normal to the boundary. These boundary conditions imply that the number of cells is conserved, i.e. $\frac{\mathrm{d}}{\mathrm{d}t}\int_\Omega \rho \mathrm{d}\mathbf{x} = \frac{\mathrm{d}}{\mathrm{d}t}N_0 = 0$, since ρ_t can be

expressed as a pure divergence of something, $\rho\nabla(\beta U + \sigma \log \rho)$, that vanishes normal to $\partial\Omega$. Acrasin is not conserved, but its total tends exponentially toward $\bar{U}|\Omega| = N_0 s/\gamma$. ($|\Omega| = \int_\Omega \mathrm{d}\mathbf{x}$ is the measure of the domain.)

Although each of equations (1.1) is linear and homogeneous in the variable whose time-derivative it determines, the system as a whole is nonlinear because of the quadratic $\rho\nabla U$ term. To be clear, if both ρ and U are doubled (and if ρ alone is doubled, then in the long run $\int U$ will likewise be doubled), the magnitude of the $\rho\nabla U$ term increases four-fold, and its importance relative to other terms increases two-fold. Subtle though this nonlinearity may seem, it has two dramatic consequences: density-dependent instability and finite-time blowup.

1.4.1 Density-dependent instability

This is the effect for which the Keller-Segel model was conceived. System (1.1) always has a uniform equilibrium: $\rho(t, \mathbf{x}) = \bar{\rho} = N_0/|\Omega|$, $U(t, \mathbf{x}) = \bar{U} = \bar{\rho}s/\gamma$. On a very large domain, i.e. $|\Omega| \to \infty$, the uniform equilibrium is stable if average density $\bar{\rho}$ is below the threshold density $\rho_{\text{thresh}} = \sigma\gamma/(\beta s)$ and unstable if $\bar{\rho} > \rho_{\text{thresh}}$. Equivalently there is a threshold for equilibrium acrasin concentration $U_{\text{thresh}} = \sigma/\beta$. The parameter dependence is in the expected direction for each parameter: faster random cell movement (high σ) and greater instability of the attractant (higher γ) oppose the formation of aggregates, i.e., raise the threshold for aggregation, while stronger response to acrasin (high β) and increased acrasin secretion (high s) favor aggregation, i.e. lower the threshold. Aggregation is more difficult on small domains (fewer cells overall), as I will presently show. The argument for density-dependent instability by linear stability analysis is simple enough to be worth outlining here. We imagine a system close to the uniform equilibrium and express density and signal concentration as sums of the equilibrium functions and a small deviation. We then derive PDEs for the deviation from the original PDEs. If the deviations are small, these PDEs can be approximated by a system of linear homogeneous PDEs, which can be solved exactly. The exact form of these solutions is not so important as their time dependence—do they grow or shrink? If they shrink, the equilibrium is stable, and the organisms can remain at equilibrium indefinitely. If the deviations grow with time the equilibrium is unstable, and typically cannot be maintained for long.

Consider a population near the uniform equilibrium $\rho(0, \mathbf{x}) \approx \bar{\rho}$, $U(0, \mathbf{x}) \approx \bar{U}$. Then, let $\rho(t, \mathbf{x}) = \bar{\rho} + \delta\rho(t, \mathbf{x})$, $U(t, \mathbf{x}) = \bar{U} + \delta U(t, \mathbf{x})$. Because $(\bar{\rho}, \bar{U})$ is an equilibrium, $\rho_t(t, \mathbf{x}) = \delta\rho_t(t, \mathbf{x})$ and $U_t(t, \mathbf{x}) = \delta U_t(t, \mathbf{x})$. Substituting into (1.1),

$$\delta\rho_t(t,\mathbf{x}) = -\nabla\cdot\left(\beta\delta\rho\nabla\bar{U} + \beta\bar{\rho}\nabla\delta U\right) - \nabla\cdot(\beta\delta\rho\nabla\delta U) + \sigma\nabla^2\bar{\rho} + \sigma\nabla^2\delta\rho \tag{1.3}$$

$$\delta U_t(t,\mathbf{x}) = -\gamma\delta U + D\nabla^2\delta U + s\delta\rho \tag{1.4}$$

$\nabla\bar{U} = \nabla^2\bar{\rho} = 0$. Ignoring the second order term $\nabla\cdot(\beta\delta\rho\nabla\delta U)$, we have, to first order, the linear vector PDE,

$$\frac{\partial}{\partial t}\begin{pmatrix}\delta\rho\\ \delta U\end{pmatrix} = \begin{pmatrix}\sigma\nabla^2 & -\beta\bar{\rho}\nabla^2\\ s & -\gamma + D\nabla^2\end{pmatrix}\begin{pmatrix}\delta\rho\\ \delta U\end{pmatrix} \tag{1.5}$$

This is easily solved by separation of variables. Eigenfunctions are of the form

$$\begin{pmatrix}\delta\rho(t,\mathbf{x})\\ \delta U(t,\mathbf{x})\end{pmatrix} = \begin{pmatrix}\rho_{\mathbf{k}}e^{\lambda_{\mathbf{k}}t}e^{i\mathbf{k}\cdot\mathbf{x}}\\ U_{\mathbf{k}}e^{\lambda_{\mathbf{k}}t}e^{i\mathbf{k}\cdot\mathbf{x}}\end{pmatrix} \tag{1.6}$$

$\mathbf{k}$ is a wavenumber vector, i.e., a vector of frequency in each spatial direction. Substituting into (1.5) produces the 2×2 matrix eigenvalue problem,

$$\lambda_{\mathbf{k}}\begin{pmatrix}\rho_{\mathbf{k}}\\ U_{\mathbf{k}}\end{pmatrix} = \begin{pmatrix}-\sigma k^2 & \beta\bar{\rho}k^2\\ s & -\gamma - Dk^2\end{pmatrix}\begin{pmatrix}\rho_{\mathbf{k}}\\ U_{\mathbf{k}}\end{pmatrix} \tag{1.7}$$

where $k^2 = \|\mathbf{k}\|^2$. Every solution of the linearized system (1.7) is a linear combination of functions (1.6) where $(\rho_{\mathbf{k}}, U_{\mathbf{k}})^\intercal$ is an eigenvector of the matrix in (1.7). If, for every $\mathbf{k}$, $\mathrm{Re}(\lambda_{\mathbf{k}}) < 0$ then any small fluctuation away from the uniform equilibrium will die away, and it will be stable. If, however, there exists a $\mathbf{k}$ such that the matrix has an eigenvalue with positive real part, then the uniform equilibrium is unstable. The trace of the matrix (which is the sum of the two eigenvalues) is negative, $-\sigma k^2 - \gamma - Dk^2 < 0$, so the only possible way to have an eigenvalue with positive real part is if both eigenvalues are real, one positive and one negative. Thus, instability is expected if and only if the determinant is negative,

$$\begin{vmatrix}-\sigma k^2 & \beta\bar{\rho}k^2\\ s & -\gamma - Dk^2\end{vmatrix} < 0 \tag{1.8}$$

$$D\sigma k^4 + (\gamma\sigma - \beta s\bar{\rho})\,k^2 < 0 \tag{1.9}$$

Obviously, (1.9) can hold only if $\gamma\sigma - \beta s\bar{\rho} < 0$, and, if that condition holds, then for some small enough k^2, the negative k^2 term will dominate the positive k^4 term and the determinant

will be negative. Thus, ignoring boundary conditions, first-order instability occurs if and only if $\gamma\sigma - \beta s\bar{\rho} < 0$. This is the condition I gave above.

It will be important later that condition (1.9) has no nontrivial minimum wavenumber. That is, there is no natural maximum scale for the aggregates that form when the density exceeds threshold. It is true that the acrasin has a natural range, $\kappa = \sqrt{D/\gamma}$—the distance an average molecule diffuses before it decays. However, cells attract each other, albeit weakly, even when they are further from each other than this. There is thus no mechanism in the minimal model (1.1) that would not favor the merging of aggregates to unlimited size. I will eventually be forced to propose a two-signal (attractant + repellent) model in order to explain the experimental observation that aggregates of *C elegans* L1s have a characteristic size. Keller and Segel (1970) were aware of this weakness: in an appendix, they lament the inability of their linearized model to account for the pattern formation observed in actual *Dictyostelium discoideum* aggregation.

In accord with this, restricting the size of aggregates, for instance by making the domain Ω smaller, makes aggregation more difficult, increasing the threshold density. When the domain Ω is finite, there will be a minimum wavenumber nontrivial eigenfunction of the Laplacian consistent with boundary conditions. For instance, in the one-dimensional problem with $\Omega = [0, L]$, the real eigenfunctions consistent with Neumann boundary conditions (1.2) are $\cos(kx), k \in (\pi/L)\mathbb{Z}_+$. Instability results only if determinant (1.8) is negative for $k = \pi/L$, leading to this threshold for instability

$$\rho_{\text{thresh}} = \frac{\sigma}{\beta s}\left(\gamma + \frac{\pi^2 D}{L^2}\right) \tag{1.10}$$

1.4.2 Finite-time blow-up

The second consequence of nonlinearity is even more dramatic. Although global time solutions always exist in one dimension, in two or more dimensions, aggregation, once it begins, may not halt short of infinite density. Even more surprising, infinite density is reached with the formation of a Dirac delta function-like singularity in finite time, called "blow-up". In two dimensions blow-up can occur only if a minimum critical number of cells is present. In three or more dimensions, blow-up is possible with any number of cells. The possibility of blow-up was first conjectured by Childress and Percus (1981) and subsequently proved in a series of papers by other authors (Ferkey et al. 2007; Miguel A. Herrero and Velázquez 1996; M A Herrero et al. 1997; Nagai and Senba 1997; Nagai and Senba 1997; Toshitaka Nagai et al. 1997; Senba and Suzuki 2001; W. Jäger and Luckhaus 1992), usefully summarized by Horstmann (2003; 2004).

One may discern two attitudes towards blow-up in the Keller-Segel literature. To authors whose primary interest is mathematics, blow-up is clearly the most fascinating characteristic of the system. But for those who are interested in the Keller-Segel system as a model of biology, blow-up is at least an annoyance (if not a catastrophic failure of the model). It goes without saying that aggregating *Dictyostelium discoideum* amoebae don't actually collapse into miniature black holes. Some, e.g. Horstmann (2004) argue (not entirely implausibly) that blow-up has meaningful biological interpretations. But blow-up is particularly a problem for those, like me, who are interested in equilibria of the system.

Some authors refer to blow-up in the Keller-Segel model as "chemotactic collapse" (Childress and Percus 1981). This is a misleading name, because chemotaxis *per se* can never lead to collapse to infinite density. Rather, the collapse is a consequence of a biologically unrealistic model. It is not difficult to see which features of the model lead to this absurdity. First, there is nothing in the minimal model (1.1) that reflects the reality that cells take up space. The random movement term of the ρ PDE, $\sigma\nabla^2\rho$, does indeed produce a kind of pressure that resists compression, but it can be overwhelmed by a stronger attractive force. And the force of attraction $\beta\nabla U$, is unbounded. It is plausible, if you like chocolate, that you will experience an impulse to move from places where chocolate is scarce to places where chocolate is abundant. But the strength of this impulse does not increase without bound as the gradient of chocolate becomes steeper. It is a near-universal characteristic of biological responses that they saturate, i.e., the response levels out as the strength of the stimulus becomes large (Kahneman and Tversky 1979; Fechner 1860).

Researchers interested in the Keller-Segel model as a model of biology therefore typically use versions more complicated than the minimal model The Hillen and Painter (2009) review, for instance, is largely a description of biologically plausible modifications of the minimal model whose solutions exist globally in time. The U PDE is an unproblematic reaction diffusion equation and is often used exactly as presented in (1.1). Most model modifications affect the ρ PDE. For instance, a general form of the ρ PDE with no cell growth or death is,

$$\rho_t(t,\mathbf{x}) = -\boldsymbol{\nabla}\cdot\rho(t,\mathbf{x})\mathbf{v}\left(\rho(t,\mathbf{x}), U(t,\mathbf{x}), \nabla\rho(t,\mathbf{x}), \nabla U(t,\mathbf{x})\right) \tag{1.11}$$

$\mathbf{v}(\rho, U, \nabla\rho, \nabla U)$ is the mean velocity of cells as a function of density, acrasin concentration, and their gradients. Equation (1.11) is so general as to be virtually useless. I will use the following system for worms, with appropriately chosen V_U and V_ρ:

$$\rho_t = \nabla\cdot\left(\rho\nabla\left(V_U(U) + V_\rho(\rho) - \sigma\log\rho\right)\right) \tag{1.12}$$

$$U_t = -\gamma U + D\nabla^2 U + s\rho \tag{1.13}$$

The design of PDE (1.12) and the functions V_U and V_ρ is described in section 3.1.2. PDE (1.12) corresponds to (1.11) with

$$\mathbf{v}(\rho, U, \nabla\rho, \nabla U) := -\nabla\left(V_U(U) + V_\rho(\rho) - \sigma\log\rho\right) \tag{1.14}$$

$$= -\left(V_U'(U)\nabla U + V_\rho'(\rho)\nabla\rho - \frac{\sigma}{\rho}\nabla\rho\right) \tag{1.15}$$

The intention behind this form is to regard $V(t, \mathbf{x}) = V_U(U(t, \mathbf{x})) + V_\rho(\rho(t, \mathbf{x}))$ as a potential energy down which worms want to move. The minimal model (1.1) is recovered with $V_U(U) = -\beta U$, $V_\rho(\rho) = 0$.

1.4.3 Free energy functionals

Free-energy functionals are one of the most useful tools in analysis of the Keller-Segel system. A free energy functional maps a pair of functions $\rho, U \in C^1(\mathbb{R} \times \Omega)$ to a single real number. Like thermodynamic free energy, it has the form $E - TS$, where E is a functional that looks like some sort of energy, T is a positive number (like a temperature) that quantifies cell activity, and $S = -\int_\Omega \rho\log\rho\,\mathrm{d}\mathbf{x}$ is entropy (Baek and Kim 2017). (The value of $0\log 0$ is taken to be 0, as usual in entropy calculations.) In the Keller-Segel literature, these free energy functionals are usually referred to as Lyapunov functionals, even though they may not be locally positive definite. In fact, under conditions where blow-up occurs, the free energy is not even bounded below.

A free-energy functional for the minimal system (1.1) was described independently in three papers (Biler 1998; Gajewski et al. 1998; Nagai and Senba 1997). Here it is

$$\mathscr{F}(\rho, U) \coloneqq \int_\Omega \left(\frac{\beta}{s} \left(\frac{D}{2} \|\nabla U\|^2 + \frac{\gamma}{2} U^2 \right) - \beta \rho U + \sigma \rho \log \rho \right) \mathrm{d}\mathbf{x} \tag{1.16}$$

$$= E_U + E_\rho - T S_\rho$$

$$E_U = \frac{\beta}{s} \int_\Omega \left(\frac{D}{2} \|\nabla U\|^2 + \gamma U^2 \right) \mathrm{d}\mathbf{x} \tag{1.17}$$

$$E_\rho = -\beta \int_\Omega \rho U \mathrm{d}\mathbf{x} \tag{1.18}$$

$$T = \sigma \tag{1.19}$$

$$S_\rho = -\int_\Omega \rho \log \rho \mathrm{d}\mathbf{x} \tag{1.20}$$

$\mathscr{F}$ is the free energy functional

$\rho, U, \beta, D, \gamma$ and σ are as in (1.1)

E_U is energy that can be ascribed to the nonuniform distribution of acrasin

E_ρ is energy ascribed to the interaction of cells with acrasin

S_ρ is the entropy of the distribution of cells

T plays the role of a temperature, i.e. a measure of random movement

Free energy functional $\mathscr{F}$ is designed to have the property of decreasing with time: $\dot{\mathscr{F}} = \partial \mathscr{F}(\rho(t, \mathbf{x}), U(t, \mathbf{x})/\partial t \leq 0$, with equality only at equilibrium. There is no explanation for the form of (1.16) other than that it is a functional of ρ, U that accomplishes this goal. To see that it does, differentiate (1.16) with respect to time:

$$\dot{\mathscr{F}} = \int_\Omega \left(\frac{\beta}{s} \left(D \nabla U \cdot \nabla \dot{U} + \gamma U \dot{U} \right) - \beta \rho \dot{U} - \beta U \dot{\rho} + \sigma \dot{\rho} + \sigma \dot{\rho} \log \rho \right) \mathrm{d}\mathbf{x} \tag{1.21}$$

Since cells are conserved (with boundary condition (1.2)), $\int_\Omega \dot{\rho} \mathrm{d}\mathbf{x} = 0$ and the term $\sigma \dot{\rho}$ vanishes on integration. We can isolate a factor of $\dot{U}$ from the $\nabla U \cdot \nabla \dot{U}$ term by integration by parts (IBP):

$$\int_\Omega \nabla U \cdot \nabla \dot{U} \mathrm{d}\mathbf{x} = -\int_{\partial\Omega} \dot{U} \nabla U \cdot \mathrm{d}\mathbf{n} - \int_\Omega \dot{U} \nabla \cdot \nabla U \mathrm{d}\mathbf{x} = -\int_\Omega \dot{U} \nabla^2 U \mathrm{d}\mathbf{x} \tag{1.22}$$

The boundary integral vanishes because of the boundary condition (1.2). (Henceforth, I will silently omit vanishing boundary integrals.) Thus (1.21) becomes

$$\dot{\mathscr{F}} = \frac{\beta}{s}\int_{\omega}(-D\nabla^2 U + \gamma U - s\rho)\dot{U}\mathrm{d}\mathbf{x} + \int_{\Omega}(-\beta U + \sigma\log\rho)\dot{\rho}\mathrm{d}\mathbf{x} \tag{1.23}$$

$$= \frac{\beta}{s}\int_{\Omega} -(-\gamma U + D\nabla^2 U + s\rho)(-\gamma U + D\nabla^2 U + s\rho)\mathrm{d}\mathbf{x} \tag{1.24}$$

$$+ \int_{\Omega}\nabla\cdot(\rho(\nabla(-\beta U + \sigma\log\rho)))\,(-\beta U + \sigma\log\rho)\mathrm{d}\mathbf{x}$$

after using (1.1) to replace $\dot{U}$ and $\dot{\rho}$. Integrating by parts in the second integral,

$$\dot{\mathscr{F}} = -\frac{\beta}{s}\int_{\Omega}(-\gamma U + D\nabla^2 U + s\rho)^2\mathrm{d}\mathbf{x} - \int_{\Omega}\rho\|\nabla(-\beta U + \sigma\log\rho)\|^2\mathrm{d}\mathbf{x} \leq 0 \tag{1.25}$$

Most of the terms in the free energy integrand have straightforward origins and can be identified with single terms in the PDEs (conveniently labeled by the parameters D, γ, σ). The exception is the potential energy term $-\beta\rho U$. When differentiated this term gives rise via the Leibnitz rule to terms that match the $-\beta\nabla U$ advection term in the ρ PDE and to the $s\rho$ secretion term in the U PDE. With adroit scaling (the β/s factor in the E_U integral), these can be made to match up. It is not always possible, for an arbitrary Keller-Segel model (1.11), (1.12) to achieve this fortuitous correspondence.

The worm system (1.12) cannot be analyzed by approaches previously used for Keller-Segel variants. Horstmann (2001) developed a systematic approach for the construction of free energy functionals. Applied to the worm system (1.12), it is as follows. If there exists a function $R(\rho)$ such that

$$R''(\rho) = s\frac{\rho V_\rho'(\rho) + \sigma}{-\rho V_U'(U)}, \tag{1.26}$$

and $R''(\rho) \geq 0$, then a time-decreasing free energy functional exists

$$\mathscr{H}(\rho, U) = \int_{\Omega}\left(\frac{D}{2}\|\nabla U\|^2 + \frac{\gamma}{2} + R(\rho) - s\rho U\right)\mathrm{d}\mathbf{x} \tag{1.27}$$

In the minimal system (1.1) R is the entropy term of the functional. It may seem that condition (1.26) is simple to fulfill—one need only integrate the right-hand-side twice. The functional $\mathscr{H}$ is useful even if R'' is not positive, since equilibria of the PDE system are stationary

points of $\mathscr{H}$ even if R is not convex. The problem, however, is that R must depend only on ρ. In general the right-hand-side of (1.26) depends on U. This will be true for all models I propose to explain *C elegans* L1 aggregation.

I have developed a different method of finding free energy functionals, which I will describe in chapter 2. This method produces useful approximate results even for the worm system.

1.4.4 Free energy and blow-up

Let us use the free energy functional (1.16) to better understand blow-up in the minimal system. Following earlier work (Horstmann 2003; Horstmann 2004, and papers cited therein), I will show conditions under which $\mathscr{F}$ is not bounded below. Let $\Omega = \mathbb{R}^d$. (The argument I am about to make works equally well on finite domains, but the Green's functions are messy. For purposes of exposition, the infinite domain is simpler.) Assume that $N_0 = \int_\Omega \rho \mathrm{d}\mathbf{x} < \infty$. I will now show conditions under which $\mathscr{F}(\rho, U)$ can be made arbitrarily negative. For $r > 0$, Define

$$\rho_r(\mathbf{x}) \coloneqq \frac{N_0}{|B_r|}\theta(r - \|\mathbf{x}\|) \tag{1.28}$$

B_r is the open ball of radius r centered at the origin and $|B_r|$ is its measure, i.e. $2r$ in one dimension, πr^2 in two, $\frac{4}{3}\pi r^3$ in three. The Heaviside θ function is, as usual,

$$\theta(x) \coloneqq \begin{cases} 0 & \text{if } x \leq 0 \\ 1 & \text{if } x > 0 \end{cases} \tag{1.29}$$

Thus ρ_r is the configuration of N_0 cells distributed uniformly in the ball of radius r. Now, let U_r be the acrasin concentration function in equilibrium with ρ_r, i.e. the solution of

$$0 = -\gamma U_r(\mathbf{x}) + D\nabla^2 U_r(\mathbf{x}) + s\rho_r(\mathbf{x}) \tag{1.30}$$

$U_r = g_d * \rho_r$, i.e. the convolution of the Green's function for (1.30) with the density function. (See Section 2.4.1.) The Green's functions in 1, 2, and 3 dimensions are as follows

$$g_1(x) = \frac{s}{2\gamma\kappa} e^{-\frac{|x|}{\kappa}} \tag{1.31}$$

$$g_2(\mathbf{x}) = \frac{s}{2\pi\gamma\kappa^2} K_0(\|\mathbf{x}\|/\kappa) \tag{1.32}$$

$$g_3(\mathbf{x}) = \frac{s}{4\pi\gamma\kappa^2} \frac{e^{-\|\mathbf{x}\|/\kappa}}{\|\mathbf{x}\|} \tag{1.33}$$

$$\kappa = \sqrt{D/\gamma}$$

K_0 is a modified Bessel function of the second kind

Now I will estimate $\mathscr{F}(\rho_r, U_r)$ for $d = 1, 2, 3$ and how it varies as a function of r.

$$\mathscr{F}(\rho_r, U_r) = \int_\Omega \left(\frac{\beta}{s} \left(\frac{D}{2} \|\nabla U_r\|^2 + \frac{\gamma}{2} U_r^2 \right) - \beta \rho_r U_r + \sigma \rho_r \log \rho_r \right) \mathrm{d}\mathbf{x} \tag{1.34}$$

Using integration by parts, $\int \|\nabla U\|^2 \mathrm{d}\mathbf{x} = \int \nabla U \cdot \nabla U \mathrm{d}\mathbf{x} = -\int U \nabla^2 U \mathrm{d}\mathbf{x}$,

$$\mathscr{F}(\rho_r, U_r) = \int_\Omega \left(\frac{\beta}{s} \left(-\frac{D}{2} U_r \nabla^2 U_r + \frac{\gamma}{2} U_r^2 \right) - \frac{\beta \rho_r U_r}{2} - \frac{\beta \rho_r U_r}{2} + \sigma \rho_r \log \rho_r \right) \mathrm{d}\mathbf{x} \tag{1.35}$$

$$= \int_\Omega \left(\frac{\beta}{s} \left(-\frac{D}{2} U_r \nabla^2 U_r + \frac{\gamma}{2} U_r^2 - \frac{s \rho_r U_r}{2} \right) - \frac{\beta \rho_r U_r}{2} + \sigma \rho_r \log \rho_r \right) \mathrm{d}\mathbf{x} \tag{1.36}$$

$$= \int_\Omega \left(-\frac{1}{2} \frac{\beta}{s} \left(D \nabla^2 U_r - \gamma U_r + s \rho_r \right) U_r - \frac{\beta \rho_r U_r}{2} + \sigma \rho_r \log \rho_r \right) \mathrm{d}\mathbf{x} \tag{1.37}$$

$$= \int_\Omega \left(-\frac{\beta \rho_r U_r}{2} + \sigma \rho_r \log \rho_r \right) \mathrm{d}\mathbf{x}, \tag{1.38}$$

using (1.30) in the last step. To proceed, we need an estimate of U_r within B_r. The distance from any point in B_r to any other is less than $2r$. At equilibrium, then, the concentration of acrasin at any point in B_r is greater than that produced by a point source of N_0 cells at a distance $2r$, i.e.,

$$\forall \mathbf{x} \in B_r, \quad U_r(\mathbf{x}) > N_0 g_d(2r), \tag{1.39}$$

whence

$$\int_\Omega \rho_r(\mathbf{x})U_r(\mathbf{x})\mathrm{d}\mathbf{x} = \int_{B_r} \frac{N_0}{|B_r|}U_r(\mathbf{x})\mathrm{d}\mathbf{x} \tag{1.40}$$

$$> \int_{B_r} \frac{N_0}{|B_r|}N_0 g_d(2r)\mathrm{d}\mathbf{x} \tag{1.41}$$

$$= N_0^2 g_d(2r) \tag{1.42}$$

The entropy term is

$$\int_\Omega \sigma\rho_r \log\rho_r \mathrm{d}\mathbf{x} = \int_{B_r} \log\frac{N_0}{B_r} = \sigma N_0 \log\frac{N_0}{B_r} \tag{1.43}$$

Let's deal first with $d = 1, 3$, since those are the simplest. In one dimension we have not only a lower bound for U_r within B_r but also an upper bound, since the Green's function is finite at $x = 0$.

$$N_0 g_1(2r) < U_r(x) < N_0 g_1(0) \tag{1.44}$$

$$\frac{N_0 s}{2\gamma\kappa} < U_r(x) < \frac{N_0 s}{2\gamma\kappa} \tag{1.45}$$

$$\mathscr{F}(\rho_r, U_r) = \int_\Omega \left(-\frac{\beta\rho_r U_r}{2} + \sigma\rho_r\log\rho_r\right)dx \tag{1.46}$$

$$-\frac{\beta s N_0^2}{2\gamma\kappa} + \sigma N_0 \log\frac{N_0}{2r} < \mathscr{F}(\rho_r, U_r) < -\frac{\beta s N_0^2}{2\gamma\kappa}e^{-2r/\kappa} + \sigma N_0\log\frac{N_0}{2r} \tag{1.47}$$

In one dimension, $\lim_{r\to 0}\mathscr{F}(\rho_r, U_r) = +\infty$. There is thus no tendency to collapse to a point.

In three dimensions

$$\mathscr{F}(\rho_r, U_2) = \int_\Omega \left(-\frac{\beta\rho_r U_r}{2} + \sigma\rho_r\log\rho_r\right)\mathrm{d}\mathbf{x} \tag{1.48}$$

$$< -\frac{\beta s N_0^2}{8\gamma\pi\kappa^2}\frac{e^{-r/\kappa}}{r} + \sigma N_0 \log\frac{N_0}{4\pi r^3/3} \tag{1.49}$$

$$= -\frac{\beta s N_0^2}{8\gamma\pi\kappa^2}\frac{e^{-r/\kappa}}{r} + \sigma N_0 \log\frac{N_0}{4\pi/3} - 3\sigma\log r \tag{1.50}$$

$$\lim_{r\to 0}\mathscr{F}(\rho_r, U_r) = -\infty \tag{1.51}$$

As $r \to 0$ the first term tends to $-\infty$. At the same time, $-3\sigma \log r \to +\infty$, but the logarithmic divergence of this term is of lower order than the $-1/r$ of the first, so the negative term dominates.

Finally, in the two-dimensional case,

$$\mathcal{F}(\rho_r, U_r) = \int_\Omega \left(-\frac{\beta \rho_r U_r}{2} + \sigma \rho_r \log \rho_r \right) \mathrm{d}\mathbf{x} \tag{1.52}$$

$$< -\frac{\beta s N_0^2}{2\pi\gamma\kappa^2} K_0(2r/\kappa) + \sigma N_0 \log \frac{N_0}{2\pi r^2} \tag{1.53}$$

$$= -\frac{\beta s N_0^2}{2\pi\gamma\kappa^2} K_0(2r/\kappa) + \sigma N_0 \log \frac{N_0}{2\pi} - 2\sigma N_0 \log r \tag{1.54}$$

For small r,

$$K_0(r) = -\log r - \gamma_{\text{Euler}} + \log 2 + \mathcal{O}\left(r^2\right) \tag{1.55}$$

where $\gamma_{\text{Euler}} \approx 0.577$ is one of Euler's many constants. The limiting behavior of $\mathcal{F}(\rho_r, U_r)$ in two dimensions thus depends on the sign of the coefficient of $\log r$ in the asymptotic form. That is, if $\frac{\beta s n_0^2}{2\pi\gamma\kappa^2} > 2\sigma N_0$, then $\lim_{r\to 0} \mathcal{F}(\rho_r, U_r) = -\infty$. Eq (1.54) only establishes an upper bound, but more careful estimation of $\mathcal{F}(\rho_r, U_r)$ establishes that the condition, which simplifies to $N_0 > \frac{4\pi\sigma D}{\beta s}$, is necessary and sufficient for $\mathcal{F}(\rho_r, U_r)$ to be unbounded below in the limit of small r.

Of course, these results do not prove that blow-up can occur, or establish the conditions. For that, see Horstmann (2003; 2004, and papers cited therein). Nevertheless, this failure of $\mathcal{F}$ to be bounded below in the limit of collapse to a point is at the heart of blow-up (Horstmann 2003; Horstmann 2004). In fact, the conditions for blow-up are exactly those suggested by the calculations above. Blow-up never occurs in one dimension, can occur in two if the number of cells exceeds $4\pi\sigma D/(\beta s)$ (this threshold is lower at the edge or the corner of a bounded domain), and can occur with any number of cells in three or more dimensions. Once the cells begin to fall into that pit, there is no place short of $-\infty$ for the energy to stop.

1.4.5 Free energy and pressure

Free energy is also unbounded below in the limit of large r for $\Omega = \mathbb{R}^d$ for any d, because the entropy increases without bound as the cells spread out. (For finite Ω, of course, entropy has an

upper bound). I mentioned above that the diffusion term of the ρ PDE produces a pressure that opposes collapse. In thermodynamics pressure is the negative of the derivative of energy with respect to volume, i.e. the energy change due to a volume change is $dE = -pdV \iff p = -\,\mathrm{d}E/\mathrm{d}V$. The diffusion term of the PDE is the origin of the entropy component $-TS$ of the free energy functional. We can therefore identify the diffusional energy with $-TS$, $E_{\text{diffusion}} \coloneqq -TS$. Thus, if N_0 cells are distributed uniformly within a volume $V \subset \Omega$,

$$\rho(\mathbf{x}) = \begin{cases} N_0/|V| & \text{if } x \in V \\ 0 & \text{if } x \notin V \end{cases} \tag{1.56}$$

$$p_{\text{diffusion}} = -\frac{\mathrm{d}E_{\text{diffusion}}}{\mathrm{d}|V|} \tag{1.57}$$

$$= -\frac{\mathrm{d}(-TS)}{\mathrm{d}|V|} = T\frac{\mathrm{d}S}{\mathrm{d}|V|} = \sigma\frac{\mathrm{d}S}{\mathrm{d}|V|} \qquad (1.19) \tag{1.58}$$

$$S = -\int_\Omega \rho(\mathbf{x}) \log \rho(\mathbf{x}) \mathrm{d}\mathbf{x} \qquad (1.20) \tag{1.59}$$

$$= -\int_V \frac{N_0}{|V|} \log \frac{N_0}{|V|} \mathrm{d}\mathbf{x} \qquad (1.56) \tag{1.60}$$

$$= -N_0 \left(\log N_0 - \log|V|\right) \tag{1.61}$$

$$p = \sigma\frac{N_0}{|V|} \tag{1.62}$$

$$p|V| = \sigma N_0 \tag{1.63}$$

This is the Ideal Gas Law, $pV = nT$. (The Ideal Gas Law is more often seen in the forms $pV = nRT$ or $pV = nk_BT$, according as n is measured in moles or molecules, R and k_B being the gas constant and Boltzmann's constant. These constants, however, are just unit conversion factors: they have the same status as $2.54\,\mathrm{cm/in}$——they express 1 in terms of interconvertible units.)

The random movement of the cells thus produces a positive pressure that resists collapse of aggregates to a point. The V_U term of the general form of the ρ PDE (1.12) produces a negative pressure (if V_U is a decreasing function) that promotes collapse. In the minimal model (1.1) $V_U(U) = -\beta U$ produces a negative pressure capable of overcoming the diffusion pressure in 3 or more dimensions or in two dimensions when the number of cells exceeds threshold. If V_ρ is an increasing function, the V_ρ term of (1.12) produces a positive pressure that will oppose collapse.

There are thus two ways of engineering the Keller-Segel system (1.1,1.12) so as to prevent blow-up: (1) Design a space-filling function V_ρ that produces a positive pressure as space is filled. As just illustrated, positive pressure means that energy increases as cells are crowded into a small space. Any convex dependence of energy on density will have this effect. (2) Design a response function V_U that produces less negative pressure. Negative pressure means that energy decreases as cells are crowded into smaller spaces. The blow-up calculations (Section 1.4.4) illustrated how an attractant has that effect. Since aggregation, by definition, means cells crowding together, some negative pressure is necessary for aggregation. It is not however necessary that energy be unbounded below.

Both of these strategies are in the direction of better biological realism. I use both in my models (section 3.1). To fully understand how terms in the PDEs produce pressures, it is necessary to understand how a free energy function arises from the PDEs. This is the subject of chapter 2.

Chapter 2

Equilibrium and free energy functionals

2.1 Introduction and plan

This chapter develops free energy functionals for two versions of the Keller-Segel system, the minimal system of Childress and Percus (1981) (2.1, 2.2) and the more versatile worm system (2.1, 2.3) that will be used to model L1 aggregation. I describe the worm system as more versatile than the minimal system because the minimal system is a special case of the worm system (with $V_U(U) = -\beta U, V_\rho(\rho) = 0$), but by designing different response and density functions V_U, V_ρ, one can produce a wider range of behaviors with the worm system than seen in the minimal system.

A real functional is a map from one or more spatial functions $U \in H^2(\Omega)$ to the reals. (Here $H^2(\Omega) = W^{2,2}(\Omega)$ is a Sobolev function space containing functions with weak second derivatives defined on the open set Ω.) Free energy functionals are inspired by Lyapunov functionals. A Lyapunov functional is a locally positive definite functional with negative definite time derivative. In the best cases, the free energy functionals developed here are also Lyapunov functionals. However, in some cases free energy functionals satisfy only weaker conditions: for instance, that the functional be stationary if and only if the PDE system is at equilibrium.

Free energy functionals are useful tools in the investigation of the Keller-Segel system. I demonstrated in chapter 1 how they can be used to find conditions in which solutions blow up (and therefore, also conditions in which solutions don't blow up). They have at least three additional uses

- They are helpful in providing intuition about the behavior of solutions. For instance, free

energies have a natural scale, that allows one to understand which differences are big, and which small.

- They can be used to investigate properties of equilibria of the PDEs. For instance, I will use a free energy functional to show that density of organisms follows a Boltzmann distribution at equilibrium.
- They can be used in computations to search for equilibria.

In later chapters, I will use the free energy functionals developed here to evaluate numerical solutions of the PDE system.

After setting out some definitions and notation for later use (Preliminaries section), I prove some basic theorems that reduce the problem of finding a functional with negative semidefinite time derivative to that of finding a functional with a specified functional derivative. I then describe a general method of constructing a functional with a given functional derivative, radial integration. I prove that some functions don't have a functional antiderivative. However, I suggest that the functional constructed by radial integration may be a useful approximation, in the sense that the difference between its functional derivative and the desired functional derivative is small. I produce an upper bound for the error of this approximation when certain conditions hold. I then proceed to use radial integration to construct free energy functionals for the minimal system. No exact free energy functional can be constructed for the general worm system by these methods, but I construct approximations, which are used in later chapters.

2.2 Preliminaries

The minimal system of Childress and Percus (1981) and the more general worm system share the same PDE for the chemical signal

$$\dot{U} = U_t = -\gamma U + D\nabla^2 U + s\rho \tag{2.1}$$

The density PDE for the minimal system is

$$\dot{\rho} = \rho_t = -\beta\nabla \cdot (\rho\nabla U) + \sigma\nabla^2\rho \tag{2.2}$$

The density PDE for the worm system is

$$\dot{\rho} = \rho_t = \nabla \cdot (\rho \nabla (V_U(U) + V_\rho(\rho) + \sigma \log \rho)) \tag{2.3}$$

Functions and parameters appearing in the PDEs are

$\rho(t, \mathbf{x}) > 0$ is the local density of cells
$U(t, \mathbf{x}) > 0$ is the local concentration of chemical signal
$d \in \mathbb{Z}_{>0}$ is the spatial dimension
$\beta > 0$ is the chemotactic sensitivity of the cells to signal
$\sigma > 0$ quantifies the random movement of the cells
$\gamma > 0$ is the spontaneous decay rate of signal
$D > 0$ is the diffusion constant of signal
$s > 0$ is the rate of secretion of signal per cell
$V_U(U)$ is a potential function that describes the worm's response to signal
$V_\rho(\rho)$ is a potential function that describes the worms' direct response to other worms

The functions $\rho(t, \mathbf{x})$ representing density of worms and $U(t, \mathbf{x})$ representing concentration of chemical signal are defined on $[0, \infty) \times \Omega$. It is convenient to define $U(t)$ as the spatial function at time t, i.e.

$$U(t) \coloneqq \mathbf{x} \mapsto U(t, \mathbf{x}), \tag{2.4}$$

and similarly for $\rho(t)$. $U(t, \mathbf{x})$ and $\rho(t, \mathbf{x})$ are assumed to have continuous time derivatives and the spatial functions are members of the Sobalev space $H^2(\Omega)$, i.e. $U(t), \rho(t) \in H^2(\Omega)$.

I assume that both ρ and U are defined for all $\mathbf{x} \in \mathbb{R}^d$, but I also assume that both ρ and U are periodic with period 1 in each spatial dimension, so that it is sufficient to study them on $\Omega = (0, 1)^d$, and periodic boundary conditions hold. I restrict attention to periodic functions to simplify the exposition below. Also, for reasons described in Chapter 3, most of the numeric solutions focus on the periodic case. Most of the arguments below work with little change for Neumann boundary conditions. Dirichlet and Robin boundary conditions are more problematic because there can be net loss of worms and signals at the boundary.

$$
\begin{aligned}
T\rho(t,\mathbf{x}) &= T\rho(t,\mathbf{x}+\mathbf{e}_i), \qquad \mathbf{x}\in\partial\Omega \\
TU(t,\mathbf{x}) &= TU(t,\mathbf{x}+\mathbf{e}_i), \qquad \mathbf{x}\in\partial\Omega \\
T\nabla\rho(t,\mathbf{x}) &= T\nabla\rho(t,\mathbf{x}+\mathbf{e}_i), \qquad \mathbf{x}\in\partial\Omega \\
T\nabla U(t,\mathbf{x}) &= T\nabla U(t,\mathbf{x}+\mathbf{e}_i), \qquad \mathbf{x}\in\partial\Omega \\
&\mathbf{e}_i \text{ is the usual unit Cartesian basis vector for } i=1,\dots,d
\end{aligned}
\tag{2.5}
$$

(Here T is the trace operator that extends $U \in H^1(\Omega)$ continuously to $\partial\Omega$.) I define $H^2_P(\Omega)$ as the subspace of $H^2(\Omega)$ containing functions that satisfy boundary conditions (2.5). Also, for notational convenience, I define $C^1([0,\infty) \to H^2_P(\Omega)) \coloneqq \{U \in C^{1,2}([0,\infty)\times\Omega) : U(t) \in H^2_P(\Omega)\}$. These assumptions imply that boundary integrals over $\partial\Omega$ that arise from integration by parts vanish. I will omit these vanishing boundary integrals without remark. Any function $f \in H^2_P(\Omega)$ can be written as a Fourier series

$$
f(\mathbf{x}) = \sum_{\mathbf{k}\in 2\pi\mathbb{Z}^d} \tilde{f}_{\mathbf{k}} e^{i\mathbf{k}\cdot\mathbf{x}} \tag{2.6}
$$

In the Neumann boundary condition case, (2.6) is replaced with a Fourier cosine series.

The marginal potential functions V_U and V_ρ are the main levers through which I engineer worm behavior in the model. It is convenient to define their integrals

$$
W_U(U) \coloneqq \int_{u=0}^{U} V_U(u)\mathrm{d}u \tag{2.7}
$$

$$
W_\rho(\rho) \coloneqq \int_{r=0}^{\rho} V_\rho(r)\mathrm{d}r \tag{2.8}
$$

The average potentials $W_U(U)/U$ and $W_\rho(\rho)/\rho$ will appear frequently. They are taken to have their limiting values at zero

$$
\left.\frac{W_U(U)}{U}\right|_{U=0} \coloneqq V_U(0) \tag{2.9}
$$

$$
\left.\frac{W_\rho(\rho)}{\rho}\right|_{\rho=0} \coloneqq V_\rho(0) \tag{2.10}
$$

The minimal model (2.2) is a special case of (2.3) with $V_U(U) = -\beta U$ and $V_\rho(\rho) = 0$. (The $\sigma\nabla^2\rho$ term in (2.2) arises from (2.3) as $\nabla \cdot (\rho\nabla(\sigma \log \rho))$.) After developing tools, I will work through each calculation first with the minimal model, because it is mathematically simple, and we already know the answers (chapter 1). I will then show results for the worm model.

The signal potential $V_U(U)$ is, for an attractant, a decreasing function of U. I will have occasion to consider repellent signals as well. For a repellent, $V_U(U)$ is an increasing function. $V_\rho(\rho)$ will always be increasing——its main use is to make the worms take up space. For computational examples, I will use the following forms

$$V_U(U) \coloneqq -\beta \log(\alpha + U) \tag{2.11}$$

The parameters $\alpha > 0$ and $\beta \in \mathbb{R}$ control the concentration scale and the direction and strength of the response. For an attractant, $\beta > 0$, for a repellent, $\beta < 0$.

$$V_\rho(\rho) = \sigma \frac{\texttt{scale}}{2}\left(1 + \tanh\left(\frac{\rho - \texttt{rhomax}}{\texttt{cushion}}\right)\right) \tag{2.12}$$

`scale`, `rhomax`, and `cushion` are positive real parameters. In chapter 3 I will explain these functional forms.

A functional $\mathfrak{F}$ maps one or more positive functions of space $U : \Omega \to (0, \infty)$ to a number. For this dissertation, I will usually restrict attention to positive functions of space. I denote by $H^2_{P+}(\Omega)$ the subset of $H^2_P(\Omega)$ containing positive real functions, $H^2_{P+}(\Omega) \coloneqq \{U \in H^2_P(\Omega) : \forall \mathbf{x} \in \Omega \quad U(\mathbf{x}) \in \mathbb{R} \text{ and } U(\mathbf{x}) > 0\}$, and $C^1([0,\infty) \to H^2_{P+}(\Omega)) \coloneqq \{U \in C^{1,2}([0,\infty) \times \Omega) : U(t) \in H^2_{P+}(\Omega)\}$. Of course, in other contexts functionals may act on more general functions. In fact, I will have occasion below to use complex functionals of complex functions to simplify proofs involving Fourier series.

With $U(t) \coloneqq \mathbf{x} \mapsto U(t, \mathbf{x})$, $\mathfrak{F}(U(t))$ is a real function of time, because $\mathfrak{F}$ maps each spatial function $U(t)$ to a real number. Henceforth the t dependence will be implicit—i.e., $\mathfrak{F}(U)$ will be shorthand for $\mathfrak{F}(U(t))$. Furthermore,

$$\dot{\mathfrak{F}}(U) \coloneqq \frac{\mathrm{d}\mathfrak{F}(U(t))}{\mathrm{d}t} \tag{2.13}$$

This time derivative can be calculated with a version of the chain rule.

$$\dot{\mathscr{F}}(U) = \int_\Omega \frac{\delta \mathscr{F}(U)}{\delta U(\mathbf{x})} \frac{\partial U(t,\mathbf{x})}{\partial t} \mathrm{d}\mathbf{x} = \int_\Omega \frac{\delta \mathscr{F}(U)}{\delta U(\mathbf{x})} \dot{U}(\mathbf{x}) \mathrm{d}\mathbf{x} \tag{2.14}$$

$$\dot{U}(\mathbf{x}) \coloneqq \frac{\partial U(t)(\mathbf{x})}{\partial t} = \frac{\partial U(t,\mathbf{x})}{\partial t} \tag{2.15}$$

Definition 2.1. The functional derivative $\delta \mathscr{F}(U)/\delta U(\mathbf{x})$ is defined by

$$\lim_{\epsilon \to 0} \frac{\mathscr{F}(U + \epsilon\phi) - \mathscr{F}(U)}{\epsilon} = \int_\Omega \frac{\delta \mathscr{F}(U)}{\delta U(\mathbf{x})} \phi(\mathbf{x}) \mathrm{d}\mathbf{x}, \tag{2.16}$$

where $\phi \in H^2_P(\Omega)$ is a test function. The functional derivative is a representation of the Frèchet derivative. A functional is differentiable if a function of $\mathbf{x}$ $\delta \mathscr{F}(U)/\delta U(\mathbf{x})$ exists such that (2.16) holds for all variations $\phi(\mathbf{x})$ for which $\mathscr{F}(U + \epsilon\phi)$ exists for small enough $\epsilon > 0$. If the functional derivatives exist, then (2.14) can be used to calculate the time derivative of the functional. The notation $\delta \mathscr{F}(U)/\delta U(\mathbf{x})$ is intended to encourage thinking of $\mathscr{F}(U)$ as a function of many variables, one $U(\mathbf{x})$ for each $\mathbf{x} \in \Omega$, and $\delta \mathscr{F}(U)/\delta U(\mathbf{x})$ as the rate of change of $\mathscr{F}(U)$ when one of these $U(\mathbf{x})$ is changed. Thus, the functional derivative $\delta \mathscr{F}(U)/\delta U(\mathbf{x})$ is analogous to a partial derivative $\partial F(\mathbf{U})/\partial U_i$ of a scalar function of a vector $\mathbf{U}$.

Remark 2.2. When a functional is simply the integral of a pointwise function $f : \mathbb{R} \to \mathbb{R}$ of $U(\mathbf{x})$, the functional derivative reduces to the ordinary derivative.

$$\frac{\delta}{\delta U(\mathbf{x})} \int_\Omega f(U(\mathbf{x})) \mathrm{d}\mathbf{x} = f'(U(\mathbf{x})) \tag{2.17}$$

Demonstration. For $U, \phi \in H^2_P(\Omega)$, $f \in C^2(\mathbb{R} \to \mathbb{R})$, Let

$$\mathscr{F}(U) \coloneqq \int_\Omega f(U(\mathbf{x})) \mathrm{d}\mathbf{x}$$

Then

$$\mathscr{F}(U+\epsilon\phi) = \int_\Omega (f(U\mathbf{x}) + \epsilon\phi(\mathbf{x}))\mathrm{d}\mathbf{x} \tag{2.18}$$

$$= \int_\Omega (f(U(\mathbf{x})) + \epsilon f'(U(\mathbf{x}))\phi(U(\mathbf{x})) + \mathscr{O}\left(\epsilon^2\right)\mathrm{d}\mathbf{x} \tag{2.19}$$

$$\mathscr{F}(U+\epsilon\phi) - \mathscr{F}(U) = \epsilon \int_\Omega f'(U(\mathbf{x}))\phi(\mathbf{x})\mathrm{d}\mathbf{x} + \mathscr{O}\left(\epsilon^2\right) \tag{2.20}$$

$$\frac{\mathscr{F}(U+\epsilon\phi) - \mathscr{F}(U)}{\epsilon} = \int_\Omega f'(U(\mathbf{x}))\phi(\mathbf{x})\mathrm{d}\mathbf{x} + \mathscr{O}(\epsilon) \tag{2.21}$$

$$\lim_{\epsilon\to 0} \frac{\mathscr{F}(U+\epsilon\phi) - \mathscr{F}(U)}{\epsilon} = \int_\Omega f'(U(\mathbf{x}))\phi(\mathbf{x})\mathrm{d}\mathbf{x} \tag{2.22}$$

Comparing (2.22) with definition (2.16), it is evident that

$$\frac{\delta\mathscr{F}(U)}{\delta U(\mathbf{x})} = f'(U(\mathbf{x})),$$

which is (2.17) □

Definition 2.3. A functional $\mathscr{F}(U)$ is stationary at U_0 if,

$$\lim_{\epsilon\to 0} \frac{\mathscr{F}(U_0+\epsilon\phi) - \mathscr{F}(U_0)}{\epsilon} = 0, \tag{2.23}$$

for every variation $\phi \in H^2_P(\Omega)$ for which the limit exists.

Thus, the following are equivalent:

- $\mathscr{F}(U)$ is stationary at U_0
- $\frac{\delta\mathscr{F}(U)}{\delta U(\mathbf{x})}\Big|_{U=U_0} = 0$ for almost every $\mathbf{x}$.

Definition 2.4. A functional $\mathscr{F}(U)$ is Positive Definite (PD), Negative Definite (ND), Positive Semidefinite (PSD), or Negative Semidefinite (NSD) if, for every nonzero function $U : \Omega \to (0,\infty)$

$$0 < \mathscr{F}(U) \qquad \text{PD} \tag{2.24}$$
$$0 > \mathscr{F}(U) \qquad \text{ND} \tag{2.25}$$
$$0 \leq \mathscr{F}(U) \qquad \text{PSD} \tag{2.26}$$
$$0 \geq \mathscr{F}(U) \qquad \text{NSD} \tag{2.27}$$

These definitions obviously imply that every PD functional is also PSD, and every ND functional is also NSD.

2.3 Finding functionals with negative semidefinite time derivatives

2.3.1 Basic Theorems

Theorem 2.5. *Let $U \in C^1([0,\infty) \to H^2_{P+}(\Omega))$ be a function that satisfies the PDE*

$$\dot{U}(\mathbf{x}) = \mathfrak{D}U(t)(\mathbf{x}), \tag{2.28}$$

where $\mathfrak{D} : C^2(\Omega) \to C(\Omega)$ is a spatial differential operator that depends on $U(t) := \mathbf{x} \mapsto U(t,\mathbf{x})$ and its spatial derivatives. Then, if $\mathscr{F} : H^2_{P+}(\Omega) \to \mathbb{R}$ is a functional with functional derivative

$$\frac{\delta\mathscr{F}(U)}{\delta U(\mathbf{x})} = -p(\mathbf{x})\mathfrak{D}U(t)(\mathbf{x}), \tag{2.29}$$

where $p(\mathbf{x}) > 0$ is some positive scale function, the time derivative $\dot{\mathscr{F}}(U)$ is negative semidefinite. Furthermore, U_0 is an equilibrium of (2.28) if and only if $\mathscr{F}(U)$ is stationary at U_0.

Proof. Suppose $U \in C^1([0,\infty) \to H^2_{P+}(\Omega))$ is a function of time and space satisfying (2.29) for some positive $p(\mathbf{x})$ and $\mathfrak{D}$ as described above. From (2.14),

$$\dot{\mathfrak{F}}(U) = \int_\Omega \frac{\delta \mathfrak{F}(U)}{\delta U(\mathbf{x})} \dot{U}(\mathbf{x}) \mathrm{d}\mathbf{x} \qquad (2.14) \qquad (2.30)$$

$$= \int_\Omega (-p(\mathbf{x}) \mathfrak{D}U(t)(\mathbf{x}))(\mathfrak{D}U(t)(\mathbf{x})) \mathrm{d}\mathbf{x} \qquad (2.28, 2.29) \qquad (2.31)$$

$$= -\int_\Omega p(\mathbf{x}) |\mathfrak{D}U(t)(\mathbf{x})|^2 \mathrm{d}\mathbf{x} \qquad (2.32)$$

$$\leq 0, \qquad (2.33)$$

with equality only if $\mathfrak{D}U(t)(\mathbf{x}) = 0$ for almost every $\mathbf{x}$. Thus, equilibrium of (2.28) implies stationarity of $\mathfrak{F}(U)$. Also, if $\mathfrak{F}(U)$ is stationary at U_0, then $\delta \mathfrak{F}(U)/\delta U(\mathbf{x}) \big|_{U=U_0} = 0$ for almost every $\mathbf{x}$ and (2.30) implies $\dot{\mathfrak{F}}(U_0) = 0$, i.e., U_0 is an equilibrium.

□

Remark 2.6. If $U \in C^1([0, \infty) \to H^2_{P+}(\Omega))$ is a function that satisfies the PDE

$$\dot{U}(\mathbf{x}) = \mathfrak{D}U(t)(\mathbf{x}), \qquad (2.34)$$

where $\mathfrak{D} : C^2(\Omega) \to C(\Omega)$ is a spatial differential operator that depends on $U(t) \coloneqq \mathbf{x} \mapsto U(t, \mathbf{x})$ and its spatial derivatives, and if $\mathfrak{F} : H^2_{P+}(\Omega) \to \mathbb{R}$ is a functional with functional derivative

$$\frac{\delta \mathfrak{F}(U)}{\delta U(\mathbf{x})} = -\mathfrak{D}U(t)(\mathbf{x}), \qquad (2.35)$$

the time derivative $\dot{\mathfrak{F}}(U)$ is negative semidefinite. Furthermore, U_0 is an equilibrium of (2.28) if and only if $\mathfrak{F}(U)$ is stationary at U_0.

Proof. This is Theorem 2.5 with $p(\mathbf{x}) = 1$. □

Theorem 2.7. *Let $\rho \in C^1([0, \infty) \to H^2_{P+}(\Omega))$ be a function that satisfies the conservation PDE*

$$\dot{\rho}(\mathbf{x}) = -\nabla \cdot \boldsymbol{\phi}(\rho(t))(\mathbf{x}), \qquad (2.36)$$

where $\boldsymbol{\phi}(\rho(t)) : \Omega \to \mathbb{R}^d$ is a differentiable flux vector function (that will in general depend on $\mathbf{x}$ via $\rho(t)(\mathbf{x})$ and $U(t)(\mathbf{x})$ and their spatial derivatives). If $\mathscr{F}(\rho)$ is a functional with differentiable functional derivative whose spatial gradient satisfies

$$\nabla\left(\frac{\delta\mathscr{F}(\rho)}{\delta\rho(\mathbf{x})}\right) = -p(\mathbf{x})\boldsymbol{\phi}(\rho(t))(\mathbf{x}), \tag{2.37}$$

where $p : \Omega \to (0,\infty)$ is some positive scale function, then $\dot{\mathscr{F}}(\rho)$ is negative semidefinite. Furthermore, ρ_{eq} is an equilibrium of (2.36) if and only if $\delta\mathscr{F}(\rho)/\delta\rho(\mathbf{x})$ is constant (i.e., independent of $\mathbf{x}$) at $\rho = \rho_{eq}$.

Proof. Suppose $\rho \in C^1([0,\infty) \to H^2_{P+}(\Omega))$ is a function of time and space satisfying (2.37) for some positive $p(\mathbf{x})$ and $\boldsymbol{\phi}$ as described above. From (2.14),

$$\begin{aligned}
\dot{\mathscr{F}}(\rho) &= \int_\Omega \frac{\delta\mathscr{F}(\rho)}{\delta\rho(\mathbf{x})}\dot{\rho}(\mathbf{x})\mathrm{d}\mathbf{x} && (2.14) && (2.38)\\
&= -\int_\Omega \left(\frac{\delta\mathscr{F}(\rho)}{\delta\rho(\mathbf{x})}\right)(\nabla\cdot\boldsymbol{\phi}(\rho(t))(\mathbf{x})) && (2.36) && (2.39)\\
&= \int_\Omega \nabla\left(\frac{\delta\mathscr{F}(\rho)}{\delta\rho(\mathbf{x})}\right)\cdot\boldsymbol{\phi}(\rho(t))(\mathbf{x})\mathrm{d}\mathbf{x} && \text{(IBP)} && (2.40)\\
&= -\int_\Omega p(\mathbf{x})\boldsymbol{\phi}(\rho(t))(\mathbf{x})\cdot\boldsymbol{\phi}(\rho(t))(\mathbf{x})\mathrm{d}\mathbf{x} && (2.37) && (2.41)\\
&= -\int_\Omega p(\mathbf{x})\|\boldsymbol{\phi}(\rho(t))(\mathbf{x})\|^2_{L^2(\mathbb{R}^d)}\mathrm{d}\mathbf{x} && && (2.42)\\
&\le 0, && && (2.43)
\end{aligned}$$

with equality only if $\boldsymbol{\phi}(\rho(t)) = 0$ for almost every $\mathbf{x}$.

Now, to prove the final statement, the equivalence of equilibrium and constant $\delta\mathscr{F}(\rho)/\delta\rho(\mathbf{x})$, suppose first that ρ_{eq} is an equilibrium. Then $\dot{\mathscr{F}}(\rho)\big|_{\rho=\rho_{\text{eq}}} = 0$, since a functional of ρ cannot change if ρ doesn't change. As just argued, $\dot{\mathscr{F}}(\rho) = 0$ implies $\boldsymbol{\phi}(\rho(t)) = 0$ almost everywhere, which implies (via (2.37)) that $\nabla(\,\delta\mathscr{F}(\rho)/\delta\rho(\mathbf{x})\,) = 0$ almost everywhere, i.e. $\delta\mathscr{F}(\rho)/\delta\rho(\mathbf{x})$ is constant. This demonstrates equilibrium $\implies$ constant $\delta\mathscr{F}(\rho)/\delta\rho(\mathbf{x})$.

The converse (constant $\delta\mathscr{F}(\rho)/\delta\rho(\mathbf{x})$ $\implies$ equilibrium) is more straightforward.

$$\left.\frac{\delta \mathcal{F}(\rho)}{\delta \rho(\mathbf{x})}\right|_{\rho=\rho_{\text{eq}}} \text{ is constant } \implies \nabla\left(\left.\frac{\delta \mathcal{F}(\rho)}{\delta \rho(\mathbf{x})}\right)\right|_{\rho=\rho_{\text{eq}}} = 0 \qquad \text{a.e.}$$

$$\implies \left.\boldsymbol{\phi}(\boldsymbol{\rho})(\mathbf{x})\right|_{\rho=\rho_{\text{eq}}} = 0 \qquad \text{a.e.} \tag{2.37}$$

$$\implies \dot{\rho}(\mathbf{x}) = 0 \qquad \text{a.e.} \tag{2.36}$$

□

The following version of Theorem 2.7 applies when the flux $\boldsymbol{\phi}$ takes the specific form of a positive density ρ times the gradient of a potential.

Theorem 2.8. *Let $\rho \in C^1([0,\infty) \to H^2_{P+}(\Omega))$ be a positive function of time and space that satisfies the PDE*

$$\dot{\rho}(\mathbf{x}) = \nabla \cdot (\rho \nabla G(\mathbf{x}, \rho(\mathbf{x}))), \tag{2.44}$$

where $G : (\Omega \times \mathbb{R}_{>0}) \to \mathbb{R}$ is a scalar function with continuous derivatives. Let $\mathcal{F}(\rho)$ be a functional with functional derivative

$$\frac{\delta \mathcal{F}(\rho)}{\delta \rho(\mathbf{x})} = q(G(\mathbf{x}, \rho(\mathbf{x}))), \tag{2.45}$$

where $q : \mathbb{R} \to \mathbb{R}$ is a differentiable increasing function (i.e., $q'(G) > 0$).

Then the time derivative $\dot{\mathcal{F}}(\rho)$ is negative semidefinite. Furthermore, if ρ_{eq} is an equilibrium of (2.44), then $G(\mathbf{x}, \rho_{eq}(\mathbf{x}))$ is constant (i.e., independent of $\mathbf{x}$).

Proof. Suppose ρ, G, $\mathcal{F}$, and q are as above. Then,

$$\dot{\mathscr{F}}(\rho) = \int_\Omega \frac{\delta \mathscr{F}(\rho)}{\delta \rho(\mathbf{x})} \dot{\rho}(\mathbf{x}) \mathrm{d}\mathbf{x} \qquad (2.14) \qquad (2.46)$$

$$= \int_\Omega q(G(\mathbf{x}, \rho(\mathbf{x}))) \nabla \cdot (\rho \nabla G(\mathbf{x}, \rho(\mathbf{x}))) \mathrm{d}\mathbf{x} \qquad (2.45, 2.44) \qquad (2.47)$$

$$= -\int_\Omega \nabla (q(G(\mathbf{x}, \rho(\mathbf{x})))) \cdot (\rho \nabla G(\mathbf{x}, \rho(\mathbf{x}))) \mathrm{d}\mathbf{x} \qquad \text{(IBP)} \qquad (2.48)$$

$$= -\int_\Omega (q'(G) \nabla G) \cdot (\rho(\mathbf{x}) \nabla G) \mathrm{d}\mathbf{x} \qquad (2.49)$$

$$= -\int_\Omega q'(G) \rho(\mathbf{x}) \|\nabla G\|^2_{L^2(\mathbb{R}^d)} \mathrm{d}\mathbf{x} \qquad (2.50)$$

$$\leq 0, \qquad (2.51)$$

since $q'(G) > 0$, $\rho(\mathbf{x}) > 0$, and $\|\nabla G\|^2 \geq 0$. (For concision, the arguments of G were elided in (2.49, 2.50).) Equality holds only if $\nabla G = 0$ almost everywhere, i.e. if $G(\mathbf{x}, \rho(\mathbf{x}))$ is constant in $\mathbf{x}$.

□

Corollary 2.9. *Let $\rho \in C^1([0, \infty) \to H^2_{P+}(\Omega))$ be a positive function of time and space, that satisfies PDE (2.44) where $G : (\Omega \times \mathbb{R}) \to \mathbb{R}$ is a scalar function with continuous derivatives. Let $\mathscr{F}(\rho)$ be a functional with functional derivative*

$$\frac{\delta \mathscr{F}(\rho)}{\delta \rho(\mathbf{x})} = G(\mathbf{x}, \rho(\mathbf{x})), \qquad (2.52)$$

Then the time derivative $\dot{\mathscr{F}}(\rho)$ is negative semidefinite. Furthermore, if ρ_{eq} is an equilibrium of (2.44), then $G(\mathbf{x}, \rho_{eq}(\mathbf{x}))$ is independent of $\mathbf{x}$.

Proof. This is Theorem 2.8 with q the identity function: $q(G) \coloneqq G$, $q'(G) = 1$. □

Theorem 2.10. *Let $\rho, U \in C^1([0, \infty) \to H^2_{P+}(\Omega))$ be functions of time and space that satisfy the PDEs*

$$\dot{U}(\mathbf{x}) = \mathfrak{D}(\rho(t)) U(t)(\mathbf{x}) \qquad (2.53)$$

$$\dot{\rho}(\mathbf{x}) = -\nabla \cdot \boldsymbol{\phi}(\rho(t), U(t))(\mathbf{x}), \qquad (2.54)$$

where $\mathfrak{D}(\rho(t))$ is a spatial differential operator that depends on $\rho(t)$, $\boldsymbol{\phi}(\rho(t), U(t)) : \Omega \to \mathbb{R}^d$ is a flux vector function of $\mathbf{x}$ that depends on $\rho(t)$, $U(t)$, and their derivatives. ($d \in \mathbb{Z}_{>0}$ is the spatial dimension of Ω.) Then, if $\mathscr{F}(\rho, U)$ is a functional with differentiable functional derivatives such that

$$\nabla\left(\frac{\delta\mathscr{F}(\rho,U)}{\delta\rho(\mathbf{x})}\right) = -p(\mathbf{x})\boldsymbol{\phi}(\rho,U)(\mathbf{x}) \tag{2.55}$$

$$\frac{\delta\mathscr{F}(\rho,U)}{\delta U(\mathbf{x})} = -\mathfrak{D}(\rho)U(\mathbf{x}), \tag{2.56}$$

Here $p : \Omega \to (0,\infty)$ is a positive scale function (which typically depends on $\mathbf{x}$ via $\rho(t)(\mathbf{x})$ and $U(t)(\mathbf{x})$).

Then the time derivative $\dot{\mathscr{F}}(\rho, U)$ is negative semidefinite. Furthermore, if ρ_{eq}, U_{eq} is an equilibrium of (2.53, 2.54), then $\mathscr{F}(\rho, U)$ is stationary in ρ at ρ_{eq}, U_{eq}, and $\delta\mathscr{F}(\rho, U)/\delta\rho(\mathbf{x})$ is constant (i.e., independent of $\mathbf{x}$) at ρ_{eq}, U_{eq}.

Proof. Let ρ, U, $\mathscr{D}$, $\boldsymbol{\phi}$, $\mathscr{F}$, and p be as above. The chain rule here takes the form

$$\dot{\mathscr{F}}(\rho,U) = \int_\Omega \frac{\delta\mathscr{F}(\rho,U)}{\delta\rho(\mathbf{x})}\dot{\rho}(\mathbf{x})\mathrm{d}\mathbf{x} \tag{2.57}$$

$$+ \int_\Omega \frac{\delta\mathscr{F}(\rho,U)}{\delta U(\mathbf{x})}\dot{U}(\mathbf{x})\mathrm{d}\mathbf{x} \tag{2.58}$$

Each of the integrals (2.57) and (2.58) is negative semidefinite—the arguments are essentially identical to those made in Theorem 2.7 and Remark 2.6.

□

Theorem 2.11. *Let $\rho, U \in C^1([0,\infty) \to H^2_{P+}(\Omega))$ and $U : [0,\infty) \times \Omega \to (0,\infty)$ be functions of time and space that satisfy the PDEs*

$$\dot{U}(\mathbf{x}) = \mathfrak{D}(\rho(t))U(t)(\mathbf{x}) \tag{2.59}$$

$$\dot{\rho}(\mathbf{x}) = \nabla\cdot(\rho(t)\nabla G(\mathbf{x}, \rho(t)(\mathbf{x}), U(t)(\mathbf{x}))), \tag{2.60}$$

where $\mathfrak{D}(\rho)$ is a spatial differential operator that depends on ρ and where $G : (\Omega \times \mathbb{R} \times \mathbb{R}) \to \mathbb{R}$ is a scalar function with continuous derivatives. Let $\mathfrak{F}(\rho)$ be a functional with functional derivatives

$$\frac{\delta \mathfrak{F}(\rho, U)}{\delta \rho(\mathbf{x})} = q(G(\mathbf{x}, \rho(\mathbf{x}), U(\mathbf{x}))) \tag{2.61}$$

$$\frac{\delta \mathfrak{F}(\rho, U)}{\delta U(\mathbf{x})} = -p(\mathbf{x})\mathfrak{D}(\rho)U(\mathbf{x}), \tag{2.62}$$

where p and q are as in Theorems 2.5, 2.8.

Then the time derivative $\dot{\mathfrak{F}}(\rho, U)$ is negative semidefinite. Furthermore, if ρ_{eq}, U_{eq} is an equilibrium of (2.59, 2.60), then $\mathfrak{F}(\rho, U)$ is stationary in U at ρ_{eq}, U_{eq} and $G(\mathbf{x}, \rho_{eq}(\mathbf{x}), U_{eq}(\mathbf{x}))$ is independent of $\mathbf{x}$.

Proof. The proof of this theorem combines the chain rule (2.57, 2.58) with the arguments of Theorems 2.5 and 2.8.

□

Theorems 2.5, 2.7, 2.8, and 2.11 reduce the problem of finding a functional whose value decreases with time to the functional antidifferentiation problem: given a function (possibly involving derivatives) of $\mathbf{x}$, ρ, and U, find a functional whose functional derivative is that function. This problem cannot always be solved. Some functions do not have functional antiderivatives. The difficulty is familiar from multivariate calculus. There is no function $F(x, y)$ such that $\partial F/\partial x = 2y$ and $\partial F/\partial y = x$. If such an F existed, then its mixed partial derivatives would be unequal:

$$\frac{\partial^2 F}{\partial y \partial x} = \frac{\partial \frac{\partial F}{\partial x}}{\partial y} = \frac{\partial (2y)}{\partial y} = 2 \neq 1 = \frac{\partial x}{\partial x} = \frac{\partial \frac{\partial F}{\partial y}}{\partial x} = \frac{\partial^2 F}{\partial x \partial y}$$

The following lemma provides a method to construct a functional antiderivative, providing one exists.

Lemma 2.12 (Radial Integration)**.** *Let $\mathfrak{F} : H^2_P(\Omega) \to \mathbb{R}$ be a differentiable functional with functional derivative $\delta \mathfrak{F}(U)/\delta U(\mathbf{x})$. $\mathfrak{F}$ can be computed from its functional derivative as follows, provided the integral exists*

$$\mathscr{F}(U) = \int_{r=0}^{1} \left(\int_{\Omega} \frac{\delta \mathscr{F}(rU)}{\delta U(\mathbf{x})} U(\mathbf{x}) \mathrm{d}\mathbf{x} \right) \mathrm{d}r + C, \tag{2.63}$$

where C is a constant of integration. (That is, C is any expression such that $\delta C / \delta U(\mathbf{x}) = 0$.)

Proof. Fix a $U \in H_P^2(\Omega)$ and define $\mathscr{f}_U : [0,1] \to \mathbb{R}$ by

$$\mathscr{f}_U(r) = \mathscr{F}(rU) \tag{2.64}$$

The derivative of $\mathscr{f}_U$ is

$$\begin{aligned} \frac{\mathrm{d}\mathscr{f}_U(r)}{\mathrm{d}r} &= \lim_{\epsilon \to 0} \frac{\mathscr{f}_U(r+\epsilon) - \mathscr{f}_U(r)}{\epsilon} \\ &= \lim_{\epsilon \to 0} \frac{\mathscr{F}\left((r+\epsilon)U\right) - \mathscr{F}(rU)}{\epsilon} \\ &= \lim_{\epsilon \to 0} \frac{\mathscr{F}\left(rU + \epsilon U\right) - \mathscr{F}(rU)}{\epsilon} \\ &= \int_{\Omega} \frac{\delta \mathscr{F}(rU)}{\delta U(\mathbf{x})} U(\mathbf{x}) \mathrm{d}\mathbf{x}, \end{aligned} \tag{2.65}$$

using the definition of the functional derivative (2.16) for the last step, with $\phi = U$. It follows that $\mathscr{f}_U(r)$ is an antiderivative of the function (2.65) of r, i.e.

$$\mathscr{f}_U(R) = \int_{r=0}^{R} \left(\int_{\Omega} \frac{\delta \mathscr{F}(rU)}{\delta U(\mathbf{x})} U(\mathbf{x}) \mathrm{d}\mathbf{x} \right) \mathrm{d}r + C, \tag{2.66}$$

provided the integral in (2.66) exists. Finally, note that by its definition, $\mathscr{f}_U(1) = \mathscr{F}(U)$ and substitute $R = 1$ into (2.66) to get (2.63). □

Remark 2.13. This lemma provides a test for the existence of a functional antiderivative. Given a function $\mathscr{d}(U(\mathbf{x}))$ (possibly involving spatial derivatives or integrals of U), compute the integral $\mathscr{F}(U) = \int_{r=0}^{1} \left(\int_{\Omega} \mathscr{d}(rU) U(\mathbf{x}) \mathrm{d}\mathbf{x} \right) \mathrm{d}r$. The function $\mathscr{d}$ may not have a functional antiderivative, but if it does, it must, assuming the integral exists, be $\mathscr{F}$ (up to a constant of integration). To complete the test, find the functional derivative of $\mathscr{F}$. If $\delta \mathscr{F}(U) / \delta U(\mathbf{x}) = \mathscr{d}(U(\mathbf{x}))$, then $\mathscr{d}$ has a functional antiderivative and it is $\mathscr{F}$. If, however, $\delta \mathscr{F}(U) / \delta U(\mathbf{x}) \neq \mathscr{d}(U(\mathbf{x}))$, no functional antiderivative of $\mathscr{d}$ exists. (To see this, assume for contradiction that $\mathscr{d}$ has a functional antiderivative. Then, as just proved, that functional antiderivative must be $\mathscr{F}$ plus some constant of integration. If $\delta \mathscr{F}(U) / \delta U(\mathbf{x}) \neq \mathscr{d}(\mathbf{x})$ we have a contradiction and must

reject the hypothesis that a functional antiderivative of $\mathcal{d}$ exists.) This test of course depends on the existence of the integral $\int_{r=0}^{1} \left(\int_\Omega \mathcal{d}(rU)U(\mathbf{x})\, \mathrm{d}\mathbf{x} \right) \mathrm{d}r$, but the existence of this integral says nothing, by itself, about whether a functional antiderivative of $\mathcal{d}$ exists. I exhibit examples of both cases in the following sections.

The radial integration trick extends in a straightforward way to a functional of two functions

$$\mathscr{F}(\rho, U) = \int_{r=0}^{1} \left(\int_\Omega \frac{\delta \mathscr{F}(r\rho, rU)}{\delta \rho(\mathbf{x})} \rho(\mathbf{x}) \mathrm{d}\mathbf{x} + \int_\Omega \frac{\delta \mathscr{F}(r\rho, rU)}{\delta U(\mathbf{x})} U(\mathbf{x}) \mathrm{d}\mathbf{x} \right) \mathrm{d}r + C \tag{2.67}$$

2.3.2 The Horstmann functional

Horstmann (Horstmann 2003; Horstmann 2004; Dirk Horstmann 2001) describes a Lyapunov functional for a general version of the Keller-Segel system. Horstmann's functional can be constructed using the tools developed above.

Horstmann's general version of the Keller-Segel system is as follows

$$\dot{\rho} = \nabla \cdot (k(\rho, U)\nabla\rho - h(\rho, U)\nabla U) \tag{2.68}$$
$$\dot{U} = D\nabla^2 U - f(U)U + g(\rho, U) \tag{2.69}$$

The functions k and h describe the random movement and chemotactic response of the organisms. As before, $D > 0$ is the diffusion constant of the chemical signal. Functions f and g describe the decay of signal and its production or consumption by the organisms. Horstmann makes the following assumptions

$$k(\rho, U) > 0 \tag{2.70}$$
$$f(U) \geq const \tag{2.71}$$
$$g_\rho(\rho, U) \neq 0 \tag{2.72}$$

The system is not completely general—it doesn't include models in which the total number of organisms changes with time (death or reproduction).

Horstmann's construction is as follows. Define

$$F(U) \coloneqq \int_0^U f(s)s \, \mathrm{d}s \tag{2.73}$$

$$G(\rho, U) \coloneqq -\int_0^U g(\rho, s)\mathrm{d}s \tag{2.74}$$

Now, find a function $R(\rho)$ such that

$$k(\rho, U)(G_{\rho\rho}(\rho, U) + R''(\rho)) + h(\rho, U)G_{\rho U} = 0 \tag{2.75}$$

$$G_{\rho\rho}(\rho, U) + R''(\rho) > 0 \tag{2.76}$$

Then the following functional has a negative semidefinite time derivative

$$\mathscr{H}(\rho, U) = \int_\Omega \left(\frac{D}{2} \|\nabla U\|^2 + F(U) + G(\rho, U) + R(\rho) \right) \mathrm{d}\mathbf{x} \tag{2.77}$$

To arrive at this result using the tools developed above, use Theorem 2.10. It is easiest to start with U. We need to find a functional $\mathscr{H}$ such that

$$\frac{\delta \mathscr{H}(\rho, U)}{\delta U(\mathbf{x})} = -\big(D\nabla^2 U - f(U)U + g(\rho, U)\big) \tag{2.78}$$

$$= -D\nabla^2 U + f(U)U - g(\rho, U) \tag{2.79}$$

Let's take this term by term. Remark 2.2 makes it easy to handle the f and g terms

$$\frac{\delta}{\delta U(\mathbf{x})} \int_\Omega (F(U) + G(\rho, U))\mathrm{d}\mathbf{x} = f(U)U - g(\rho, U) \tag{2.80}$$

(Radial integration can also be used to arrive at the same result.) That leaves only the $-D\nabla^2 U$ term, whose functional antiderivative $\mathscr{D}(U)$ we find by radial integration.

$$\mathscr{D}(U) = \int_{r=0}^{1} \left(\int_{\Omega} -D\nabla^2(rU(\mathbf{x}))U(\mathbf{x})\mathrm{d}\mathbf{x} \right) \mathrm{d}r + C \tag{2.81}$$

$$= \int_{r=0}^{1} \left(r \int_{\Omega} -D\nabla^2(U(\mathbf{x}))U(\mathbf{x})\mathrm{d}\mathbf{x} \right) \mathrm{d}r + C \tag{2.82}$$

$$= \left(\int_{r=0}^{1} r\mathrm{d}r \right) \left(\int_{\Omega} -D\nabla^2(U(\mathbf{x}))U(\mathbf{x})\mathrm{d}\mathbf{x} \right) + C \tag{2.83}$$

$$= -\int_{\Omega} \frac{D}{2} U\nabla^2 U \mathrm{d}\mathbf{x} + C \tag{2.84}$$

$$= \int_{\Omega} \frac{D}{2} \nabla U \cdot \nabla U \mathrm{d}\mathbf{x} + C \qquad \text{(IBP)} \tag{2.85}$$

$$= \int_{\Omega} \frac{D}{2} \|\nabla U\|^2 \mathrm{d}\mathbf{x} + C \tag{2.86}$$

When using the radial integration lemma, it is always necessary to check the functional derivative.

$$\begin{aligned}
\mathscr{D}(U + \epsilon\phi) &= \int_{\Omega} \frac{D}{2} \nabla(U + \epsilon\phi) \cdot \nabla(U + \epsilon\phi) \mathrm{d}\mathbf{x} + C \\
&= \int_{\Omega} \frac{D}{2} \big(\nabla U \cdot \nabla U + 2\epsilon \nabla U \cdot \nabla\phi + \epsilon^2 \nabla\phi \cdot \nabla\phi \big) \mathrm{d}\mathbf{x} + C \\
\mathscr{D}(U + \epsilon\phi) - \mathscr{D}(U) &= \epsilon \int_{\Omega} D\nabla U \cdot \nabla\phi \, \mathrm{d}\mathbf{x} + \epsilon^2 \int_{\Omega} \frac{D}{2} \nabla\phi \cdot \nabla\phi \, \mathrm{d}\mathbf{x} \\
\lim_{\epsilon \to 0} \frac{\mathscr{D}(U + \epsilon\phi) - \mathscr{D}(U)}{\epsilon} &= \int_{\Omega} D\nabla U \cdot \nabla\phi \, \mathrm{d}\mathbf{x} \\
&= \int_{\Omega} -D\nabla^2 U \phi \, \mathrm{d}\mathbf{x} \qquad \text{(IBP)} \\
\frac{\delta \mathscr{D}(U)}{\delta U(\mathbf{x})} &= -D\nabla^2 U,
\end{aligned}$$

as desired. Putting this all together, we have the following functional

$$\mathscr{H}(\rho, U) = \int_{\Omega} \left(\frac{D}{2} \|\nabla U\|^2 + F(U) + G(\rho, U) \right) \mathrm{d}\mathbf{x} + C \tag{2.87}$$

The constant of integration C offers some flexibility. In fact, in this context "constant" means only "doesn't depend on U". C can be any object such that $\delta C/\delta U(\mathbf{x}) = 0$. In particular, it can be a functional of ρ. To arrive at the Horstmann functional, we assume that C is the integral of some function $R(\rho)$. (This is not the only possibility, but it is the one that will take us to our current destination.)

$$C = \int_\Omega R(\rho(\mathbf{x}))\mathrm{d}\mathbf{x} \tag{2.88}$$

$$\mathscr{H}(\rho, U) = \int_\Omega \left(\frac{D}{2}\|\nabla U\|^2 + F(U) + G(\rho, U) + R(\rho)\right)\mathrm{d}\mathbf{x} \tag{2.89}$$

Now we need only work out what R has to be to satisfy the hypothesis of Theorem 2.10.

$$\frac{\delta\mathscr{H}}{\delta\rho(\mathbf{x})} = G_\rho(\rho, U) + R'(\rho) \tag{2.90}$$

$$\nabla\left(\frac{\delta\mathscr{H}}{\delta\rho(\mathbf{x})}\right) = (G_{\rho\rho}(\rho, U) + R''(\rho))\nabla\rho + G_{\rho U}(\rho, U)\nabla U \tag{2.91}$$

To use Theorem 2.10 we need the quantity (2.91) to be

$$\nabla\left(\frac{\delta\mathscr{H}}{\delta\rho(\mathbf{x})}\right) = p(\mathbf{x})(k(\rho, U)\nabla\rho - h(\rho, U)\nabla U) \tag{2.92}$$

Matching the coefficient of $\nabla\rho$, we have

$$(G_{\rho\rho}(\rho, U) + R''(\rho)) = p(\mathbf{x})k(\rho, U) \tag{2.93}$$

$$p(\mathbf{x}) = \frac{1}{k(\rho, U)}(G_{\rho\rho} + R''(\rho)) \tag{2.94}$$

We must have $p(\mathbf{x}) > 0$, and since $k(\rho, U) > 0$, this requires (2.76). In addition we need $-p(\mathbf{x})h(\rho, U) = G_{\rho U}(\rho, U)$. Using (2.94) and matching the coefficients of ∇U in (2.91,2.92),

$$G_{\rho U}(\rho, U) = -\frac{h(\rho, U)}{k(\rho, U)}(G_{\rho\rho} + R''(\rho)), \tag{2.95}$$

which is (2.75).

Thus, these tools allow the systematic construction of Horstmann's functional.

There is another restriction, not an additional condition, but one that can be derived from those already shown. Since $k > 0$ and $G_{\rho\rho} + R'' > 0$, (2.95) implies that h and $G_{\rho U} = -g_\rho$ are opposite in sign—that is, the organisms either produce an attractant or destroy a repellent—which is to say, they are attracted to each other. If this is not the case, $\mathscr{H}(\rho, U)$ may increase with time. This issue reappears in the analysis of repellents in the worm model below (Section 2.4.7), where I argue that it is fundamental to the biology.

2.3.3 An example of nonexistence of the functional antiderivative

As shown below (sections 2.4.2, 2.4.3, 2.4.4), theorems 2.5, 2.8, and 2.11 together with radial integration are all that is needed to construct time-decreasing free energy functionals for the minimal system. For the worm system, however, these tools fail. The problem is the diffusion term $D\nabla^2 U$ in the U PDE (2.1). Although a functional antiderivative of $D\nabla^2 U$ can be constructed by radial integration, this construction fails when $\nabla^2 U$ is multiplied by a nonconstant function of U. For example, there is no functional whose functional antiderivative is $U\nabla^2 U$ (for $U \in H^2_P(\Omega)$).

Theorem 2.14. *Let $U \in H^2_P(\Omega)$ and $\mathscr{D} : H^2_P(\Omega) \to \mathbb{R}$ be any functional of U. Then it is not psosible to choose $\mathscr{D}$ such that the following holds:*

$$\frac{\delta \mathscr{D}(U)}{\delta U(\mathbf{x})} = U\nabla^2 U \tag{2.96}$$

I will prove this theorem in two ways. I will begin by using the radial integration test. I will then use the Fourier series, to show how this nonexistence can be framed as a problem with a function of multiple variables.

Radial integration test (Remark 2.13). The radial integration lemma says that if $U\nabla^2 U$ has a functional antiderivative, it must be

$$\mathscr{D}(U) = \int_{r=0}^{1} \left(\int_{\Omega} rU(\mathbf{x}) \nabla^2 (rU(\mathbf{x})) U(\mathbf{x}) \mathrm{d}\mathbf{x} \right) \mathrm{d}r \tag{2.97}$$

$$= \int_{r=0}^{1} \left(r^2 \int_{\Omega} U(\mathbf{x}) \nabla^2 U(\mathbf{x}) U(\mathbf{x}) \mathrm{d}\mathbf{x} \right) \mathrm{d}r \tag{2.98}$$

$$= \left(\int_{r=0}^{1} r^2 \mathrm{d}r \right) \left(\int_{\Omega} U^2(\mathbf{x}) \nabla^2 U(\mathbf{x}) U(\mathbf{x}) \mathrm{d}\mathbf{x} \right) \tag{2.99}$$

$$= \frac{1}{3} \int_{\Omega} U^2(\mathbf{x}) \nabla^2 \mathrm{d}\mathbf{x} \tag{2.100}$$

Now let's check the functional derivative of $\mathscr{D}$.

$$\mathscr{D}(U + \epsilon\phi) = \frac{1}{3} \int_{\Omega} (U + \epsilon\phi)^2 \left(\nabla^2 U + \epsilon \nabla^2 \phi \right) \mathrm{d}\mathbf{x} \tag{2.101}$$

$$= \frac{1}{3} \int_{\Omega} U^2 \nabla^2 U \mathrm{d}\mathbf{x} + \frac{2}{3} \epsilon \int_{\Omega} U \phi \nabla^2 U \mathrm{d}\mathbf{x} \tag{2.102}$$

$$+ \frac{1}{3} \epsilon \int_{\Omega} U^2 \nabla^2 \phi \mathrm{d}\mathbf{x} + \mathscr{O}\left(\epsilon^2\right)$$

$$\frac{\mathscr{D}(U + \epsilon\phi) - \mathscr{D}(U)}{\epsilon} = \frac{2}{3} \int_{\Omega} U \nabla^2 U \phi \mathrm{d}\mathbf{x} + \frac{1}{3} \int_{\Omega} U^2 \nabla^2 \phi \mathrm{d}\mathbf{x} + \mathscr{O}(\epsilon) \tag{2.103}$$

$$\lim_{\epsilon \to 0} \frac{\mathscr{D}(U + \epsilon\phi) - \mathscr{D}(U)}{\epsilon} = \frac{2}{3} \int_{\Omega} U \nabla^2 U \phi \mathrm{d}\mathbf{x} + \frac{1}{3} \int_{\Omega} U^2 \nabla^2 \phi \mathrm{d}\mathbf{x} \tag{2.104}$$

The first integral of (2.104) is already in the form (2.16). To put the second in the same form takes two integrations by parts

$$\frac{1}{3} \int_{\Omega} U^2 \nabla^2 \phi \mathrm{d}\mathbf{x} = -\frac{1}{3} \int_{\Omega} \nabla \left(U^2 \right) \cdot \nabla \phi \mathrm{d}\mathbf{x} \tag{2.105}$$

$$= \frac{1}{3} \int_{\Omega} \nabla^2 \left(U^2 \right) \phi \mathrm{d}\mathbf{x} \tag{2.106}$$

$$= \frac{2}{3} \int_{\Omega} \left(\nabla U \cdot \nabla U + U \nabla^2 U \right) \phi \mathrm{d}\mathbf{x} \tag{2.107}$$

Leading, at last, to

$$\frac{\delta\mathscr{D}(U)}{\delta U(\mathbf{x})} = \frac{4}{3}U\nabla^2 U + \frac{2}{3}\|\nabla U\|^2 \tag{2.108}$$

$$\frac{\delta\mathscr{D}(U)}{\delta U(\mathbf{x})} \neq U\nabla^2 U \tag{2.109}$$

Generalizing to $\mathscr{d}(U) = U^n\nabla^2 U$, radial integration produces

$$\mathscr{D}(U) = \frac{1}{n+2}\int_\Omega U^{n+1}\nabla^2 U \mathrm{d}\mathbf{x} \tag{2.110}$$

$$\frac{\delta\mathscr{D}(U)}{\delta U(\mathbf{x})} = \frac{n+1}{n+2}\left(2U^n\nabla^2 U + nU^{n-1}\|\nabla U\|^2\right) \tag{2.111}$$

The functional antiderivative of $U^n\nabla^2 U$ exists only for $n = 0$.

□

Fourier series coefficients. Any functional $\mathscr{D}(U)$ for periodic functions $U \in H^2_P(\Omega)$ on $\Omega = [0,1]^d$ is also a function of the Fourier coefficients of U, since every such function can be expressed as a Fourier series. I will denote this equivalent function $\widetilde{\mathscr{D}}(\tilde{U})$.

$$\widetilde{\mathscr{D}}(\tilde{\mathbf{U}}) \coloneqq \mathscr{D}\left(\mathbf{x} \mapsto \sum_{\mathbf{k}\in 2\pi\mathbb{Z}^d} \tilde{U}_{\mathbf{k}} e^{i\mathbf{k}\cdot\mathbf{x}}\right) \tag{2.112}$$

Suppose for contradiction that there exists a functional $\mathscr{D}(U)$ whose functional derivative is $U\nabla^2 U$. Then an equivalent function $\widetilde{\mathscr{D}}$ of the vector of Fourier series coefficients $\tilde{\mathbf{U}}$ also exists. How does $\widetilde{\mathscr{D}}$ depend on $\tilde{U}_{\mathbf{k}}$?

$$\frac{\partial\widetilde{\mathscr{D}}(\tilde{U})}{\partial\tilde{U}_{\mathbf{k}}} = \lim_{\epsilon\to 0}\frac{\widetilde{\mathscr{D}}\left(\tilde{\mathbf{U}} + \epsilon\mathbf{e}_{\mathbf{k}}\right) - \widetilde{\mathscr{D}}\left(\tilde{\mathbf{U}}\right)}{\epsilon} \tag{2.113}$$

Here $\mathbf{e}_{\mathbf{k}} \coloneqq (\dots, 0, 1, 0, \dots)$ represents the vector indexed by $2\pi\mathbb{Z}^d$ all of whose elements are 0 except for the one in position $\mathbf{k}$, which is 1. Then,

$$\widetilde{\mathscr{D}}(\tilde{\mathbf{U}} + \epsilon \mathbf{e}_{\mathbf{k}}) = \mathscr{D}\left(U + \epsilon e^{i\mathbf{k}\cdot\mathbf{x}}\right) \tag{2.114}$$

$$\lim_{\epsilon\to 0} \frac{\widetilde{\mathscr{D}}\left(\tilde{\mathbf{U}} + (\dots, 0, \epsilon, 0, \dots)\right) - \widetilde{\mathscr{D}}\left(\tilde{U}\right)}{\epsilon} = \lim_{\epsilon\to 0} \frac{\mathscr{D}\left(U + \epsilon e^{i\mathbf{k}\cdot\mathbf{x}}\right) - \mathscr{D}(U)}{\epsilon} \tag{2.115}$$

$$= \int_\Omega \frac{\delta \mathscr{D}(U)}{\delta U(\mathbf{x})} e^{i\mathbf{k}\cdot\mathbf{x}} \mathrm{d}\mathbf{x} \tag{2.116}$$

$$= \int_\Omega \left(\sum_{\mathbf{j}\in 2\pi\mathbb{Z}^d} \widetilde{(U\nabla^2 U)}_{\mathbf{j}} e^{i\mathbf{j}\cdot\mathbf{x}} \right) e^{i\mathbf{k}\cdot\mathbf{x}} \mathrm{d}\mathbf{x} \tag{2.117}$$

$$= \left(\sum_{\mathbf{j}\in 2\pi\mathbb{Z}^d} \widetilde{(U\nabla^2 U)}_{\mathbf{j}} \int_\Omega e^{i(\mathbf{j}+\mathbf{k})\cdot\mathbf{x}} \right) \tag{2.118}$$

$$= \left(\sum_{\mathbf{j}\in 2\pi\mathbb{Z}^d} \widetilde{(U\nabla^2 U)}_{\mathbf{j}} \delta_{\mathbf{j},-\mathbf{k}} \right) \tag{2.119}$$

$$= \widetilde{(U\nabla^2 U)}_{-\mathbf{k}} \tag{2.120}$$

That is, the partial derivative of $\widetilde{\mathscr{D}}$ with respect to $\tilde{U}_{\mathbf{k}}$ is the $-\mathbf{k}$ coefficient of the Fourier series for the functional derivative of $\mathscr{D}$. The Fourier coefficients of $\nabla^2 U$ are $\widetilde{(\nabla^2 U)}_{\mathbf{k}} = -k^2 \tilde{U}_{\mathbf{k}}$ (letting $k \coloneqq \|\mathbf{k}\|$). The coefficient vector of a product is the discrete convolution of the coefficient vectors for the factors,

$$\widetilde{(fg)} = \tilde{f} * \tilde{g} \tag{2.121}$$

$$\left(\tilde{f} * \tilde{g}\right)_{\mathbf{k}} \coloneqq \sum_{\mathbf{j}\in 2\pi\mathbb{Z}^d} \tilde{f}_{\mathbf{j}} \tilde{g}_{\mathbf{k}-\mathbf{j}} \tag{2.122}$$

$$= \sum_{\mathbf{j}\in 2\pi\mathbb{Z}^d} \tilde{g}_{\mathbf{j}} \tilde{f}_{\mathbf{k}-\mathbf{j}} \tag{2.123}$$

Thus,

$$\frac{\partial \widetilde{\mathscr{D}}(\tilde{\mathbf{U}})}{\partial \tilde{U}_{\mathbf{k}}} = \widetilde{(U\nabla^2 U)}_{-\mathbf{k}} = \sum_{\mathbf{j}\in 2\pi\mathbb{Z}^d} -j^2 \tilde{U}_{\mathbf{j}} \tilde{U}_{-\mathbf{k}-\mathbf{j}} \tag{2.124}$$

Now, to find the mixed partial derivative, $\partial^2\widetilde{\mathscr{D}}(\tilde{\mathbf{U}})/(\partial\tilde{U}_{\mathbf{m}}\partial\tilde{U}_{\mathbf{k}})$, we need to differentiate this sum with respect to $\tilde{U}_{\mathbf{m}}$. Unless $-\mathbf{k} = 2\mathbf{m}$, $\tilde{U}_{\mathbf{m}}$ appears in two terms in this sum, when $\mathbf{j} = \mathbf{m}$, and when $-\mathbf{k} - \mathbf{j} = \mathbf{m}$. If $-\mathbf{k} = 2\mathbf{m}$, these are combined in a single term

$$\begin{aligned}\frac{\partial^2\widetilde{\mathscr{D}}(\tilde{\mathbf{U}})}{\partial\tilde{U}_{\mathbf{m}}\partial\tilde{U}_{\mathbf{k}}} &= \frac{\partial}{\partial\tilde{U}_{\mathbf{m}}}\begin{cases} -m^2\tilde{U}_{\mathbf{m}}\tilde{U}_{-\mathbf{k}-\mathbf{m}} - \|\mathbf{k}+\mathbf{m}\|^2\tilde{U}_{-\mathbf{k}-\mathbf{m}}\tilde{U}_{\mathbf{m}} & \text{if } -\mathbf{k} \neq 2\mathbf{m} \\ -m^2\tilde{U}_{\mathbf{k}}^2 & \text{if } -\mathbf{k} = 2\mathbf{m}\end{cases} && (2.125)\\ &= -m^2\tilde{U}_{-\mathbf{k}-\mathbf{m}} - \|\mathbf{k}+\mathbf{m}\|^2\tilde{U}_{-\mathbf{k}-\mathbf{m}} && (2.126)\\ &= -(2m^2 + k^2 + 2\mathbf{k}\cdot\mathbf{m})\tilde{U}_{-\mathbf{k}-\mathbf{m}} && (2.127)\end{aligned}$$

This result is not symmetric to exchange of $\mathbf{k}$ and $\mathbf{m}$, so, for general $\tilde{\mathbf{U}}$ there is no function $\widetilde{\mathscr{D}}(\tilde{\mathbf{U}})$ that has the partial derivatives (2.124). Therefore there is no functional $\mathscr{D}(U)$ whose functional derivative is $U\nabla^2 U$.

□

2.3.4 Approximate functional antiderivatives

As just demonstrated, some expressions do not have functional antiderivatives. In this section I explore the possibility that an approximate functional antiderivative may sometimes be defined in such a case. The idea, admittedly, seems contradictory at first. Normally when we say "X approximates Y", we mean "X is close to Y" or "the difference between X and Y is small". If Y, provably, doesn't exist, how can any X be close to it? The paradox is resolved by defining an approximate functional antiderivative to be something whose functional derivative is close to the desired function. That is, I will call $\mathscr{F}(U)$ an approximate functional antiderivative of $\mathscr{f}(U)$ if

$$\begin{aligned}\frac{\delta\mathscr{F}(U)}{\delta U(\mathbf{x})} &\approx \mathscr{f}(U)(\mathbf{x}) && (2.128)\\ e_{\mathscr{F}}(\mathbf{x}) &\coloneqq \frac{\delta\mathscr{F}(U)}{\delta U(\mathbf{x})} - \mathscr{f}(U)(\mathbf{x}) \quad \text{is small,} && (2.129)\end{aligned}$$

where "is small" can be defined, for instance, as a bound on a norm of $e_{\mathscr{F}}$. Below I develop a bound based on the L^1 norm.

To construct a free energy functional for the worm system, we will eventually look for a functional antiderivative of $V_U'(U)\nabla^2 U$ (section 2.4.5). If V_U is affine and therefore V_U' constant, then $\mathscr{D}(U) = \frac{1}{2}\int_\Omega V_U' U \nabla^2 U \mathrm{d}\mathbf{x}$ works. However, as just demonstrated (Theorem 2.14), for nonaffine V_U there may be no functional whose functional derivative is $V_U'(U)\nabla^2 U$. One can nevertheless construct a functional by radial integration,

$$\mathscr{D}(U) = \int_{r=0}^{1} \left(\int_\Omega V_U'(rU(\mathbf{x}))\nabla^2(rU)(\mathbf{x})U(\mathbf{x})\mathrm{d}\mathbf{x} \right) \mathrm{d}r \tag{2.130}$$

$$= \left(V_U(U) - \frac{W_U(U)}{U} \right) \nabla^2 U \tag{2.131}$$

$$= f(U)\nabla^2 U \tag{2.132}$$

$$f(U) \coloneqq V_U(U) - \frac{W_U(U)}{U} \tag{2.133}$$

Define the functional derivative error function $e_{\mathscr{D}}$ as the difference between the actual and desired functional derivative,

$$e_{\mathscr{D}}(\mathbf{x}) \coloneqq \frac{\delta \mathscr{D}(U)}{\delta U(\mathbf{x})} - V_U'(U(\mathbf{x}))\nabla^2 U(\mathbf{x}) \tag{2.134}$$

Theorem 2.15. *Let*

- $U \in H^2_{P+}(\Omega)$ *be a twice-differentiable positive function of space,*
- $\mathscr{D}$ *be the functional of* U *defined in (2.130, 2.131).*
- $f(U)$ *as defined in* (2.133) *be a twice differentiable function that is either either convex (i.e.,* $f''(U(\mathbf{x})) > 0$ *for all* $\mathbf{x} \in \Omega$*) or concave (*$f''(U(\mathbf{x})) < 0$ *for all* $\mathbf{x} \in \Omega$*),*
- $V_U \in C^2(\mathbb{R})$
- $e_{\mathscr{D}}$ *be as defined in* (2.134)*.*

Then $e_{\mathscr{D}}$ *satisfies the following bounds*

I.

$$\int_\Omega U e_{\mathscr{D}} \mathrm{d}\mathbf{x} = 0 \tag{2.135}$$

II.

$$\|U\boldsymbol{e}_{\mathscr{D}}\|_1 \leq 2\left\|Uf'(U)\nabla^2 U\right\|_1 + 2\left\|f(U)\nabla^2 U\right\|_1 \tag{2.136}$$

Proof. Let $\mathscr{D}$, f, V_U, and $\boldsymbol{e}_{\mathscr{D}}, U$ be as above. Begin by collecting some useful identities. Identities (2.137) and (2.138) below are true for any f and U for which the derivatives exist; (2.139) is specific for f as defined in (2.133).

$$\begin{aligned}
\nabla^2 f(U(\mathbf{x})) &= f'(U(\mathbf{x}))\nabla^2 U(\mathbf{x}) + f''(U(\mathbf{x}))\nabla U(\mathbf{x})\cdot\nabla U(\mathbf{x}) && (2.137)\\
&= f'(U)\nabla^2 U + f''(U)\nabla U\cdot\nabla U \\
Uf''(U)\nabla U &= \nabla(Uf'(U) - f(U)) && (2.138)\\
V_U'(U) &= \frac{1}{U}\frac{d}{dU}\left(Uf(U)\right) && (2.139)
\end{aligned}$$

Assume first that f is convex, $f'' \geq 0$. This is the case when V_U is defined by (2.11) with $\beta > 0$. We will need $\delta\mathscr{D}(U)/\delta U(\mathbf{x})$

$$\begin{aligned}
\mathscr{D}(U+\epsilon\phi) &= \int_\Omega f(U+\epsilon\phi)\nabla^2(U+\epsilon\phi)\mathrm{d}\mathbf{x} \\
&= \int_\Omega \left(f(U) + \epsilon f'(U)\phi + \mathcal{O}\left(\epsilon^2\right)\right)\left(\nabla^2 U + \epsilon\nabla^2\phi\right)\mathrm{d}\mathbf{x} \\
&= \int_\Omega \left(f(U)\nabla^2 U + \epsilon f'(U)\phi\nabla^2 U + \epsilon f(U)\nabla^2\phi + \mathcal{O}\left(\epsilon^2\right)\right)\mathrm{d}\mathbf{x} \\
\lim_{\epsilon\to 0}\frac{\mathscr{D}(U+\epsilon\phi)-\mathscr{D}(U)}{\epsilon} &= \int_\Omega \left(f'(U)\phi\nabla^2 U + f(U)\nabla^2\phi\right)\mathrm{d}\mathbf{x} \\
&= \int_\Omega \left(f'(U)\nabla^2 U\phi + \nabla^2 f(U)\phi\right)\mathrm{d}\mathbf{x} && (2\text{xIBP})\\
\frac{\delta\mathscr{D}(U)}{\delta U(\mathbf{x})} &= f'(U)\nabla^2 U + \nabla^2 f(U) \\
&= f'(U)\nabla^2 U + f'(U)\nabla^2 U + f''(U)(\nabla U\cdot\nabla U) && (2.137)\\
\frac{\delta\mathscr{D}(U)}{\delta U(\mathbf{x})} &= 2f'(U)\nabla^2 U + f''(U)(\nabla U\cdot\nabla U) && (2.140)
\end{aligned}$$

Now we compute the error

$$
\begin{aligned}
e_{\mathscr{D}}(\mathbf{x}) &= \frac{\delta \mathscr{D}(U)}{\delta U(\mathbf{x})} - V_U'(U(\mathbf{x}))\nabla^2 U(\mathbf{x}) && (2.134)\\
&= 2f'(U)\nabla^2 U + f''(U)(\nabla U \cdot \nabla U) && (2.140)\\
&\quad - \frac{1}{U}\frac{d}{dU}(Uf(U))\nabla^2 U && (2.139)\\
&= 2f'(U)\nabla^2 U + f''(U)(\nabla U \cdot \nabla U)\\
&\quad - \left(\frac{1}{U}f(U) + f'(U)\right)\nabla^2 U\\
&= f'(U)\nabla^2 U + f''(U)(\nabla U \cdot \nabla U) - \frac{1}{U}f(U)\nabla^2 U && (2.141)
\end{aligned}
$$

Now we find the U-weighted total error.

$$
\begin{aligned}
\int_\Omega U e_{\mathscr{D}} \mathrm{d}\mathbf{x} &= \int_\Omega U f'(U)\nabla^2 U \mathrm{d}\mathbf{x} + \int_\Omega U f''(U)(\nabla U \cdot \nabla U)\mathrm{d}\mathbf{x}\\
&\quad - \int_\Omega f(U)\nabla^2 U \mathrm{d}\mathbf{x}\\
&= \int_\Omega U f'(U)\nabla^2 U \mathrm{d}\mathbf{x}\\
&\quad + \int_\Omega \nabla(Uf'(U) - f(U)) \cdot \nabla U)\mathrm{d}\mathbf{x} && \text{by (2.138)}\\
&\quad - \int_\Omega f(U)\nabla^2 U \mathrm{d}\mathbf{x}\\
&= \int_\Omega U f'(U)\nabla^2 U \mathrm{d}\mathbf{x}\\
&\quad - \int_\Omega (Uf'(U) - f(U))\nabla^2 U \mathrm{d}\mathbf{x} && \text{(IBP)}\\
&\quad - \int_\Omega f(U)\nabla^2 U \mathrm{d}\mathbf{x}\\
&= 0
\end{aligned}
$$

This completes the proof of part I.. For II., multiply the error by U and find the 1-norm.

$$U e_{\mathscr{D}} = U f'(U)\nabla^2 U + U f''(U)(\nabla U \cdot \nabla U) - f(U)\nabla^2 U \tag{2.142}$$

$$\|U e_{\mathscr{D}}\|_1 = \int_\Omega \left| U f'(U)\nabla^2 U + U f''(U)(\nabla U \cdot \nabla U) - f(U)\nabla^2 U \right| \mathrm{d}\mathbf{x} \tag{2.143}$$

$$\leq \int_\Omega \left| U f'(U)\nabla^2 U \right| \mathrm{d}\mathbf{x} + \int_\Omega \left| U f''(U)(\nabla U \cdot \nabla U) \right| \mathrm{d}\mathbf{x} \tag{2.144}$$

$$+ \int_\Omega \left| f(U)\nabla^2 U \right| \mathrm{d}\mathbf{x}$$

$$= \int_\Omega \left| U f'(U)\nabla^2 U \right| \mathrm{d}\mathbf{x} + \int_\Omega U f''(U)(\nabla U \cdot \nabla U) \mathrm{d}\mathbf{x} \tag{2.145}$$

$$+ \int_\Omega \left| f(U)\nabla^2 U \right| \mathrm{d}\mathbf{x}$$

In the final step I removed the absolute value signs from the middle integral, using $U > 0$ and the convexity of f to infer that $U f''(U)(\nabla U \cdot \nabla U) \geq 0$. Now, to evaluate that middle integral,

$$\int_\Omega U f''(U)(\nabla U \cdot \nabla U) \mathrm{d}\mathbf{x} = \int_\Omega (U f''(U)\nabla U) \cdot \nabla U \mathrm{d}\mathbf{x} \geq 0 \tag{2.146}$$

$$= \int_\Omega \nabla(U f'(U) - f(U)) \cdot \nabla U \mathrm{d}\mathbf{x} \qquad \text{by (2.138)} \tag{2.147}$$

$$= -\int_\Omega (U f'(U) - f(U))\nabla^2 U \mathrm{d}\mathbf{x} \geq 0 \qquad \text{(IBP)} \tag{2.148}$$

Substituting into (2.145),

$$\|U\,(e_{\mathscr{D}})\|_1 = \int_\Omega \left| U f'(U)\nabla^2 U \right| \mathrm{d}\mathbf{x} - \int_\Omega \left(U f'(U) - f(U) \right) \nabla^2 U \mathrm{d}\mathbf{x} \tag{2.149}$$

$$+ \int_\Omega \left| f(U)\nabla^2 U \right| \mathrm{d}\mathbf{x}$$

$$= \int_\Omega \left| U f'(U)\nabla^2 U \right| \mathrm{d}\mathbf{x} - \int_\Omega U f'(U)\nabla^2 U \mathrm{d}\mathbf{x} \tag{2.150}$$

$$+ \int_\Omega f(U)\nabla^2 U \mathrm{d}\mathbf{x} + \int_\Omega \left| f(U)\nabla^2 U \right| \mathrm{d}\mathbf{x}$$

$$\leq 2 \left\| U f'(U)\nabla^2 U \right\|_1 + 2 \left\| f(U)\nabla^2 U \right\|_1 \tag{2.151}$$

For the case of concave f, simply apply the argument to $-V_U$, $-f$. If f is concave, $-f$ is convex, and of course (2.136) is unchanged by a flip in the sign of f. f is concave for V_U as defined in (2.11) with $\beta < 0$.

□

There are two countervailing points to be made about this bound. First, in the context of the Keller-Segel system, the estimate is not as useful as one might hope. Since one of the main uses of a free energy functional is in analyzing equilibrium and exploring behavior near equilibrium, one would prefer that the error approach zero as the system approaches equilibrium. U and therefore $f(U)$ and $f'(U)$ are bounded but large at equilibrium. I show below that at equilibrium, $U = g * \rho$, where g is the Green's function (2.157). Since convolution is a smoothing or averaging transformation,

$$\min_{\mathbf{x}\in\Omega}\left(\frac{s}{\gamma}\rho(\mathbf{x})\right) \leq U(\mathbf{x}) \leq \max_{\mathbf{x}\in\Omega}\left(\frac{s}{\gamma}\rho(\mathbf{x})\right) \tag{2.152}$$

In principle U may transiently stray outside these bounds, when ρ changes quickly, but in practice this is essentially never observed in numerical solutions.

The mean of U at equilibrium is $s\bar{\rho}/\gamma$, where $\bar{\rho}$ is the mean of ρ, a constant. Since U and $f(U)$ remain large at equilibrium, the only possible savior in the bound (2.136) is the factor $\nabla^2 U$. Unfortunately, $\nabla^2 U$ remains substantial at equilibrium. From (2.154),

$$\nabla^2 U_{\text{eq}} = \frac{\gamma}{D}\left(U - \frac{s}{\gamma}\rho_{\text{eq}}\right) \tag{2.153}$$

$U = s\rho/\gamma$ is the local equilibrium concentration, the signal concentration that would be in equilibrium with the local density of worms if there were no diffusion. Thus, at equilibrium, $\nabla^2 U$ is proportional to the difference between U and the local equilibrium concentration. Unfortunately, this differs from zero at equilibrium.

The second countervailing point is that the actual performance of the functional (2.130) is substantially better than the estimate (2.136) suggests. Intuitively, it is evident that there will be considerable cancellation among the terms of (2.142). ($\nabla^2 U$ is negative at maxima of U and positive at minima, so it is negatively correlated with U.) The triangle inequality (2.144) amounts to making the most pessimistic possible assumptions about cancellation. In fact, cancellation is perfect, in the sense that the U-weighted average of the error is 0 (Theorem 2.15, part I.).

Based on these arguments, I will suggest that, even though (2.191) below is not a Lyapunov functional for the worm system (2.1, 2.3), it might be a good approximation. As a quick numerical test, I convolved a step function $\rho(x)$ in one dimension with the appropriate Green's function and computed the U-dependent parts of $\mathcal{F}(U)$ and $\delta\mathcal{F}(\rho, U)/\delta U(x)$, using parameters and a configuration similar to those that arise in simulations described in chapter 3. Plots are shown in Figure 2.1. Only the U-dependent components of the functional are plotted, since it is only these that are not exact. Note the change in scale from Figure 2.1B, plotting the integrand of the functional to Figure 2.1C, plotting its functional derivative with respect to U. The latter would ideally be 0. The predicted rate of change of $\mathcal{F}(\rho, U)$ is about 1/60 of its value per day. Since full simulations typically are near equilibrium after $3\,\mathrm{h}$, this is a very low rate of change.

The performance of these approximate energy functions in numerical solutions of the PDEs is explored further in Section 3.6.

2.4 Energy functionals for the Keller-Segel system

2.4.1 Chemical signal equilibrium for fixed density

Equilibria of the Keller-Segel system are those functions $\rho(\mathbf{x}), U(\mathbf{x})$ such that the time derivatives are zero, i.e. (2.154, 2.161) below. I will begin by considering the two components separately. That is, if we assume a certain fixed $\rho_0(\mathbf{x})$, what $U(\mathbf{x})$ is in equilibrium with it, and vice versa? An equilibrium of U satisfies

$$0 = -\gamma U(\mathbf{x}) + D\nabla^2 U(\mathbf{x}) + s\rho_0(\mathbf{x}) \tag{2.154}$$

This is an analytically and numerically tractable problem. Analytical solutions can be found for simple geometries (e.g., worms uniformly distributed on a disk in two dimensions). For a given $\rho_0(\mathbf{x})$, the solution $U(\mathbf{x})$ is unique and globally stable (shown below) and can be computed as a convolution of ρ_0 with a Green's function $g(\mathbf{x})$.

$$U(\mathbf{x}) = (g * \rho_0)(\mathbf{x}) \tag{2.155}$$

I define convolution on Ω by

$$(f * g)(\mathbf{y}) \coloneqq \int_\Omega f(\mathbf{x}) g(\mathbf{y} - \mathbf{x}) \mathrm{d}\mathbf{x} \tag{2.156}$$

A. Density and attractant concentration

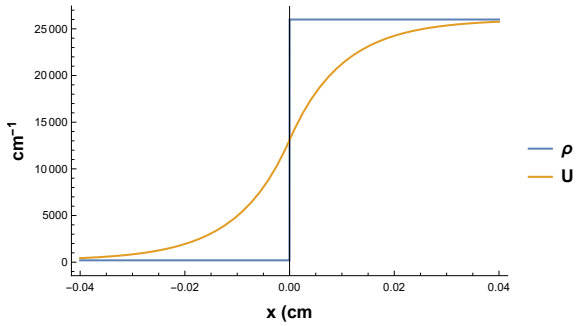

B. Integrand of components of free energy functional derived from the U PDE

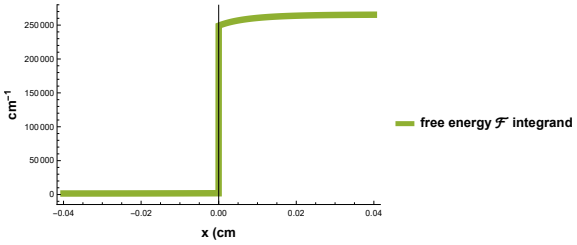

C. Functional derivative of the functional whose integrand is shown in B, with ideal derivative

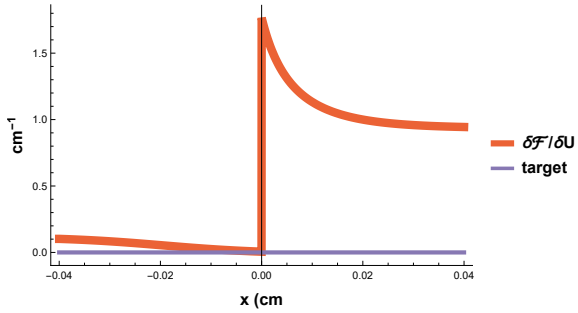

Figure 2.1: Free energy functional as an approximation.
A. Example $\rho(x)$ and $U(x)$ functions, based on typical configurations from numerical simulations. $U(x)$ is the solution to (2.154) with the $\rho(x)$ shown and parameters $s = 0.01\,\mathrm{s}^{-1}$, $\gamma = 0.01\,\mathrm{s}^{-1}$, $D = 10^{-6}\,\mathrm{cm}^2\,\mathrm{s}^{-1}$. **B**. The functional $\mathcal{F}(\rho, U)$ is an integral over x of an expression in $\rho(x)$ and $U(x)$. The sum of those terms that measure the disequilibrium of U:

$$\mathcal{F}(\rho, U) = -\gamma/s(UV_U(U) - W_U(U)) + D/s(V_U(U) - (W_U(U)/U))\nabla^2 U + \rho V_U(U)$$

is plotted. **C**. The functional derivative of the functional whose integrand is plotted in B together with the target derivative: what this would be if $\mathcal{F}$ were an exact Lyapunov functional. Since U was constructed to be in equilibrium with ρ, the target is, by construction, exactly 0.

As usual, convolution is associative, commutative, and multilinear, and the Convolution Theorem (CT), $\widetilde{(f * g)}_{\mathbf{k}} = \tilde{f}_{\mathbf{k}}\tilde{g}_{\mathbf{k}}$ is easily verified with definition (2.156) and periodic functions on $\bar{\Omega} = [0,1]^d$. (See 2.6 for Fourier series notation.)

The Green's functions are most useful in their Fourier series form

$$g(\mathbf{x}) = \sum_{\mathbf{k}\in 2\pi\mathbb{Z}^d} \tilde{g}_{\mathbf{k}}(\mathbf{x}) e^{i\mathbf{k}\cdot\mathbf{x}} \tag{2.157}$$

$$\tilde{g}_{\mathbf{k}} = \frac{s}{\gamma + D\|\mathbf{k}\|^2} \tag{2.158}$$

The $\tilde{g}_{\mathbf{k}}$ are real and even (i.e. $\tilde{g}^*_{\mathbf{k}} = \tilde{g}_{\mathbf{k}}$, $\tilde{g}_{-\mathbf{k}} = \tilde{g}_{\mathbf{k}}$), and consequently so is $g(\mathbf{x})$. Additionally, $g(\mathbf{x}) > 0$ for all $\mathbf{x} \in \Omega$.

Assuming (2.155), (2.1) becomes in the Fourier basis,

$$\begin{aligned}
\dot{U} &= \sum_{\mathbf{k}\in 2\pi\mathbb{Z}^d} \left(-\gamma\tilde{U}_{\mathbf{k}} e^{i\mathbf{k}\cdot\mathbf{x}} + D\nabla^2\tilde{U}_{\mathbf{k}} e^{i\mathbf{k}\cdot\mathbf{x}} + s\widetilde{\rho_0}_{\mathbf{k}} e^{i\mathbf{k}\cdot\mathbf{x}}\right) \\
&= \sum_{\mathbf{k}\in 2\pi\mathbb{Z}^d} \left(-\gamma\tilde{U}_{\mathbf{k}} - D\|\mathbf{k}\|^2\tilde{U}_{\mathbf{k}} + s\widetilde{\rho_0}_{\mathbf{k}}\right) e^{i\mathbf{k}\cdot\mathbf{x}} \\
&= \sum_{\mathbf{k}} \left(-\gamma\widetilde{(g*\rho_0)}_{\mathbf{k}} - D\|\mathbf{k}\|^2\widetilde{(g*\rho_0)}_{\mathbf{k}} + s\widetilde{\rho_0}_{\mathbf{k}}\right) e^{i\mathbf{k}\cdot\mathbf{x}} && \text{(2.155)} \\
&= \sum_{\mathbf{k}} \left(-\gamma\tilde{g}_{\mathbf{k}}\widetilde{\rho_0}_{\mathbf{k}} - D\|\mathbf{k}\|^2\tilde{g}_{\mathbf{k}}\widetilde{\rho_0}_{\mathbf{k}} + s\widetilde{\rho_0}_{\mathbf{k}}\right) e^{i\mathbf{k}\cdot\mathbf{x}} && \textbf{(CT)} \\
&= \sum_{\mathbf{k}} \left(-(\gamma + D\|\mathbf{k}\|^2)\tilde{g}_{\mathbf{k}} + s\right) \widetilde{\rho_0}_{\mathbf{k}} e^{i\mathbf{k}\cdot\mathbf{x}} \\
&= \sum_{\mathbf{k}} \left(-(\gamma + D\|\mathbf{k}\|^2)\frac{s}{\gamma + D\|\mathbf{k}\|^2} + s\right) \widetilde{\rho_0}_{\mathbf{k}} e^{i\mathbf{k}\cdot\mathbf{x}} && \text{(2.157)} \\
&= 0
\end{aligned}$$

Thus (2.155) is indeed an equilibrium.

2.4.2 Lyapunov (energy) functional for the chemical signal

To show that this equilibrium is unique and globally stable, I will develop a Lyapunov functional for U. We use Remark 2.6. We need a functional $\mathcal{F}(U)$ with functional derivative

$$\frac{\delta \mathscr{F}(U)}{\delta U(\mathbf{x})} = \gamma U(\mathbf{x}) - D\nabla^2 U(\mathbf{x}) - s\rho_0(\mathbf{x}) \tag{2.159}$$

The hard part was already done in section 2.3.2, where I found a functional antiderivative of $\nabla^2 U$. Putting this together with the integral of $\gamma U - s\rho_0$ gives the functional

$$\mathscr{F}(U) = \int_\Omega \left(\frac{\gamma}{2} U^2 + \frac{D}{2} \|\nabla U\|^2 - s\rho_0 U \right) \mathrm{d}\mathbf{x} \tag{2.160}$$

To verify,

$$\begin{aligned}
\mathscr{F}(U+\epsilon\phi) &= \int_\Omega \left(\frac{\gamma}{2}(U+\epsilon\phi)^2 \right. \\
&\qquad + \frac{D}{2}(\nabla U + \epsilon\nabla\phi)\cdot(\nabla U + \epsilon\nabla\phi) \\
&\qquad \left. - s\rho_0(U+\epsilon\phi) \right) \mathrm{d}\mathbf{x} \\
&= \int_\Omega \left(\frac{\gamma}{2} U^2 + \frac{D}{2}\|\nabla\|^2 - s\rho_0 U \right) \mathrm{d}\mathbf{x} \\
&\qquad + \epsilon \int_\Omega \left(\gamma U\phi + D\nabla U\cdot\nabla\phi - s\rho_0\phi \right) \mathrm{d}\mathbf{x} + \mathscr{O}\left(\epsilon^2\right) \\
\frac{\mathscr{F}(U+\epsilon\phi) - \mathscr{F}(U)}{\epsilon} &= \int_\Omega \left(\gamma U\phi + D\nabla U\cdot\nabla\phi - s\rho_0\phi \right) \mathrm{d}\mathbf{x} + \mathscr{O}(\epsilon) \\
\lim_{\epsilon\to 0} \frac{\mathscr{F}(U+\epsilon\phi) - \mathscr{F}(U)}{\epsilon} &= \int_\Omega \left(\gamma U\phi + D\nabla U\cdot\nabla\phi - s\rho_0\phi \right) \mathrm{d}\mathbf{x} \\
&= \int_\Omega \left(\gamma U\phi - D\nabla^2 U\phi - s\rho_0\phi \right) \mathrm{d}\mathbf{x} \qquad \text{(IBP)} \\
&= \int_\Omega \left(\gamma U - D\nabla^2 U - s\rho_0 \right) \phi \mathrm{d}\mathbf{x} \\
\frac{\delta \mathscr{F}(U)}{\delta U(\mathbf{x})} &= \gamma U - D\nabla^2 U - s\rho_0
\end{aligned}$$

Thus the functional derivative of (2.160) is indeed (2.159).

To confirm that $\dot{\mathscr{F}}(U) = \partial \mathscr{F}(U(t,x))/\partial t \leq 0$,

$$
\begin{aligned}
\dot{\mathscr{F}}(U) &= \int_\Omega \left(\gamma U\dot{U} + D\nabla U\cdot\nabla\dot{U} - s\rho_0\dot{U}\right) \\
&= \int_\Omega \left(\gamma U\dot{U} - D\nabla^2 U\dot{U} - s\rho_0\dot{U}\right)\mathrm{d}\mathbf{x} && \text{(IBP)} \\
&= \int_\Omega \left(\gamma U - D\nabla^2 U - s\rho_0\right)\dot{U}\mathrm{d}\mathbf{x} \\
&= \int_\Omega \left(\gamma U - D\nabla^2 U - s\rho_0\right)\left(-\gamma U + D\nabla^2 U + s\rho_0\right)\mathrm{d}\mathbf{x} && (2.1) \\
&= -\int_\Omega \left(\gamma U - D\nabla^2 U - s\rho_0\right)^2\mathrm{d}\mathbf{x} \leq 0
\end{aligned}
$$

Finally, $\mathscr{F}$ is positive definite, with a minimum at equilibrium. Let $U_0 = g*\rho_0$ be the solution of (2.154), and $U = U_0 + \phi$. Then

$$
\begin{aligned}
\mathscr{F}(U) &= \int_\Omega \left(\frac{\gamma}{2} \left(U_0 + \phi\right)^2 + \frac{D}{2} \|\nabla \left(U_0 + \phi\right)\|^2 - s\rho_0 \left(U_0 + \phi\right) \right) \mathrm{d}\mathbf{x} \\
&= \int_\Omega \Bigg(\frac{\gamma}{2} \left(U_0^2 + 2U_0\phi + \phi^2\right) \\
&\quad + \frac{D}{2} \left(\nabla U_0 \cdot \nabla U_0 + 2\nabla U_0 \cdot \nabla \phi + \nabla \phi \cdot \nabla \phi\right) \\
&\quad - s\rho_0 \left(U_0 + \phi\right) \Bigg) \mathrm{d}\mathbf{x} \\
&= \int_\Omega \left(\frac{\gamma}{2} U_0^2 + \frac{D}{2} \nabla U_0 \cdot \nabla U_0 - s\rho_0 U_0 \right) \mathrm{d}\mathbf{x} \\
&\quad + \int_\Omega \left(\gamma U_0 \phi + D \nabla U_0 \cdot \nabla \phi - s\rho_0 \phi \right) \mathrm{d}\mathbf{x} \\
&\quad + \int_\Omega \left(\frac{\gamma}{2} \phi^2 + \frac{D}{2} \nabla \phi \cdot \nabla \phi \right) \mathrm{d}\mathbf{x} \\
&= \int_\Omega \left(\frac{\gamma}{2} U_0^2 + \frac{D}{2} \nabla U_0 \cdot \nabla U_0 - s\rho_0 U_0 \right) \mathrm{d}\mathbf{x} \\
&\quad + \int_\Omega \left(\gamma U_0 \phi - D \nabla^2 U_0 \phi - s\rho_0 \phi \right) \mathrm{d}\mathbf{x} \qquad \text{(IBP)} \\
&\quad + \int_\Omega \left(\frac{\gamma}{2} \phi^2 + \frac{D}{2} \nabla \phi \cdot \nabla \phi \right) \mathrm{d}\mathbf{x} \\
&= \mathscr{F}(U_0) + \int_\Omega \left(\gamma U_0 - D \nabla^2 U_0 - s\rho_0 \right) \right) \phi \mathrm{d}\mathbf{x} + \int_\Omega \left(\frac{\gamma}{2} \phi^2 + \frac{D}{2} \nabla \phi \cdot \nabla \phi \right) \mathrm{d}\mathbf{x} \\
&= \mathscr{F}(U_0) + \int_\Omega \left(\frac{\gamma}{2} \phi^2 + \frac{D}{2} \nabla \phi \cdot \nabla \phi \right) \mathrm{d}\mathbf{x} \geq \mathscr{F}(U_0) \qquad (2.154)
\end{aligned}
$$

Thus $\mathscr{F}(U)$ is minimized at $U = U_0$, and the time derivative of $\mathscr{F}(U)$ is negative for every positive $U \neq U_0$. Together these results imply that $U = U_0$ is the unique, globally stable equilibrium of (2.1), if $\rho_0(\mathbf{x})$ is fixed.

2.4.3 Worm density equilibrium for fixed signal

If we assume a fixed chemical signal function $U_0(\mathbf{x})$, what density function(s) $\rho(\mathbf{x})$ are in equilibrium with it?

$$0 = \nabla \cdot (\rho \nabla (V_U(U_0) + V_\rho + \sigma \log \rho)) \tag{2.161}$$

Density PDE (2.3) is a continuity equation: it says that the time derivative of the density is the divergence of a vector field, $\rho \nabla G$, where $G = V_U + V_\rho + \sigma \log \rho$ is something like a free energy (actually, a marginal free energy). The minimal ρ PDE (2.2) can also be written in this form. At equilibrium (2.161), this divergence is zero. The simplest way to achieve this is $\nabla G = 0$, which I will call the Boltzmann equilibrium because of its resemblance to the Boltzmann distribution of statistical mechanics,

$$\nabla (V_U + V_\rho + \sigma \log \rho) = 0 \tag{2.162}$$

$$V_U + V_\rho + \sigma \log \rho = C \tag{2.163}$$

$$\rho = e^C e^{-(V_U + V_\rho)/\sigma} \tag{2.164}$$

$$\rho \propto e^{-V/\sigma} \tag{2.165}$$

The Boltzmann equilibrium is $P \propto e^{-E/T}$, where P is probability of occupying a state, E is the energy of the state, and T is temperature. When V doesn't depend on ρ, (2.165) allows an explicit solution

$$\rho(\mathbf{x}) = \frac{N_0}{Z(1/\sigma)} e^{-V(\mathbf{x})/\sigma} \tag{2.166}$$

$$Z(1/\sigma) \coloneqq \int_\Omega e^{-V(\mathbf{x})/\sigma} \mathrm{d}\mathbf{x} \quad \text{is the partition function} \tag{2.167}$$

This works for the minimal system, for instance. In the general case V depends on ρ via V_ρ and finding a density function $\rho(\mathbf{x})$ that satisfies (2.166) is typically not easy.

To find a Lyapunov functional for ρ with fixed $U(\mathbf{x}) = U_0(\mathbf{x})$, use Corollary 2.9. PDE (2.3) is of the form of (2.44), with $G(\mathbf{x}, \rho) \coloneqq V(\rho, U_0) + \sigma \log \rho$. Therefore choose $\mathscr{F}$ such that

$$\frac{\delta \mathscr{F}(\rho)}{\delta \rho(\mathbf{x})} = V_U(U_0(\mathbf{x})) + V_\rho(\rho(\mathbf{x})) + \sigma \log \rho(\mathbf{x}), \tag{2.168}$$

Thus, as for U, the construction of a Lyapunov functional for ρ can be reduced to a functional antidifferentiation problem. Let's find a functional that satisfies (2.168) by radial integration.

$$\mathscr{F}(\rho) = \int_{r=0}^{1} \left(\int_{\Omega} \left(\frac{\delta \mathscr{F}(r\rho)}{\delta \rho(\mathbf{x})} \right) \rho(\mathbf{x}) \mathrm{d}\mathbf{x} \right) \mathrm{d}r + C \tag{2.169}$$

$$= \int_{r=0}^{1} \left(\int_{\Omega} \left(V_U(U_0(\mathbf{x})) + V_\rho(r\rho(\mathbf{x})) + \sigma \log(r\rho(\mathbf{x})) \right) \rho(\mathbf{x}) \mathrm{d}\mathbf{x} \right) \mathrm{d}r + C \tag{2.170}$$

$$\begin{aligned} &= \int_{\Omega} V_U(U_0(\mathbf{x})) \rho(\mathbf{x}) \mathrm{d}\mathbf{x} \int_{r=0}^{1} \mathrm{d}r + \int_{\Omega} \left(\int_{r=0}^{1} V_\rho(r\rho(\mathbf{x})) \mathrm{d}r \right) \rho(\mathbf{x}) \mathrm{d}\mathbf{x} \\ &\quad + \int_{\Omega} \left(\sigma \int_{r=0}^{1} \log\left(r\rho(\mathbf{x})\right) \mathrm{d}r \right) \rho(\mathbf{x}) \mathrm{d}\mathbf{x} + C \\ &= \int_{\Omega} \rho(\mathbf{x}) V_U(U_0(\mathbf{x})) \mathrm{d}\mathbf{x} + \int_{\Omega} \left(\frac{W_\rho(\rho(\mathbf{x}))}{\rho(\mathbf{x})} \right) \rho(\mathbf{x}) \mathrm{d}\mathbf{x} \\ &\quad + \sigma \int_{\Omega} \left(\log(\rho(\mathbf{x})) - 1 \right) \rho(\mathbf{x}) \mathrm{d}\mathbf{x} + C \end{aligned}$$

$$= \int_{\Omega} \left(\rho(\mathbf{x}) V_U(U_0(\mathbf{x})) + W_\rho(\rho(\mathbf{x})) + \sigma \rho(\mathbf{x}) \log \rho(\mathbf{x}) - \sigma \rho(\mathbf{x}) \right) \mathrm{d}\mathbf{x} + C \tag{2.171}$$

Since $\int_{\Omega} \rho(\mathbf{x}) \mathrm{d}\mathbf{x}$ is constant, the term $-\sigma\rho(\mathbf{x})$ in the integrand can be absorbed into the constant of integration, leading to the following Lyapunov functional:

$$\begin{aligned} \mathscr{F}(\rho) &= \int_{\Omega} \left(\rho(\mathbf{x}) V_U(U_0(\mathbf{x})) + W_\rho(\rho(\mathbf{x})) + \sigma \rho(\mathbf{x}) \log \rho(\mathbf{x}) \right) \mathrm{d}\mathbf{x} \\ &= \int_{\Omega} \left(\rho V_U(U_0) + W_\rho(\rho) + \sigma \rho \log \rho \right) \mathrm{d}\mathbf{x} \end{aligned} \tag{2.172}$$

It is easy to confirm that the functional derivative of (2.172) is indeed (2.168). $W_\rho(\rho)\mathrm{d}\mathbf{x}$ can be understood as the total energy cost of building up to a worm density ρ in interval $\mathrm{d}\mathbf{x}$. The expression $V_\rho(\rho)$ that appears in the PDE (2.3) is the marginal cost of moving one worm to a place with density ρ. For the minimal system (2.2) Functional (2.172) reduces to

$$\mathscr{F}(\rho) = \int_{\Omega} \left(-\beta \rho U + \sigma \rho \log \rho \right) \mathrm{d}\mathbf{x} \tag{2.173}$$

This is identical to the ρ-dependent part of the minimal system free energy functional (1.16) in chapter 1.

Now, let us confirm that this construction worked, that the time derivative of (2.173) is negative semidefinite.

$$\begin{aligned}
\dot{\mathcal{F}}(\rho) &= \frac{\mathrm{d}}{\mathrm{d}t}\int_\Omega \left(\rho V_U(U_0) + W_\rho(\rho) + \sigma\rho\log\rho\right)\mathrm{d}\mathbf{x} \\
&= \int_\Omega \left(V_U(U_0)\dot{\rho} + W'_\rho(\rho)\dot{\rho} + \sigma\dot{\rho}\log\rho + \sigma\dot{\rho}\right)\mathrm{d}\mathbf{x} \\
&= \int_\Omega \left(V_U(U_0) + V_\rho(\rho) + \sigma\log\rho + \sigma\right)\dot{\rho}\mathrm{d}\mathbf{x} \\
&= \int_\Omega \left(V_U(U_0) + V_\rho(\rho) + \sigma\log\rho + \sigma\right)\cdot\left(\nabla\cdot\left(\rho\nabla\left(V_U(U_0) + V_\rho(\rho) + \sigma\log\rho\right)\right)\right)\mathrm{d}\mathbf{x} \\
&= -\int_\Omega \rho\nabla\left(V_U(U_0) + V_\rho(\rho) + \sigma\log\rho\right)\cdot\nabla\left(V_U(U_0) + V_\rho(\rho) + \sigma\log\rho\right)\mathrm{d}\mathbf{x} \qquad \text{(IBP)} \\
&= -\int_\Omega \rho\|\nabla\left(V_U(U_0) + V_\rho(\rho) + \sigma\log\rho\right)\|^2_{L^2(\mathbb{R}^d)}\mathrm{d}\mathbf{x} \leq 0
\end{aligned}$$

This result also demonstrates that the Boltzmann distribution (2.165) always holds at equilibrium. For the minimal system, the equilibrium, if it exists, is unique. This is not so easily shown for the worm system (2.3).

2.4.4 Construction of the free energy functional for the minimal system

In the previous sections, I showed how to use functional integration to construct Lyapunov functionals for the uncoupled U and ρ systems. Now I will attempt to find a time-decreasing functional for the minimal system, with both ρ and U time-dependent. Use Corollary 2.11, with

$$\mathfrak{D}(\rho)U \coloneqq -\gamma U + D\nabla^2 U + s\rho \tag{2.174}$$

$$G(\mathbf{x},\rho,U) \coloneqq -\beta U + \sigma\log\rho \tag{2.175}$$

To apply the theorem, we need

$$\frac{\delta\mathcal{F}(\rho,U)}{\delta\rho(\mathbf{x})} = q(-\beta U + \sigma\log\rho) \tag{2.176}$$

$$\frac{\delta\mathcal{F}(\rho,U)}{\delta U(\mathbf{x})} = p(\mathbf{x})(\gamma U - D\nabla^2 U - s\rho), \tag{2.177}$$

where q is some increasing function of G and $p(\mathbf{x})$ is a positive function.

If (2.176) and (2.177) hold, then

$$\frac{\delta^2 \mathscr{F}(\rho, U)}{\delta U(\mathbf{x}) \delta \rho(\mathbf{x})} = -\beta q'(-\beta U + \sigma \log \rho) \tag{2.178}$$

$$\frac{\delta^2 \mathscr{F}(\rho, U)}{\delta \rho(\mathbf{x}) \delta U(\mathbf{x})} = -p(\mathbf{x}) s, \tag{2.179}$$

assuming p has no explicit dependence on ρ. We must choose p and q so that these two expressions are equal. This is easily done. Let $q(G) \coloneqq G, q' = 1$, and $p(\mathbf{x}) \coloneqq p = \beta/s$. Then

$$\frac{\delta \mathscr{F}(\rho, U)}{\delta \rho(\mathbf{x})} = -\beta U + \sigma \log \rho \tag{2.180}$$

$$\frac{\delta \mathscr{F}(\rho, U)}{\delta U(\mathbf{x})} = \frac{\beta}{s}(\gamma U - D \nabla^2 U - s\rho) \tag{2.181}$$

Now,

$$\frac{\delta^2 \mathscr{F}(\rho, U)}{\delta U(\mathbf{x}) \delta \rho(\mathbf{x})} = -\beta \tag{2.182}$$

$$\frac{\delta^2 \mathscr{F}(\rho, U)}{\delta \rho(\mathbf{x}) \delta U(\mathbf{x})} = -sp = -\beta \tag{2.183}$$

By radial integration we arrive at the functional

$$\mathscr{F}(\rho, U) = \int_\Omega \left(\frac{\beta}{s} \left(\frac{\gamma}{2} U^2 + D \|\nabla U\|^2 \right) + \sigma \rho \log \rho - \beta \rho U \right) \mathrm{d}\mathbf{x} \tag{2.184}$$

Delightfully, this is a complete success. It has the desired functional derivatives (2.182) and (2.183). In fact, (2.184) is identical to the free energy functional (1.16) for the minimal system shown in chapter 1, where I also showed that its time derivative is negative semidefinite.

2.4.5 Construction of an approximate free energy functional for the worm system

Next I will attempt the same program for the worm system (2.1) and (2.3). We seek a functional with the following functional derivatives

$$\frac{\delta \mathscr{F}(\rho, U)}{\delta \rho(\mathbf{x})} = V_U(U) + V_\rho(\rho) + \sigma \log \rho \tag{2.185}$$

$$\frac{\delta \mathscr{F}(\rho, U)}{\delta U(\mathbf{x})} = p(U)(\gamma U - D\nabla^2 U - s\rho) \tag{2.186}$$

The mixed partial derivatives implied by (2.185) and (2.186) are

$$\frac{\delta^2 \mathscr{F}(\rho, U)}{\delta U(\mathbf{x}) \delta \rho(\mathbf{x})} = V_U'(U) \tag{2.187}$$

$$\frac{\delta^2 \mathscr{F}(\rho, U)}{\delta \rho(\mathbf{x}) \delta U(\mathbf{x})} = -sp(U) \tag{2.188}$$

We must choose $p(U)$ so that these are equal: $p(U) = -V_U'(U)/s$. For an attractant V_U is a decreasing function of U, $V_U'(U) < 0$, so $p(U)$ is indeed positive. We are thus left with the following functional antidifferentiation problem

$$\frac{\delta \mathscr{F}(\rho, U)}{\delta \rho(\mathbf{x})} = V_U(U) + V_\rho(\rho) + \sigma \log \rho \tag{2.189}$$

$$\frac{\delta \mathscr{F}(\rho, U)}{\delta U(\mathbf{x})} = -\frac{1}{s} V_U'(U)(\gamma U - D\nabla^2 U - s\rho) \tag{2.190}$$

Radial integration yields the candidate free energy functional

$$\mathscr{F}(\rho, U) = \int_\Omega \left(\begin{array}{l} -\dfrac{\gamma}{s}\left(U V_U(U) - W_U(U)\right) + \dfrac{D}{s}\left(V_U(U) - \dfrac{W_U(U)}{U}\right)\nabla^2 U \\ + \rho V_U(U) + W_\rho(\rho) + \sigma \rho \log \rho \end{array} \right) \mathrm{d}\mathbf{x} \tag{2.191}$$

This candidate loses, alas. Its functional derivative with respect to $U(\mathbf{x})$ is not (2.190). There is one problematic term, the diffusion term $(D/s)V_U'(U)\nabla^2 U$. As shown in Theorem 2.14, this expression does not have a functional antiderivative if V_U' is not constant. Denote the error in the functional derivative $\delta\mathscr{F}(\rho,U)/\delta U(\mathbf{x})$ by $e_{\mathscr{F}}$,

$$e_{\mathscr{F}} := \frac{\delta\mathscr{F}(\rho,U)}{\delta U(\mathbf{x})} + \frac{1}{s}V_U'(U)(\gamma U - D\nabla^2 U - s\rho) \tag{2.192}$$

Error function $e_{\mathscr{F}}$ can be written in terms of the previously defined error $e_{\mathscr{D}}$ (2.134).

$$e_{\mathscr{F}}(\mathbf{x}) = \frac{D}{s}e_{\mathscr{D}} \tag{2.193}$$

The following bounds follow from Theorem 2.15.

$$\int_\Omega U e_{\mathscr{F}} \mathrm{d}\mathbf{x} = 0 \tag{2.194}$$

$$\|U e_{\mathscr{F}}\|_1 \leq 2\frac{D}{s}\left\|U f'(U)\nabla^2 U\right\|_1 + 2\frac{D}{s}\left\|f(U)\nabla^2 U\right\|_1, \tag{2.195}$$

with $f(U)$ as in (2.133).

2.4.6 The nature of the problem, and the radial integration functional as an approximation

Of the six terms in the ρ and U PDEs, only one is a problem for functional integration: the diffusion term $D\nabla^2 U$ in the U PDE. Why is this term uniquely problematic? All the other terms to be integrated are local pointwise functions of $\mathbf{x}$, either via $U(\mathbf{x})$ or $\rho(\mathbf{x})$. These terms create no opportunity for unequal mixed partial derivatives: if $\mathbf{x} \neq \mathbf{y}$, $\delta^2\mathscr{F}(f)(\delta f(\mathbf{x})\delta f(\mathbf{y})) = 0$ for any such term, and it is easy to show that a functional antiderivative exists for any such pointwise function.

The chemical diffusion term, in contrast, represents action at a distance. Action at a distance is the first element needed to make the construction of a functional antiderivative impossible. It is not sufficient, since $\nabla^2 U$ by itself has a functional antiderivative, as seen, for instance, in the case of the free energy functional for the minimal model. What is needed in addition is a complication that introduces an asymmetry that makes mixed partial derivatives unequal, as seen in the Fourier coefficient proof of Theorem 2.14.

2.4.7 Repellents and multiple chemical signals

The model I will eventually develop has two chemical signals, a short-range attractant and a long-range repellent. Individually, each signal is governed by PDE (2.1), albeit with different parameters D, γ, s. The ρ PDE is almost the same as (2.3), but there is now a V_U term for each signal

$$\dot{\rho} = \nabla \cdot \left(\rho \nabla \left(V_{U_a}(U_a) + V_{U_r}(U_r) + V_\rho(\rho) + \sigma \log \rho\right)\right) \tag{2.196}$$

The signal concentrations are $U_a(\mathbf{x})$ for attractant and $U_r(\mathbf{x})$ for repellent. V_{U_a} and V_{U_r} have the same form but different parameters

$$\begin{aligned} V_{U_a} &\coloneqq -\beta_a \log(\alpha_a + U_a) \\ V_{U_r} &\coloneqq -\beta_r \log(\alpha_r + U_r) \end{aligned} \tag{2.197}$$

The most important difference is that $\beta_a > 0$, $\beta_r < 0$, so that V_{U_a} (and therefore $V = V_{U_a} + V_{U_r} + V_\rho$ is a decreasing function of U_a while V_{U_r} (and V) is an increasing function of U_r.

A free energy functional is constructed by a straightforward generalization of the procedure described above, but there are two problems. The desired functional derivatives are

$$\begin{aligned} \frac{\delta \mathscr{F}(\rho, U_a, U_r)}{\delta \rho(\mathbf{x})} &= V_{U_a}(U_a) + V_{U_r}(U_r) + V_\rho(\rho) + \sigma \log \rho \\ \frac{\delta \mathscr{F}(\rho, U_a, U_r)}{\delta U_a(\mathbf{x})} &= -\frac{1}{s_a} V'_{U_a}(U_a) \left(\gamma_a U_a - D_a \nabla^2 U_a - s_a \rho\right) \\ \frac{\delta \mathscr{F}(\rho, U_a, U_r)}{\delta U_r(\mathbf{x})} &= -\frac{1}{s_r} V'_{U_r}(U_r) \left(\gamma_r U_r - D_r \nabla^2 U_r - s_r \rho\right) \end{aligned} \tag{2.198}$$

The first problem is the factor $p(U_r) = -V'_{U_r}(U_r)/s_r$ in front of the derivative $\delta \mathscr{F}/\delta U_r$. This factor is needed so that the mixed partial derivatives $\delta^2 \mathscr{F}/(\delta U_r(\mathbf{x}) \delta \rho(\mathbf{x}))$ and $\delta^2 \mathscr{F}/(\delta \rho(\mathbf{x}) \delta U_r(\mathbf{x}))$ are equal. But Corollary 2.11 also placed a requirement on the scale function p: that $p(U_r) > 0$. For a repellent V_{U_r} is an increasing function of U_r——that's what makes it a repellent. Thus $p(U_r) < 0$. As a consequence, the time derivative of a free energy functional that had the functional derivatives (2.198) would not be negative semidefinite. It may increase as a result of changes in the repellent distribution.

This is not merely a mathematical inconvenience—it is a reflection of biology. Free energy is meant to measure how unhappy the worm population is to be where it is. The worms move

in such a way as to make themselves less unhappy, and this is why we design differential equations that cause the free energy to decrease with time. (Since worms are living animals with goals, the adjectives "happy" and "unhappy" are not merely figurative. We may operationally define "happiness" as an internal state towards which worms strive, and "unhappiness" as an internal state they try to avoid. These states are even related, at a molecular level, to human emotion. Worms strive towards states in which the biogenic amines serotonin and dopamine are present (Horvitz et al. 1982; Sawin et al. 2000; Song and Avery 2012). Dopamine release in the human brain is associated with euphoria (Chen et al. 2017), and reduction of serotonin release with depression (Dell'Osso et al. 2016).)

But the distribution of worms is not the only thing that changes. As the worms move, the distributions of chemical signals also move. They are made by the worms and degrade as they diffuse away, so the location of the chemicals is correlated with the location of the worms. For an attractant, this causes no difficulty, because the attractant lowers the free energy of the worms in its vicinity (via the decreasing function V_{U_a}), and the movement of attractant consequent to the movement of worms thus tends to decreased free energy. For repellent, however, free energy increases as signal distribution becomes better correlated with that of the worms.

A functional with derivatives (2.198) is still a useful object. Although it would not necessarily be minimized at equilibrium, the functional would be stationary if and only if the system were at equilibrium.

This is the first problem. The second problem has already been explored: except for affine V_U, no functional can be constructed whose derivative properly reconstructs the diffusion term in the U_a and U_r PDEs. The free energy functional constructed by radial integration of (2.198), which I propose as a useful albeit approximate tool, is

$$\mathscr{F}(\rho, U_a, U_r) = \int_\Omega \begin{pmatrix} -\frac{\gamma_a}{s_a}\left(U_a V_{U_a}(U_a) - W_{U_a}(U_a)\right) + \frac{D_a}{s_a}\left(V_{U_a} - \frac{W_{U_a}}{U_a}\right)\nabla^2 U_a \\ -\frac{\gamma_r}{s_r}\left(U_r V_{U_r}(U_r) - W_{U_r}(U_r)\right) + \frac{D_r}{s_r}\left(V_{U_r} - \frac{W_{U_r}}{U_r}\right)\nabla^2 U_r \\ +\rho V_{U_a}(U_a) + \rho V_{U_r}(U_r) + W_\rho(\rho) + \sigma\rho\log\rho \end{pmatrix} \mathrm{d}\mathbf{x} \quad (2.199)$$

2.4.8 Total energy functional of density

I will eventually search for equilibria by looking for stationary points (e.g., minima) of free energy functionals. It is difficult to search a function space each of whose members is a vector function with two or three (in the case of models with two chemical signals) components. But there is an obvious shortcut: given ρ, it is straightforward computationally to find U that is in

equilibrium with it. For the periodic functions and rectangular domains Ω I am considering, this U is the convolution $g * \rho$, where g is the Green's function (2.157). This idea works (chapter 5), but some care is needed in the design of the functional whose stationary points are to be sought. The obvious choice is (2.172), the free energy functional for density in the presence of a known attractant distribution, but with U_0 replaced by $g * \rho$,

$$\mathcal{T}(\rho) = \int_\Omega (\rho V_U(g * \rho) + W_\rho(\rho) + \sigma \log \rho)\, \mathrm{d}\mathbf{x} \tag{2.200}$$

This, however, is wrong. It has a new dependence on ρ via $V_U(g * \rho)$, with the result that its functional derivative is not the desired marginal free energy $V_U(g * \rho) + V_\rho(\rho) + \sigma \log \rho$. To see this, we can use the chain rule, which for functional derivatives takes the form

$$\frac{\delta \mathcal{T}(\rho, U(\rho))}{\delta \rho(\mathbf{x})} = \frac{\partial \mathcal{T}(\rho, U(\rho))}{\partial \rho(\mathbf{x})} + \int_\Omega \left(\frac{\delta U(\rho)(\mathbf{y})}{\delta \rho(\mathbf{x})}\right)\left(\frac{\partial \mathcal{T}(\rho, U(\rho))}{\partial U(\rho)(\mathbf{y})}\right) \mathrm{d}\mathbf{y} \tag{2.201}$$

Two notational clarifications: First, the derivatives $\partial \mathcal{T}(\rho, U(\rho))/\partial \rho(\mathbf{x})$ and $\partial \mathcal{T}(\rho, U(\rho))/\partial U(\rho)(\mathbf{y})$ are functional derivatives, but I write them with ∂ to clarify that the derivative is being taken with one argument of $\mathcal{T}$ allowed to vary while the other is held constant. Second, in $\delta U(\rho)(\mathbf{y})/\delta \rho(\mathbf{x})$, $U(\rho)(\mathbf{y})$ is a functional of ρ that maps ρ to the number resulting from evaluation of the function $U(\rho)$ at point $\mathbf{y}$. Specifically, we will need the following,

$$\begin{aligned}
(g * (\rho + \epsilon\phi))(\mathbf{y}) &= \int_\Omega g(\mathbf{y} - \mathbf{x})(\rho + \epsilon\phi)(\mathbf{x})\mathrm{d}\mathbf{x} \\
&= \int_\Omega g(\mathbf{y} - \mathbf{x})\rho(\mathbf{x})\mathrm{d}\mathbf{x} + \epsilon \int_\Omega g(\mathbf{y} - \mathbf{x})\phi(\mathbf{x})\mathrm{d}\mathbf{x} \\
\lim_{\epsilon \to 0} \frac{(g * (\rho + \epsilon\phi)(\mathbf{y}) - (g * \rho)(\mathbf{y})}{\epsilon} &= \int_\Omega g(\mathbf{y} - \mathbf{x})\phi(\mathbf{x})\mathrm{d}\mathbf{x} \\
\frac{\delta (g * \rho)(\mathbf{y})}{\delta \rho(\mathbf{x})} &= g(\mathbf{y} - \mathbf{x}) = g(\mathbf{x} - \mathbf{y}),
\end{aligned} \tag{2.202}$$

where I used the even symmetry of g in the last step. Combining (2.200), (2.201), and (2.202)

$$\frac{\delta \mathcal{T}(\rho, g * \rho)}{\delta \rho(\mathbf{x})} = \frac{\partial \mathcal{T}(\rho, g * \rho)}{\partial \rho(\mathbf{x})} + \int_\Omega \rho(\mathbf{x}) V_U'((g * \rho)(\mathbf{x})) g(\mathbf{x} - \mathbf{y})\mathrm{d}\mathbf{y} \tag{2.203}$$

$$\begin{aligned}
&= V_U((g * \rho)(\mathbf{x})) + V_\rho(\rho(\mathbf{x})) + \sigma(\log \rho(\mathbf{x}) + 1) \\
&\quad + (g * \rho V_U')(\mathbf{x})
\end{aligned} \tag{2.204}$$

This, unfortunately, is not the desired result. A stationary point of (2.200) will not in general be an equilibrium of the ρ PDE (2.3). The first three terms $V_U + V_\rho + \sigma \log \rho$ are what we want. (The constant σ is of no consequence—it vanishes when the gradient of the functional derivative is taken.) The last term, however, $g * \rho V_U'$, is nothing but trouble.

Fortunately, at this point we know how to fix the problem. Since we know what we want the functional derivative of $\mathcal{T}$ to be, try to find a functional antiderivative.

$$\frac{\delta \mathcal{T}(\rho)}{\delta \rho(\mathbf{x})} = V_U(g * \rho) + V_\rho(\rho) + \sigma \log \rho \tag{2.205}$$

$$\begin{aligned} \mathcal{T}(\rho) &= \int_{r=0}^{1} \left(\int_\Omega \left(V_U(g * r\rho) + V_\rho(r\rho) + \sigma \log(r\rho) \right) \rho \mathrm{d}\mathbf{x} \right) \mathrm{d}r + C \\ &= \int_\Omega \left(\rho \frac{W_U(g * \rho)}{g * \rho} + W_\rho(\rho) + \sigma \rho \log \rho \right) \mathrm{d}\mathbf{x} + C \end{aligned} \tag{2.206}$$

For the minimal model, $V_\rho = W_\rho = 0$, $V_U = -\beta U$, $W_U = \int_{u=0}^{U} V_U(u) du = -\beta U^2/2$, and (2.206) simplifies (with $C = 0$) to

$$\mathcal{T}(\rho) = \int_\Omega \left(-\frac{\beta \rho (g * \rho)}{2} + \sigma \rho \log \rho \right) \mathrm{d}\mathbf{x} \tag{2.207}$$

This result is exact, in the sense that the functional derivative of (2.207) is the desired $-\beta(g * \rho) + \sigma \log \rho$ (plus a constant of no importance).

For the general worm model (2.3), however, a familiar problem arises. For non-affine V_U, $V_U(g * \rho)$ does not in general possess a functional antiderivative. $(g * \rho)^n$ possesses a functional antiderivative for $n = 0, 1$ but not for any $n > 1$. The problem is almost identical to that that arose from trying to find a functional antiderivative of $V_U'(U)\nabla^2 U$ previously. Like $\nabla^2 U$, $g * \rho$ describes an action at a distance. In fact, the Laplacian and convolution with g have similar effects in the Fourier basis: each of these multiplies the Fourier coefficient $\widetilde{\square}_\mathbf{k}$ by a function of $\|\mathbf{k}\|^2$, and the argument for the existence of unequal mixed partial derivatives with respect to Fourier series coefficients is *mutatis mutandis* virtually the same.

2.4.9 Relation of the total energy functional to the free energy functional

Total energy functional (2.206) is closely related to the free energy functional (2.191).

Theorem 2.16. *Let*

- $\rho, U \in H^2_{P+}(\Omega)$
- *Free energy functional* $\mathscr{F}(\rho, U)$ *be as defined by* (2.191)
- *Total energy functional* $\mathscr{T}(\rho)$ *be as defined by* (2.206)
- *Green's function* $g(\mathbf{x})$ *be as defined by* (2.157)

Then

$$\mathscr{T}(\rho) = \mathscr{F}(\rho, g * \rho) \tag{2.208}$$

Proof. Let ρ, U, $\mathscr{F}$, $\mathscr{T}$, and g be as defined above. Then, as argued above (Section 2.4.1), $U = g * \rho$ is an equilibrium of the U PDE

$$0 = -\gamma(g * \rho) + D\nabla^2(g * \rho) + s\rho \tag{2.209}$$

$$D\nabla^2(g * \rho) = \gamma(g * \rho) - s\rho \tag{2.210}$$

Thus,

$$\begin{aligned}
\mathscr{F}(\rho, g * \rho) = \int_\Omega \Bigg(& -\frac{\gamma}{s}((g * \rho)V_U(g * \rho) - W_U(g * \rho)) \\
& + \frac{D}{s}\left(V_U(g * \rho) - \frac{W_U(g * \rho)}{g * \rho}\right)\nabla^2(g * \rho) \\
& + \rho V_U(g * \rho) + W_\rho(\rho) + \sigma\rho\log\rho\Bigg)\mathrm{d}\mathbf{x} && (2.211) \\
= \int_\Omega \Bigg(& -\frac{\gamma}{s}((g * \rho)V_U(g * \rho) - W_U(g * \rho)) \\
& + \frac{1}{s}\left(V_U(g * \rho) - \frac{W_U(g * \rho)}{g * \rho}\right)(\gamma(g * \rho) - s\rho) && (2.210) \\
& + \rho V_U(g * \rho) + W_\rho(\rho) + \sigma\rho\log\rho\Bigg)\mathrm{d}\mathbf{x} && (2.212) \\
= \int_\Omega & \left(\rho\frac{W_U(g * \rho)}{g * \rho} + W_\rho(\rho) + \sigma\rho\log\rho\right)\mathrm{d}\mathbf{x} && (2.213) \\
= \mathscr{T}(\rho) & && (2.214)
\end{aligned}$$

□

2.4.10 Error of the approximate total energy functional

Define the total energy error function $\mathscr{e}_{\mathcal{T}}(\rho)$

$$\mathscr{e}_{\mathcal{T}}(\rho)(\mathbf{x}) \coloneqq \frac{\delta \mathcal{T}(\rho)}{\delta \rho(\mathbf{x})} - (V_U((g*\rho)(\mathbf{x})) + V_\rho(\rho(\mathbf{x})) + \sigma \log \rho(\mathbf{x}) + \sigma) \tag{2.215}$$

$$= \frac{\delta\left(\rho \frac{W_U(g*\rho)}{g*\rho}\right)}{\delta \rho(\mathbf{x})} - V_U((g*\rho)(\mathbf{x})) \tag{2.216}$$

The final simplification follows from the fact that $\delta W_\rho(\rho)/\delta\rho(\mathbf{x}) = V_\rho(\rho)$ and $\delta(\sigma\rho\log\rho)/\delta\rho(\mathbf{x}) = \sigma\log\rho + \sigma$.

Using Theorem 2.16, the error function $\mathscr{e}_{\mathcal{T}}$ can be expressed in terms of the free energy error function $\mathscr{e}_{\mathcal{F}}$ (2.192).

Theorem 2.17. *Let $\mathscr{e}_{\mathcal{T}}$ and $\mathscr{e}_{\mathcal{F}}$ be as defined in* (2.192) *and* (2.215).

Then

$$\mathscr{e}_{\mathcal{T}}(\mathbf{x}) = \left(g * \mathscr{e}_{\mathcal{F}}\Big|_{U=g*\rho}\right)(\mathbf{x}) \tag{2.217}$$

Proof. If $e_{\mathcal{T}}$ and $e_{\mathcal{F}}$ as as above, Then

$$\begin{aligned}
\frac{\delta \mathcal{T}(\rho)}{\delta \rho(\mathbf{x})} &= \frac{\delta \mathcal{F}(\rho, g*\rho)}{\delta \rho(\mathbf{x})} && \text{(Theorem 2.16)} \\
&= \frac{\partial \mathcal{F}(\rho, g*\rho)}{\partial \rho(\mathbf{x})} + \int_\Omega \left(\frac{\delta (g*\rho)(\mathbf{y})}{\delta \rho(\mathbf{x})} \frac{\partial \mathcal{F}(\rho, g*\rho)}{\partial (g*\rho)(\mathbf{y})} \right) \mathrm{d}\mathbf{y} && (2.218) \\
&= V_U(g*\rho) + V_\rho(\rho) + \sigma \log \rho + \int_\Omega \left(g(\mathbf{x}-\mathbf{y}) \frac{\partial \mathcal{F}(\rho, g*\rho)}{\partial (g*\rho)(\mathbf{y})} \right) \mathrm{d}\mathbf{y} \\
&= V_U(g*\rho) + V_\rho(\rho) + \sigma \log \rho + g * \left(\frac{\delta \mathcal{F}(\rho, U)}{\delta U}\bigg|_{U=g*\rho} \right) \\
e_{\mathcal{T}} &= g * \left(\frac{\delta \mathcal{F}(\rho, U)}{\delta U}\bigg|_{U=g*\rho} \right) && (2.215) \\
& && (2.219)
\end{aligned}$$

As before, in (2.218) ∂ is used to indicate a functional derivative taken with respect to one argument of $\mathcal{F}$ while the other argument is held constant. Now we need only evaluate $\delta \mathcal{F}(\rho, U)/\delta U$ for $U = g * \rho$. Using the definition of $e_{\mathcal{F}}$ (2.192),

$$\begin{aligned}
\frac{\delta \mathcal{F}(\rho, U)}{\delta U} &= e_{\mathcal{F}} - \frac{1}{s} V_U'(U)(\gamma U - D\nabla^2 U - s\rho) \\
\frac{\delta \mathcal{F}(\rho, U)}{\delta U}\bigg|_{U=g*\rho} &= \left(e_{\mathcal{F}} - \frac{1}{s} V_U'(U)(\gamma U - D\nabla^2 U - s\rho) \right)\bigg|_{U=g*\rho} \\
&= e_{\mathcal{F}}\Big|_{U=g*\rho}
\end{aligned}$$

The final simplification follows from the fact that $g * \rho$ is an equilibrium of the U PDE, i.e. $(-\gamma U + D\nabla^2 U + s\rho)\big|_{U=g*\rho} = 0$. Substituting this result into (2.219) gives (2.217).

□

2.4.11 Total energy functional with repellent

Total energy functional (2.206) can be modified in an obvious way to accommodate a repellent,

$$\mathcal{T}(\rho) = \int_\Omega \left(\rho \frac{W_{U_a}(g_a * \rho)}{g_a * \rho} + \rho \frac{W_{U_r}(g_r * \rho)}{g_r * \rho} + W_\rho(\rho) + \sigma \log \rho \right) \mathrm{d}\mathbf{x} \tag{2.220}$$

Then, of course, a second familiar problem arises: it may not be a strictly decreasing function of time, and, in principle, may not be minimized at equilibrium. As the worms move, the distributions of chemical signals also move. Total energy (2.220) decreases as attractant becomes better correlated with worms, but increases as repellent becomes better correlated with worms. However, if attractant is stronger in its influence on $\mathcal{T}$ than repellent, $\mathcal{T}$ may nevertheless be minimized at equilibrium. In practice, this appears to be the case with the numerical models I will consider, which feature a short-range attractant (small D_a, large γ_a) and a long-range repellent (large D_r, small γ_r). This has the effect that repellent is poorly correlated with worms while attractant is tightly correlated, so that free energy changes caused by movement of repellent are relatively muted.

2.5 Summary of free energy functionals

For convenience, I collect here all the free energy functionals developed in this chapter.

2.5.1 Minimal model

These functionals are exact, in the sense that their time derivatives are negative semidefinite, and their functional derivatives are exactly those they aim to produce (except in some cases for a constant of no consequence).

Model	Ref
Chemical signal equilibrium for fixed worm density	
$\mathcal{F}(U) = \int_\Omega \left(\frac{\gamma}{2} U^2 + \frac{D}{2} \|\nabla U\|^2 - s\rho_0 U \right) \mathrm{d}\mathbf{x}$	(2.160)
derivative	
$\frac{\delta \mathcal{F}(U)}{\delta U(\mathbf{x})} = \gamma U(\mathbf{x}) - D\nabla^2 U(\mathbf{x}) - s\rho_0(\mathbf{x})$	(2.159)

Worm density equilibrium for fixed signal

$$\mathscr{F}(\rho) = \int_\Omega \left(-\beta\rho U + \sigma\rho\log\rho\right)\mathrm{d}\mathbf{x} \tag{2.173}$$

derivative

$$\frac{\delta\mathscr{F}(\rho)}{\delta\rho(\mathbf{x})} = -\beta U + \sigma\log\rho$$

Coupled system

$$\mathscr{F}(\rho, U) = \int_\Omega \left(\frac{\beta}{s}\left(\frac{\gamma}{2}U^2 + D\|\nabla U\|^2\right) + \sigma\rho\log\rho - \beta\rho U\right)\mathrm{d}\mathbf{x} \tag{2.184}$$

derivatives

$$\frac{\delta\mathscr{F}(\rho, U)}{\delta\rho(\mathbf{x})} = -\beta U + \sigma\log\rho$$
$$\frac{\delta\mathscr{F}(\rho, U)}{\delta U(\mathbf{x})} = \frac{\beta\gamma}{s}U - \frac{\beta D}{s}\nabla^2 U - \beta\rho$$

Total energy functional of worm density

$$\mathscr{T}(\rho) = \int_\Omega \left(-\frac{\beta\rho(g*\rho)}{2} + \sigma\rho\log\rho\right)\mathrm{d}\mathbf{x} \tag{2.207}$$

derivative

$$\frac{\delta\mathscr{T}(\rho)}{\delta\rho(\mathbf{x})} = -\beta(g*\rho) + \sigma\log\rho$$

2.5.2 Worm model

These are the functionals for the worm system (2.1), (2.3) (and, in two cases, an extended version that models an attractant and a repellent signal). Notes indicate various imperfections.

Notes	Model	Ref
	Chemical signal equilibrium for fixed worm density	
1	$\mathscr{F}(U) = \int_\Omega \left(\frac{\gamma}{2} U^2 + \frac{D}{2} \|\nabla U\|^2 - s\rho_0 U \right) \mathrm{d}\mathbf{x}$	(2.160)
	derivative	
	$\frac{\delta \mathscr{F}(U)}{\delta U(\mathbf{x})} = \gamma U(\mathbf{x}) - D\nabla^2 U(\mathbf{x}) - s\rho_0(\mathbf{x})$	(2.159)
	Worm density equilibrium for fixed signal	
	$\mathscr{F}(\rho) = \int_\Omega \left(\rho V_U(U_0) + W_\rho(\rho) + \sigma\rho\log\rho \right) \mathrm{d}\mathbf{x}$	(2.172)
	derivative	
	$\frac{\delta \mathscr{F}(\rho)}{\delta \rho} = V_U(U_0) + V_\rho(\rho) + \sigma\log\rho$	(2.168)
	Coupled system	
	$\mathscr{F}(\rho, U) = \int_\Omega \begin{pmatrix} -\frac{\gamma}{s}\left(UV_U(U) - W_U(U)\right) \\ +\frac{D}{s}\left(V_U(U) - \frac{W_U(U)}{U}\right)\nabla^2 U \\ +\rho V_U(U) + W_\rho(\rho) + \sigma\rho\log\rho \end{pmatrix} \mathrm{d}\mathbf{x}$	(2.191)

derivatives

$$\frac{\delta \mathscr{F}(\rho, U)}{\delta \rho(\mathbf{x})} = V_U(U) + V_\rho(\rho) + \sigma \log \rho \tag{2.189}$$

2
$$\frac{\delta \mathscr{F}(\rho, U)}{\delta U(\mathbf{x})} \approx -\frac{1}{s} V_U'(U)(\gamma U - D\nabla^2 U - s\rho) \tag{2.190}$$

Coupled system with repellent

3
$$\mathscr{F}(\rho, U_a, U_r) = \int_\Omega \left(\begin{array}{l} -\dfrac{\gamma_a}{s_a}\left(U_a V_{U_a}(U_a) - W_{U_a}(U_a)\right) \\ +\dfrac{D_a}{s_a}\left(V_{U_a}(U_a) - \dfrac{W_{U_a}(U_a)}{U_a}\right)\nabla^2 U_a \\ -\dfrac{\gamma_r}{s_r}\left(U_r V_{U_r}(U_r) - W_{U_r}(U_r)\right) \\ +\dfrac{D_r}{s_r}\left(V_{U_r}(U_r) - \dfrac{W_{U_r}(U_r)}{U_r}\right)\nabla^2 U_r \\ +\rho V_{U_a}(U_a) + \rho V_{U_r}(U_r) + W_\rho(\rho) + \sigma\rho\log\rho \end{array} \right) \mathrm{d}\mathbf{x}$$

derivatives

$$\frac{\delta \mathscr{F}(\rho, U_a, U_r)}{\delta \rho(\mathbf{x})} = V_{U_a}(U_a) + V_{U_r}(U_r) + V_\rho(\rho) + \sigma \log \rho$$

2
$$\frac{\delta \mathscr{F}(\rho, U_a, U_r)}{\delta U_a(\mathbf{x})} \approx -\frac{1}{s_a} V_{U_a}'(U_a)(\gamma U_a - D_a\nabla^2 U_a - s_a\rho)$$

2,3
$$\frac{\delta \mathscr{F}(\rho, U_a, U_r)}{\delta U_r(\mathbf{x})} \approx -\frac{1}{s_r} V_{U_r}'(U_r)(\gamma U_r - D_r\nabla^2 U_r - s_r\rho)$$

Total energy functional of worm density

$$\mathcal{T}(\rho) = \int_\Omega \left(\rho \frac{W_U(g * \rho)}{g * \rho} + W_\rho(\rho) + \sigma \log \rho \right) \mathrm{d}\mathbf{x} \tag{2.200}$$

derivative

2 $$\frac{\delta \mathcal{T}(\rho)}{\delta \rho(\mathbf{x})} \approx V_U(g * \rho) + V_\rho(\rho) + \sigma \log \rho \tag{2.205}$$

Total energy functional of worm density with repellent

$$\mathcal{T}(\rho) = \int_\Omega \left(\rho \frac{W_{U_a}(g_a * \rho)}{g_a * \rho} + \rho \frac{W_{U_r}(g_r * \rho)}{g_r * \rho} + W_\rho(\rho) + \sigma \log \rho \right) \mathrm{d}\mathbf{x} \tag{2.220}$$

derivative

2,3 $$\frac{\delta \mathcal{T}(\rho)}{\delta \rho(\mathbf{x})} \approx V_{U_a}(g_a * \rho) + V_{U_r}(g_r * \rho) + V_\rho(\rho) + \sigma \log \rho$$

Notes:
1. Same as minimal model
2. This functional is approximate. It becomes exact in the limit in which V_U is affine, or $D = 0$.
3. Because it models a repellent, the time derivative of this functional is not necessarily negative semidefinite.

Chapter 3

Numerical solutions and numerical analysis

Parts of this chapter were published in Avery et al (2018).

3.1 Development of the worm model

3.1.1 Strategy

This model incorporates some strategic choices. In particular, it is a *model*—that is, a deliberately simplified construct that does not attempt to describe behavior in photorealistic detail. It is not a defect that the model is simpler than reality. Being simpler than reality is, in fact, the purpose of a model.

Accordingly, this model simply assumes the existence (which has been experimentally demonstrated, Bargmann 2006; Bargmann and Mori 1997) of taxis mechanisms that allow worms to move to where they want to be. Although taxis mechanisms have been investigated for years and much is known about them (e.g. Mori 1999; Dunn et al. 2004; Roberts et al. 2016; Pierce-Shimomura et al. 1999; Ferrée and Lockery 2020), the model presented here is based on the idea that the end result of taxis (movement towards favored places) is sufficient to understand aggregation, and that mechanistic details are not essential.

Any attempt to realistically model taxis mechanisms would have to pay attention to the fact that worms are worm-shaped. I.e., a worm is long and thin, with a head at one end and a tail at

the other. Worm geometry is central to some other published models of *C elegans* aggregation (Rogers et al. 2006; Ding et al. 2019; Sugi et al. 2019). Typically the worm has an orientation in space and moves in the direction its head points or (with lower probability) in the direction its tail points. The straightforward way of incorporating this into the behavioral model would be to make the worm density function ρ depend not just on location $\mathbf{x} \in \mathbb{R}^d$ in space, but also on orientation $\boldsymbol{\theta} \in S^{d-1}$. Chapter 4 describes some problems that result from the approximation of worm locations by a continuous density function—these problems would become more severe if density depended on more variables (and therefore dropped well below 1 for certain combinations of $\mathbf{x}$ and $\boldsymbol{\theta}$). Even this complication only scratches the surface. Worms can bend. They change direction by bending. Bending is critical to taxis mechanisms (Pierce-Shimomura et al. 1999).

Aside from the obvious advantages of promoting intuitive understanding and of analytical and numerical tractability, simple biological models have another important advantage. Complicated models almost inevitably have more parameters: numerical constants on which the modeled behavior depends. Different parameter values may produce qualitatively different results. (See, for instance, the discussion of density-dependent instability in Chapter 1.) Unfortunately, these parameters are not things like Planck's constant or even the viscosity of water that can be readily found in reference materials. In fact, some, such as the dependence of the probability of reversing on the time-derivative of the concentration of an unknown attractant, cannot even be measured. It is not uncommon for biological models to have dozens or even hundreds of poorly identifiable parameters. Simple models minimize this problem.

3.1.2 Design of the PDEs

In designing a model for L1 aggregation, I sought to reproduce certain general characteristics that were obvious in recordings of worm aggregation. First, the worms aggregate. This suggests that they are somehow attracted to each other. Given what we know about *C elegans* biology, it is an obvious guess that this attraction is mediated by a diffusible chemical signal with limited range. PDE (2.1) is essentially the simplest physically plausible that meets these criteria. Keller and Segel (1970), after designing more complicated signal models, arrived at the identical reaction-diffusion equation for the same reasons.

The design of the PDE describing the movement of the worms was more complicated. On the time scale of the experiments, there is neither birth nor death of new worms. This suggested that it should be possible to express the rate of change of worm density as a pure divergence of some flow field. Since flux occurs by movement of worms, the net flux vector at any point is the density times the mean velocity of worms at that point. These considerations lead to a

general equation of the form (1.11), in which velocity is a vector field depending on density, signal concentration, and their gradients. I decided to assume that the velocity field is conservative, i.e. that it can be represented as the gradient of some scalar potential field. There is no compelling biological necessity for this assumption. I made it for two reasons: First it makes the PDE system more tractable analytically. For instance, it enables the simple description of the equilibrium as a Boltzmann distribution (2.165). Second, in recordings of worm behavior, we see that the worms eventually approach an equilibrium in which there is little net flow of animals, and certainly no cyclic flows are obvious.

If the velocity field is conservative, then the ρ PDE can be expressed in terms of the gradient of some potential field V. I chose a potential function that is a sum of a signal-dependent potential V_U and a density-dependent potential V_ρ, for convenience in separately engineering signal and density dependence. This led to the final form (2.3).

For an attractant, V_U must be a decreasing function of signal. In early simulations with a linear V_U numerical instability was a problem. Steep signal gradients frequently occur in the course of simulation. With a linear V_U, these led to large velocities, which meant that worm density at one location was affected by density at distant locations. As a result it was impractical to satisfy the Courant–Friedrichs–Lewy (CFL) stability condition. I therefore sought a potential function whose dependence on U was convex. The Weber-Fechner Law, which is approximately true for many sensory responses (Fechner 1860), holds that response depends linearly on the logarithm of the stimulus intensity. (Keller and Segel (1970) used a Weber-Fechner Law chemotactic response function.) The Weber-Fechner Law has a serious defect: it implies that response sensitivity becomes infinite as concentration approaches zero. (I.e., $\lim_{U\to 0^+} \mathrm{d}(\log U)/\mathrm{d}U = \infty$.) For this reason I chose the function $V_U(U) = -\beta \log(\alpha + U)$, (2.11). At high signal concentrations this approximates a Weber-Fechner Law response. But at low signal concentrations, the response is linear. Parameter α determines where the transition from linear to logarithmic dependence takes place.

I speculated that the circular shape of the aggregates (figure 1.1) results from the worms packing together as tightly as possible. To reproduce this effect in simulations, I designed a potential that would reflect worms taking up space. The ideal would have been a hard sphere potential

$$V_\rho(\rho) = \begin{cases} 0 & \text{if } \rho < \rho_{\max} \\ \infty & \text{if } \rho \geq \rho_{\max} \end{cases} \tag{3.1}$$

This potential function implies discontinuous time or spatial derivatives of density, and therefore functions poorly with numerical methods for solving the PDE system. I therefore approximated the discontinuity with a $\tanh$ function, as described above (2.12).

$$V_\rho(\rho) = \sigma \frac{\texttt{scale}}{2} \left(1 + \tanh\left(\frac{\rho - \texttt{rhomax}}{\texttt{cushion}}\right)\right) \tag{3.2}$$

Four parameters determine the exact shape of V_ρ: σ, `rhomax`, `scale`, and `cushion`. (I refer to the latter three by the symbols I use to represent them in software code, since they will play little role in the mathematics. Also, I wish to distinguish between the parameter `rhomax` and the variable $\rho_{\max}$.) Two parameters, σ and `scale`, determine the vertical scale. σ is the parameter that appears in the ρ PDE (2.3), and in the Boltzmann distribution (2.165). V_ρ rises from near 0 for small values of ρ to $\sigma \times$ `scale` for large ρ. `rhomax` is the density at which V_ρ reaches half its maximum possible value. It is the point at which the V_ρ curve is steepest, and therefore the closest approximation to $\rho_{\max}$ of (3.1). `cushion` determines how abrupt the rise of V_ρ is.

The Keller-Segel literature describes other models in which organism take up space. In these models the strength of chemotactic attraction is modified by density. Hillen and Painter (2009) describe two such models, with the following ρ PDEs

$$\dot{\rho} = \nabla \cdot \left(-\beta\rho\left(1 - \frac{\rho}{\rho_{\max}}\right)\nabla U + \sigma\nabla\rho\right) \tag{M3a}$$

$$\dot{\rho} = \nabla \cdot \left(-\beta\frac{\rho}{1 + \epsilon\rho}\nabla U + \sigma\nabla\rho\right) \tag{M3b}$$

(Equation numbers are from Hillen and Painter (2009). I have changed their symbols to more closely match those used here.) Here $\rho_{\max}$ and ϵ are parameters that control the strength of the volume-filling effect. These models reduce to the minimal model for $\rho_{\max} \to \infty$ (M3a) and $\epsilon \to 0$ (M3b). I did not use these models for two reasons. First, they mix the effects of density and chemotaxis, which I wanted to be able to separately engineer, in a single expression. Second, the effect of density is softer than the hard-sphere potential (3.1) that I thought would most accurately reflect the physics. (I.e., a worm is mostly water, and water is essentially incompressible at ordinary temperatures and pressures).

3.2 Weak forms of the PDEs

Epshteyn and Kurganov (2009) described an interior penalty Discontinuous Galerkin (DG) numerical solution of the Keller-Segel system. Our numerical scheme resembles theirs in general outline, but differs in many details. One of these details (the definition of flow velocity, (3.6) below) is numerically significant.

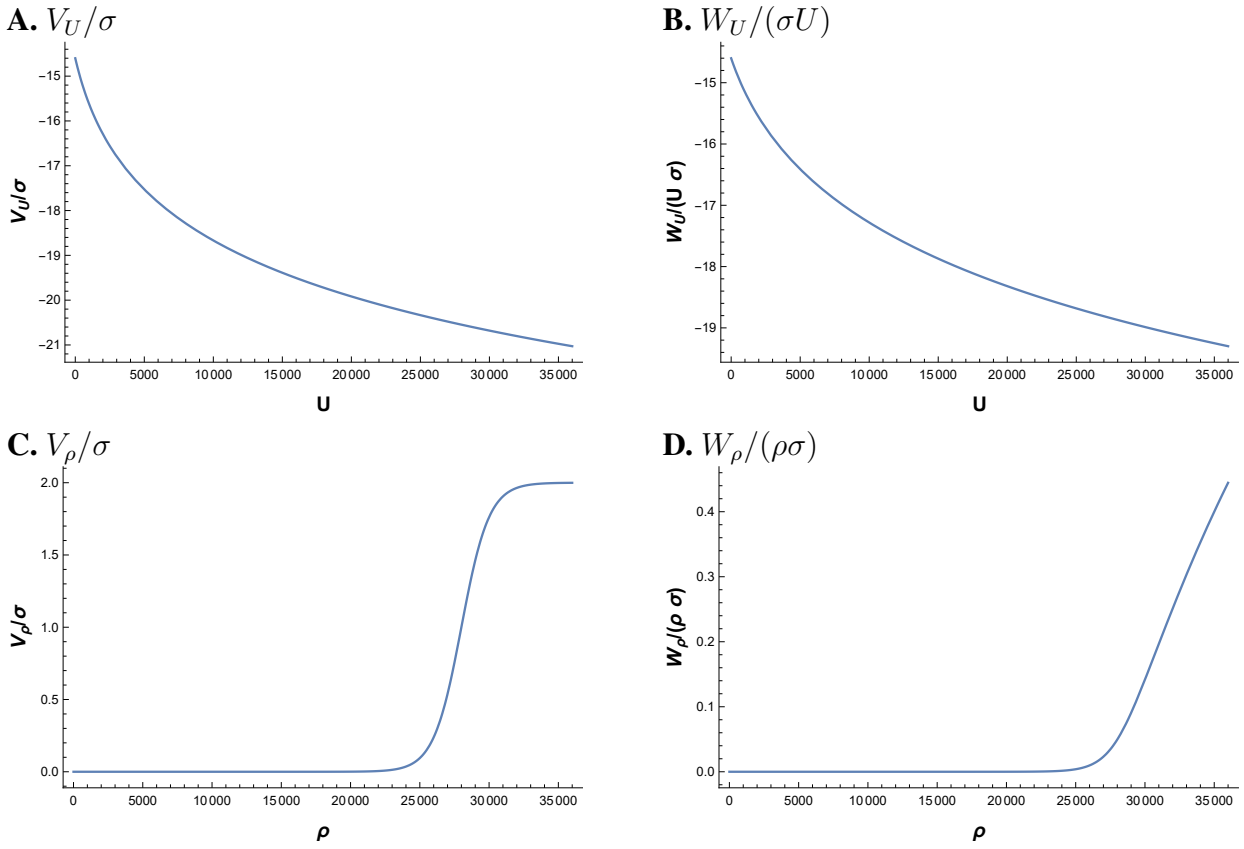

Figure 3.1: Potential function plots
Potential functions that appear in the ρ PDE (2.3), and integrals that appear in the free energy function (2.191). All functions are scaled by σ, since $e^{-V/\sigma}$ is the probability that appears in the Boltzmann equilibrium (2.165). The density free energy integral W_ρ is plotted as a per worm value. Parameter values are $\sigma = 2.7848 \times 10^{-4}$, $\alpha = 1500$, $beta = 5.56 \times 10^{-4}$, $\texttt{rhomax} = 28000$, $\texttt{cushion} = 2000$, $\texttt{scale} = 2$. These values are used in simulations later in this chapter.

The domain Ω is tiled with a set of elements $\mathscr{E}$. (An element $E \in \mathscr{E}$ is a triangle in two dimensions or a line segment in one.) Let Γ be the set of all interior facets, i.e. a facet $e \in \Gamma$ is a side of a triangle in two dimensions or a point in one dimension. Then the U PDE (2.1) is represented by the following weak formulation

$$\begin{aligned}\int_\Omega \dot{U} w_U \mathrm{d}\mathbf{x} = &-\gamma \sum_{E\in\mathscr{E}} \int_E U w_U \mathrm{d}\mathbf{x} + s \sum_{E\in\mathscr{E}} \int_E \rho w_U \mathrm{d}\mathbf{x} \\ &+ D \sum_{e\in\Gamma} \int_e [w_U \nabla U \cdot \mathbf{n_e}] \mathrm{d}\mathbf{x} - D \sum_{E\in\mathscr{E}} \int_E \nabla U \cdot \nabla w_U \mathrm{d}\mathbf{x} \\ &- \frac{p_U r^2}{h} \sum_{e\in\Gamma} \int_e [U][w_u] \mathrm{d}\mathbf{x} - p_{\nabla U} r^2 \sum_{e\in\Gamma} \int_e [\nabla U \cdot \mathbf{n_e}][\nabla w_U \cdot \mathbf{n_e}] \mathrm{d}\mathbf{x}\end{aligned} \tag{3.3}$$

The left-hand-side and the first four terms on the right (those containing parameters γ, s, and D) are arrived at by multiplying the PDE (2.1) by an arbitrary test function w_U and integrating over Ω. The integral over Ω is broken into a sum of integrals over $E \in \mathscr{E}$. The diffusion term $D \int_E w_U \nabla^2 U \mathrm{d}\mathbf{x}$ is integrated by parts to produce $D \int_e w_U \nabla U \cdot \mathbf{n_e} \mathrm{d}\mathbf{x} - D \int_E \nabla U \cdot \nabla w_U \mathrm{d}\mathbf{x}$.

For numerical solution, U and w_U are chosen from a finite-dimensional function space in which each function is approximated by a polynomial within each element $E \in \mathscr{E}$. These functions and their derivatives need not be continuous from one element to the next (this is why the numerical scheme is called "discontinuous" Galerkin). In a DG solution, U can in principle become discontinuous, an undesirable result. In the last two terms (those containing parameters p_U and $p_{\nabla U}$—the"interior penalty" terms), r is the degree of the polynomial approximation, h is a measure of the average element size, and p_U and $p_{\nabla U}$ are parameters controlling the strength of the penalty terms. Each edge $e \in \Gamma$ has an arbitrarily designated '+' and '–' side. $\mathbf{n_e}$ is a unit vector normal to the edge pointing from the '+' side to the '–' side. For a function f having values $f(+)$ on the '+' side and $f(-)$ on the '–' side, the jump of f is $[f] \coloneqq f(+) - f(-)$ (0 if f is continuous). The penalty terms depend on the jump in U or ∇U across the edges $e \in \Gamma$. These terms are zero if U and ∇U are continuous. Furthermore, their signs are such as to coerce any discontinuities that arise in the course of solution to vanish.

Although (3.3) is different in detail from the weak formulation used by Epshteyn and Kurganov (2009) it is substantially similar. The weak formulation of the ρ PDE (2.3), however, is substantially different from that of Epshteyn and Kurganov (2009).

$$\int_\Omega \dot{\rho} w_\rho \mathrm{d}\mathbf{x} = \sum_{E\in\mathscr{E}} \int_E \boldsymbol{\phi}\cdot\nabla w_\rho \mathrm{d}\mathbf{x} - \sum_{e\in\Gamma}\int_e \phi_{\mathbf{UW}}(e)[w_\rho]\mathrm{d}\mathbf{x} \tag{3.4}$$
$$- \frac{p_\rho r^2}{h}\sum_{e\in\Gamma}\int_e [\rho][w_\rho]\mathrm{d}\mathbf{x} - p_{\nabla\rho} r^2 \sum_{e\in\Gamma}\int_e [\nabla\rho\cdot\mathbf{n_e}][\nabla w_\rho\cdot\mathbf{n_e}]\mathrm{d}\mathbf{x}$$

Here w_ρ, p_ρ, and $p_{\nabla\rho}$ are a test function and penalty parameters distinct from but analogous to the similarly named w_U, p_U, and $p_{\nabla U}$. Velocity vector $\mathbf{v}$, flux vector $\boldsymbol{\phi}$ and upwind flux $\phi_{\mathbf{UW}}$ are as follows.

$$V(\mathbf{x}) \coloneqq V_U(U(\mathbf{x})) + V_\rho(\rho(\mathbf{x})) \tag{3.5}$$
$$\mathbf{v} \coloneqq -\nabla V - \frac{\sigma}{\rho}\nabla\rho = -\nabla(V + \sigma\log\rho) \tag{3.6}$$
$$\boldsymbol{\phi} \coloneqq \mathbf{v}\rho \tag{3.7}$$
$$v_e \coloneqq \max(\mathbf{v}\cdot\mathbf{n_e}, 0) \tag{3.8}$$
$$\phi_{\mathbf{UW}} \coloneqq v_e(+)\rho(+) - v_e(-)\rho(-) \tag{3.9}$$

Velocity $\mathbf{v}$ is the sum of the advective velocity ∇V and an imputed diffusive velocity $-\sigma\nabla\rho/\rho$, designed to reconstruct the Fick's Law diffusive flux $\boldsymbol{\phi} = -\sigma\nabla\rho$. At equilibrium $\mathbf{v} = \mathbf{0}$ everywhere. Epshteyn and Kurganov (2009) instead use a upwind flux based on advective velocity $-\nabla V$, and handle the diffusive term $\sigma\nabla^2\rho$ separately, in the same way as $D\nabla^2 U$ is handled in (3.3).

The two schemes are mathematically equivalent, but quite different numerically, particularly near equilibrium. At equilibrium, every term of each sum in (3.4) is individually 0, because $\mathbf{v}$ and $\boldsymbol{\phi}$ are identically $\mathbf{0}$. In the Epshteyn and Kurganov (2009) formulation, the 0 on the right-hand-side at equilibrium is computed as the difference between sums of opposite sign and large but nearly equal absolute value, and round-off error can be substantial. In fact, I coded both schemes, and I found that with the Epshteyn and Kurganov formulation worms would appear from nowhere, at the expense of negative worms appearing nearby. (Epshteyn and Kurganov were not concerned with performance near equilibrium, because their solutions were all carried out under conditions where, because of blow-up, there is no equilibrium.)

3.3 Parameter estimates

I don't have a precise estimate of any of the model parameters. Parameters for initial exploration were chosen as follows. First, I estimated that freely moving L1s spread about $1\,\mathrm{cm}$ in an hour. Thus I estimate $\sigma = 1\,\mathrm{cm}^2\mathrm{h}^{-1} = 2.7778 \times 10^{-4}\,\mathrm{cm}^2\mathrm{s}^{-1}$.

An L1 is approximately a cylinder of diameter $15\,\mu\mathrm{m}$ and length $242\,\mu\mathrm{m}$ (Avery and Shtonda 2003). Since worms lie on their sides, a worm occupies approximate area $15 \times 242 \approx 3600\ \mu\mathrm{m}^2$. I chose the inverse of this area, $28\,000\,\mathrm{cm}^{-2}$ as the parameter `rhomax`. (This is undoubtedly an underestimate of the true maximum density. When looked at from the side, one can see that L1 aggregates have slightly mounded shape. Thus worms must be heaped up on each other in the center. I do not, however, have a better estimate of the true maximum density. Also, the specific number has little effect on the solutions except for scaling the density, since it merely sets the units in which density is measured.) Parameters `cushion` and `scale` have no real biological significance. Parameter `cushion` makes the ideal hard-sphere potential (3.1) continuous and differentiable, so that the PDEs can be solved numerically with differentiable functions. The value $2000\,\mathrm{cm}^{-2}$ worked. The `scale` parameter need only be chosen large enough to constrain the maximum density—I chose 2.

I chose a mean density of $9000\,\mathrm{cm}^{-2}$ so that aggregates would occupy about $1/3$ (i.e. $9000/28000$) of the area.

Small molecules in water typically have diffusion constants in the range $1 \times 10^{-6}\,\mathrm{cm}^2\mathrm{s}^{-1}$ to $1 \times 10^{-5}\,\mathrm{cm}^2\mathrm{s}^{-1}$. I chose D, the diffusion constant of attractant, at the lower end of this range. The aggregates that form have diameters of hundreds of micrometers. I therefore chose the decay rate of attractant to give it a range $\sqrt{D/\gamma}$ of $100\,\mu\mathrm{m}$.

I will always choose units of concentration such that s and γ are numerically equal. (That is, if concentration is measured in "amount of stuff"/cm^{d}, I choose the units in which "amount of stuff" is measured to be the amount secreted by one worm in one mean lifetime of the stuff, i.e. γ^{-1}. This has the effect that if $\gamma = \langle\text{number}\rangle\ \mathrm{s}^{-1}$, then $s = \langle\text{number}\rangle$"stuff units" $\mathrm{cm}^{-\mathrm{d}}\mathrm{s}^{-1}$, with the number being the same in the two cases.) This ensures that concentration U and worm density ρ are in the same range numerically.

Alex Artyukhin found that the minimum worm density for aggregation is $1500\,\mathrm{cm}^{-2}$ (Alexander B Artyukhin et al. 2015). I identified this with the density threshold for instability. I chose $\alpha = 1500\,\mathrm{cm}^{-2}$, to make V_U linear near the threshold, and to be obviously convex near `rhomax`. I then chose $\beta = 5.56 \times 10^{-4}\,\mathrm{cm}^2\mathrm{s}^{-1}$ to reproduce the $1500\,\mathrm{cm}^{-2}$ density threshold for instability.

These numbers are summarized in Table 3.1.

$\bar{\rho}$	mean density	$9000\,\mathrm{cm}^{-\mathrm{d}}$
σ	random worm movement	$2.7778 \times 10^{-4}\,\mathrm{cm}^2\mathrm{s}^{-1}$
`rhomax`	midpoint of V_ρ potential rise	$28\,000\,\mathrm{cm}^{-\mathrm{d}}$
`cushion`	breadth of V_ρ rise	$2000\,\mathrm{cm}^{-\mathrm{d}}$
`scale`	height of V_ρ rise	2
β	strength of attraction	$5.56 \times 10^{-4}\,\mathrm{cm}^2\mathrm{s}^{-1}$
α	concentration scale	$1500\,\mathrm{cm}^{-\mathrm{d}}$
γ	attractant decay rate	$0.01\,\mathrm{s}^{-1}$
D	attractant diffusion constant	$1 \times 10^{-6}\,\mathrm{cm}^2\mathrm{s}^{-1}$
s	secretion rate	$0.01\,\mathrm{cm}^{-\mathrm{d}}\mathrm{s}^{-1}$

Table 3.1: Chapter 3 parameter values

3.4 Numerical methods and software

3.4.1 Software

Because Epshteyn and Kurganov (2009) had sucessfully implemented a numerical solution of tyhe Keller-Segel PDEs using an interior penalty discontinuouis Galerkin fintie element method, I implemented the solution of (3.3, 3.4) in the finite-element package FEniCS (Logg et al. 2010) with backend PETSc (Balay, Abhyankar, et al. 2019a; Balay, Abhyankar, et al. 2019b; Balay, Gropp, et al. 1997). FEniCS is a specialized Computer Algebra System (CAS), in which the integrals that arise in finite element formulations of PDEs can be written in a form closely related to their mathematical representation. FEniCS is written mostly in `C++`, but has python language bindings. For instance, the following term in the U weak form (3.3)

$$-\gamma \sum_{E\in\mathscr{E}} \int_E U w_U \mathrm{d}\mathbf{x} \tag{3.10}$$

was implemented by the following python code

```
self.U_decay = -self.gamma * self.iU * self.wU * self.dx
```

In this expression, `self.gamma` was previously defined as a FEniCS `Constant`, `self.iU` as a `Function`, `self.wU` as a `TestFunction`, and `self.dx` as a `Measure`. Multiplication of a `Function` by a `Measure` implies integration. The `Functions` were defined on a

`Mesh` that defines a tiling of the domain with elements (intervals or triangles). The FEniCS expression (3.10) is represented by a `Form`. FEniCS constructs the sum over elements in (3.10), and writes and compiles `C++` code to "`assemble`", i.e. evaluate, it. The `Form` is a linear function of the test function `self.wU`, and when `assembled` produces a vector of floating point numbers that approximate the coefficients of this function.

PETSc is the "Portable Extensible Toolkit for Scientific computation". (As for why "computation" is not capitalized, your guess is as good as mine.) It "is a suite of data structures and routines for the scalable (parallel) solution of scientific applications modeled by partial differential equations" (Balay, Abhyankar, et al. 2019a). Among the tools included is the `TS` (time-stepper) package, a library of Ordinary Differential Equation (ODE)/Differential Algebraic Equation (DAE) solvers (Abhyankar et al. 2018).

FEniCS allows the mathematical formulation of the problem to be changed with little coding effort. PETSc provides similar flexibility in numerical methods—for instance, one can select different linear solvers and ODE solvers at run time with the use of command line options. This makes it possible to quickly test dozens of different solvers and choose the one with the best performance. Both FEniCS and PETSc are designed for parallel computation under the Message Passing Interface (MPI) standard.

3.4.2 Random initial conditions

To reveal Keller-Segel instability, I start each simulation with a uniform initial condition perturbed by a small random variation

$$\rho(0, \mathbf{x}) = \frac{N_0}{|\Omega|} + \epsilon(\mathbf{x}) \tag{3.11}$$

$$U(0, \mathbf{x}) = \frac{s}{\gamma}\rho(0, \mathbf{x}) \tag{3.12}$$

This left me with the problem of constructing a random continuously differentiable function $\epsilon(\mathbf{x})$. Begin by tiling the domain $\Omega = [0, 1]^d$ with a grid of small intervals or squares of linear dimension $1/n$, with vertexes

$$\mathscr{V} = \frac{1}{n}\{1, \ldots, n\}^d \tag{3.13}$$

Define the kernel function

$$k(x) = \begin{cases} |x| < 1 & 2|x|^3 - 3|x|^2 + 1 \\ |x| \geq 1 & 0 \end{cases} \tag{3.14}$$

k has a continuous first derivative, $\text{supp}(k) = [-1, 1]$, and $\forall i \in \mathbb{Z}, k(i) = \delta_{i0}$. Now, select a random number $\epsilon_{\mathbf{v}}$ for each vertex $\mathbf{v} \in \mathscr{V}$, for instance by sampling from a normal distribution. Finally, define the random function $\epsilon(\mathbf{x})$

$$\epsilon(\mathbf{x}) = \sum_{\mathbf{v} \in \mathscr{V}} \epsilon_{\mathbf{v}} \prod_{i=1}^{d} k(n \times (x_i - v_i)) \tag{3.15}$$

This function has a continuous derivative, since it is a sum of products of continuously differentiable functions. At a vertex $\mathbf{v} \in \mathscr{V}$, the value of the function is $\epsilon(\mathbf{v}) = \epsilon_{\mathbf{v}}$. Because it is a piecewise polynomial of degree $3d$, it will not be possible to project this function exactly onto the broken Sobolev space in which ρ and U are represented by by polynomials of degree $r < 3d$. To alleviate the problem caused by this mismatch, I choose a grid $\mathscr{V}$ sparser than the vertexes of the mesh on which ρ and U are defined.

3.4.3 Numerical details

The remainder of this chapter will present several simulations produced by numerical solution of the PDEs (2.3), (2.1). The following numerical details are common to all the following simulations.

Unless otherwise noted, the parameter values in Table 3.1 are used.

The initial condition for each simulation was a uniform density of $9000\,\text{cm}^{-\text{d}}$, with normally distributed random noise of standard deviation $90\,\text{cm}^{-\text{d}}$ added. Simulations ran for $200\,000\,\text{s}$ ($2.3\,\text{d}$). All one-dimensional simulations in this chapter started from the same initial state (i.e., the pseudorandom noise was identical among all runs), and all two-dimensional simulations started from the same initial state. In this document I show plots of the final state, which is close to equilibrium. A time point of a single simulation is represented by two plots, one for ρ and one for U. (Later, when I introduce repellent, there will be plots for U_a and U_r.) I also attach movie files showing how these plots change with time (Appendix 1).

One dimensional simulations take place on a mesh of 128 equal-width intervals. Functions are approximated by polynomials of degree 3, so there are 4 degrees of freedom per interval

per function, for a total of 2 functions $\times$ 4 df/element/function $\times$ 128 elements = 1024 degrees of freedom. Each degree of freedom is the value of the polynomial at some specific x. The degrees of freedom at the end of an interval have the same coordinate location as those at the ends of the adjacent interval—in principle this allows functions to be discontinuous. In practice, the penalty terms of the weak forms (3.3,3.4) coerce the functions to continuity. Spatial resolution is therefore $1/(3 \times 128) = 1/384$ cm.

Two dimensional simulations take place on a mesh of $2 \times 128 \times 128$ triangles. To construct this mesh, the 1×1 cm square domain is divided into 128×128 equal squares, and each square is bisected into two isosceles right triangles. Functions are approximated by polynomials of degree 3. There are 10 degrees of freedom per triangle per function. Nine of these are on the boundary and share coordinate locations with degrees of freedom of adjacent elements. There are thus $2 \times 10 \times 2 \times 128 \times 128 = 655360$ degrees of freedom (983040 with repellent).

The left-hand-side of each of the weak forms (3.3,3.4), i.e.

$$\int_\Omega \dot{\rho} w_\rho \mathrm{d}\mathbf{x} \tag{3.16}$$

$$\int_\Omega \dot{U} w_U \mathrm{d}\mathbf{x} \tag{3.17}$$

is a bilinear function of the trial function $\dot{\rho}$, $\dot{U}$ and the test function w_ρ, w_U, respectively. FEniCS `assembles` this `Form` to a matrix. The time derivative $\dot{\boldsymbol{\rho}}$ at any point is computed by solving

$$\mathbf{A} \begin{pmatrix} \dot{\boldsymbol{\rho}} \\ \dot{\boldsymbol{U}} \end{pmatrix} = \mathbf{b}(\boldsymbol{\rho}, \mathbf{U}) \tag{3.18}$$

where $\mathbf{A}$ is the matrix produced by `assembleing` (3.16) and $\mathbf{b}$ the vector produced by `assembleing` the entire right-hand side of (3.4) and a similar weak form expression for U. In this equation $\boldsymbol{\rho}$ and $\mathbf{U}$ represent the vector of degrees of freedom of the finite-dimensional approximations of the functions $\rho(\mathbf{x})$ and $U(\mathbf{x})$. That is, the space of degree 3 DG polynomial functions $\rho(\mathbf{x}), U(\mathbf{x})$ has dimension 655360. Any pair of functions in the space is represented by list of 655360 real numbers, which can be treated as a vector in a vector space. (3.18) is a system of linear equations in that vector space. (3.18) is thus a large system of ODEs. Numerical solution of the PDEs thus reduces to solution of this ODE. Linear equations were solved with the MUMPS parallel direct solver (Amestoy, Guermouche, et al. 2006; Amestoy, Duff, et al. 2001).

The following solutions were produced with the PETSc Rosenbrock-W solver `ra34pw2` (Rang and Angermann 2005), an implicit third-order method. I used PETSc's basic adaptive step size mechanism. This method uses error estimates from the embedded stepper to adjust step size so as to maintain error below predetermined absolute and relative tolerances. Step sizes were small at early times, when ρ and U were changing rapidly. Towards the end step sizes became large as the system approached equilibrium.

PETSc supplies a few dozen different ODE/DAE solvers (Abhyankar et al. 2018). I tried all of them and the ROSW methods gave the best results. Implicit Runge-Kutta solvers also worked well. The implicit Runge-Kutta steppers were more accurate, so that larger time steps were feasible. However, each step took longer than for the ROSW methods. ROSW was quickest overall, while also providing better temporal resolution.

Implicit methods require the Jacobian of the nonlinear vector function $\mathbf{b}$ (3.18). This was computed using the FEniCS function `derivative`, which can automatically differentiate a `Form`.

3.4.4 Periodic boundary conditions from Dirichlet and Neumann boundary conditions on odd and even components

When I began simulations of the worm system I used Neumann boundary conditions (1.2). This is equivalent to assuming the domain is surrounded by an impermeable wall through which neither worms nor attractant can pass. A problem quickly became evident. With Neumann boundary conditions, a worm on the boundary is twice as attractive to others as a worm in the interior (assuming the range of the attractant is much less than the dimension of the domain) , as follows: The attractant released by a worm on the border diffuses into a hemiball of half the volume of the ball into which the attractant released by a worm in the interior diffuses. A worm in the corner of a two-dimensional square domain is likewise four times as attractive as a worm in the interior. As a result, the formation of aggregates is biased towards the boundary, although they do also form in the interior (Figure 3.2).

This problem has an obvious solution: periodic boundary conditions. Under periodic boundary conditions there is perfect translational symmetry: each point in the domain is equivalent to every other. In principle the implementation of periodic boundary conditions is straightforward. One merely identifies the left boundary with the right boundary and the bottom boundary with the top, thus creating a logical space that has the topology of a torus. There is even a mechanism in FEniCS to do exactly this. Unfortunately, there is also a bug in FEniCS: periodic boundary conditions don't work with discontinuous Galerkin methods, (FEniCS DG periodic

A. Neumann boundary conditions, $d = 1$

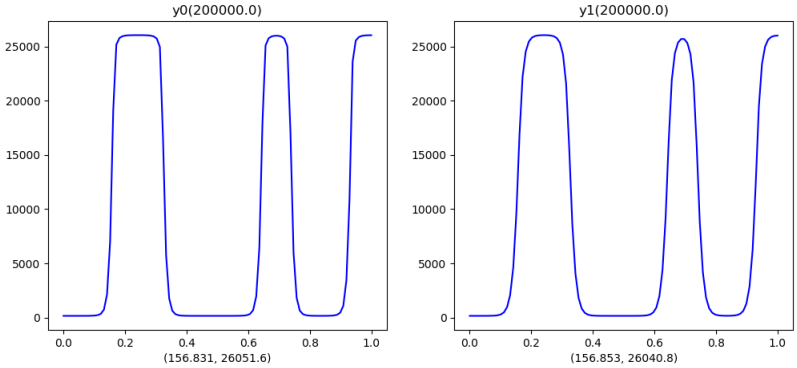

B. Neumann boundary conditions, $d = 2$

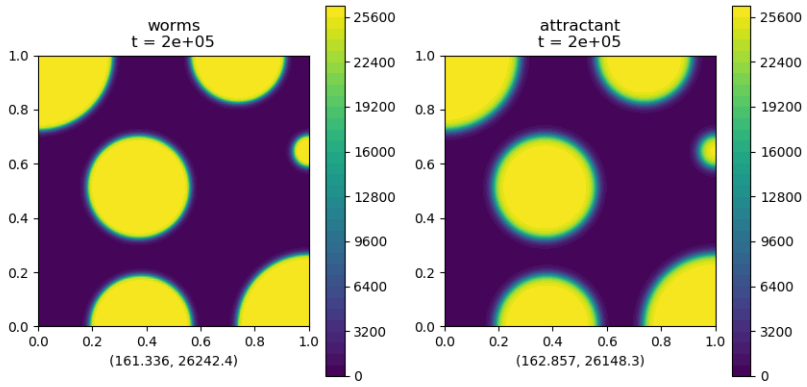

Figure 3.2: Simulation with Neumann boundary conditions
The left plot in each panel shows density ρ—the right plot shows attractant concentration U. The two numbers below the plot are the minimum and maximum values of the plotted function over the entire domain.

boundary conditions bug). This bug was first noted in 2016. As of August 2019, it has not been fixed.

I developed a workaround that allows production of solutions that satisfy periodic boundary conditions by solving a system satisfying Dirichlet and Neumann boundary conditions.

The key trick is to separate the even and odd components of the function. I will begin by showing how this works in one dimension, then explain how to extend the trick to two or more dimensions. In the following I use the assumption that ρ and U are periodic with period 1, i.e. $\forall x \in \mathbb{R}, n \in \mathbb{Z}$, $\rho(x+n) = \rho(x)$, $U(x+n) = U(x)$. Define

$$\rho_e(x) \coloneqq \frac{\rho(x) + \rho(-x)}{2} = \frac{\rho(x) + \rho(1-x)}{2} \tag{3.19}$$

$$\rho_o(x) \coloneqq \frac{\rho(x) - \rho(-x)}{2} = \frac{\rho(x) - \rho(1-x)}{2} \tag{3.20}$$

$$U_e(x) \coloneqq \frac{U(x) + U(-x)}{2} = \frac{U(x) + U(1-x)}{2} \tag{3.21}$$

$$U_o(x) \coloneqq \frac{U(x) - U(-x)}{2} = \frac{U(x) - U(1-x)}{2} \tag{3.22}$$

It is easy to verify that ρ_e and U_e are even and periodic, that ρ_o and U_o are odd and periodic, and that

$$\rho(x) = \rho_e(x) + \rho_o(x) \tag{3.23}$$

$$\rho(1-x) = \rho_e(1-x) + \rho_o(1-x) = \rho_e(x) - \rho_o(x) \tag{3.24}$$

$$U(x) = U_e(x) + U_o(x) \tag{3.25}$$

$$U(1-x) = U_e(1-x) + U_o(1-x) = U_e(x) - U_o(x) \tag{3.26}$$

Now, every odd periodic function is odd about every half-integer multiple of its period. E.g. $\rho_o(1/2 - x) = -\rho_o(1/2 + x)$

$$\begin{aligned} \rho_o\left(\frac{1}{2} - x\right) &= -\rho_o\left(x - \frac{1}{2}\right) && \rho_o \text{ odd} \\ &= -\rho_o\left(x + \frac{1}{2}\right) && \rho_o \text{ periodic} \end{aligned}$$

It follows that $\rho_o(1/2) = 0$. Of course, as for any odd function, $\rho_o(0) = 0$. Similarly an even periodic function is even about every half-integer multiple of its period. Furthermore, if an even function is differentiable, then its derivative is zero at every point of even symmetry. Thus, ρ_o, ρ_e, U_o, and U_e satisfy the following Dirichlet and Neumann boundary conditions on $[0, 1/2]$,

$$\rho_o(0) = \rho_o(1/2) = 0 \tag{3.27}$$
$$U_o(0) = U_o(1/2) = 0 \tag{3.28}$$
$$\rho_e'(0) = \rho'(1/2) = 0 \tag{3.29}$$
$$U_e'(0) = U_e'(1/2) = 0 \tag{3.30}$$

This works in reverse, as well. If ρ_o and U_o are continuously differentiable functions on $[0, 1/2]$ satisfying Dirichlet boundary conditions (3.27, 3.28) and ρ_e and U_e continuously differentiable functions on $[0, 1/2]$ satisfying Neumann boundary conditions (3.29,3.30), then the functions ρ and U defined on $[0, 1]$ by (3.23 – 3.26) are continuous and differentiable and satisfy periodic boundary conditions on $[0, 1]$ for both function values and derivatives. The periodic boundary condition problem can thus be solved by the following steps

1. From the ρ, U initial conditions, use (3.19 – 3.22) to compute ρ_o, ρ_e, U_o, U_e initial conditions.

2. Solve the ρ_o, ρ_e, U_o, U_e time-dependent PDE system (3.31, 3.32, 3.33, 3.34 below) on $[0, 1/2]$ with boundary conditions (3.27 – 3.30).

3. Use (3.23 – 3.26) to compute ρ and U on $[0, 1]$ from ρ_o, ρ_e, U_o, U_e. Since we only have ρ_o, ρ_e, U_o, U_e on $[0, 1/2]$, use (3.23) and (3.25) to find ρ and U on [0,1/2] and (3.24) and (3.26) to find ρ and U on $[1/2, 1]$.

Time-dependent PDEs for ρ_o, ρ_e, U_o, U_e can be derived from the ρ and U PDEs (2.1,2.3). Because the U PDE is linear, the U_o and U_e PDEs have the same form as the U PDE

$$\begin{aligned}
\dot{U}_o(x) &= \frac{\dot{U}(x) - \dot{U}(-x)}{2} && (3.31)\\
&= \frac{1}{2}\big(-\gamma U(x) + D\nabla^2 U(x) + s\rho(x)\big)\\
&\quad - \frac{1}{2}\big(-\gamma U(-x) + D\nabla^2 U(-x) + s\rho(-x)\big)\\
&= -\gamma\frac{U(x) - U(-x)}{2} + D\nabla^2\frac{U(x) - U(-x)}{2} + s\frac{\rho(x) - \rho(-x)}{2}\\
&= -\gamma U_o(x) + D\nabla^2 U_o(x) + s\rho_o(x)\\
\dot{U}_e(x) &= -\gamma U_e(x) + D\nabla^2 U_e(x) + s\rho_e(x) && (3.32)
\end{aligned}$$

The PDEs for ρ_o and ρ_e are more complicated. Using the shorthand $V(x) \coloneqq V_U(U(x)) + V_\rho(\rho(x))$,

$$\begin{aligned}
\dot{\rho_o} &= \frac{\dot{\rho}(x) - \dot{\rho}(-x)}{2} && (3.33)\\
&= \frac{1}{2}(\nabla\cdot(\rho\nabla(V(x) + \sigma\log\rho(x))))\\
&\quad - \frac{1}{2}(\nabla\cdot(\rho\nabla(V(1-x) + \sigma\log\rho(1-x))))\\
\dot{\rho_e} &= \frac{1}{2}(\nabla\cdot(\rho\nabla(V(x) + \sigma\log\rho(x))))\\
&\quad + \frac{1}{2}(\nabla\cdot(\rho\nabla(V(1-x) + \sigma\log\rho(1-x)))) && (3.34)
\end{aligned}$$

To evaluate the weak forms derived from these PDEs, it is necessary to find $\rho(x), \rho(1-x)$ and $V(x), V(1-x)$ for each $x \in [0, 1/2]$ from ρ_o, ρ_e, U_o, U_e. $\rho(x), \rho(1-x), U(x), U(1-x)$ are computed from (3.23 – 3.26). Then

$$\begin{aligned}
V(x) &= V_U(U(x)) + V_\rho(\rho(x)) && (3.35)\\
V(1-x) &= V_U(U(1-x)) + V_\rho(\rho(1-x)) && (3.36)
\end{aligned}$$

The trick works similarly in two or more dimensions. However, instead of two component functions, there are 2^d. In two dimensions each of ρ and U is the sum of four functions: one

even in x_1, x_2, one even in x_1 and odd in x_2, one odd in x_1 and even in x_2, and one odd in both x_1 and x_2. The original system of two PDEs becomes a system of 8 PDEs on $[0, 1/2]^2$.

This workaround is less costly than one might at first imagine. Steps 1 and 3 are computationally trivial. As in the original version of the problem, numerical solution of the time-dependent PDE system is the computationally intensive step. Because the odd/even system is solved only on $[0, 1/2]^d$, the number of degrees of freedom is the same as for the ρ, U system on $[0, 1]^d$. There is, however, a computational cost from the nonlinear ρ PDEs (3.33,3.34). Because of all the cross-talk among the component equations, the matrices that arise have more non-zero elements and take longer to factor.

There is also a cost in code complexity. Coding steps 1 and 2 in a scalable (i.e., parallel-executable) way took some effort. My code for step 3 runs only sequentially. This step is carried out as post-processing on a solution stored in terms of odd/even component functions.

At my thesis defense, I was informed that the finite element package Firedrake, a fork of FEniCS, does not have the DG-periodic boundary conditions bug. In retrospect, I might have been better advised to use Firedrake. Because one of my officemates was using it, I was aware of Firedrake at the time as a comparatively poorly documented and poorly supported alternative to FEniCS. I had no reason at the time to think that switching to Firedrake would improve anything.

There are two conspicuous differences between the results with Neumann boundary conditions (Figure 3.2) and periodic boundary conditions (Figure 3.3). First, as expected, the bias towards edges and corners with Neumann boundary conditions vanishes with periodic boundary conditions. Second, in two dimensions all the aggregates coalesced into a single large aggregate.

All remaining simulations in this chapter employ periodic boundary conditions.

3.5 A repellent is necessary

The coalescence of the aggregates is a problem for this model. In movies of aggregating worms one sees that, at densities between the threshold for aggregation and densities so high that worms fill the entire area, the aggregates that form have a roughly constant size and spacing (Figure 1.1). I could not reproduce this behavior in numerical experiments with attractant-only models. There is also theoretical reason to believe it is unlikely. As pointed out in chapter 1, there is no natural maximum scale for instability in the minimal model (1.9). This is true for any attractant-only model.

A. Periodic boundary conditions, $d = 1$

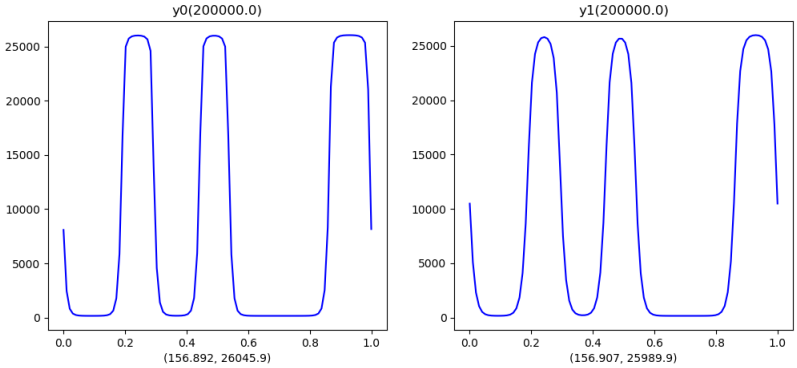

B. Periodic boundary conditions, $d = 2$

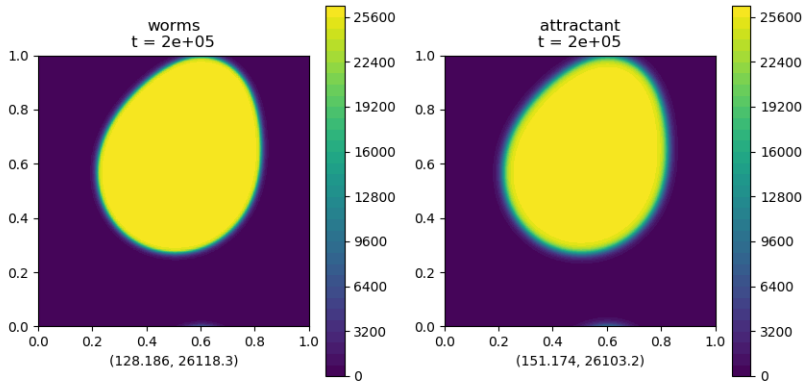

Figure 3.3: Simulation with Periodic boundary conditions
The left plot in each panel shows density ρ—the right plot shows attractant concentration U. The two numbers below the plot are the minimum and maximum values of the plotted function over the entire domain.

Brian Ingalls suggested, by analogy with activator-inhibitor models of biological pattern formation, that the addition of a negative signal to oppose the attractant, a repellent, would solve the scale problem. Linear stability analysis supports this intuition.

3.5.1 Linear stability analysis

Intuitively, and by analogy with activator-inhibitor models, what one requires is a short-range attractant and a long-range repellent. I therefore added to the model a repellent with diffusion constant $D_r = 10D_a = 1 \times 10^{-5}\,\mathrm{cm^2 s^{-1}}$ and decay rate $\gamma_r = 0.1\gamma_a = 0.001\,\mathrm{s^{-1}}$. The range of this repellent $\kappa_r = \sqrt{D_r/\gamma_r} = 1\,\mathrm{mm}$ is ten times that of attractant, and is approximately equal to the observed spacing between aggregates. As explained above, I choose units of repellent concentration such that s_r and γ_r are numerically equal, i.e. $s_r = 0.001\,\mathrm{cm^{-d} s^{-1}}$.

For simplicity, I will assume $V_\rho = 0$ in the following. With the parameter values in Table 3.1, this is very close to true in the vicinity of the instability threshold.

Linearization of the PDE system around a uniform equilibrium at $\rho(\mathbf{x}) = \bar{\rho}$, $U_i(\mathbf{x}) = \bar{U}_i = s_i\bar{\rho}/\gamma_i$ produces the following linear PDE system

$$\frac{\mathrm{d}}{\mathrm{d}t}\begin{pmatrix}\delta\rho\\ \delta U_a\\ \delta U_r\end{pmatrix} = \begin{pmatrix}\sigma\nabla^2 & \bar{\rho}V'_{U_a}(\bar{U}_a)\nabla^2 & \bar{\rho}V'_{U_r}(\bar{U}_r)\nabla^2\\ s_a & -\gamma_a + D_a\nabla^2 & 0\\ s_r & 0 & -\gamma_r + D_r\nabla^2\end{pmatrix}\begin{pmatrix}\delta\rho\\ \delta U_a\\ \delta U_r\end{pmatrix} \tag{3.37}$$

The ansatz

$$\begin{pmatrix}\delta\rho\\ \delta U_a\\ \delta U_r\end{pmatrix} = \begin{pmatrix}\rho_{\mathbf{k}}\\ U_{a\mathbf{k}}\\ U_{r\mathbf{k}}\end{pmatrix} e^{\lambda_{\mathbf{k}}t}e^{i\mathbf{k}\cdot\mathbf{x}} \tag{3.38}$$

yields the eigenvalue problem

$$\lambda_{\mathbf{k}}\begin{pmatrix}\rho_{\mathbf{k}}\\ U_{a\mathbf{k}}\\ U_{r\mathbf{k}}\end{pmatrix} = \begin{pmatrix}-\sigma k^2 & -\bar{\rho}V'_{U_a}(\bar{U}_a)k^2 & -\bar{\rho}V'_{U_r}(\bar{U}_r)k^2\\ s_a & -\gamma_a - D_a k^2 & 0\\ s_r & 0 & -\gamma_r - D_r k^2\end{pmatrix}\begin{pmatrix}\rho_{\mathbf{k}}\\ U_{a\mathbf{k}}\\ U_{r\mathbf{k}}\end{pmatrix} \tag{3.39}$$

$$= \begin{pmatrix}-\sigma k^2 & -\bar{\rho}k^2(\mathbf{V}'(\bar{\mathbf{U}}))^\intercal\\ \bar{\rho}\mathbf{s} & -\mathbf{\Gamma} - \mathbf{D}k^2\end{pmatrix}\begin{pmatrix}\rho_{\mathbf{k}}\\ \mathbf{U}_{\mathbf{k}}\end{pmatrix} \tag{3.40}$$

$$= -\mathbf{N}(\bar{\rho}, k^2)\begin{pmatrix}\rho_{\mathbf{k}}\\ \mathbf{U}_{\mathbf{k}}\end{pmatrix} \tag{3.41}$$

In (3.40), the matrix is in a block form that can be extended easily to any number of signals, with

$$\mathbf{s} = \begin{pmatrix} s_a \\ s_r \end{pmatrix} \tag{3.42}$$

$$\mathbf{U_k} = \begin{pmatrix} U_{a\mathbf{k}} \\ U_{r\mathbf{k}} \end{pmatrix} \tag{3.43}$$

$$\mathbf{V}'(\bar{\mathbf{U}}) = \begin{pmatrix} V'_{U_a}(\bar{U}_a) \\ V'_{U_r}(\bar{U}_r) \end{pmatrix} \tag{3.44}$$

$$\mathbf{\Gamma} = \begin{pmatrix} \gamma_a & 0 \\ 0 & \gamma_r \end{pmatrix} \tag{3.45}$$

$$\mathbf{D} = \begin{pmatrix} D_a & 0 \\ 0 & D_r \end{pmatrix} \tag{3.46}$$

In (3.41), $\mathbf{N}(\bar{\rho}, k^2)$ is defined as the negative of the matrix in (3.40). (I define $\mathbf{N}$ as the negative to avoid an annoying factor of $(-1)^{1+n_{\text{signals}}}$ in the determinant I am about to calculate.) The uniform equilibrium is unstable at mean density $\bar{\rho}$ if for some k, $\mathbf{N}(\bar{\rho}, k^2)$ has an eigenvalue with negative real part. If $|\mathbf{N}(\bar{\rho}, k^2)| < 0$, the equilibrium is certainly unstable. After some tedious spadework, this leads to the following criterion for instability

$$-\sigma > \bar{\rho}(\mathbf{V}'(\bar{\mathbf{U}}))^\intercal(\mathbf{\Gamma} + \mathbf{D}k^2)^{-1}\mathbf{s} \tag{3.47}$$

$$= \bar{\rho} \sum_{i \in \{a,r\}} \frac{\mathbf{V}'_{U_i}(\bar{U}_i)s_i}{\gamma_i + D_i k^2} \tag{3.48}$$

$$= \bar{\rho}\left(\frac{\mathbf{V}'_{U_a}(\bar{U}_a)s_a}{\gamma_a + D_a k^2} + \frac{\mathbf{V}'_{U_r}(\bar{U}_r)s_r}{\gamma_r + D_r k^2} \right) \tag{3.49}$$

How does this work? Remember that $V'_{U_r} > 0$ because it is a repellent and $V'_{U_a} < 0$ because it is an attractant. Thus the two terms in (3.49) are opposite in sign. Also, $\gamma_r < \gamma_a$ and $D_r > D_a$, because the repellent is a longer-range signal than the attractant. Thus, at low k, if the relative magnitudes of $V'_{U_r}s_r$ and $V'_{U_a}s_a$ are appropriately adjusted (by evolution or the modeler), the sum in (3.49) is positive and the uniform equilibrium is stable to perturbations of small wavenumber = large scale. As k rises the $D_r k^2$ factor in the denominator of the repellent term makes the positive term small compared to the negative attractant term. The sum in parentheses can become negative, and if $\bar{\rho}$ is large enough, the right-hand-side drops below $-\sigma$, and

A. Attractant+repellent model, $d = 1$

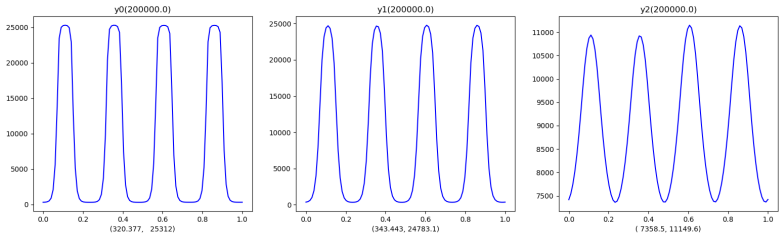

B. Attractant+repellent model, $d = 2$

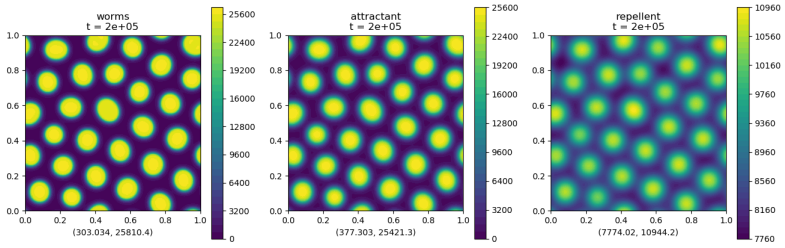

Figure 3.4: Attractant+repellent simulation
The left plot in each panel shows density ρ—the right plot shows attractant concentration U. The two numbers below the plot are the minimum and maximum values of the plotted function over the entire domain. Note the different scale of the attractant and repellent plots. The means are the same, but because repellent is a longer-range signal, it is smoothed much more by the convolution with density and varies less than attractant.

instability to perturbations of intermediate wavenumber = medium scale results. For large k the right-hand-side approaches zero because of the Dk^2 factors in the denominators. The uniform equilibrium is thus stable to perturbations of large wavenumber = small scale. It is therefore possible for an attractant-repellent Keller-Segel model to have a finite natural scale.

Based on calculations of this sort I chose $\beta_r = -\beta_a = -5.56 \times 10^{-4}\,\mathrm{cm^2 s^{-1}}$. Attractant parameters remained as in Table 3.1. The addition of a repellent increases the threshold for instability, but the uniform equilibrium is still predicted to be unstable at $\bar{\rho} = 9000\,\mathrm{cm^{-}d}$.

As shown in Figure 3.4, addition of a repellent to the model produced the predicted effect. Aggregates formed with characteristic size and spacing approximately matching those seen in experiments on worms. There is even a hint of pattern formation, with the aggregates in an approximate hexagonal array. If there is a problem with the result, it is that the array is too per-

fect. More irregularity is seen in experiments with real animals.

3.6 Free and total energy

In order to evaluate the numerical solutions, I computed the free energy functional $\mathcal{F}(\rho(t), U(t))$ (2.191), (2.199) and total energy functional $\mathcal{T}(\rho(t))$ (2.206), (2.220) at each time point of each numerical solution above. Figure 3.5 shows plots corresponding to the solutions shown in Figure 3.3 and Figure 3.4. Ideally these energy functions would be strictly decreasing functions of time. This expectation might fail for three reasons. First, numerical solutions of the PDE system calculated with finite time steps on a finite element spatial mesh only approximate the true solutions of the PDEs. Second, as described in the previous chapter, free energy functionals for systems that include repellents (Figure 3.5C and D) can have positive time derivatives. Third, the diffusion term of the PDE is only approximated by the functional derivative of the free energy functional, and similarly the convolution term of the total energy derivative is only approximated by the the functional derivative of the total energy functional.

In fact, the energy functionals perform well. In the model without repellent (Figure 3.5A and B) both energy functionals appear to be strictly decreasing. More careful analysis of the numbers shows very small increases at some time steps. These increases can be ascribed to the discretization error in the numerical PDE solutions. (For instance, the increases become smaller when the time steps are reduced.)

The influence of the repellent, in contrast, is clear. At very early times ($t < 10\,\mathrm{s}$) free energy rises (Figure 3.5C, D), and analysis of the individual components of the free energy functional show that this is caused by the movement of repellent towards its equilibrium with the worms—as repellent becomes better aligned with the worms, the energy rises. Total energy also rises during these early times, but the rise is small, and is not visible in Figure 3.5C, D. However, in other solutions based on models with stronger repulsion, I have seen quite large increases in free energy and smaller but noticeable increases in total energy attributable to repellent at early times. These effects vanish as equilibrium is approached.

Also, because the free energy functional becomes the total energy functional when chemical signals approach equilibrium with the worms (Theorem 2.16), we expect that at late times the two functions should converge. This does indeed occur to the numerical precision of the calculations—in each plot, the two curves superimpose at late times.

The upshot of these computations is that, except at very early times ($t < 10\,\mathrm{s}$), the total energy functional appears to function as a near-perfect numerical Lyapunov functional.

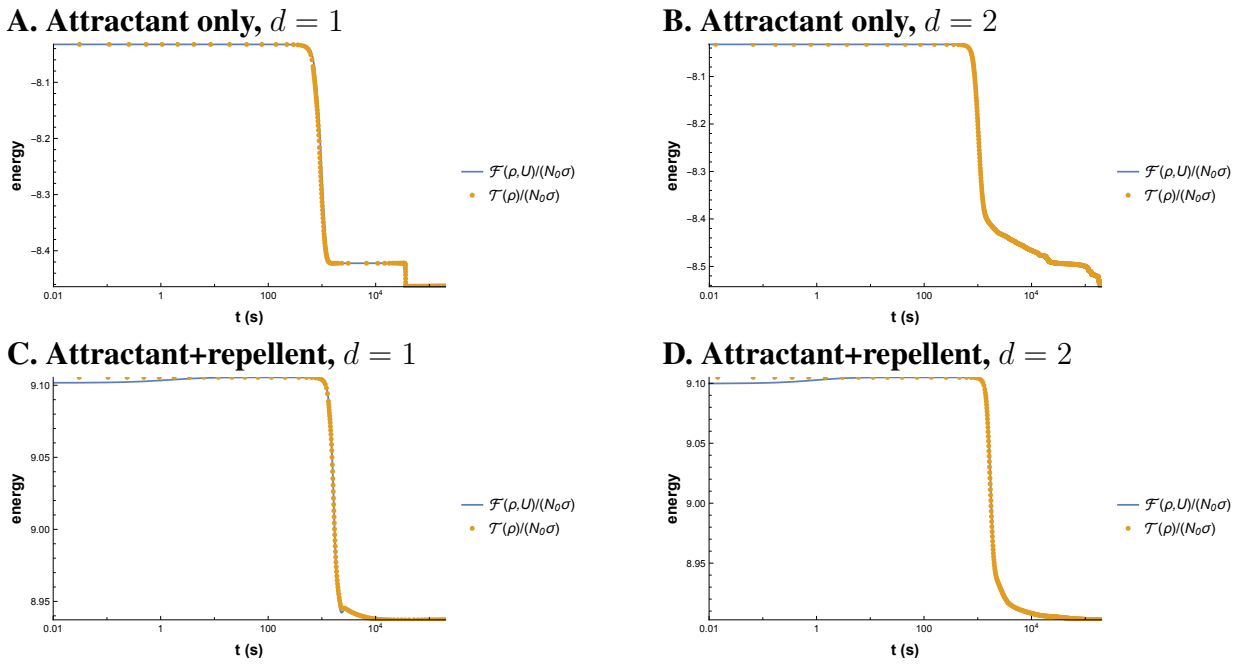

Figure 3.5: Free and total energy functionals
These plots show the free energy and total energy functionals as a function of time for one and two-dimensional attractant only and one- and two- dimensional attractant+ repellent models. They correspond to the solutions of Figures 3.3 A and B and 3.4 A and B.

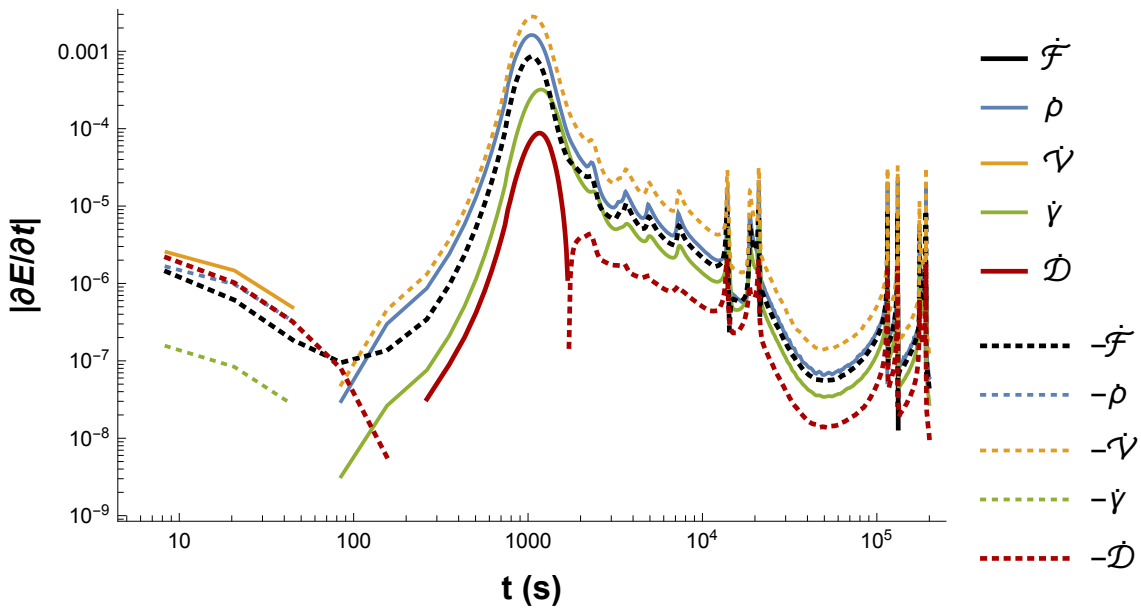

Figure 3.6: Components of the free energy functional
Absolute values of time derivatives of the free energy functional $\mathcal{F}$ (in black) and its component terms (in color) are plotted. These curves are for a two-dimensional attractant-only model (i.e. they correspond to Figure 3.5B). Each curve plots a term of the free energy functional (2.191), the integrands of which are listed below. Curves are plotted as solid where the time derivative is positive, dotted where it is negative.

label	**integrand**
ρ	$W_\rho(\rho) + \sigma\rho\log\rho$
$\mathcal{V}$	$\rho V_U(U)$
γ	$-\frac{\gamma}{s}(UV_U(U) - W_U(U))$
$\mathcal{D}$	$\frac{D}{s}\left(V_U(U) - \frac{W_U(U)}{U}\right)\nabla^2 U$
$\mathcal{F}$	$\rho + \mathcal{V} + \gamma + \mathcal{D}$

As a first step towards understanding the effects of the approximation of the diffusion term of the U PDE by a functional whose functional derivative is not correct, I decomposed the free energy functional into components derived from different terms of the PDEs and plotted their time derivatives in Figure 3.6. (This plot is based on the attractant-only model, so the energy-increasing effect of a repellent is absent.) I struggled (with scant success) to present this information in an informative way. Curves are plotted as dotted lines where the time derivative is negative, solid where positive, on a log scale to allow plots of all components over their wide ranges. The desired behavior is that $\dot{\mathscr{F}}(\rho, U)$ should always be negative, i.e., the black curve should be dotted over its entire length, and it is. The dominant terms of the free energy functional (both in terms of point values and time derivatives) are the ones labeled ρ and $\mathscr{V}$ in Figure 3.6. These measure the effects of the distribution of the worms and of their accumulation in places where attractant concentration is high. Two terms derive from the attractant itself: the plot labeled γ, which roughly measures the mean square of attractant concentration and the plot labeled $\mathscr{D}$ (in red), which measures how steeply the attractant concentration varies (in space). These terms are most easily understood by reference to the corresponding terms of the free energy functional for the minimal model (2.184), in which the γ term is proportional to U^2 and the $\mathscr{D}$ term to $\|\nabla U\|^2$. $\mathscr{D}$ is also the term to which the error $e_{\mathscr{F}}$ contributes. These signal-derived energy contributions make their maximum contribution to $\dot{\mathscr{F}}$ at around $1000\,\mathrm{s}$, the time when aggregates are forming. This is expected, as the attractant concentration becomes more varied and steeper as it follows the worms, whose distribution is also becoming more varied and steeper.

There is no evidence that the approximation errors $e_{\mathscr{F}}$, or $e_{\mathscr{T}}$—analysis not shown—detectably distort the performance of either the free energy or the total energy functional as a Lyapunov functional. As Figure 3.6 shows, $\dot{\mathscr{D}}$ is small compared to $\dot{\mathscr{F}}$, even when it is positive. Likewise, $\mathscr{D}$ is small compared to $\mathscr{F}$: the maximum value of $\mathscr{D}$ over the entire time course is 0.042, while $\mathscr{F}$ ranges between -8.54 and -8.03.

These results are encouraging as far as they go, but of course they are specific to the particular problem and parameter choices here analyzed, and may not generalize. In future, I plan to analyze more specifically how the error $e_{\mathscr{F}}$ contributes to the movement of $\mathscr{F}$ by computing the error contribution to the time-derivative of $\mathscr{F}$ as follows:

$$e_{\dot{\mathscr{F}}}(t) \coloneqq \langle \dot{U}, e_{\mathscr{F}} \rangle_{L^2} = \int_\Omega \dot{U}(t, \mathbf{x}) e_{\mathscr{F}}(t, \mathbf{x}) \mathrm{d}\mathbf{x} \tag{3.50}$$

It is obvious that this quantity approaches zero as the system approaches equilibrium, because $\dot{U} = 0$ at equilibrium. My hope, however, is that by computing the behavior of this quantity and the angle

$$\theta := \arccos\left(\frac{\langle \dot{U}, \boldsymbol{e}_{\mathcal{F}} \rangle_{L^2}}{\left\|\dot{U}\right\|_{L^2} \|\boldsymbol{e}_{\mathcal{F}}\|_{L^2}}\right), \tag{3.51}$$

for numerical solutions I will observe regularities that can be proved in general.

3.7 Cooldown and the animal crackers phenotype

In the movies of the attractant+repellent simulation, one sees formation of irregularly shaped aggregates at early times. These aggregates reminded me of an unpublished result of Alex Artyukhin's. Attempting to understand molecular mechanisms of L1 aggregation, Alex measured gene expression in starved L1s. He identified a gene, *srh-2*, whose activity increases at the time that starved L1s become capable of aggregation. *srh-2* is predicted to encode a sensory receptor, i.e., a protein expressed on the surface of a sensory neuron, capable of detecting chemicals in the environment. (Unfortunately, it is not possible from gene sequences alone to predict what chemicals it responds to.) To find out if *srh-2* places a role in L1 aggregation, Alex knocked the gene out. (That is, he genetically engineered a mutant strain that lacks a functional *srh-2* gene.) He then tested them for aggregation. As shown in Figure 3.7, these mutant worms still aggregate, but the aggregates remain irregular in shape. (Alex calls this the "animal crackers" phenotype.)

Watching movies of aggregating L1s, I had noticed that there is a lot of rapid movement at early times, but that as time goes on, fewer worms are seen moving. This suggested to me that worm movement might cool down with time, perhaps because the worms run low on energy. (They are, after all, starving.) When I saw that irregular aggregates form at early times in simulations, it suggested a hypothesis for the animal crackers *srh-2* phenotype—perhaps the movement of these mutant worms slows down faster. In the model, such a movement cooldown would be reflected in the decrease of the parameters σ (representing random worm movement) and β_a, β_r (representing signal- responsive movement) with time. I therefore added model parameters to the differential equation model as additional degrees of freedom.

When the attractant+repellent simulation is run with cooldown (i.e., with σ, β_a, and β_r decaying exponentially with time constant $1000\,\mathrm{s}$), the result was indeed the formation of persistent irregular aggregates (Figure 3.8).

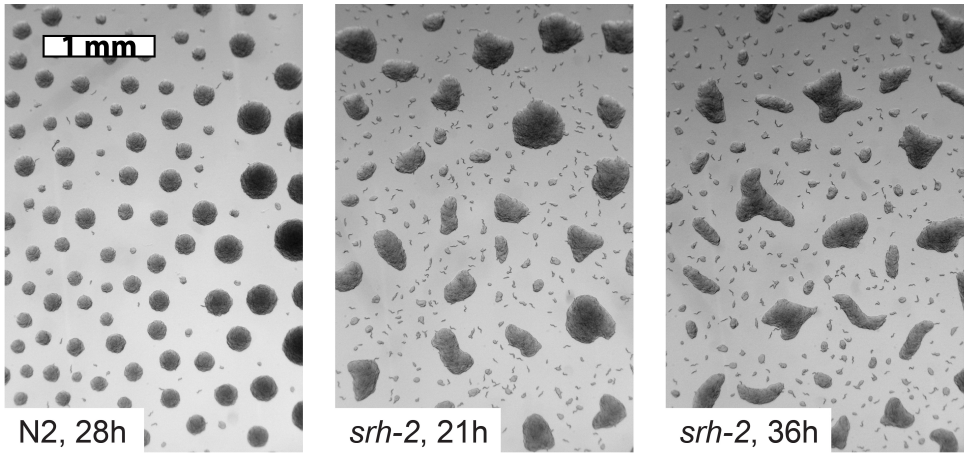

Figure 3.7: *srh-2* mutants form irregular aggregates
Starved L1s of mutant worms lacking a functional *srh-2* gene aggregate, but the aggregates they form are irregularly shaped. Alex Artyukhin calls this the "animal crackers" phenotype.

3.8 Convergence tests

To test whether the numerical solution of the worm system PDEs (2.3, 2.1) approximates the correct solution, I compared a numerical solution of the one-dimensional attractant+repellent system (Figure 3.4A) to an analytical solution of the linearized PDE system (3.37).

$$\rho_{\text{lin}}(t,x) = \bar{\rho} + a_\rho e^{\lambda t}\sin(\phi + 2\pi k_0 x) \tag{3.52}$$

$$U_{a,\text{lin}}(t,x) = \frac{s_a}{\gamma_a}\bar{\rho} + a_\rho U_{ak_0} e^{\lambda t}\sin(\phi + 2\pi k_0 x) \tag{3.53}$$

$$U_{r,\text{lin}}(t,x) = \frac{s_r}{\gamma_r}\bar{\rho} + r_\rho U_{rk_0} e^{\lambda t}\sin(\phi + 2\pi k_0 x) \tag{3.54}$$

Here $a_\rho, \phi \in \mathbb{R}$ and $k_0 \in \mathbb{Z}$ are parameters that can be freely chosen. I chose $\phi = \pi/2$ arbitrarily and chose $k_0 = 4$ to match the solution shown in Figure 3.4A. The choice of a_ρ is discussed below. λ is the positive eigenvalue of matrix $-\mathbf{N}(\bar{\rho}, k_0^2)$ (3.41), with corresponding eigenvector $(1, U_{ak_0}, U_{rk_0})^\intercal$ (as in (3.38), but normalized so that $\rho_{k_0} = 1$). Numerical values $\lambda \approx 0.003\,97$, $U_{ak_0} \approx 0.685$, $U_{rk_0} \approx 0.0886$ were estimated to 15-digit precision by numerical diagonalization of the computed matrix $-\mathbf{N}(\bar{\rho}, k_0^2)$.

A. Cooldown model, $d = 1$

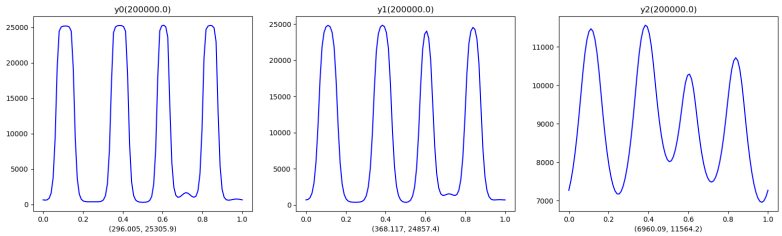

B. Cooldown model, $d = 2$

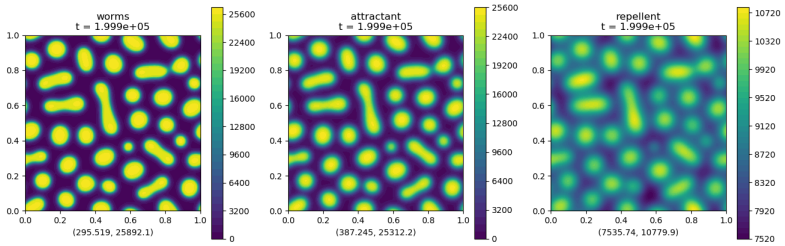

Figure 3.8: Cooldown simulation
The left plot in each panel shows density ρ—the right plot shows attractant concentration U. The two numbers below the plot are the minimum and maximum values of the plotted function over the entire domain. This simulation is identical to that of Figure 3.4, except that parameters σ, β_a, and β_r decay exponentially with time constant $1000\,\mathrm{s}$ from initial values used in the previous simulation.

Functions $(\rho_{\text{lin}}(t,x), U_{a,\text{lin}}(t,x), U_{r,\text{lin}}(t,x))^\intercal$ are of course not an exact solution of the full nonlinear PDEs (2.3, 2.1). To produce a closely related system with this exact solution for convergence testing, I modified the ρ PDE (2.3) by addition of a source term.

$$\dot{\rho} = \nabla \cdot (\rho \nabla (V_{U_a}(U_a) + V_{U_r}(U_r) + V_\rho(\rho) + \sigma \log \rho)) + S(t, \mathbf{x}) \tag{3.55}$$

$$\begin{aligned} S(t,x) = \frac{\partial \rho_{\text{lin}}(t,x)}{\partial t} - \frac{\partial}{\partial x}\big(\rho_{\text{lin}}(t,x) \frac{\partial}{\partial x} \\ \big(V_{U_a}(U_{a,\text{lin}}(t,x)) + V_{U_r}(U_{r,\text{lin}}(t,x)) \\ + V_\rho(\rho_{\text{lin}}(t,x)) \\ + \sigma \log \rho_{\text{lin}}(t,x)\big)\big) \end{aligned} \tag{3.56}$$

It is unnecessary to modify the U_a and U_r PDEs since they are linear. Source function (3.56) was computed symbolically from linear solutions (3.52-3.54) and converted to a 1520-character C++ expression with Mathematica (Wolfram Research 2019).

Two series of tests are shown. In the first (Table 3.2), the exponential growth of the sinusoidal variation was from amplitude 1 to 3897. Because of the large exponential growth, this test is particularly sensitive to small changes in the rate of exponential growth. That is, if numerical error leads to growth at a rate different from λ, the final error could be large and depend exponentially on numerical error. In the second series (Table 3.3), growth was from an amplitude of 1000 to 3568. Over this smaller range, strong exponential dependence on numerical error would not be expected. In fact, error trends in the two series are similar (although the errors are smaller in the second series, as expected), suggesting that the exponential growth rate of the numerical solution was close to λ.

In both series, error was close to its minimum at $\Delta t = 4\,\text{s}$ and $\Delta x = 1/128\,\text{cm}$, and improved little with smaller steps or a finer spatial grid. This suggests that at these levels error results from the limited precision of floating point calculations, not from the discrete approximation of the PDEs.

3.9 Summary

I have developed methods for the numerical solution of the worm PDE system (2.1,2.3) and an expanded version of the model that includes a repellent signal in addition to the attractant. This exercise was successful in the limited sense that the simulations produce results that, by a

time step size series				
	$\|error\|$ (cm^{-1})		convergence rate	
Δt (s)	L^2	L^∞	L^2	L^∞
2	0.0123	0.0303	−0.07	−0.001
4	0.0117	0.0302	0.65	0.47
8	0.0183	0.0418	2.39	2.28
16	0.0963	0.0203	3.26	3.25
32	0.924	1.944		

spatial element size series				
	$\|error\|$ (cm^{-1})		convergence rate	
Δx (cm)	L^2	L^∞	L^2	L^∞
1/256	0.0114	0.0259	0.11	0.23
1/128	0.0123	0.0303	2.38	2.43
1/64	0.0640	0.163	3.71	3.83
1/32	0.838	2.311		

Table 3.2: Convergence test results, growth from amplitude 1 to 3897
For these series, a_ρ, the starting amplitude of the sinusoid, was set to 1, and the numerical solution was run from $t = 0$ to $t = 2080$, at which point the amplitude was $e^{2080\lambda} \approx 3897$. The first table shows the results of varying the time step size from 2 to 32 s (with a fixed spatial element size of $1/128\,\mathrm{cm}$) and the second the result of varying the spatial element size from $1/256$ to $1/32$ cm (with a fixed time step of 2 s). The error in ρ at the final time point was calculated at the difference between the numerical solution result and exact result (3.52). L^2 and L^∞ norms of the error are tabulated. Convergence rate is calculated between consecutive rows as $\log(\|\text{error}_1\|/\|\text{error}_2\|)/\log(h_1/h_2)$, with h being either Δt or Δx, as appropriate. The mean of ρ was $9000\,\mathrm{cm}^{-1}$ in all cases. Thus the relative error is about $1/9000$ times the error shown—e.g. $0.0123/9000 \approx 1.4 \times 10^{-6}$ for $\Delta t = 2\,\mathrm{s}$, $\Delta x = 1/128$ cm. Errors in U_a and U_r (not shown) were smaller but otherwise behaved similarly. All numerical solutions used the PETSc Rosenbrock-W solver `ra34pw2` (nominally an order 3 method), and a degree 3 spatial representation.

time step size series				
	$\|error\|$ (cm^{-1})		convergence rate	
Δt (s)	L^2	L^∞	L^2	L^∞
2	0.005 28	0.0128	−0.03	−0.26
4	0.005 16	0.0107	1.54	1.40
8	0.0150	0.0281	2.24	2.15
16	0.0708	0.125	1.92	1.94
32	0.268	0.479		

spatial element size series				
	$\|error\|$ (cm^{-1})		convergence rate	
Δx (cm)	L^2	L^∞	L^2	L^∞
1/256	0.003 62	0.009 34	0.55	0.46
1/128	0.005 28	0.0128	3.40	3.54
1/64	0.0559	0.149	3.74	3.78
1/32	0.748	2.048		

Table 3.3: Convergence test results, growth from amplitude 1000 to 3568
For these series, a_ρ, the starting amplitude of the sinusoid, was set to 1000, and the numerical solution was run from $t = 0$ to $t = 320$ s, at which point the amplitude was $e^{320\lambda} \approx 3568$. All else is as in Table 3.2.

subjective visual evaluation, resemble the behavior of the animals they are meant to represent. With 11 only weakly constrained biologically meaningful parameters in the final model, this result is perhaps not surprising.

In fact, I believe the most encouraging result of this chapter is a failure. I was not able to achieve a tolerable match of model predictions to experimental results with the attractant-only model (the closest thing to the classic Keller-Segel model tried). This failure suggests that, in addition to the attractive force suggested by the worms coming together, there is some sort of repulsive force. Of course, neither of these forces need take the form of an unstable, diffusible chemical signal. That is only a simple mechanism made plausible by what we know of *C elegans* biology.

Further work is necessary to systematically evaluate how well model results match experiment (Chapter 4) and to explore how tightly constrained the model is by experimental results (Chapter 5).

Chapter 4

Morphological analysis

Near the end of chapter 3, I alluded to the need for more objective methods of comparing the results of PDE solutions to the observed behavior of aggregating worms. For this purpose I adopted Fourier analysis and the mathematical morphology toolkit (Serra 1982). These are independent methods of comparing experimental results to PDE solutions.

4.1 Fourier analysis to measure spatial patterning

At late times, the aggregates that form in PDE solutions of the attractant- repellent model (Figure 3.4) are regularly arranged. One can also perceive a much less convincing hint of regularity in experimental images. Fourier transforms are a way to measure such patterning.

Figure 4.1 shows such an analysis of the final time point of a solution of the attractant+repellent model. It is of course perfectly periodic on the $0.5\,\mathrm{cm} \times 0.5\,\mathrm{cm}$ domain, because it was solved with periodic boundary conditions. But an approximate hexagonal symmetry is also evident. (Exact hexagonal symmetry is impossible on a square domain with periodic boundary conditions.) The power spectrum vividly confirms that the arrangement is regular. At low wavenumbers all the power is in discrete regularly arranged points. The points at $\mathbf{k} = (13, 6) \times 4\pi$ and $\mathbf{k} = (7, 14) \times 4\pi$ are diagnostic of approximate hexagonal symmetry—the angle between these two wavenumber vectors $\tan^{-1}(14/7) - \tan^{-1}(6/13)$ is 38°—for perfect hexagonal symmetry the angle would be 30°. All the other spots are at integer linear combinations of these two generator wavenumber vectors.

Since there was no imposition of periodicity on the experimental aggregates, no such perfect regularity is to be expected. I hoped to see what is known in X-ray crystallography as a pow-

A. Original image

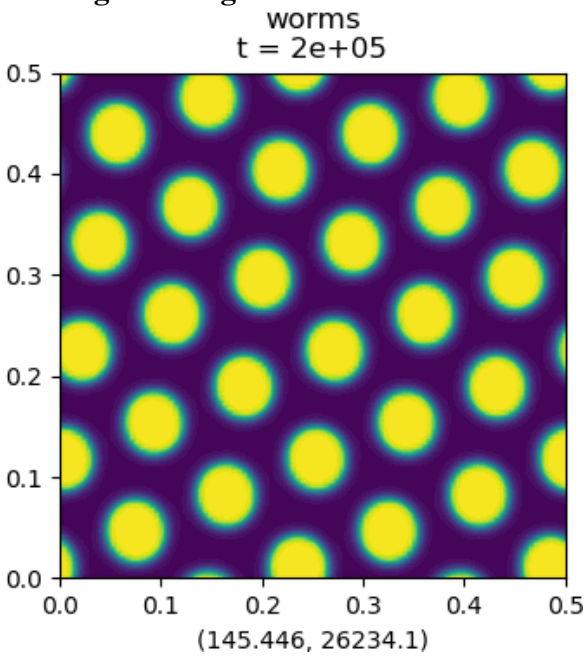

B. Power spectrum

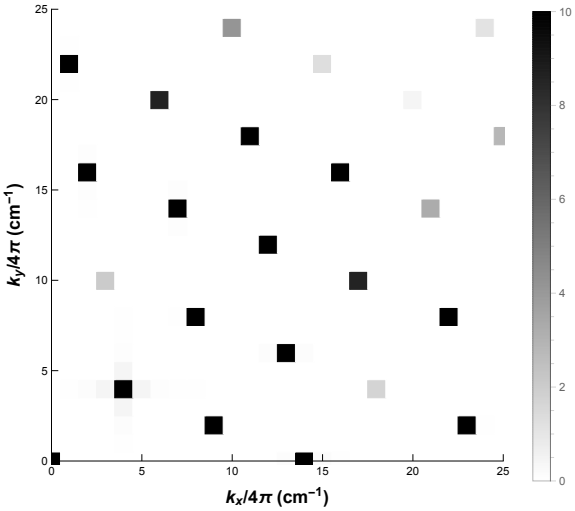

Figure 4.1: Fourier analysis of simulation results

A. Image of density from a solution of the attractant+repellent model. Parameters as in Figure 3.4, except for $\beta_a = 0.0011\,\mathrm{cm^2 s^{-1}}$, $\beta_r = -0.0094\,\mathrm{cm^2 s^{-1}}$. This solution was carried out on an $0.5\,\mathrm{cm}$ square for better resolution. **B** Low wavenumber region of the power spectrum of the image in A. (Densities were normalized to extend up to 1.0 before computing the power spectrum, for better comparison to the power spectra of Figure 4.2.) This image shows the region extending from 0 wavenumber up to $25 \times 4\pi$, i.e. waves whose wavelength is $1/25$ the $0.5\,\mathrm{cm}$ width of the domain.

der diffraction pattern. When a collimated X-ray beam is sent through a crystal, the X-rays are scattered by the electrons. The result is a pattern that is the Fourier transform of the electron density. Since a crystal is a near-perfect periodic array of molecules, the result is a pattern of spots (each called a reflection in the jargon of crystallography) very like Figure 4.1B. Suppose, instead of sending the X-ray beam through a single crystal, you aim it at a box of powdered sugar. Each particle of sugar is a crystal and diffracts the beam into spots. But because the crystals in the powder are in all possible orientations, each reflection gives rise to a ring of X-ray intensity. This pattern of rings is called a powder diffraction pattern.

Figure 4.2 shows that an experimental image does indeed produce a powder diffraction pattern. Two rings are evident in Figure 4.2B, a sharp one at $k = 8 \times 2\pi$ and a more diffuse one around $k = 20 \times 2\pi$. Do these features in fact arise from the aggregates? There is a simple way to test. I filtered the spectrum by setting the amplitudes at all wavenumbers outside $[6 \times 2\pi, 30 \times 2\pi]$ to 0 (Figure 4.2C), then inverted the Fourier transform to produce a filtered image arising only from the two rings. The result, Figure 4.2D, shows that the rings do indeed arise from the pattern of aggregates. Further filtering shows that the ring at $20 \times 2\pi$ arises from the patterning of individual aggregates, while that at $8 \times 2\pi/8$ arises from a series of concentric rings of aggregates surrounding the central blob.

I have not yet attempted to fit the diffraction pattern to a hexagonal symmetry pattern.

4.2 Morphological analysis of PDE solutions and experimental results

Mathematical morphology provides algorithms for identifying objects in an image (segmentation) and quantifying their characteristics. I used Mathematica's (Wolfram Research 2019) implementation of the mathematical morphology toolkit.

4.2.1 Segmentation and measurement

Figure 4.3 shows how aggregates were identified in video images. First, the image was binarized (i.e., each pixel was assigned a value 0—bright—or 1—dark) by comparing its brightness to the median brightness over all pixels. Next, connected components were identified. A connected component is a maximal set of dark pixels each of which is adjacent to at least one other dark pixel in the same component. (Pixels at $\mathbf{x}$, $\mathbf{y}$ are considered adjacent if $\|\mathbf{x} - \mathbf{y}\|_\infty \leq 1$ in pixel coordinates.) This step is particularly straightforward (both for the experimental images

A. Original image

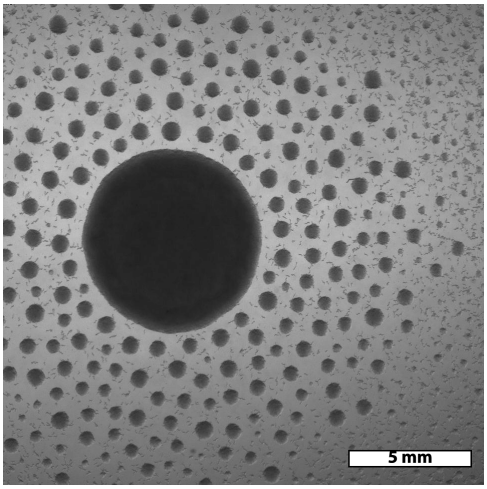

B. Power spectrum

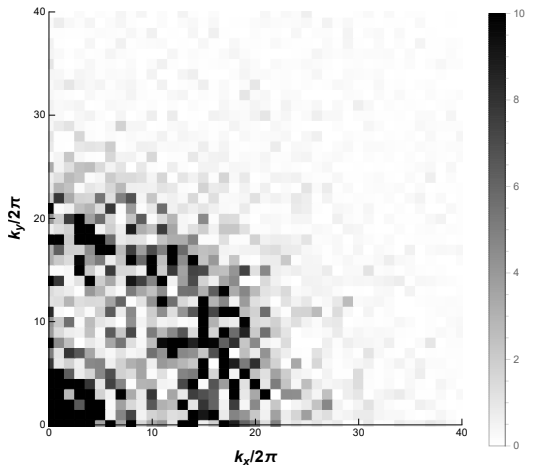

C. Filtered spectrum, $5 \leq 2\pi/k \leq 30$

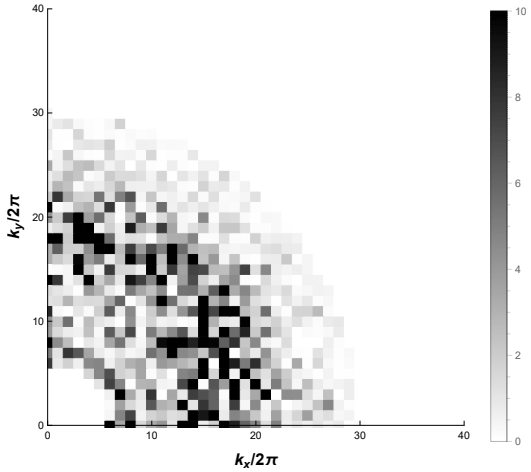

D. Filtered image, $6 \times 2\pi \leq k \leq 30 \times 2\pi$

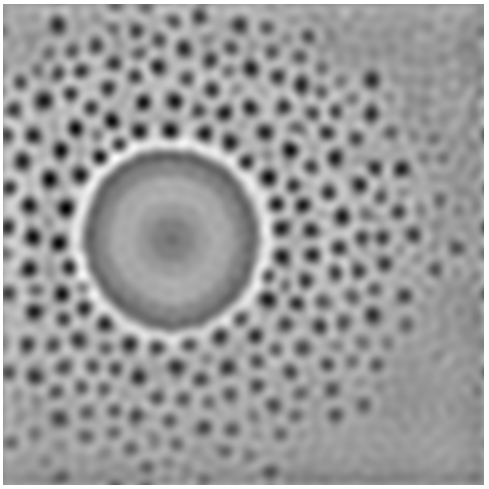

Figure 4.2: Fourier analysis of experimental results
A. Image at $719\,\mathrm{min}$ from a video recording of aggregating worms. **B** Low wavenumber region of the power spectrum of the image in A. This image shows the region extending from 0 wavenumber up to $40 \times 2\pi$ (in units of the inverse width of the image), i.e. waves whose wavelength is $1/40$ the width of the image. In this image and in C, power has been artificially truncated at 10 arbitrary units. **C.** Spectrum in B filtered by setting the amplitudes of all wavenumbers not between $6 \times 2\pi$ and $30 \times 2\pi$ to 0. **D.** Inverse Fourier transform of the amplitudes whose power spectrum is shown in C.

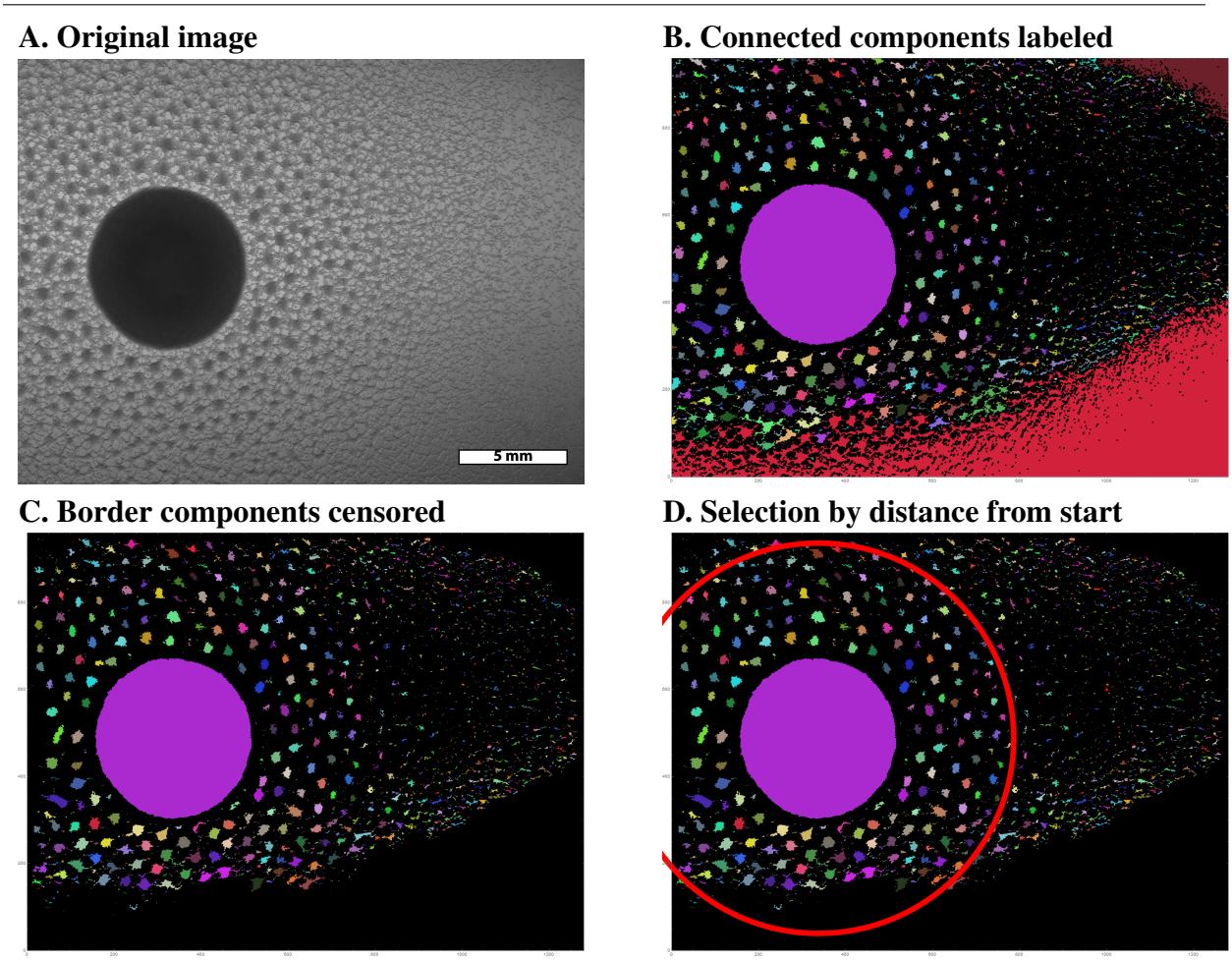

Figure 4.3: Image segmentation
A. Image from a video recording of 5×10^5 aggregating L1s after $100\,\mathrm{min}$. Starved L1s were concentrated and pipetted onto an agar surface in a $6\,\mathrm{cm}$ diameter petri plate. The worms initially disperse, producing a convenient gradient of density. The large circular spot in the center is where the worms were initially placed, and where the density remains above the maximum. **B.** The image in A was binarized by selecting those pixels darker than the median brightness and connected components identified. A unique color was assigned to each component. **C.** Every component that touches the edge of the original image is deleted. **D.** Those components within a acceptable radius (determined by the distance from the center of the start spot to the top or bottom edge) of the start spot are selected for further analysis.

and PDE solutions) because the density rapidly evolves to a near binary distribution, in which the density at every point is either maximal or low. (The pronounced bimodality of the density distribution is the focus of chapter 5.) Figure 4.3A shows an image from an early time in the recording, before the density had become convincingly binary—nevertheless it is straightforward to segment. Furthermore, the aggregates that form are in almost every case simply connected—no holes. After identifying connected components I eliminate the following: (1) components at the edges of the image, since their shapes are not completely known, (2) components that are further from the start point than the nearest horizontal edge (to remove a large number of irregular small structures at low density), (3) very small structures (in order not to count individual worms), and (4) the large structure in the center.

The segmentation of density functions from PDE solutions was slightly different. First, the 1×1 periodic domain on which the solution was computed was extended to a 3×3 area by replication. The image was binarized into high and low-density by comparison with a threshold determined by Ostu's method (Otsu 1979) and connected high-density components identified. Finally only components whose centroids were within the central square of the 3×3 area were kept.

I selected four experimental images (taken at times 100, 200, 500, and 719 min after the beginning of the aggregation experiment) and nine images from a PDE solution (times 500, 1,000, 2,000, 5,000, 10,000, 20,000, 50,000, 100,000, and 200,000 s).

After identifying components in these 13 images, their properties were measured with the Mathematica function `ComponentMeasurements`. This function produces a dataset listing, for each aggregate, 83 properties. Examples of properties are `Centroid`, "center of mass coordinates", `Circularity`, "ratio of equivalent disk perimeter to the perimeter length", `Holes`, "number of holes in each component", and `Shape`, "shape of the component given as a binary image". (Quotes are from documentation of the Mathematica function `ComponentMeasurements`.) For the following analysis I discarded all but scalar properties, i.e., I kept only those properties whose value is a single number. Thus, `Centroid` and `Shape` were discarded at this step, leaving me with 61 properties. I then discarded properties that didn't vary. For instance, `Holes` was discarded at this stage because it was 0 for all aggregates. This left me with 48 measurements of each aggregate.

4.3 Dimensional reduction and comparison

Many of these 48 measurements were highly correlated with others. I therefore turned to dimensional reduction. I began by clustering the properties with the mean-shift algorithm (Cheng

`Count`	number of pixels (area)
`BoundingDiskCoverage`	coverage of bounding disk area by the component area
`CaliperElongation`	$1 -$ (caliper width/caliper height)
`Circularity`	ratio of equivalent disk perimeter to the perimeter length
`Elongation`	elongation, computed as $1 -$ width/height
`MinCentroidDistance`	minimum distance of all pixels from the centroid

Table 4.1: Aggregate shape properties

and Cheng 1995), using as distance measure $1 - |r_s|$, where r_s is the Spearman rank correlation coefficient. The Spearman rank correlation coefficient is an ordinary correlation coefficient, except that is is computed not on the property values themselves, but on their ranks (i.e., their positions after sorting into an ordered list). Rank correlation r_s therefore ranges from -1 to 1. The value 1 means that the two properties are in exactly the same order, and -1 that they are in exactly opposite order. Thus $|r_s|$ ranges from 0 to 1, with the value 1 indicating a perfectly monotonic (either increasing or decreasing) relationship.

This procedure grouped the 48 properties into 11 clusters (Figure 4.4). All of these clusters were easily interpretable. For instance, the largest cluster, comprising 24 properties, contained properties that in effect measure the size of the aggregate. Four clusters contained properties concerned with the statistics of the signal values (i.e., darkness for experimental data, ρ for simulations) within the aggregate. Since the contrast mechanism for experimental data and simulation images are not easily related, I discarded these four clusters. I also discarded `Orientation`. That left me with six clusters. I chose one representative property from each cluster (Table 4.1). (Although there are more sophisticated dimensional reduction techniques than simply choosing a subset, I elected this method because it leaves one with measurements whose meanings are clear.)

4.3.1 Multidimensional scaling

Six is still an inconveniently large number for easy visualization. I therefore resorted to Multidimensional Scaling (MDS) to visualize the relationships of the 13 images. MDS works as follows: one defines a measure that quantifies how far each of the 13 images is from each of the others. The images are then embedded in a low (two, in this case) dimensional space such that their 2 or 3-space distances from each other match as closely as possible the distance measure. *Measure* and *distance* are used loosely here. In general the distance measure need not be a proper metric: for instance, MDS can be used with measures that don't satisfy the triangle

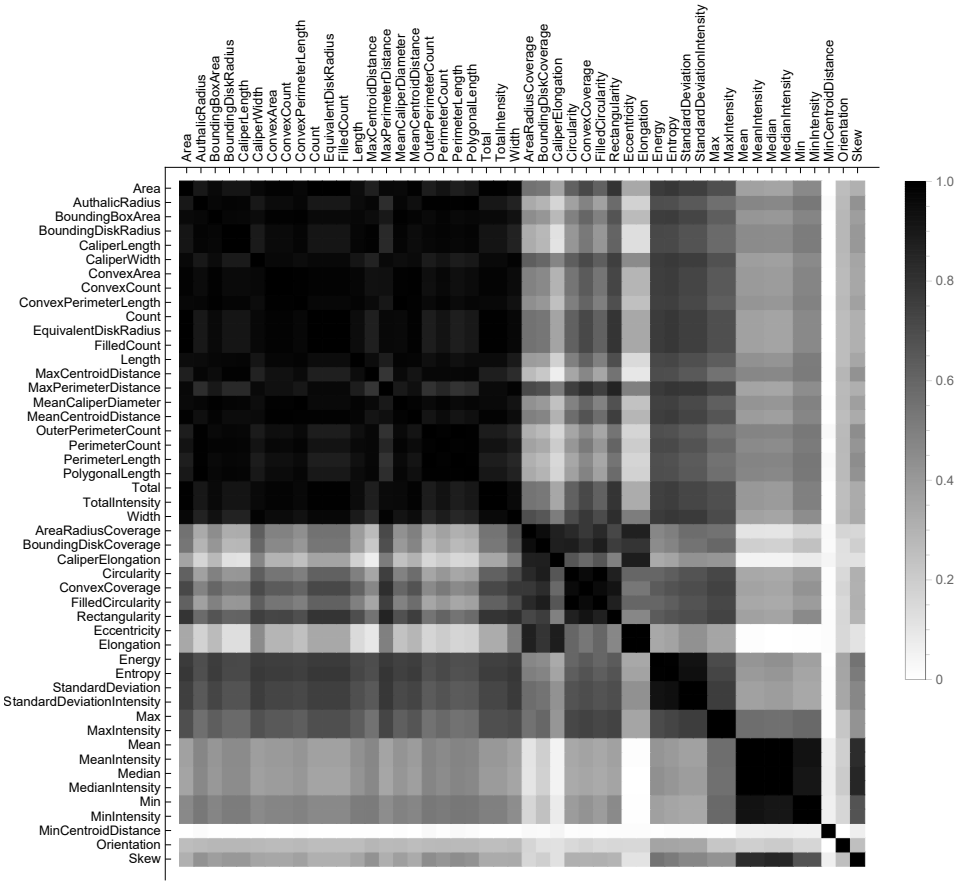

Figure 4.4: Properties clustered by rank correlation
Clusters of component properties. The darkness of each square indicates $|r_s|$ the absolute value of the Spearman rank correlation coefficient.

inequality. This is, in fact, the strength of the method: it is very flexible in how one defines a distance.

The distance measure to use requires some thought. We don't want to simply ask whether the aggregates in one image are individually like those in another. For instance, we would like to score an image in which the aggregates vary widely in `Circularity` as similar to another image in which aggregates vary widely in `Circularity`. That is, we want to consider two images similar when the *distribution* of a property is similar in one image to the distribution in the other. The Kolmogorov-Smirnov (KS) statistic $D_{ij} = \sup_x |F_i(x) - F_j(x)|$, where F_i is the Cumulative Distribution Function (CDF) of sample i, is a useful measure of the difference between two distributions. It ranges from 0 for identical distributions to 1 for distributions that do not overlap at all.

I rapidly found, however, that the Kolmogorov-Smirnov statistic didn't work well for comparing experimental data to simulation results. Figure 4.5A illustrates the problem. This compares the distribution of `Circularity` for the experimental image taken at $719\,\mathrm{min}$ and the $50\,000\,\mathrm{s}$ image from simulation. Superficially these images are similar—in both cases the worms have stabilized in a distribution in which most are found in circular aggregates, but a few are moving around between the aggregates. The `Circularity` distributions, however, do not overlap at all, and the KS Statistic is 1, indicating that the two images are, for this property, as far apart as possible.

This result is easy to understand. The aggregates in the simulation are almost perfectly circular. However, the aggregates in the experimental image are made of worms, large enough to be individually visible. In addition, because worms are still actively entering and leaving aggregates, some of the aggregates are imaged with part (or all) of a worm protruding from the edge, and this worm is counted as part of the aggregate. Neither of these facts is in conflict with the simulation results. In particular, the density of worms outside aggregates in the $50\,000\,\mathrm{s}$ image is about $200\,\mathrm{cm}^{-2}$, or 2 per square millimeter. Because in the simulations worms are approximated by a continuous density function, imperfections in aggregate shape are not represented.

A crude workaround for this problem is to assume a degree of imprecision for each measurement. The Kernel Density Function (KDF) is a convenient tool for this purpose. It is constructed essentially by replacing each observation with a distribution. Figure 4.5B compares KDFs constructed from the v719 and $50\,000\,\mathrm{s}$ images by convolving them with a normal distribution with standard deviation 0.1. The KS statistic for these two KDFs is 0.206, indicating a substantial but not huge difference between the images with regard to `Circularity`. I developed a computationally efficient method of approximating KS statistics between KDFs and used it to compute pairwise distances for each of the six properties for each pair of images.

Four of the six properties are dimensionless and can be directly compared between simula-

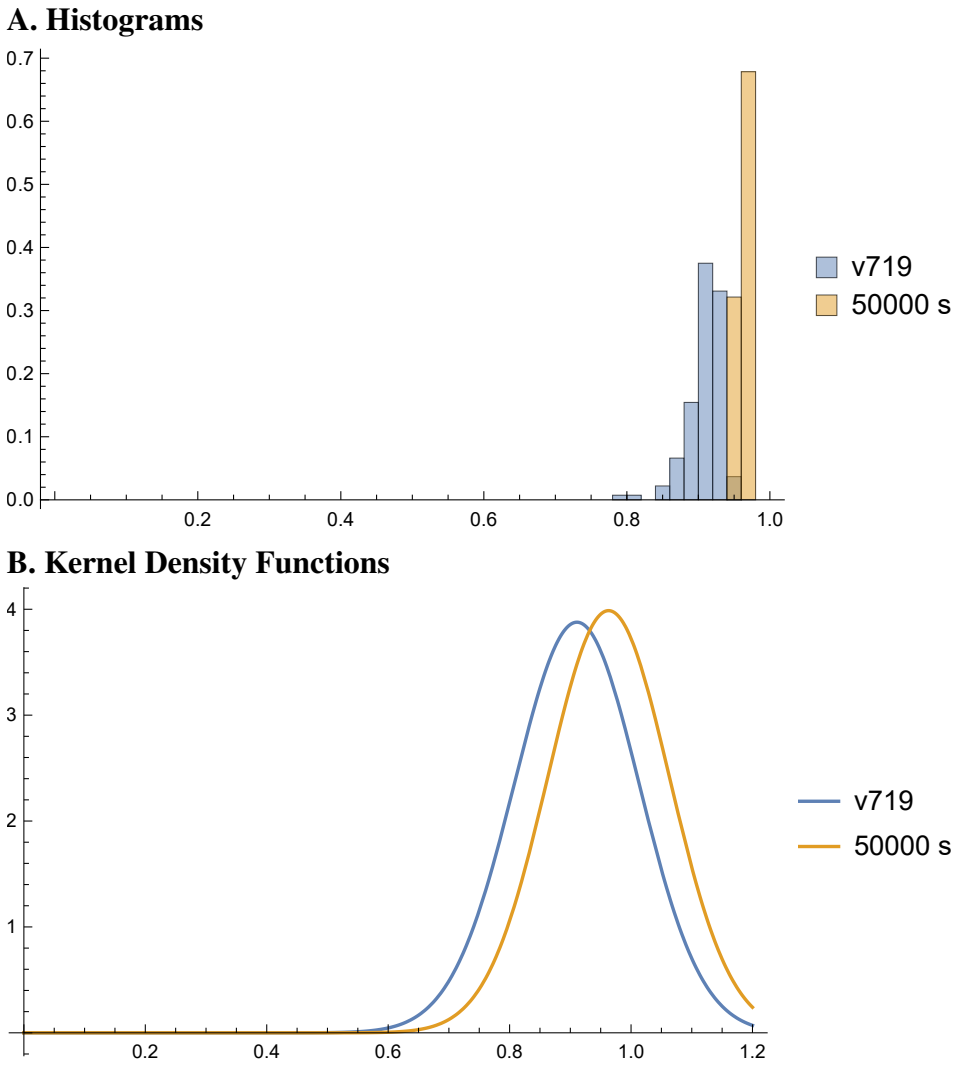

Figure 4.5: Comparison of `Circularity` distributions
Plots of the distribution of `Circularity` in the experimental image "v719" and the PDE solution image "50000 s". **A.** Histograms. Kolmogorov-Smirnov statistic 1. **B.** Kernel Density functions with a Gaussian of standard deviation $\sigma = 0.1$. Kolmogorov-Smirnov statistic 0.206.

tions and experimental images. The exceptions are `Count` and `MinCentroidDistance`. I normalized these by their medians before computing the KS statistic of the KDFs.

I used the python machine learning package `sklearn.manifold.MDS` to find nonmetric MDS embeddings in two dimensions of the images based on KDF KS statistics. Because MDS depends only on the distances between points in the embedding, any Euclidean transformation (i.e., translation, rotation, or reflection) of an embedding yields another embedding of equal quality. Since `sklearn.manifold.MDS.fit` initiates its search with random coordinates, the results are not reproducible from run to run. I therefore normalized embeddings by translating them so that the mean of all points was the origin, rotating the coordinate system so that the point representing image v100 was on the positive x-axis, and reflecting if necessary to make the y-coordinate of image v200 positive.

Figure 4.6 shows embeddings based on each of the six properties. Since the shapes of aggregates evolve in a generally consistent way with time, I hoped to see points within a series arranged roughly in order of time. Based on these results and other considerations, I narrowed the list of six properties (Table 4.1) to three, discarding `Count`, `CaliperElongation`, and `MinCentroidDistance`.

`Count` is the property that measures aggregate size. While this is clearly an important measurement, Figure 4.6A suggests it provides little useful information in this analysis. I believe that aggregate size is best addressed as a component of spatial patterning. That is, if you know the mean density of worms, the spacing of aggregates, and how they are arranged (e.g., hexagonal vs rectangular array), then the size of the aggregates is determined. I will show this calculation explicitly in chapter 5.

The `MinCentroidDistance` looks quite random. In retrospect, this is predictable from how it is calculated. `MinCentroidDistance` is the smallest distance from the centroid of an aggregate to one of the pixels within it. That is, it is basically the distance (in pixel coordinates) from the centroid to the nearest location in $\mathbb{Z}^2$. While this is a useful property for nonconvex shapes, in the context of *C elegans* L1 aggregation, it is essentially a random number.

`CaliperElongation` also looks very noisy. Furthermore, a close look at Figure 4.4 shows that it is highly correlated with `Eccentricity` and `Elongation`—this appears to be the highest intercluster correlation among the 48 properties. It is even a little puzzling that it was not clustered with `Eccentricity` and `Elongation`. I believe I can explain this. The aggregates in the simulation evolve towards near perfect circles at late times. `Elongation` and `CaliperElongation` are zero for a perfect circle. Thus in many of the images these properties have values very near zero, and a small change in the way elongation is measured can produce large relative change in these small numbers, degrading the rank correlation.

Figure 4.7 shows the MDS embedding based on `BoundingDiskCoverage`, `Elongation`,

A. Count

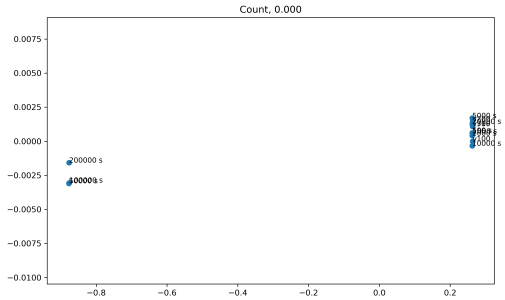

B. BoundingDiskCoverage

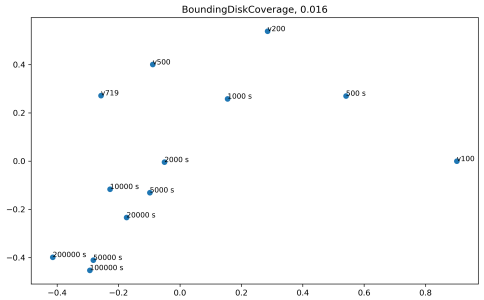

C. CaliperElongation

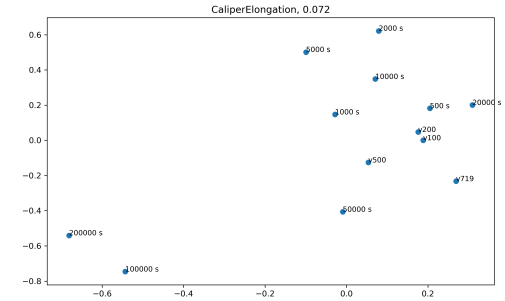

D. Circularity

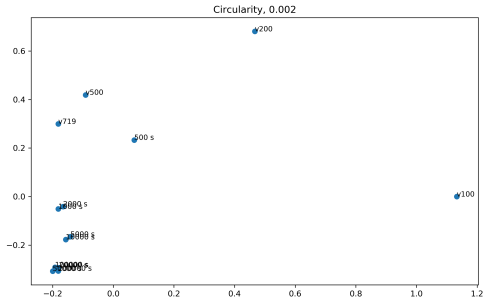

E. Elongation

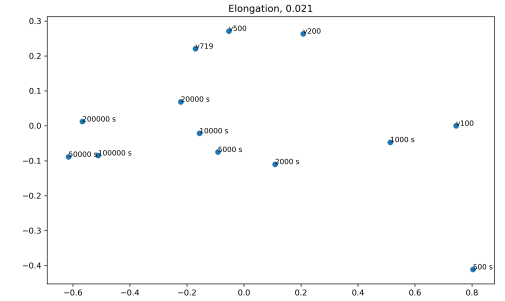

F. MinCentroidDistance

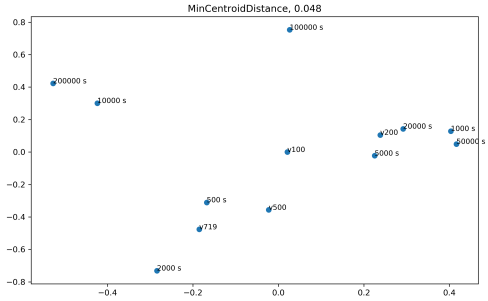

Figure 4.6: Image MDS based on single properties
MDS based on the distribution of the named property was used to place images in two dimensions. Each point represents one image. Those labeled v100, v200, v500, and v719 are experimental, those labeled 500 s – 200000 s are from a PDE solution. The number above each plot is the stress: a small number means that the distance measures are well matched.

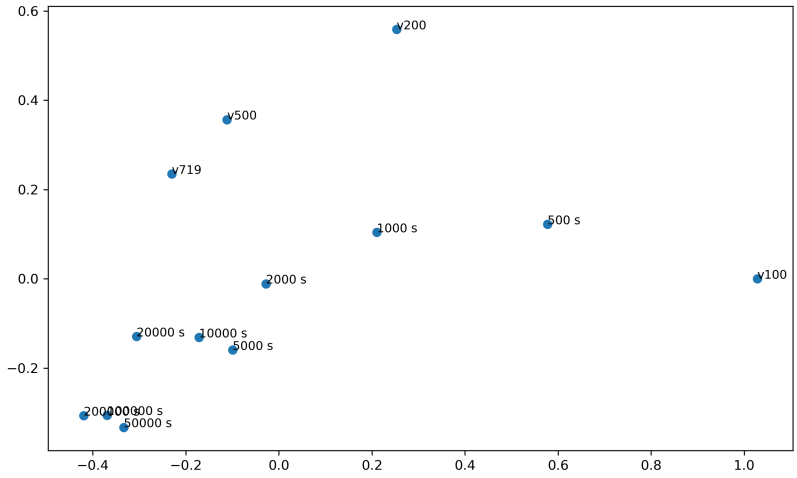

Figure 4.7: Image MDS based on `BoundingDiskCoverage`, `Elongation`, and `Circularity`

and `Circularity` collectively. More usefully, since three is a small enough number of properties to be visualized directly, Figure 4.8 shows scatter plots of all aggregates in all images, colored by the image of origin.

There is a general similarity between the evolution of aggregates in experimental data and in simulations. At early times aggregates are diverse, poorly circular, often elongated. As time passes, there is an evolution towards near-perfect circles. The aggregates in simulations are arranged close to a one-dimensional curve in 3-space. Experimental results are scattered below this curve.

This is not a once-and-done analysis. The choice of properties to characterize the aggregates was based on their correlations among 13 selected images: 9 from simulation and 4 from one experiment. We have more than 200 movies of *C elegans* L1 aggregation, of different genotypes, taken under varying conditions. There is no limit to the number of numerical simulations that can be done. It is to be expected that some of the correlations seen among characteristics in the 13 images analyzed above will be different in a broader dataset.

Although this analysis is a qualified success, the mismatch between experimental results and PDE solutions is unquestionably a problem, and to some degree a failure. The crucial question is whether it is a failure of the PDE model or of the morphological analysis. The first would be

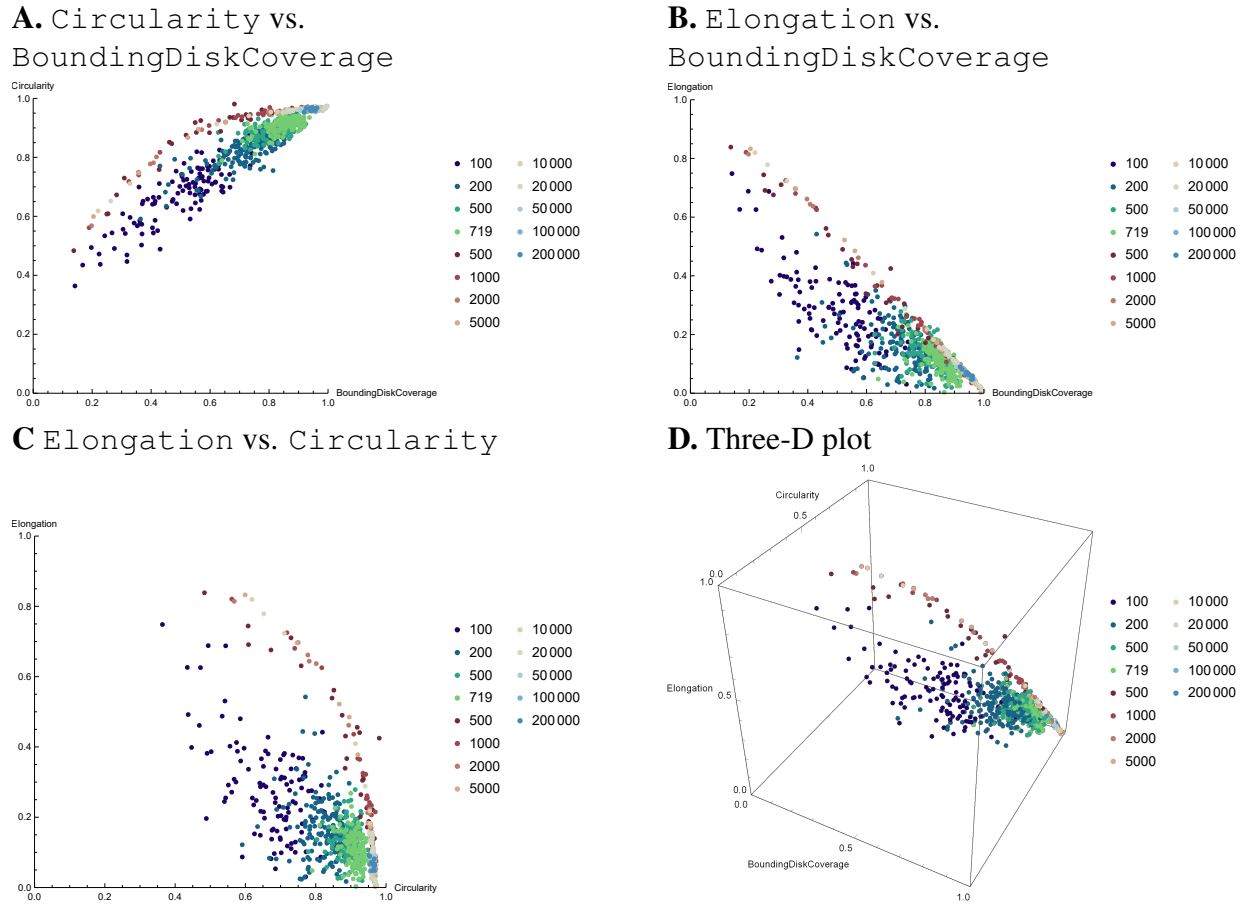

Figure 4.8: Scatter plots of three shape properties for all aggregates
Each aggregate is plotted as a single point, colored by the image of origin, and located according to the values of properties `BoundingDiskCoverage`, `Elongation`, and `Circularity`.

a very serious problem—the second merely an issue to be corrected. I am at present inclined to be optimistic on the question. I have already pointed out how modeling worms as a continuous density leads inevitably to discrepancies between experimental images and images from simulations. This is not an insuperable problem.

4.4 Summary

This chapters describes two independent methods of quantifying aggregate formation. Fourier analysis measures the spatial patterning of aggregates. Mathematical morphology measures the shapes of the aggregates. Eventually I hope to use them to fit models to experimental results.

Chapter 5

The binary density approximation

5.1 PDE solutions give density fields that are close to binary

In both experiments and simulation, worm density ρ rapidly evolves to an approximately binary function of space (Figure 5.1). By calling it a "binary function", I mean that ρ takes on only two values. For some $\mathbf{x} \in \Omega$, $\rho(\mathbf{x}) = \rho_{\text{max}}$, the density at which the animals are tightly packed. For other $\mathbf{x}$, $\rho(\mathbf{x}) = \rho_{\text{min}}$, a value much less than the close-packed density. (It is, of course, only approximately binary. Since ρ is a continuous function, at least when it is the solution of a PDE, it necessarily takes on all values between ρ_{min} and ρ_{max}.)

The rapid evolution of ρ to a binary state is easily documented for the PDE solutions (Figure 5.1B, D). Even after only $1\,\text{h}$, the distribution of pixel intensities in an image of ρ is obviously bimodal (Figure 5.1B). (The peaks of this histogram are $\rho_{\text{min}} \approx 200\,\text{cm}^{-2}$ and $\rho_{\text{max}} \approx 26\,000\,\text{cm}^{-2}$. I use these values in calculations below.) As a simple way of quantifying this evolution, I computed the Bimodality Coefficient (BC) (Pfister et al. 2013) as a function of time. The Bimodality Coefficient (5.1) is a crude measure of bimodality based on excess kurtosis m_4 (peakiness) and skewness m_3 of the distribution.

$$\text{BC} := \frac{m_3^2 + 1}{m_4 + 3 \cdot \frac{(n-1)^2}{(n-2)(n-3)}} \tag{5.1}$$

For a normal distribution, $\text{BC} = 1/3$—for a Bernoulli Distribution (the ideal binary distribution), it is 1. Thus one typically expects BC to take on values between $1/3$ and 1, with larger values indicating bimodality. For $t < 440\,\text{s}$, $\text{BC} \approx 1/3$ for the simulation results, as expected,

A. Experimental image histogram, t = 719 min

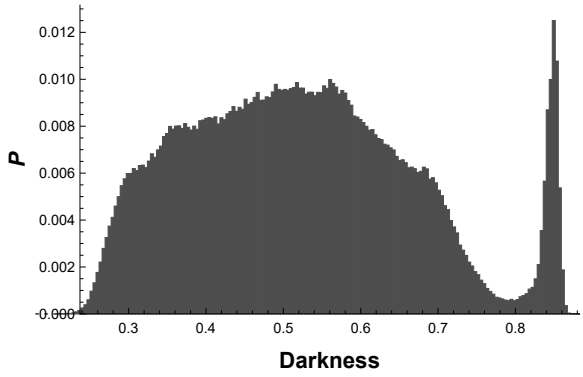

B. Simulation density histogram, t = 56 min

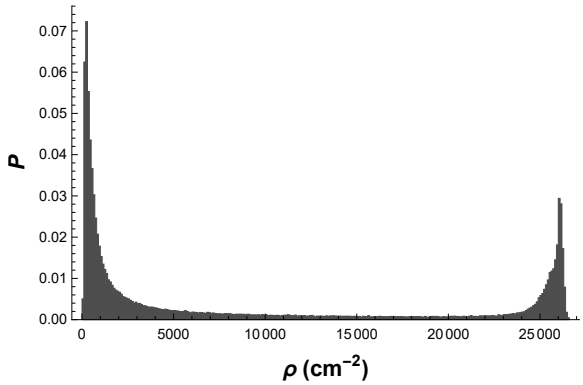

C. Experimental image, t =719 min

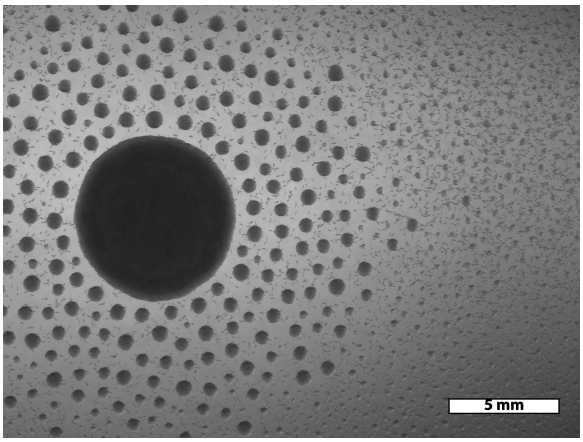

D. Bimodality Coefficient as a function of time

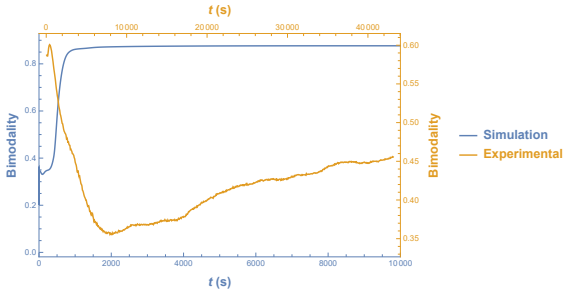

Figure 5.1: Worm density becomes bimodal
A. Histogram of pixel darkness in the experiment image taken after 719 min of aggregation. (The brightness axis is inverted, so that worm density increases to the right.) **B.** Histogram of ρ from a PDE solution at $t = 3347$ s. **C.** The experimental image at 719 min. (This is the image from which the histogram in A is derived. **D.** Bimodality coefficient as a function of time.

since the simulation was initiated with normally distributed random fluctuations. During the first $440\,\mathrm{s}$, the small initial fluctuations grow exponentially while V_ρ remains close to zero everywhere. Thereafter the distribution of densities abruptly becomes strikingly bimodal, and remains so for as long as the simulation continues.

In experiments density also evolves quickly toward a binary state. The best way to convince oneself of this is simply to look at the images (e.g. Figure 5.1C) and let the image-processing supercomputer in the occipital lobe of your brain process them. Measurements confirm the bimodality, but less dramatically than for PDE solutions. The histogram (Figure 5.1A) of the image in Figure 5.1C is clearly bimodal. The low density peak is broad because of uneven illumination of the field, and the bimodality coefficient is consequently 0.456, only modestly above $1/3$. (It is of course possible to correct the image for uneven illumination, but the more one massages the data to make the density distribution look bimodal, the less convincing the demonstration becomes.) Because the experiment is initiated by pipetting 5×10^5 worms onto the center of the agar surface, the density distribution is almost perfectly bimodal at time 0. The bimodality coefficient drops rapidly as the worms spread out, approaching $1/3$ at $136\,\mathrm{min}$. Thereafter worms outside the central blob come together in aggregates of maximal density and the bimodality coefficient grows modestly to its final value 0.456.

5.2 Plan for this chapter

In the rest of this chapter, I will take the observation that density is binary as an assumption and work out its consequences. That is, I will assume that ρ has the form

$$\rho(\mathbf{x}) = \rho_{\text{min}} + (\rho_{\text{max}} - \rho_{\text{min}})\mathbb{I}_{\mathscr{A}(t)}(\mathbf{x}), \tag{5.2}$$

Here $\mathscr{A}(t)$ is the set of points occupied by aggregates at time t and the indicator function $\mathbb{I}_{\mathscr{A}(t)}(\mathbf{x})$ is 1 for $\mathbf{x} \in \mathscr{A}(t)$, 0 elsewhere. I will assume $\mathscr{A}$ is as nice as convenient (i.e., a Borel set with piecewise smooth boundaries).

One consequence is immediate. The measure of $\mathscr{A}(t)$ is constant, Remember that the number of worms is constant, and consequently the mean density, $\bar{\rho}$, is also constant. Thus, the total number of worms is

$$\bar{\rho}|\Omega| = \rho_{\max}|\mathscr{A}(t)| + \rho_{\min}(|\Omega| - |\mathscr{A}(t)|) \tag{5.3}$$

$$|\mathscr{A}(t)| = \frac{\bar{\rho} - \rho_{\min}}{\rho_{\max} - \rho_{\min}}|\Omega| \tag{5.4}$$

$$a := \frac{|\mathscr{A}(t)|}{|\Omega|} = \frac{\bar{\rho} - \rho_{\min}}{\rho_{\max} - \rho_{\min}} \tag{5.5}$$

The proportion of the area occupied by aggregates is the constant a. Thus, for instance, with $\bar{\rho} = 9000\,\mathrm{cm}^{-\mathrm{d}}$, $\rho_{\max} = 26\,000\,\mathrm{cm}^{-\mathrm{d}}$, and $\rho_{\min} = 200\,\mathrm{cm}^{-\mathrm{d}}$, $a = 44/129 \approx 0.341$.

5.3 Equilibrium and Pattern formation

Figure 4.1 shows that at equilibrium a simulation produces aggregates with an approximate hexagonal pattern. Figure 4.2 suggests that some sort of patterning also takes place in experiments. How can such a pattern be explained? Can we do better than "That's the result the numerical solution produces"?

No linear stability analysis of the type described in chapters 1 and 3 can explain a preference for a hexagonal pattern over other patterns composed of waves of the same wavenumbers. That is in fact the burden of Appendix A of Keller and Segel (1970), "Further Discussion of Stability Theory". To quote (note: Keller and Segel's q corresponds to my k):

> According to linear analysis all perturbations having the same value of q will behave in exactly the same way, as will sums of such perturbations. For example, our linear analysis will not distinguish among perturbations proportional to
>
> $$\cos qx, \cos\left(½qx - ½\sqrt{3}qy\right) \text{ and } \cos\left(½qx + ½\sqrt{3}qy\right) \tag{A.1}$$
>
> According to our linearized analysis, however, any linear combination of two-dimensional waves like those in (A.1) is just as likely as to appear as a single two dimensional wave. Particularly relevant is the combination
>
> $$\cos ax + \cos\left(½qx - ½\sqrt{3}qy\right) + \cos\left(½qx + ½\sqrt{3}qy\right)$$
>
> which can be shown to give hexagonal symmetry, as in Fig. 3. Observations show regularly spaced "clouds" of relatively high density, as in Fig. 3, not "streaks" of

relatively high density as in Fig. 2. As mentioned, our linearized analysis cannot give reasons favoring either "streaks" or "clouds" or any other pattern made up of a superposition of "streaks".

It is certainly true that a hexagonal pattern can arise as a combination of sinusoidal density fluctuations. In particular, the sum of any two sinusoids of the same wavelength the angle between whose wavenumber vectors is $60°$ is a hexagonal pattern. However, in an isotropic system the stability of any sinusoid $e^{i\mathbf{k}\cdot\mathbf{x}}$ depends only on the magnitude $\|\mathbf{k}\|$ of the wavenumber. In a linear system, the stability of each sinusoid is independent of any others to which it is added. There is thus no mechanism that can prefer the angle $60°$ over, for instance $90°$, producing a rectangular array, or indeed an equal sum of all angles, producing a Bessel function.

The free energy functions developed in chapter 2 offer a possible approach to this question. In particular, the equilibrium density ρ_{eq} is, subject to two *caveats*, expected to be a minimum of the total energy functional (2.220). The two *caveats* are (1) $\mathcal{T}(\rho)$ is at best an approximate functional antiderivative, and is therefore not necessarily exactly stationary at equilibrium. (2) Because of the repellent, the time derivative of $\mathcal{T}(\rho)$ is not necessarily negative. Thus an equilibrium is not necessarily a minimum. However, a minimum, if one exists, is certainly a stationary point and therefore an equilibrium (ignoring point 1).

I will therefore proceed to search for binary functions $\rho(\mathbf{x})$ that minimize $\mathcal{T}(\rho)$. One simplification is immediate. $\mathcal{T}(\rho)$ is the integral of functions of $U_a = g_a * \rho$ and $U_r = g_r * \rho$ and a function of ρ: $W_\rho(\rho) + \sigma \log \rho$. The latter integral is constant:

$$\begin{aligned}\int_\Omega (W_\rho(\rho) + \sigma \log \rho)\mathrm{d}\mathbf{x} \\ = (a(W_\rho(\rho_{\text{max}}) + \sigma \log \rho_{\text{max}}) + (1-a)(W_\rho(\rho_{\text{min}}) + \sigma \log \rho_{\text{min}}))|\Omega|\end{aligned} \tag{5.6}$$

These terms can therefore be ignored in the minimization problem, leaving

$$\mathcal{T}_U(\rho) = \int_\Omega \left(\rho \frac{W_{U_a}(U_a)}{U_a} + \rho \frac{W_{U_r}}{U_r}\right)\mathrm{d}\mathbf{x} \tag{5.7}$$

as the quantity to be minimized. It is convenient to divide this quantity by the constant number of worms $N_0 = \int_\Omega \rho \mathrm{d}\mathbf{x}$ to define

$$\begin{aligned}\bar{T}_U(\rho) &= \frac{1}{N_0}\int_\Omega \rho \frac{W_{U_a}(U_a)}{U_a}\mathrm{d}\mathbf{x} + \frac{1}{N_0}\int_\Omega \rho \frac{W_{U_r}(U_r)}{U_r}\mathrm{d}\mathbf{x} \\ &= \bar{T}_a(U_a) + \bar{T}_r(U_r)\end{aligned} \tag{5.8}$$

$\bar{T}_a(U_a)$ is the mean value of $W_{U_a}(U_a)/U_a$ experienced by a worm, and likewise for $\bar{T}_r$. Using (2.11) it is convenient to define

$$T_U(U) \coloneqq \frac{W_U(U)}{U} \tag{5.9}$$

$$= \beta \frac{U + \alpha \log \alpha - (U + \alpha) \log(U + \alpha)}{U} \tag{5.10}$$

$$= \beta \left(1 - \log \alpha - \frac{\log(1 + U/\alpha)}{U/\alpha} - \log(1 + U/\alpha) \right) \tag{5.11}$$

Form (5.11) is convenient as it requires only a dimensionless form of the concentration, U/α, and the constant $\beta(1 - \log \alpha)$ can be ignored for minimization.

5.3.1 Optimization in one dimension

While there are an infinite number of possible periodic patterns in one dimension, symmetry suggests the optimum is likely to be an infinite series of equally sized, equally spaced mesas—i.e., a square wave. That is, $\rho(x)$ is periodic with period λ (a parameter to be optimized), with mesas of density ρ_{max} and width λa separated by lowlands of density ρ_{min} and width $\lambda(1 - a)$. To find the optimum wavelength λ, we calculate $\bar{T}_U$ as a function of λ and search for the minimum. I will show how to calculate $\bar{T}_U$ for a single signal, in particular an attractant with $\beta = 1$. $\bar{T}$ will depend on the ratio λ/κ, where κ is the range of the signal $\kappa = \sqrt{D/\gamma}$. In the following, I write $\bar{T}_U(\lambda/\kappa, a, U_{\text{max}}, r)$ to indicate the dependence on dimensionless parameters λ/κ and a, as well as $U_{\text{max}} = (\rho_{\text{max}} s/\gamma)/\alpha$ and $r = \rho_{\text{min}}/\rho_{\text{max}}$.)

Two limiting cases can easily be calculated: $\lambda/\kappa \to 0$ and $\lambda/\kappa \to \infty$. The first case represents a wavelength much shorter than the diffusion range of the signal. In this limit U approaches its mean everywhere: $U(x) = (a\rho_{\text{max}} + (1 - a)\rho_{\text{min}})s/\gamma$ for all x. Since U is constant, $T_U(U)$ is also constant and its mean is that constant:

$$\bar{T}_U(0, a, U_{\text{max}}, r) = T_U \left(\frac{a\rho_{\text{max}} + (1 - a)\rho_{\text{min}})s}{\gamma\alpha} \right) \tag{5.12}$$

$$= T_U \left(\frac{(a + (1 - a)r)\rho_{\text{max}} s}{\gamma\alpha} \right) \tag{5.13}$$

$$= T_U \left((a + (1 - a)r) U_{\text{max}} \right) \tag{5.14}$$

In the $\lambda/\kappa \to \infty$ limit, the signal has a very short diffusion range, so it is everywhere in local equilibrium with the worm density, $U(x) = \rho(x)s/\gamma$. Thus

$$\bar{T}_U(\infty, a, U_{\text{max}}, r) = aT_U(U_{\text{max}}) + (1-a)T_U(rU_{\text{max}}) \tag{5.15}$$

The trick, of course, is to evaluate $\bar{T}_U(\lambda/\kappa, a, U_{\text{max}}, r)$ for finite λ/κ. In the following demonstration I will use parameters based on the attractant in the PDE solution of Figure 5.1B,D, but (for this example) in only one dimension. In particular

$$\lambda/\kappa = 1\,\text{cm}/0.01\,\text{cm} = 100 \tag{5.16}$$
$$a = 44/129 \tag{5.17}$$
$$\rho_{\text{max}} = 26\,000\,\text{cm}^{-1} \tag{5.18}$$
$$\rho_{\text{min}} = 200\,\text{cm}^{-1} \tag{5.19}$$
$$U_{\text{max}} = \rho_{\text{max}}s/\gamma(1500\,\text{cm}^{-1}) = 52/3 \tag{5.20}$$
$$r = \rho_{\text{min}}/\rho_{\text{max}} = 1/130 \tag{5.21}$$

Now, to estimate $\bar{T}_U(100, 44/129, 52/3, 1/130)$ represent a $1\,\text{cm}$ wavelength by 512 points (Figure 5.2). We will set $\rho = \rho_{\text{max}}$ at 175 of these points and $\rho = \rho_{\text{min}}$ at the remaining 337. We will thus estimate $\bar{T}_U(100, \underline{175/512}, 52/3, 1/130)$. Note that $44/129 \approx 0.3411 < 0.3418 \approx 175/512$. To estimate the desired $\bar{T}_U(100, \underline{44/129}, 52/3, 1/130)$, we can estimate, for instance $\bar{T}_U(100, \underline{174/512}, 52/3, 1/130)$ and interpolate.

Now calculate $U = g * \rho$ by computing the Fast Fourier Transform (FFT) of ρ, multiplying by the Fourier coefficients (2.157) of the Green's function, then inverting the Fourier transform. Calculate $T_U(U/\alpha)$. (In plotting this example I dropped the $-\beta \log \alpha$ constant term, which has the convenient effect of making $T_U(0) = 0$.) Multiply by ρ, total the product, and divide by the total of ρ itself. The quotient estimates $\bar{T}_U(100, 175/512, 52/3, 1/130)$. Because $\rho_{\text{max}} \gg \rho_{\text{min}}$, this is very close to the mean of T_U in the central mesa where $\rho = \rho_{\text{max}}$, but there is also a small energy contribution from the low density plain. The estimate is $\bar{T}_U(100, 175/512, 52/3, 1/130) \approx -2.02122$. The long and short-range limiting values are $\bar{T}_U(0, 175/512, 52/3, 1/130) = -1.27161$, $\bar{T}_U(\infty, 175/512, 52/3, 1/130) = -2.04715$. The estimate for $\lambda/\kappa = 100$ is close to the limiting value for $\lambda/\kappa = \infty$, as expected, since this is a short-range signal and U closely follows ρ (Figure 5.2A). The small difference between -2.02 and -2.05 is because U is smaller than its maximum value $\rho_{\text{max}}s/\gamma$ just inside the boundary of the mesa. Consequently the energy is a little higher there. For a short-range signal, the energy cost of failure to perfectly follow ρ occurs at the boundary of the high-density mesa.

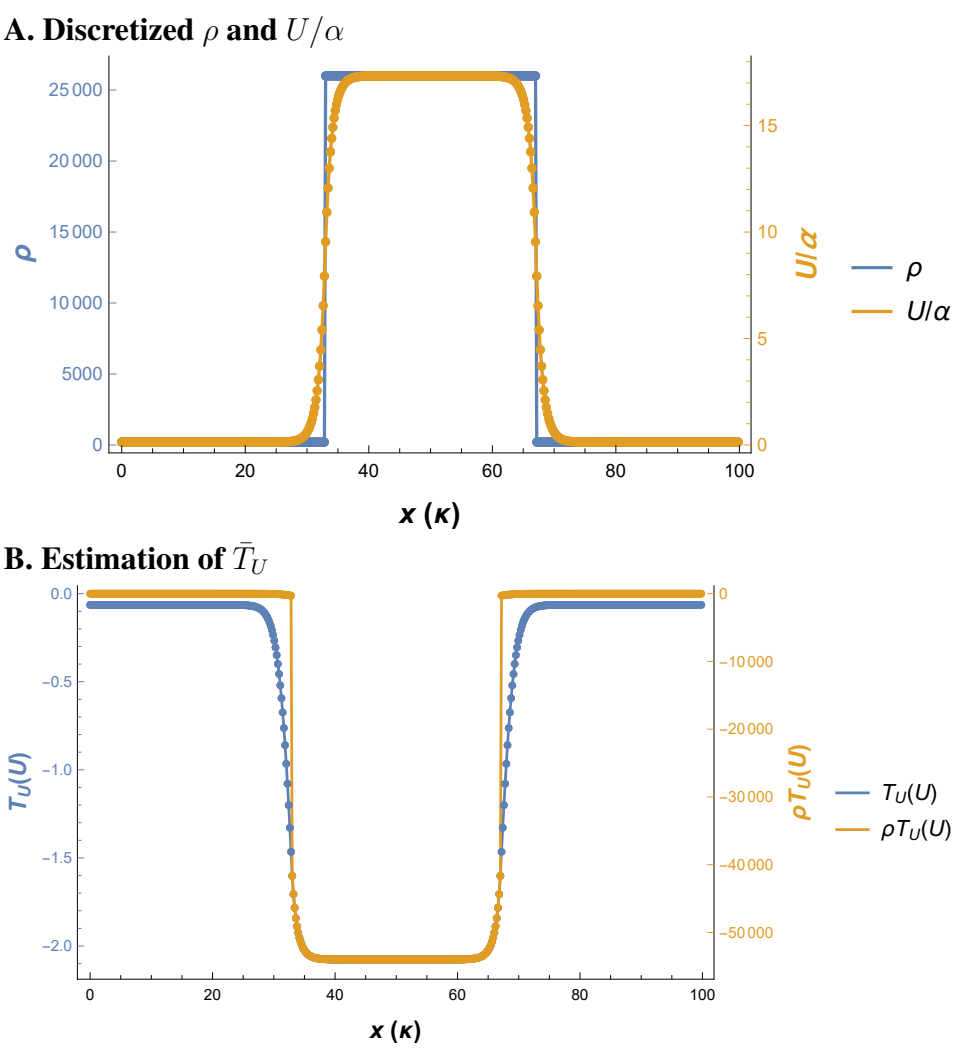

Figure 5.2: Estimation of $\bar{T}_U$
A. Discretized ρ and U on a $\lambda \quad = 1\,\mathrm{cm}$ interval. The units of x are $\kappa \quad = 0.01\,\mathrm{cm}$, the range of the signal. U is computed by convolution of ρ with the Green's function (2.157) and tends exponentially towards ρ with space constant κ. **B.** $T_U(U/\alpha)$ is plotted in blue. It is negative, since the signal is an attractant. In orange is plotted the product $\rho T_U(U)$. Since ρ is very small outside its central mesa, this product is almost flat there. $\bar{T}_U$ is estimated by totalling these numbers and dividing by the total of ρ.

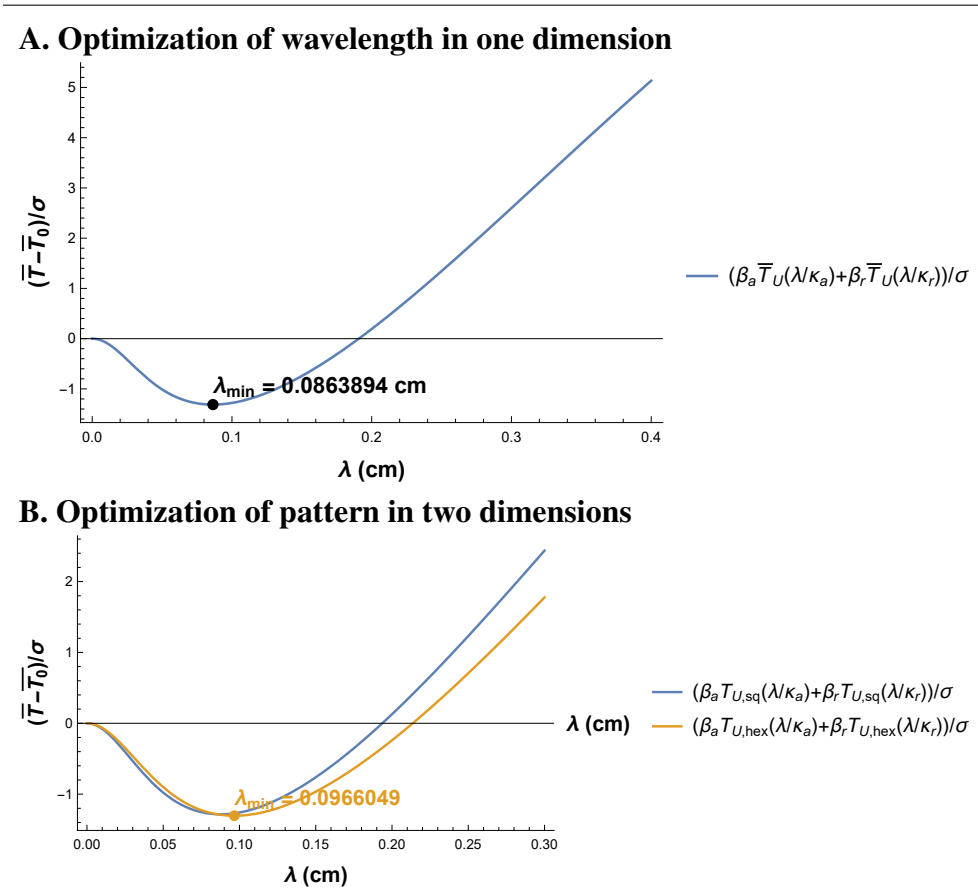

Figure 5.3: Optimization of pattern

A. Mean energy $\bar{T}_U$ as a function of λ, calculated as the β-weighted sum of attractant and repellent contributions. To aid in interpretation, $\bar{T}_U$ is normalized by division by the energy scale σ and by subtracting the $\lambda = 0$ value. The minimum occurs at $\lambda \approx 0.086\,\mathrm{cm}$. **B.** Normalized $\bar{T}_U$ as a function of λ for the square array (blue) and the hexagonal (orange) patterns. The minimum energy occurs on the hexagonal curve at $\lambda \approx 0.097\,\mathrm{cm}$. Compare to Figure 4.1A.

We are now ready to search for the optimum wavelength. The dimensionless function $\bar{T}_U(\lambda/\kappa, a, U_{\text{max}}, r)$ is tabulated for a range of values of $\lambda/\kappa \in [0, \infty]$, $a \in [0, 1]$, $U_{\text{max}} \in [0, \infty)$, $r = 1/130$. (Since r matters little as long as it is small, I only tabulated $\bar{T}_U$ for one r.) Then a polynomial interpolation is used to estimate $\beta_a \bar{T}_U(\lambda/\kappa_a, 44/129, 52/3, 1/130)$ and $\beta_r \bar{T}_U(\lambda/\kappa_r, 44/129, 52/3, 1/130)$ as a function of λ. The result is plotted in Figure 5.3A. The minimum occurs at $\lambda \approx 0.086\,\text{cm}$.

Three independent solutions of the PDE on a $1\,\text{cm}$ interval with periodic boundary conditions and these parameters, but different pseudorandom initial conditions in each case evolved to final equilibria with 10, 11, and 12 equally spaced mesas, corresponding to wavelengths $\lambda \approx 0.01$, 0.091 and $0.083\,\text{cm}$, in reasonable agreement with the predicted $\lambda \approx 0.086\,\text{cm}$. (Perfect agreement is not expected, since, with periodic boundary conditions, the wavelength must be an integer divisor of the domain size.)

5.3.2 Optimization in two dimensions

The two-dimensional calculation is similar to the one-dimensional case, but there is a new complication. There is only one way of arranging balls periodically in one dimension such that each ball is equivalent to every other. In two dimensions there are several. I will now do the calculation for two of them, a square array and a hexagonal array, and compare the results.

The calculation begins by defining, for each pattern, a unit cell that produces the pattern when the plane is tiled with it. For the square array this is easy: the unit cell is a 1×1 square with a circle centered in it. The radius of the circle can be up to 0.5 without overlap. Given an a, we must choose the radius such that

$$a = \pi R^2 \tag{5.22}$$

$$R = \sqrt{a/\pi} \tag{5.23}$$

Thus the largest possible a on a square array of nonoverlapping circles is $a = \pi/4 \approx 0.7854$. You should imagine that we will scale the unit cell up by a factor λ before tiling the plane, so we will end up with circles of radius $\lambda\sqrt{a/\pi}$ separated from each other by distance λ.

Figure 5.4 shows the unit cell for a hexagonal array. It is a $\sqrt{3} \times 1$ rectangle containing the centers of two disks at $(\sqrt{3}/4, 3/4)$, $(3\sqrt{3}/4, 1/4)$ relative to the lower left corner. The distance between the centers is 1, so the maximum possible radius without overlap is $1/2$. Given a, we choose the radius such that

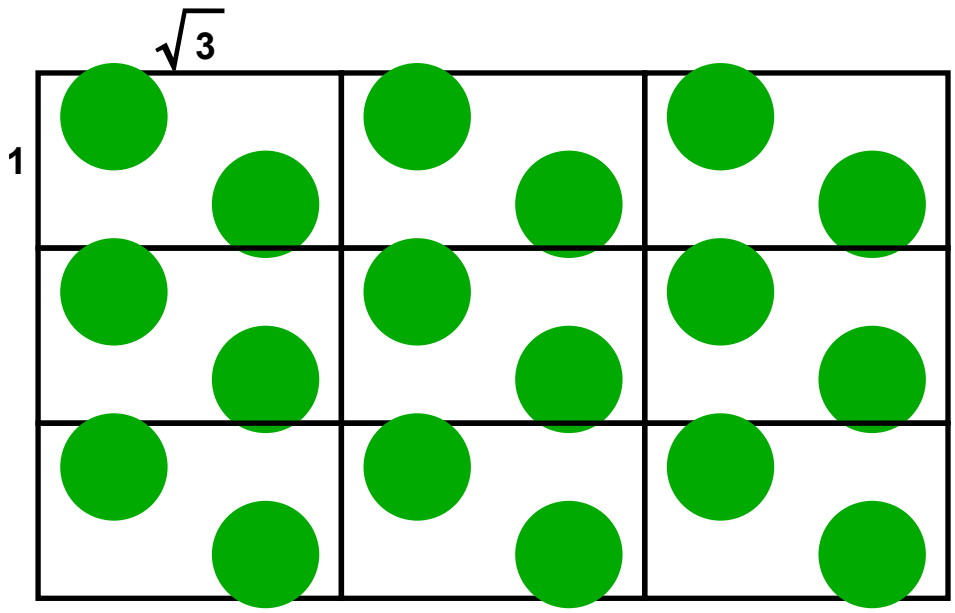

Figure 5.4: Hexagonal array unit cells
Each unit cell is a $\sqrt{3} \times 1$ rectangle containing the centers of two disks at $(\sqrt{3}/4, 3/4)$, $(3\sqrt{3}/4, 1/4)$ relative to the lower left corner. A unit cell may contain segments of disks centered in the cells above and below, as in this example. This figure was drawn with $a = 44/129$, corresponding to $\bar{\rho} = 9000\,\mathrm{cm}^{-2}$, as in previous examples.

$$a = \frac{2\pi R^2}{\sqrt{3} \times 1} \tag{5.24}$$

$$R = \sqrt{\frac{a\sqrt{3}}{2\pi}} \tag{5.25}$$

The maximum value of a is thus $\pi/(2\sqrt{3}) \approx 0.9069$.

The $\lambda \to 0$ and $\lambda \to \infty$ limits of $\bar{T}_U$ are the same as in one dimension (5.12, 5.15). Estimation of $\bar{T}_U$ for finite positive λ/κ is similar to the one-dimensional case (Figure 5.5). The $\sqrt{3} \times 1$ unit cell is represented by an 888×514 grid. Since $\sqrt{3}/888 \neq 1/514$, the spacing of points in the horizontal dimension is slightly different from the vertical. It is convenient to think of the $\sqrt{3} \times 1$ unit cell as divided into rectangular (but not quite square) elements. This slight discrepancy can be accounted for in the distance measure used to assign low or high density to each element (Figure 5.5A). It also needs to be accounted for in the convolution $g * \rho$ to calculate U (Figure 5.5B). Then $T_U(U)$ is calculated using (5.11) (Figure 5.5C). Finally, multiply T_U by ρ, add up the product and divide by the total of ρ to estimate $\bar{T}_U$.

In this way I tabulated estimates of $\bar{T}_U$ for the square and hexagonal arrays. Figure 5.3B plots $\bar{T}_U$ as a function of λ for both geometries. With the parameters used in the solution imaged in Figure 4.1A, the minimum mean energy for these two geometries is achieved at $\lambda \approx 0.0966\,\mathrm{cm}$ with the hexagonal array. Since the distance from the center of each circle to the centers of the nearest circles is 1 in the canonical unit cell, the prediction from this analysis is that with these parameters a hexagonal pattern is preferred over a square pattern, and that the spacing should be $0.0966\,\mathrm{cm}$. The actual spacing of circles in the numerical simulation of this equilibrium is $0.102\,\mathrm{cm}$ (Figure 4.1A). As in the one dimensional case, perfect agreement is not expected, because the periodic boundary conditions constrain possible spacings. (In fact, since the domain was only $0.5\,\mathrm{cm} \times 0.5\,\mathrm{cm}$ for this simulation as opposed to $1\,\mathrm{cm}$ for the one-dimensional solution, the constraints are even tighter.)

Even ignoring doubts that inevitably arise from the use of numerical approximations, and restricting attention to those patterns that consist of circles all equivalent to each other under the symmetry of the pattern, this is of course not a proof that the hexagonal pattern is optimal, because I did not exhaustively test all possible patterns. However, such an exhaustive test is possible in principle and probably not even terribly taxing. There are only 17 classes of repeating patterns in two dimensions (not including quasiperiodic patterns such as Penrose tilings)—the 17 wallpaper groups (Schattschneider 1978). (This is far less daunting than the 230 three-dimensional space groups.)

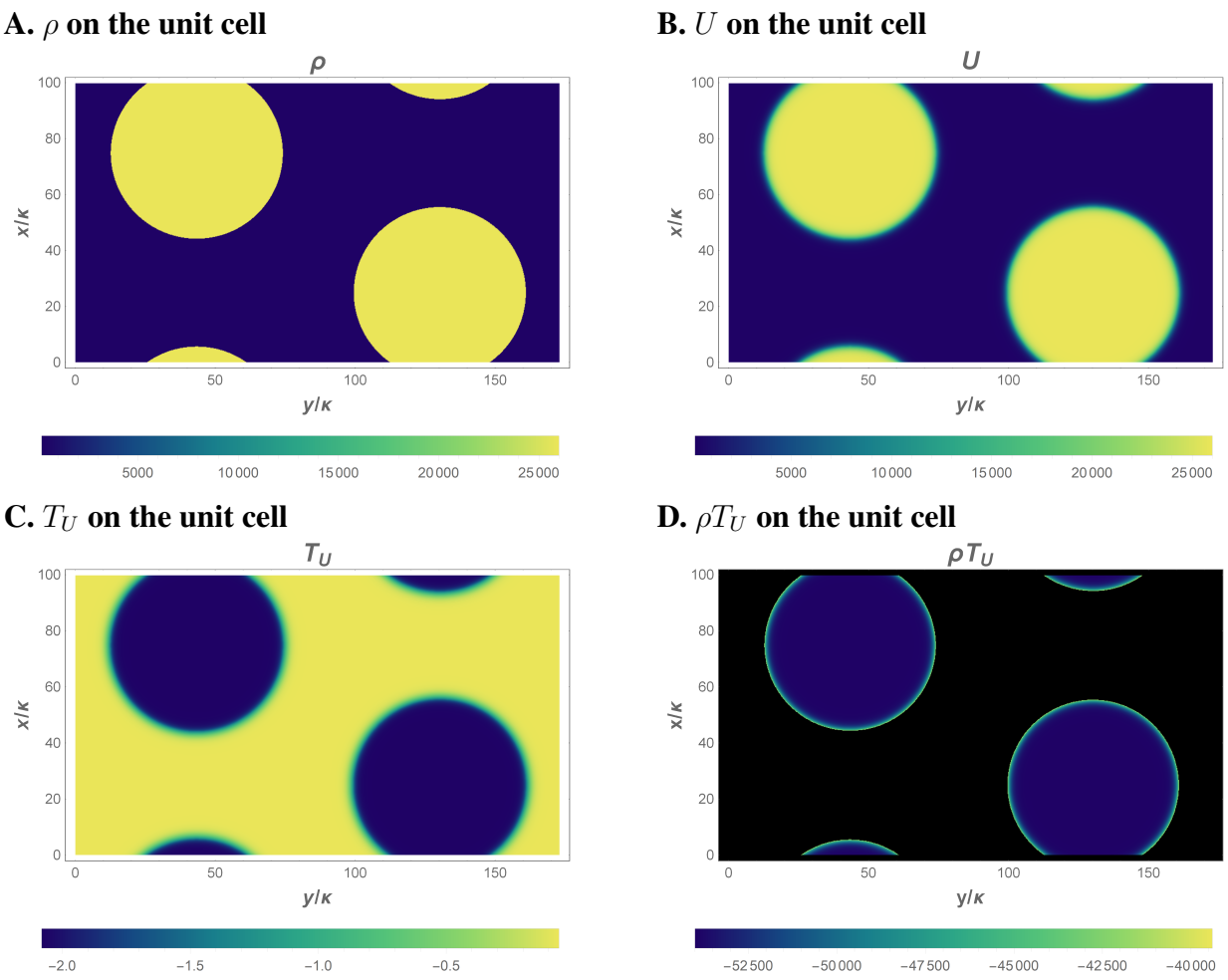

Figure 5.5: Estimation of $\bar{T}_U$ in two dimensions
A. Shows ρ on a 888×514 grid. The radius of the disks was chosen to approximate $a = 44/129 \approx 0.3411$. The actual coverage of this pattern is $a = 0.3422$. **B.** Convolution of ρ with the Green's function blurs the edges. For this calculation $\lambda/\kappa = 100$, i.e., a short-range signal, so the blurring is slight. **C.** $T_U(U)$ calculated using an attractant potential. Thus T_U is negative where U is large and positive. **D.** T_U is multiplied by ρ in order to compute the ρ-weighted mean $\bar{T}_U$. In this plot I have artificially set the background color black in regions of low ρ, in order to make the yellow (less negative) edges of the high-density disks more visible. It is these bright rims that are mainly responsible for making $\bar{T}_U$ more positive than the minimum achieved with a signal whose range is 0. The black regions contribute little to the ρ-weighted mean $\bar{T}_U$, since ρ is so low there.

Thus, this approach, minimizing energy of binary density functions, offers the prospect of solving the problem Keller and Segel's (1970) appendix lamented their inability to solve.

5.4 Simplifying approximations

To get an intuitive understanding of how the binary model works, it is useful to make some further approximations. First, we can neglect the worms in the low density region. Since we are minimizing a ρ-weighted approximation of $\bar{T}_U$, the low-density regions have little effect. The second and third approximations are much less good than the first one. Second: assume that the range of the attractant is much shorter than λ, the spacing between aggregates, i.e. $\lambda/\kappa_a \gg 1$. Third, assume that the range of repellent is much larger than λ, i.e. $\lambda/\kappa_r \ll 1$.

Under the approximation $\lambda/\kappa_a \gg 1$, there is an energy cost to small aggregates. This cost results from the lower attractant concentration at the surface of the aggregate and the consequent higher energy. Figures 5.2B, 5.5D show this clearly. (In fact they show it somewhat too clearly—the calculations in these figures are based on $\lambda = 1\,\mathrm{cm}$, whereas the optimal λ is actually close to $1\,\mathrm{mm}$.) This cost manifests as a $\bar{T}_U$ contribution approximately proportional to the perimeter/area ratio. Using (5.23) and (5.25) as well as the obvious analogs for the line segment, the following formulas for P/A ratio are easily derived

Segment in one dimension:

$$\mathrm{PA}_{\text{segment}} = \frac{2}{a\lambda} \tag{5.26}$$

Square array in two dimensions:

$$\mathrm{PA}_{\text{square}} = \frac{2\sqrt{\pi}}{\lambda\sqrt{a}} \approx \frac{3.55}{\lambda\sqrt{a}} \tag{5.27}$$

Hexagonal array in two dimensions:

$$\mathrm{PA}_{\text{hex}} = \frac{2\sqrt{2\pi}}{3^{1/4}\lambda\sqrt{\lambda}} \approx \frac{3.81}{\lambda\sqrt{a}} \tag{5.28}$$

The cost (in this approximation) is always inversely proportional to λ, confirming the oft-reiterated conclusion that an attractant-only model has no natural maximum length scale.

It is interesting to use these formulas to calculate P/A ratios for the optimal λs from Figure 5.3. They are

$$\begin{aligned} \text{PA}_{\text{segment}} &= 67.875\,\text{cm}^{-1} \\ \text{PA}_{\text{square}} &= 69.199\,\text{cm}^{-1} \\ \text{PA}_{\text{hex}} &= 67.52\,\text{cm}^{-1} \end{aligned}$$

No such simple heuristic is available for the repellent. The effect of λ on the energy due to repellent has two components. First, because repellent can diffuse long distances, the energy of worms in an aggregate is increased by the repellent that diffuses in from other aggregates. To a first approximation, there is little influence of λ on this cost: increased λ means adjacent aggregates are further away, and thus less influential, but also bigger and thus more influential. These factors cancel approximately. Second and more important, the positive influence of an aggregate's own repellent on itself increases as the aggregate gets bigger. Asymptotic forms can be derived for this cost (In fact, they are closely related to (1.47, 1.54).) The important points are that $\bar{T}_{U_r}$ has a finite limit as $\lambda \to 0$ while $\bar{T}_{U_a}$ is blowing up approximately as $1/\lambda$. However, as λ grows, $\bar{T}_{U_r}$ grows and can, if its strength (i.e. β_r) is great enough overcome the influence of attractant and make larger scales costly. Thus, energy minima exist (Figure 5.3).

5.5 The dynamics of binary density fields

I had little success in developing a theoretical understanding of the dynamics of binary density fields from the PDEs. However, during the thesis defense I was made aware of previous work that describes the development of a binary density field as a limiting case of a space-filling Keller-Segel model (Dolak and Schmeiser 2005). I will study how their arguments apply to the worm model (2.1,2.3).

5.6 Summary

In conclusion, PDE solutions and aggregation experiments show that the distribution of worms rapidly approaches a state in which the density function is close to binary, i.e., having only two values. Incorporating this observation into the model is a computationally tractable way to predict equilibria of the PDE model, which seems to agree with the results of PDE solutions. As a nonlinear model, it can even account for patterning, e.g. the apparent preference

for hexagonal symmetry. The theory is tractable in the sense of producing clear results. Those results are clearly wrong, so more work is needed.

Chapter 6

Prospects

6.1 This dissertation is a prolog

The long-term goals of this research are to determine the mechanisms of *C elegans* L1 aggregation—ultimately, both the proximate mechanism ("how" questions) and ultimate causation ("why" questions). The work presented in this dissertation obviously falls far short of those ambitious goals. I have not addressed "why" questions at all. A satisfactory answer to the "how" questions would necessarily have experimental and mathematical components. The experimental part of the answer would probably include identification of the chemical signals mediating the behavior as well as the molecular mechanisms of the sensory response. Alex Artyukhin has made some progress on this, for instance the identification of a sensory receptor gene *srh–2* that may be involved.

Previous chapters address the mathematical question, whether proposed physical mechanisms can produce behavior like that observed. This question also is incompletely answered. I believe I have shown that a model of the type proposed (i.e., PDEs (2.1) and (2.3) with an attractant and a repellent signal) can produce behavior that resembles that experimentally observed, at least superficially.

I would also like to claim that no simpler model based on known plausible biological and physical mechanisms can do this. Of course, without some formal way of ordering models by simplicity, I cannot prove this assertion. For instance, I have considered models in which a single signal acts as a repellent at long range and an attractant at short range by virtue of distinct negative and positive perceptual mechanisms. I can only get these models to work with careful fine-tuning of perceptual parameters (i.e., the function V_U). It is a matter of judgment whether

the need for fine-tuning does greater damage to the elegance of the model than having two signals does.

It is for these reasons that I say this dissertation is a prolog. It is not in any respect a complete study.

Even if one accepts the claim to having identified simple mechanisms that can produce something very like the observed behavior, the work justifying this claim is incomplete. In the course of the previous chapters I have frequently pointed out questions needing further work.

The rest of this chapter is divided into three sections. In the first, I describe questions brought up in previous chapters (or questions that arise in a straightforward way from them) and the further work needed on them. The next two sections are devoted to the bigger questions described above: What are the actual physical and biological mechanisms of *C elegans* L1 aggregation ("how", and what is its purpose ("why")?

6.2 Completion and continuation of ideas raised in previous chapters

6.2.1 Energy functional errors

Chapter 2 was devoted to the development of time-decreasing free energy functionals for the Keller-Segel system. I described a method of developing such functionals based on finding functional antiderivatives of expressions that appear in the right-hand-side of PDEs. This method fails for the worm model because the diffusion term, scaled by the derivative of a non-affine V_U, doesn't have a functional antiderivative. I suggested nevertheless that the functionals produced by radial integration of the expression from the PDEs might be useful approximations.

One thing to try is to improve on radial integration (2.63). Radial integration derives a candidate functional antiderivative by starting at $\mathscr{F}(0)$ and integrating radially out to $\mathscr{F}(U)$. There is no reason to suppose that 0 works better than any other starting point. If the function whose antiderivative you are looking for *has* a functional antiderivative, it doesn't matter where you start—you will always end up with the same answer (up to a constant of integration) . But if the best you can do is an approximation, the approximation you end up with will indeed depend on where you start. Perhaps the second most obvious place to start (after $\rho = 0$) is $U = \bar{U}$, i.e., with the density equal to the mean everywhere.

6.2.2 Dynamics of binary density fields

In chapter 5 I described a puzzling result. In both experiments and numerical solutions of PDEs, the density distribution becomes binary. Taking this observation as given, one can predict patterns of aggregation by minimization of the signal-dependent part of the total energy function.

This works. But it shouldn't, because, by using the weak forms of the PDEs to predict the dynamics of binary density fields, one gets results that don't agree with PDE solutions, and that, indeed, don't make sense. Apparently the only way to rescue these contradictions is to take the V_ρ-dependent terms into account. I suggested a possible resolution of this puzzle near the end of chapter 5. It should be possible to test whether this idea works by numerically testing the structure of the density function at the borders of aggregates.

6.2.3 Cellular automaton model of binary density fields

In chapter 5, I looked for binary density fields that minimize the total energy functional (2.220) as a way of predicting equilibria. A weakness of the approach as I described it there is that it can only explore patterns the searcher has foreseen in advance, for instance square or hexagonal arrays of circles. While this is useful—in fact, I remain enthusiastic about exhaustively testing the wallpaper groups in order to find out for certain what arrangement of circular aggregates is optimal—this approach is limited by the imagination of the searcher. For instance, in one study I didn't describe, I tried to predict the pattern that would form at higher mean density (i.e., higher a) by testing which of three patterns minimized total energy. When, however, I tested the results by numerical solution of the corresponding PDE, I found that it settled into a fourth pattern that was not one of those I had tested.

A better way of exploring the possibilities, I think, would be to initialize (for instance) a 512×512 array of cells randomly to either ρ_{max} or ρ_{min}, such that the number of ρ_{max} cells approximates the desired a, then evolve the pattern forward according to the computed $U_a = g_a * \rho$ and $U_r = g_r * \rho$. This is formally a cellular automaton model, although it violates the spirit of ordinary cellular automata by having a rule for evolution that is based on a very large neighborhood.

There are, I think, two obvious useful ways of doing this. The first, closest in spirit to the computations in chapter 5, is simply to seek minimum energy configurations by gradient descent. For instance, compute the energy for every point in the grid. Find the ρ_{max} cell with the highest energy and the ρ_{min} cell with the lowest energy, and swap them. Then adjust U_a and U_r

to account for the changed density function. Such steps can be efficiently parallelized if the adjustments to U_a and U_r are small enough not to greatly affect the energies at most points. In this way (with perhaps a Markov Chain Monte Carlo (MCMC) assist to avoid being trapped in local optima) one hopes to find equilibrium density configurations without preconceptions about the forms of those configurations.

The second way of using the cellular automaton model would attempt not just to find energy minima, but also to simulate dynamics. One would assign a propensity to every possible movement of worms from a ρ_{max} to a ρ_{min} cell. (Computation of propensities depends on progress on the dynamics of binary density fields). From there the Stochastic Simulation Algorithm (SSA) (or one of its more computationally efficient variants) is used to evolve forward in time, simulating a possible trajectory of the binary field.

6.2.4 Morphological analysis

In chapter 4 I developed two methods for quantifying the pattern of aggregates: mathematical morphology, which quantifies the shapes of the aggregates, and Fourier analysis, which quantifies their spatial pattern. These techniques can be applied to simulation results and images of aggregating L1s. In both cases, I noted differences between the experimental and simulation results.

Fourier analysis of simulation results with periodic boundary conditions predictably produces a pattern of discrete spots. Fourier analysis of experimental images produces a powder diffraction pattern, i.e., a series of rings rather than discrete spots. To compare these, I plan to produce kernel density functions for power as a function of wavenumber magnitude $k = \|\mathbf{k}\|$ for both types of results and compare them.

Simulations produce aggregates with idealized shapes (e.g., near perfect circles). The shapes observed in experiments are necessarily less ideal than those in simulations. There is an obvious explanation of this discrepancy. In PDE solutions, the worms are represented by a continuous density function of space. The reality is discontinuous, and individual worms are big enough to produce visible distortions of the shape. I believe this problem can be addressed by sampling the density function produced by simulations. That is, instead of analyzing the continuous density function directly, place 9000 worms on a $1\,\text{cm} \times 1\,\text{cm}$ square (for a simulation carried out at $\bar{\rho} = 9000\,\text{cm}^{-2}$) with location probabilities proportional to $\rho(\mathbf{x})$, replace each with a worm-shaped pattern of dark pixels (at whatever degree of realism is necessary), and *then* carry out the morphological analysis.

The analysis in chapter 4 was based on just a single simulation and a single experiment. I

have some 200 time-lapse videos of experiments made by Alex Artyukhin under different conditions.

The endgame for this part of the project is fitting and identifiability analysis. In broad strokes, one runs simulations of different models, quantifies the results, and compares the vector of numbers from Fourier and morphological analysis from the simulations with the vector of numbers from experiment and searches for the best match. "Simulations of different models" here refers not just to qualitatively different models, but to simulations of the same model with different parameter values. Because of the large number of simulations required, this process is computationally demanding. I don't believe it is computationally feasible with numerical PDE solutions of the type described in chapter 3. I hope, however, that binary density cellular automaton models will make fitting computationally feasible. (Probably the simple gradient descent computation would be adequate.)

6.2.5 Quantification of aggregation

There is one specific additional way in which morphological analysis may be useful. Many of the experiments Alex did had the aim of finding out what things are necessary for aggregation to happen. For instance, he tested mutants lacking the function of specific chemosensory neurons. These experiments were inconclusive. When he first did them, he thought that mutants lacking functional ASE and ASH neurons failed to aggregate. In later experiments, however, he did see aggregation of these genotypes. In these experiments aggregation was evaluated visually. I believe quantification of aggregation might clarify the interpretation of these experiments.

6.2.6 Three dimensional models

In the laboratory we maintain *C elegans* on agar surfaces. This two-dimensional environment is unnatural. In the wild they live and move through three dimensions, for instance the interior of a rotting apple. Furthermore, even in the experiments we have done, the agar on which the worms move is about $3\,\mathrm{mm}$ deep. The worms are confined to the surface, but diffusible chemical signals are not.

I developed an approximate method of simulating a hybrid two/three dimensional model, in which worms are confined to a two-dimensional agar surface but chemical signals diffuse into the depth of the agar. In this model the concentration of a chemical signal U is a function of space in three dimensions, which I will represent as a two-vector $\mathbf{x}$ and a depth, $z \in [0, L]$,

where $z = 0$ is the surface where the worms are and L is the depth of the agar, $3\,\mathrm{mm}$. I assume Neumann boundary conditions in the z dimension:

$$\left.\frac{\mathrm{d}U(\mathbf{x},z)}{\mathrm{d}z}\right|_{z=0} = \left.\frac{\mathrm{d}U(\mathbf{x},z)}{\mathrm{d}z}\right|_{z=L} = 0 \tag{6.1}$$

Now write $U(\mathbf{x}, z)$ as a Fourier series in z

$$U(\mathbf{x},z) = \sum_{k=0}^{\infty} \hat{U}_k(\mathbf{x}) \cos(k\pi z/L) \tag{6.2}$$

$U(\mathbf{x}, z)$ follows (2.1), but the Laplacian is now three-dimensional. I will write it as $\nabla_3^2 = \nabla_x^2 + \partial^2/\partial z^2$. Substituting (6.2) into (2.1),

$$\dot{U}(\mathbf{x},z) = \sum_{k=0}^{\infty} \left(-\gamma \hat{U}_k(\mathbf{x}) \cos(k\pi z/L) + D\nabla_3^2(\hat{U}_k(\mathbf{x}) \cos(k\pi z/L))\right) + s\rho(\mathbf{x})\delta(z) \tag{6.3}$$

$$\sum_{k=0}^{\infty} \dot{\hat{U}}_k \cos(k\pi z/L) = \left(\sum_{k=0}^{\infty} -\gamma \hat{U}_k(\mathbf{x}) + D\nabla_{\mathbf{x}}^2 \hat{U}_k(\mathbf{x}) - D\frac{k^2\pi^2}{L^2}\hat{U}_k(\mathbf{x}) + \frac{s}{L}\rho(\mathbf{x})\right) \cos(k\pi z/L) \tag{6.4}$$

$$= \left(\sum_{k=0}^{\infty} -(\gamma + D\frac{k^2\pi^2}{L^2})\hat{U}_k(\mathbf{x}) + D\nabla_{\mathbf{x}}^2 \hat{U}_k(\mathbf{x}) + \frac{s}{L}\rho(\mathbf{x})\right) \cos(k\pi z/L) \tag{6.5}$$

$$\dot{\hat{U}}_k = -(\gamma + D\frac{k^2\pi^2}{L^2})\hat{U}_k + D\nabla_{\mathbf{x}}^2 \hat{U}_k + \frac{s}{L}\rho(\mathbf{x}) \tag{6.6}$$

In (6.3), new signal released by the worms at $z = 0$ is exactly at $z = 0$, hence the Dirac δ function. To get from (6.3) to (6.4), I used the Fourier series for the Dirac δ function $\delta(z) = (1/L)\sum_k \cos(k\pi z/L)$. (The $1/L$ factor reflects the dilution of the signal into depth L—in practice, I simply absorb this factor into the parameter s.) The upshot, (6.6), is that each Fourier component $\hat{U}_k(\mathbf{x})$ satisfies a two-dimensional PDE that is exactly like (2.1), except that the decay rate is increased from γ to $\gamma + Dk^2\pi^2/L^2$. Thus this model is just like a multiple signal model, in which each of the original signals is split into an infinite series of signals of decreasing life time. For instance, with $D = 1 \times 10^{-5}\,\mathrm{cm^2 s^{-1}}$, $\gamma = 0.001\,\mathrm{s^{-1}}$ (these are the parameters

used for repellent above), the lifetimes of Fourier components 0 to 3 are $1000\,\mathrm{s}$, $477\,\mathrm{s}$, $186\,\mathrm{s}$ and $92\,\mathrm{s}$. In practice one truncates the series at some finite k on the grounds that a signal that decays very rapidly can have little effect on behavior.

I ran some PDE solutions that simulated diffusion of signals in three dimensions in this way. It had little effect on the results. The behavior was dominated by the effect of the $k = 0$ Fourier component, which acts just like the single U in two dimensions.

The obvious way to simulate both worms and signals moving in three dimensions is simply to run the finite element solution on a three-dimension mesh. In principle the PDE solutions already done in one and two dimensions could be just as easily carried out in three dimensions. This of course would be computationally intensive. I don't have any plans to try it. If, however, cellular automata models can be efficiently parallelized, it might be worth trying three dimensional versions.

6.3 What is really going on?

Can these modeling studies contribute to the elucidation of biological mechanisms of *C elegans* L1 aggregation? I will discuss two possibilities here: determining characteristics of the chemical signals, and predicting the results of an experiment that could be done to investigate the details of worm behavior.

6.3.1 Signal characteristics

The model postulates two chemical signals. Can the mathematical modeling help in identifying these molecules? Four model parameters (two for each molecule) are characteristics of the chemical signals: the diffusion constants D_a and D_r and the decay rates γ_a and γ_r. These show up in the results in two main ways. First, the decay rates set the time scale for changes in signal concentrations. Without any way to observe the chemical signals themselves, this is difficult to measure directly. More useful is the range of each molecule $\sqrt{D/\gamma}$. This determines such things as size and spacing of the aggregates. Based on a few numerical experiments, the range of the repellent is probably the main thing that determines aggregate spacing.

Diffusion constants of small molecules in water don't vary a great deal. One way to understand this is the Stokes-Einstein diffusion law (Miller 1924). A molecule of molecular mass M is predicted to have diffusion constant

$$D \approx \frac{k_B T}{\eta \sqrt[3]{6\pi^2 M \bar{v}}} \tag{6.7}$$

Here k_B is Boltzmann's constant, T is the temperature, η is the viscosity of water, and $\bar{v}$ is the partial specific volume of the molecule. The formula is based on the (dubious) assumption that molecular motions can be described by viscous drag forces, and that the molecule is spherical. It is, in that sense, an upper bound: elongated molecules diffuse more slowly than the Stokes-Einstein relation predicts. For water ($M = 18\,\mathrm{Da}$, $\bar{v} = 1\,\mathrm{cm^3 g^{-1}}$), the smallest molecule a biologist typically encounters, (6.7) predicts $D \approx 1.1 \times 10^{-5}\,\mathrm{cm^2 s^{-1}}$ at $T = 293\,\mathrm{K}$. (An experimental estimate of the diffusion constant of water is $2.3 \times 10^{-5}\,\mathrm{cm^2 s^{-1}}$ (Agmon 1995), so the Stokes-Einstein approximation is at least of the correct order of magnitude.)

Assuming $T = 293\,\mathrm{K}$, $\eta = 1\,\mathrm{cP}$, and $\bar{v} = 0.7\,\mathrm{cm^3 g^{-1}}$ (a typical value for organic molecules), the Stokes-Einstein approximation reduces to

$$D \approx 3.3 \times 10^{-5} M^{-1/3} \mathrm{cm^2 s^{-1}}, \tag{6.8}$$

for M in Da. Larger molecules have smaller diffusion constants (especially if elongated), but since it is an inverse cube root relationship, even macromolecules of modest size diffuse fairly rapidly. For instance, the molecular weight corresponding to $D \approx 1 \times 10^{-6}\,\mathrm{cm^2 s^{-1}}$ is $35\,000\,\mathrm{Da}$, e.g., a small protein.

Since the observed spacing of aggregates is about $\lambda = 1\,\mathrm{mm}$, for $D \in [10^{-6}, 10^{-5}]\,\mathrm{cm^2 s^{-1}}$ the relation $\lambda \approx \sqrt{D/\gamma}$ suggests that one of the signals has a lifetime $(1/\gamma)$ in the range 1000 to $10\,000\mathrm{s}$, i.e. hours.

6.3.2 Simulating individual worm movement

The previous section was concerned mostly with those aspects of reality that appear in the U PDE (2.1). The U PDE is mostly physics and chemistry (although the $s\rho$ term does reflect biology). The ρ PDE (2.3), in contrast, is about biology, and its relationship to reality is more fraught than that of the U PDE.

The parameter σ describes random worm movement, This movement is presumably exploratory, and presumably energetically costly. Although it is just a constant in the model, in reality it is probably a function of the worm's internal state and environment. (Indeed, exploratory behavior has been a focus of *C elegans* research, e.g. Gallagher et al (2013), Helms et al (2019).) The potential functions V_ρ, V_{U_a}, and V_{U_r} are the most complex interfaces between

the model and biology. The chemotactic response potentials V_{U_a} and V_{U_r} are based on little more than guesswork.

There is, in principle, a straightforward way to measure σ (which may be a function) and the potential functions. If we track individual worms, σ and ∇V can be measured from the second and first moments of $\Delta\mathbf{x}(t)$. We also can observe ρ directly, and, while we can't observe U_a and U_r directly, it is reasonable to presume that they decrease monotonically with distance from the center of the nearest aggregates. There is a problem with this plan: we can't track individual worms in the existing bright-field video images. There are too many of them, and they are too crowded. This problem has a solution. We can genetically engineer worms to be fluorescent (but normal in every other way). Then, by introducing a small number of the fluorescent worms into an aggregation experiment and acquiring fluorescence images in addition to bright-field, it should be possible to track the fluorescent tracer worms. Although Alex Artyukhin has done experiments with fluorescently tagged worms (e.g. Figure 1.2), he has not done this precise experiment with dilute tracer worms.

I believe it would be useful to generate the kind of data we would expect such tracer experiments to produce, and preview tracking and analysis methods. Although the PDE solutions (chapter 3) do not directly produce such data, it is, I believe, straightforward to introduce some tracer worms into the simulated environment and generate tracks for them. That is, given a PDE solution, we know $\rho(\mathbf{x})$, $U_a(\mathbf{x})$ and $U_r(\mathbf{x})$ and therefore the potentials that depend on them for every point in the domain. By placing a tracer worm randomly and simulating its movement (for instance, with normally distributed $\Delta\mathbf{x}$'s of the proper mean and variance) we can generate trajectories $\mathbf{x}(t)$. We can then test tracking and analysis methods on these simulated data to find out which experimental conditions (e.g., how many tracer worms to use?) and analysis methods produce the best results.

6.4 The "Why?" question: what is the selective advantage of aggregation, or of the mechanisms behind it?

In this work I have emphasized the use of free energy functionals (which are sometimes but not always Lyapunov functionals) because, I believe, they offer explanations at a level intermediate between "We made up these equations." and "When we solve our equations, this is what the results look like." I would like to finish by mentioning an additional reason for being interested in these functionals.

Variational principles are fundamental to classical physics. This is partly for the reason I just mentioned: they provide insights at a level between equations of motion and trajectories. But

there is a second reason—variational explanations are more fundamental—more closely linked to underlying quantum mechanical mechanisms. The question then arises—is there a fundamental underlying explanation for variational principles in biology?

There is! It is arguably even more fundamental than in physics. Organisms evolve to maximize fitness. (Now, it must be admitted that evolution does not always maximize fitness, and that fitness may not always mean what it naïvely appears to mean. It is, however, the first hypothesis to check: that a behavior evolved because animals that had the genes causing that behavior produced more offspring.) The peculiar genetics of *C elegans* makes this point even more relevant. *C elegans* has two sexes, but they are not male and female: they are male and self-fertilizing hermaphrodite. The hermaphrodite is best understood, in the words of Judith Kimble, as "a female who has become independent". That is, the hermaphrodite is a female in almost every way. However, during development she makes and stores a few hundred sperm. She then switches to producing ova. She can fertilize her own ova with stored sperm. The self-progeny of a hermaphrodite are themselves almost all hermaphrodites. She can also mate with a male and use his sperm to fertilize ova. However, in the wild self-fertilization is the predominant mode of reproduction (Barriere and Felix 2005).

Self-fertilization means that a single worm can colonize an environment. Thus, it is not uncommon that, in a single rotting apple, almost all the worms are hermaphrodites and all descended from a single hermaphrodite. (But see also Sivasundar and Hey (2005).) Under these conditions it is advantageous to maximize not arithmetic mean fitness, but geometric mean fitness. (Rivoire and Leibler (2011) give the most thorough exposition of the reasons and consequences. But the central argument is presented in a delightfully simple paper by Kelly (1956).)

When maximizing arithmetic mean fitness, it is every worm for herself—each worm is expected to behave in the way that maximizes her individual fitness. But geometric mean fitness is maximized by collective behavior, in which worms act to benefit the genotype. It therefore becomes plausible that *C elegans* L1 behavior may have evolved to maximize a functional that is a sum over the entire population.

As an example, it is striking that, even after long times, not all worms end up in aggregates. There are always a few, around 1% of the population, moving freely outside the aggregates. How can this behavior be optimal? In free energy functional terms this behavior arises from the entropy term $\sigma\rho\log\rho$. The derivative of entropy becomes infinite as ρ approaches zero. If other terms of the free energy functional are bounded, there is always some entropy benefit to be gained by increasing ρ from 0 to a small positive number. Entropy terms arise naturally from maximization of geometric mean fitness.

Suppose that there are two possible environments the worms may unpredictably find themselves in. In environment 1, which over many generations occurs with probability p_1, worms

in aggregates survive, while worms outside aggregates die. In environment 2, (probability p_2) worms in aggregates die, while those outside aggregates survive. Let us also suppose environment 1 is much more probable than 2, e.g. $p_1 = 0.99$, $p_2 = 0.01$. (This is, of course, a grossly oversimplified model for the purpose of illustration.)

If the population strategy is to place N_a worms in aggregates and $N_o = N - N_a$ outside, (where N is the population size) the mean fitness of the population (i.e., the proportion of worms that survive) is $f_1 = N_a/N$ when environment 1 happens and $f_2 = N_o/N$ in environment 2. The arithmetic mean fitness is then

$$\begin{aligned} AM(f) &= p_1 f_1 + p_2 f_2 && (6.9)\\ &= \frac{N_a}{N} p_1 + \frac{N_o}{N} p_2 && (6.10)\\ &= \frac{1}{N}\left(\sum_{i=1}^{N} \bar{f}_i\right) && (6.11)\\ &= AM(\bar{f}_i), && (6.12) \end{aligned}$$

where $\bar{f}_i = p_1$ if worm i is in an aggregate and $\bar{f}_i = p_2$ is the mean fitness (over the possible environments) of individual worm i. That is, the arithmetic mean fitness of the population is simply the arithmetic mean of the individual worm arithmetic mean fitness. With $p_1 > p_2$ as above, the strategy that optimizes $AM(f)$ is $N_a = N$, $N_o = 0$. That is, every worm should be in an aggregate.

The strategy that maximizes geometric mean fitness $GM(f)$ is different.

$$\begin{aligned} GM(f) &= f_1^{p_1} f_2^{p_2} && (6.13)\\ \log(GM(f)) &= p_1 \log(f_1) + p_2 \log(f_2) && (6.14)\\ &= p_1 \log \frac{N_a}{N} + p_2 \log \frac{N_o}{N} && (6.15)\\ &= p_1 \log(N_a) + p_2 \log(N_o) - \log N && (6.16)\\ &= AM(\log(N_i)) - \log N && (6.17) \end{aligned}$$

Since $\log$ is an increasing function, maximizing geometric mean fitness is equivalent to maximizing the arithmetic mean of the $\log$ of fitness. For optimization purposes, we can ignore the constant $\log N$. Thus, to maximize geometric mean fitness we maximize the mean of $\log(N_i)$.

Under the constraints $N_a, N_o > 0$, $N_a + N_o = N$, geometric mean fitness is maximized when $N_a = Np_1$, $N_o = Np_2$. In other words, most of the worms are in aggregates, but a small number are outside, just as observed. The optimum geometric mean fitness, then, is given by

$$\log(GM(f)) = p_1 \log(p_1) + p_2 \log(p_2) = -S, \tag{6.18}$$

where S is entropy.

Thus, the strategy that is optimal to maximize geometric mean fitness (in this oversimplified model) is the one that minimizes entropy. Although the expressions are not the same, this entropy and the $\sigma\rho\log\rho$ entropy term in the free energy functionals are related.

References

Fechner, Gustav T (1860). *Elemente der Psychophysik*. Leipzig: Druck, Verlag von Breitkopf, and Härtel.

Miller, C. C. (Dec. 1924). "The Stokes-Einstein Law for Diffusion in Solution". In: *Proceedings of the Royal Society A: Mathematical, Physical and Engineering Sciences* 106.740, pp. 724–749. ISSN: 1364-5021. DOI: 10.1098/rspa.1924.0100.

Turing, A M (1952). "The chemical basis of morphogenesis". In: *Phil Trans Roy Soc Lond B* 237, pp. 37–72.

Kelly, JL (1956). "A New Interpretation of Information Rate". In: *The Bell System Technical Journal,* 35.4, pp. 917–926.

Keller, Evelyn F. and Lee A. Segel (1970). "Initiation of slime mold aggregation viewed as an instability". In: *Journal of Theoretical Biology* 26.3, pp. 399–415. ISSN: 10958541. DOI: 10.1016/0022-5193(70)90092-5.

Schattschneider, Doris (June 1978). "The Plane Symmetry Groups: Their Recognition and Notation". In: *The American Mathematical Monthly* 85.6, p. 439. ISSN: 00029890. DOI: 10.2307/2320063. URL: https://www.jstor.org/stable/2320063?origin=crossref.

Gould, S J and R C Lewontin (Sept. 1979). "The spandrels of San Marco and the Panglossian paradigm: a critique of the adaptationist programme." In: *Proceedings of the Royal Society of London. Series B, Biological sciences* 205.1161, pp. 581–98. ISSN: 0950-1193. DOI: 10.1098/rspb.1979.0086. URL: http://www.ncbi.nlm.nih.gov/pubmed/42062.

Kahneman, Daniel and Amos Tversky (Mar. 1979). "Prospect Theory: An Analysis of Decision under Risk". In: *Econometrica* 47.2, p. 263. ISSN: 00129682. DOI: 10.2307/1914185. URL: https://www.jstor.org/stable/1914185?origin=crossref.

Otsu, Nobuyuki (Jan. 1979). "A Threshold Selection Method from Gray-Level Histograms". In: *IEEE Transactions on Systems, Man, and Cybernetics* 9.1, pp. 62–66. ISSN: 0018-9472. DOI: 10.1109/TSMC.1979.4310076. URL: http://ieeexplore.ieee.org/document/4310076/.

Childress, S. and J.K. Percus (Oct. 1981). “Nonlinear aspects of chemotaxis”. In: *Mathematical Biosciences* 56.3-4, pp. 217–237. ISSN: 0025-5564. DOI: 10.1016/0025-5564(81)90055-9. URL: https://www.sciencedirect.com/science/article/pii/0025556481900559.

Horvitz, H R et al. (1982). “Serotonin and octopamine in the nematode Caenorhabditis elegans”. In: *Science* 216.4549, pp. 1012–1014.

Serra, Jean Paul. (1982). *Image analysis and mathematical morphology*. Academic Press.

Golden, J W and D L Riddle (1985). “A gene affecting production of the Caenorhabditis elegans dauer-inducing pheromone”. eng. In: *Mol Gen Genet* 198.3, pp. 534–536. URL: http://www.ncbi.nlm.nih.gov/entrez/query.fcgi?cmd=Retrieve&db=PubMed&dopt=Citation&list_uids=3859733.

Williamson, V M et al. (Aug. 1991). “Isolation of Caenorhabditis elegans mutants lacking alcohol dehydrogenase activity.” In: *Biochemical genetics* 29.7-8, pp. 313–23. ISSN: 0006-2928. URL: http://www.ncbi.nlm.nih.gov/pubmed/1747095.

W. Jäger, W. and S. Luckhaus (1992). “No Title”. In: *Trans. Am. Math. Soc.* 329, pp. 817–824.

Agmon, Noam (Oct. 1995). “The Grotthuss mechanism”. In: *Chemical Physics Letters* 244.5-6, pp. 456–462. ISSN: 00092614. DOI: 10.1016/0009-2614(95)00905-J. URL: https://linkinghub.elsevier.com/retrieve/pii/000926149500905J.

Cheng, Yizong and Yizong Cheng (1995). “Mean shift, mode seeking, and clustering”. In: *IEEE TRANSACTIONS ON PATTERN ANALYSIS AND MACHINE INTELLIGENCE*. URL: https://citeseerx.ist.psu.edu/viewdoc/summary?doi=10.1.1.510.1222.

Dennett, Daniel Clement. (1996). *Darwin’s dangerous idea : evolution and the meanings of life*. Penguin. ISBN: 014016734X.

Herrero, Miguel A. and Juan J.L. Velázquez (1996). “Singularity patterns in a chemotaxis model”. In: *Mathematische Annalen* 306.3, pp. 583–624.

Balay, Satish, William D Gropp, et al. (1997). “Efficient Management of Parallelism in Object Oriented Numerical Software Libraries”. In: *Modern Software Tools in Scientific Computing*. Ed. by E Arge et al. Birkhäuser Press, pp. 163–202.

Bargmann, C I and I Mori (1997). “Chemotaxis and Thermotaxis”. In: *C. elegans II*. Ed. by D L Riddle et al. New York: Cold Spring Harbor Press, pp. 717–737.

Herrero, M A et al. (Nov. 1997). “Finite-time aggregation into a single point in a reaction - diffusion system”. In: *Nonlinearity* 10.6, pp. 1739–1754. ISSN: 0951-7715. DOI: 10.1088/0951-7715/10/6/016. URL: http://stacks.iop.org/0951-7715/10/i=6/a=016?key=crossref.ddb02e04a973a0949c409f03fd24d519.

Nagai, T and T. Senba (1997). “Global existence and blow-up of radial solutions to a parabolic-elliptic system of chemotaxis”. In: *Nonlinear Anal., Theory Methods* 30, pp. 3837–3842.

Nagai, Toshitaka et al. (1997). “ApplicationoftheTrudinger-MoserInequah.tytoaParabolicSystemofChemotaxis”. In: *FunkcialajEkvacioj* 40, pp. 411–433.

Biler, Piotr (1998). “Local and global solvability of some parabolic system modelling chemotaxis”. In: *Adv. Math. Sci. Appl.* 8, pp. 715–743.

Bono, M de and C I Bargmann (1998). “Natural variation in a neuropeptide Y receptor homolog modifies social behavior and food response in C. elegans”. In: *Cell* 94.5, pp. 679–689. URL: http://www.ncbi.nlm.nih.gov/entrez/query.fcgi?cmd=Retrieve&db=PubMed&dopt=Citation&list_uids=9741632.

Gajewski, Herbert et al. (Jan. 1998). “Global Behaviour of a Reaction-Diffusion System Modelling Chemotaxis”. In: *Mathematische Nachrichten* 195.1, pp. 77–114. ISSN: 0025584X. DOI: 10.1002/mana.19981950106. URL: http://doi.wiley.com/10.1002/mana.19981950106.

Mori, I (1999). “Genetics of chemotaxis and thermotaxis in the nematode Caenorhabditis elegans”. In: *Annu Rev Genet* 33, pp. 399–422. URL: http://www.ncbi.nlm.nih.gov/entrez/query.fcgi?cmd=Retrieve&db=PubMed&dopt=Citation&list_uids=10690413.

Pierce-Shimomura, J T et al. (Nov. 1999). “The fundamental role of pirouettes in Caenorhabditis elegans chemotaxis.” In: *The Journal of neuroscience : the official journal of the Society for Neuroscience* 19.21, pp. 9557–69. ISSN: 1529-2401. DOI: 10.1523/JNEUROSCI.19-21-09557.1999. URL: http://www.ncbi.nlm.nih.gov/pubmed/10531458%20http://www.pubmedcentral.nih.gov/articlerender.fcgi?artid=PMC6782915.

Sawin, E R et al. (2000). “C. elegans locomotory rate is modulated by the environment through a dopaminergic pathway and by experience through a serotonergic pathway”. eng. In: *Neuron* 26.3, pp. 619–631. URL: http://www.ncbi.nlm.nih.gov/pubmed/10896158.

Amestoy, P R, I S Duff, et al. (2001). “A Fully Asynchronous Multifrontal Solver Using Distributed Dynamic Scheduling”. In: *SIAM Journal on Matrix Analysis and Applications* 23.1, pp. 15–41.

Horstmann, Dirk (2001). “Lyapunov functions and Lp-estimates for a class of reaction-diffusion systems”. In: *Coll. Math* 87, pp. 113–127.

Senba, T. and T. Suzuki (2001). “Behavior of solutions to a system related to chemotaxis”. In: *Nonlinear Analysis* 47, pp. 2551–2562.

Yoshida, Masasuke et al. (Sept. 2001). “ATP synthase — a marvellous rotary engine of the cell”. In: *Nature Reviews Molecular Cell Biology* 2.9, pp. 669–677. ISSN: 14710072. DOI: 10.1038/35089509. URL: http://www.nature.com/doifinder/10.1038/35089509.

Bono, M de, D M Tobin, et al. (2002). “Social feeding in Caenorhabditis elegans is induced by neurons that detect aversive stimuli”. In: *Nature* 419.6910, pp. 899–903. URL: http://www.ncbi.nlm.nih.gov/entrez/query.fcgi?cmd=Retrieve&db=PubMed&dopt=Citation&list_uids=12410303.

Avery, L and B B Shtonda (2003). “Food transport in the C. elegans pharynx”. In: *J Exp Biol* 206.Pt 14, pp. 2441–2457. URL: http://www.ncbi.nlm.nih.gov/entrez/query.fcgi?cmd=Retrieve&db=PubMed&dopt=Citation&list_uids=12796460.

Horstmann, D (2003). “From 1970 until present: the Keller-Segel model in chemotaxis and its consequences. I.” In: *Jahresber. Deutsch. Math.-Verein.* 105.3, pp. 103–165. ISSN: 0012-0456. URL: http://citeseerx.ist.psu.edu/viewdoc/summary?doi=10.1.1.94.3876.

Stein, L D et al. (2003). “The genome sequence of Caenorhabditis briggsae: a platform for comparative genomics”. eng. In: *PLoS Biol* 1.2, E45. DOI: 10.1371/journal.pbio.0000045. URL: http://www.ncbi.nlm.nih.gov/pubmed/14624247.

Dunn, Nathan A. et al. (Sept. 2004). “A Neural Network Model of Chemotaxis Predicts Functions of Synaptic Connections in the Nematode Caenorhabditis elegans”. In: *Journal of Computational Neuroscience* 17.2, pp. 137–147. ISSN: 0929-5313. DOI: 10.1023/B:JCNS.0000037679.42570.d5. URL: http://www.ncbi.nlm.nih.gov/pubmed/15306736%20http://link.springer.com/10.1023/B:JCNS.0000037679.42570.d5.

Horstmann, D (2004). “From 1970 until present: The Keller-Segel model in chemotaxis and its consequences II.” In: *Jahresber. Deutsch. Math.-Verein.* 106.2, pp. 51–69. ISSN: 0012-0456.

Barriere, A and M A Felix (2005). “High local genetic diversity and low outcrossing rate in Caenorhabditis elegans natural populations”. eng. In: *Curr Biol* 15.13, pp. 1176–1184. DOI: S0960-9822(05)00655-X[pii]10.1016/j.cub.2005.06.022. URL: http://www.ncbi.nlm.nih.gov/entrez/query.fcgi?cmd=Retrieve&db=PubMed&dopt=Citation&list_uids=16005289.

Dolak, Yasmin and Christian Schmeiser (Jan. 2005). “The Keller–Segel Model with Logistic Sensitivity Function and Small Diffusivity”. In: *SIAM Journal on Applied Mathematics* 66.1, pp. 286–308. ISSN: 0036-1399. DOI: 10.1137/040612841. URL: http://epubs.siam.org/doi/10.1137/040612841.

Edelstein-Keshet, Leah. (2005). *Mathematical models in biology*. Society for Industrial and Applied Mathematics, p. 586. ISBN: 0898715547.

Rang, J and L Angermann (2005). “New Rosenbrock W-methods of order 3 for partial differential algebraic equations of index 1”. In: *BIT Numerical Mathematics* 45.4, pp. 761–787.

Sivasundar, Arjun and Jody Hey (Sept. 2005). “Sampling from Natural Populations with RNAi Reveals High Outcrossing and Population Structure in Caenorhabditis elegans”. In: *Current Biology* 15.17, pp. 1598–1602. ISSN: 09609822. DOI: 10.1016/j.cub.2005.08.034. URL: http://www.ncbi.nlm.nih.gov/pubmed/16139217%20https://linkinghub.elsevier.com/retrieve/pii/S096098220500953X.

Amestoy, P R, A Guermouche, et al. (2006). “Hybrid scheduling for the parallel solution of linear systems”. In: *Parallel Computing* 32.2, pp. 136–156.

Bargmann, C I (2006). “Chemosensation in C. elegans”. eng. In: *WormBook*, pp. 1–29. DOI: 10.1895/wormbook.1.123.1. URL: http://www.ncbi.nlm.nih.gov/entrez/query.fcgi?cmd=Retrieve&db=PubMed&dopt=Citation&list_uids=18050433.

Chang, A J et al. (2006). “A distributed chemosensory circuit for oxygen preference in C. elegans”. eng. In: *PLoS Biol* 4.9, e274. DOI: 06-PLBI-RA-0332R3[pii]10.1371/journal.pbio.0040274. URL: http://www.ncbi.nlm.nih.gov/entrez/query.fcgi?cmd=Retrieve&db=PubMed&dopt=Citation&list_uids=16903785%20http://www.ncbi.nlm.nih.gov/pubmed/16903785.

Rogers, C et al. (2006). “Behavioral motifs and neural pathways coordinating O2 responses and aggregation in C. elegans”. eng. In: *Curr Biol* 16.7, pp. 649–659. DOI: S0960-9822(06)01316-9[pii]10.1016/j.cub.2006.03.023. URL: http://www.ncbi.nlm.nih.gov/entrez/query.fcgi?cmd=Retrieve&db=PubMed&dopt=Citation&list_uids=16581509.

Ferkey, D M et al. (2007). “C. elegans G protein regulator RGS-3 controls sensitivity to sensory stimuli”. In: *Neuron* 53.1, pp. 39–52. URL: http://www.ncbi.nlm.nih.gov/entrez/query.fcgi?cmd=Retrieve&db=PubMed&dopt=Citation&list_uids=17196529.

Baugh, L Ryan et al. (Apr. 2009). “RNA Pol II accumulates at promoters of growth genes during developmental arrest.” In: *Science (New York, N.Y.)* 324.5923, pp. 92–4. ISSN: 1095-9203. DOI: 10.1126/science.1169628. URL: http://www.ncbi.nlm.nih.gov/pubmed/19251593.

Butcher, R A et al. (2009). “Biosynthesis of the Caenorhabditis elegans dauer pheromone”. eng. In: *Proc Natl Acad Sci U S A* 106.6, pp. 1875–1879. DOI: 0810338106[pii]10.1073/pnas.0810338106. URL: http://www.ncbi.nlm.nih.gov/entrez/query.fcgi?cmd=Retrieve&db=PubMed&dopt=Citation&list_uids=19174521.

Epshteyn, Yekaterina and Alexander Kurganov (Jan. 2009). “New Interior Penalty Discontinuous Galerkin Methods for the Keller–Segel Chemotaxis Model”. In: *SIAM Journal on Numerical Analysis* 47.1, pp. 386–408. ISSN: 0036-1429. DOI: 10.1137/07070423X. URL: http://epubs.siam.org/doi/abs/10.1137/07070423X%20http://epubs.siam.org/doi/10.1137/07070423X.

Hillen, T. and K. J. Painter (Jan. 2009). “A user’s guide to PDE models for chemotaxis”. In: *Journal of Mathematical Biology* 58.1-2, pp. 183–217. ISSN: 0303-6812. DOI: 10.1007/s00285-008-0201-3. URL: http://link.springer.com/10.1007/s00285-008-0201-3.

Joo, Hyoe-Jin et al. (Aug. 2009). “Caenorhabditis elegans utilizes dauer pheromone biosynthesis to dispose of toxic peroxisomal fatty acids for cellular homoeostasis.” In: *The Biochemical journal* 422.1, pp. 61–71. ISSN: 1470-8728. DOI: 10.1042/BJ20090513. URL: http://www.ncbi.nlm.nih.gov/pubmed/19496754.

Felix, M A and C Braendle (2010). “The natural history of Caenorhabditis elegans”. eng. In: *Curr Biol* 20.22, pp. 965–9. DOI: S0960-9822(10)01168-1[pii]10.1016/j.cub.2010.09.050. URL: http://www.ncbi.nlm.nih.gov/entrez/query.fcgi?cmd=Retrieve&db=PubMed&dopt=Citation&list_uids=21093785.

Gart, Sean et al. (Dec. 2010). “The collective motion of nematodes in a thin liquid layer”. In: URL: http://arxiv.org/abs/1012.4798.

Logg, Anders et al., eds. (2010). *Automated Solution of Differential Equations by the Finite Eelment Method – The FEniCS Book*. Springer Heidelberg Dordrecht London, p. 723.

Rivoire, Olivier and Stanislas Leibler (Oct. 2011). “The Value of Information for Populations in Varying Environments”. In: *J Stat Phys* 142, pp. 1124–1166. DOI: 10.1007/s10955-011-0166-2. URL: http://arxiv.org/abs/1010.5092%20http://dx.doi.org/10.1007/s10955-011-0166-2.

Alaimo, Joseph T. et al. (Nov. 2012). “Ethanol Metabolism and Osmolarity Modify Behavioral Responses to Ethanol in ¡i¿C. elegans¡/i¿”. In: *Alcoholism: Clinical and Experimental Research* 36.11, pp. 1840–1850. ISSN: 01456008. DOI: 10.1111/j.1530-0277.2012.01799.x. URL: http://doi.wiley.com/10.1111/j.1530-0277.2012.01799.x.

Choe, A et al. (2012). “Ascaroside signaling is widely conserved among nematodes”. eng. In: *Curr Biol* 22.9, pp. 772–780. DOI: 10.1016/j.cub.2012.03.024. URL: http://www.ncbi.nlm.nih.gov/pubmed/22503501.

Félix, Marie-Anne et al. (2012). “Population dynamics and habitat sharing of natural populations of Caenorhabditis elegans and C. briggsae”. In: *BMC Biology* 10.1, p. 59. ISSN: 1741-7007. DOI: 10.1186/1741-7007-10-59. URL: http://bmcbiol.biomedcentral.com/articles/10.1186/1741-7007-10-59.

Lee, Inhwan et al. (Sept. 2012). “Metabolic Rate Regulates L1 Longevity in C. elegans”. In: *PLoS ONE* 7.9. Ed. by Patrick Callaerts, e44720. ISSN: 1932-6203. DOI: 10.1371/journal.pone.0044720. URL: http://dx.plos.org/10.1371/journal.pone.0044720.

Reuss, Stephan H. von et al. (2012). “Comparative Metabolomics Reveals Biogenesis of Ascarosides, a Modular Library of Small-Molecule Signals in C. elegans”. In:

Song, B M and L Avery (2012). “Serotonin activates overall feeding by activating two separate neural pathways in Caenorhabditis elegans”. In: *J Neurosci* 32.6, pp. 1920–1931. DOI: 10.1523/JNEUROSCI.2064-11.2012. URL: http://www.ncbi.nlm.nih.gov/pubmed/22323705.

Srinivasan, Jagan et al. (Jan. 2012). "A Modular Library of Small Molecule Signals Regulates Social Behaviors in Caenorhabditis elegans". In: *PLoS Biology* 10.1. Ed. by Piali Sengupta, e1001237. ISSN: 1545-7885. DOI: 10.1371/journal.pbio.1001237. URL: http://dx.plos.org/10.1371/journal.pbio.1001237.

Starrfelt, Jostein and Hanna Kokko (Aug. 2012). "Bet-hedging-a triple trade-off between means, variances and correlations". In: *Biological Reviews* 87.3, pp. 742–755. ISSN: 14647931. DOI: 10.1111/j.1469-185X.2012.00225.x. URL: http://doi.wiley.com/10.1111/j.1469-185X.2012.00225.x.

Artyukhin, A B et al. (2013). "Succinylated Octopamine Ascarosides and a New Pathway of Biogenic Amine Metabolism in Caenorhabditis elegans". eng. In: *J Biol Chem* 288.26, pp. 18778–18783. DOI: 10.1074/jbc.C113.477000. URL: http://www.ncbi.nlm.nih.gov/pubmed/23689506.

Artyukhin, Alexander B. et al. (Sept. 2013). "Density dependence in Caenorhabditis larval starvation". en. In: *Scientific Reports* 3, p. 2777. ISSN: 2045-2322. DOI: 10.1038/srep02777. URL: http://www.nature.com/articles/srep02777%20http://www.nature.com/srep/2013/130927/srep02777/full/srep02777.html.

Baugh, L Ryan (July 2013). "To Grow or Not to Grow: Nutritional Control of Development During Caenorhabditis elegans L1 Arrest". eng. In: *Genetics* 194.3, pp. 539–555. ISSN: 1943-2631. DOI: 10.1534/genetics.113.150847. URL: http://www.ncbi.nlm.nih.gov/pubmed/23824969%20http://www.pubmedcentral.nih.gov/articlerender.fcgi?artid=PMC3697962.

Gallagher, T et al. (2013). "The Geometry of Locomotive Behavioral States in C. elegans". In: *PLoS One* 8.3, e59865. DOI: 10.1371/journal.pone.0059865. URL: http://www.ncbi.nlm.nih.gov/pubmed/23555813.

Ludewig, A H and F C Schroeder (2013). "Ascaroside signaling in C. elegans". eng. In: *WormBook*, pp. 1–22. DOI: 10.1895/wormbook.1.155.1. URL: http://www.ncbi.nlm.nih.gov/pubmed/23355522.

Pfister, Roland et al. (2013). "Good things peak in pairs: a note on the bimodality coefficient". In: *Frontiers in Psychology* 4. DOI: 10.3389/FPSYG.2013.00700. URL: https://www.ncbi.nlm.nih.gov/pmc/articles/PMC3791391/.

Avery, Leon (July 2014). "A Model of the Effect of Uncertainty on the C elegans L2/L2d Decision". In: *PLoS ONE* 9.7. Ed. by Paulo Lee Ho, e100580. ISSN: 1932-6203. DOI: 10.1371/journal.pone.0100580. URL: http://dx.plos.org/10.1371/journal.pone.0100580.

Artyukhin, Alexander B et al. (Jan. 2015). "Starvation-induced collective behavior in C. elegans." en. In: *Scientific reports* 5, p. 10647. ISSN: 2045-2322. DOI: 10.1038/srep10647. URL: http://www.nature.com/srep/2015/150527/srep10647/full/srep10647.html.

Dell'Osso, Liliana et al. (Feb. 2016). "Depression, Serotonin and Tryptophan". In: *Current Pharmaceutical Design* 22.8, pp. 949–954. ISSN: 13816128. DOI: 10.2174/1381612822666151214104822. URL: http://www.eurekaselect.com/openurl/content.php?genre=article&issn=1381-6128&volume=22&issue=8&spage=949.

Roberts, William M et al. (Jan. 2016). "A stochastic neuronal model predicts random search behaviors at multiple spatial scales in C. elegans". In: *eLife* 5. ISSN: 2050-084X. DOI: 10.7554/eLife.12572. URL: https://elifesciences.org/articles/12572.

Baek, Seung Ki and Beom Jun Kim (Dec. 2017). "Free energy of a chemotactic model with nonlinear diffusion". In: *Scientific Reports* 7.1, p. 8909. ISSN: 2045-2322. DOI: 10.1038/s41598-017-09369-w. URL: http://www.nature.com/articles/s41598-017-09369-w.

Chen, Wan et al. (July 2017). "Role of Dopamine Signaling in Drug Addiction". In: *Current Topics in Medicinal Chemistry* 17.21. ISSN: 15680266. DOI: 10.2174/1568026617666170504100642. URL: http://www.eurekaselect.com/152147/article.

Abhyankar, Shrirang et al. (2018). "PETSc/TS: A Modern Scalable ODE/DAE Solver Library". In: *arXiv preprint arXiv:1806.01437*.

Avery, Leon et al. (Jan. 2018). "Numerical Modelling of C. elegans L1 Aggregation". In: *IFAC-PapersOnLine* 51.19, pp. 12–15. ISSN: 2405-8963. DOI: 10.1016/J.IFACOL.2018.09.012. URL: https://www.sciencedirect.com/science/article/pii/S2405896318316690.

Gurusamy, A. and K. Balachandran (June 2018). "Finite element method for solving Keller–Segel chemotaxis system with cross-diffusion". In: *International Journal of Dynamics and Control* 6.2, pp. 539–549. ISSN: 2195-268X. DOI: 10.1007/s40435-017-0335-5. URL: http://link.springer.com/10.1007/s40435-017-0335-5.

Balay, Satish, Shrirang Abhyankar, et al. (2019a). {*PETS*}*c* {*W*}*eb page*. \url{https://www.mcs.anl.gov/petsc}. URL: https://www.mcs.anl.gov/petsc.

— (2019b). {*PETS*}*c Users Manual*. Tech. rep. ANL-95/11 - Revision 3.11. Argonne National Laboratory. URL: https://www.mcs.anl.gov/petsc.

Ding, Siyu Serena et al. (Apr. 2019). "Shared behavioral mechanisms underlie C. elegans aggregation and swarming". In: *eLife* 8. ISSN: 2050-084X. DOI: 10.7554/eLife.43318. URL: https://elifesciences.org/articles/43318.

Helms, Stephen J. et al. (Aug. 2019). "Modelling the ballistic-to-diffusive transition in nematode motility reveals variation in exploratory behaviour across species". In: *Journal of The Royal Society Interface* 16.157, p. 20190174. ISSN: 1742-5689. DOI: 10.1098/rsif.2019.0174. URL: https://royalsocietypublishing.org/doi/10.1098/rsif.2019.0174.

Sugi, Takuma et al. (Dec. 2019). “C. elegans collectively forms dynamical networks”. In: *Nature Communications* 10.1, p. 683. ISSN: 2041-1723. DOI: 10.1038/s41467-019-08537-y. URL: http://www.nature.com/articles/s41467-019-08537-y.

Wolfram Research, Inc (2019). *Mathematica*. Champaign, Illinois.

Ferrée, T C and S R Lockery (2020). “Computational rules for chemotaxis in the nematode C. elegans.” In: *Journal of computational neuroscience* 6.3, pp. 263–77. ISSN: 0929-5313. DOI: 10.1023/a:1008857906763. URL: http://www.ncbi.nlm.nih.gov/pubmed/10406137.

APPENDICES

Appendix: Videos

Several video files are provided.

N2_5e5_washed.avi This video (courtesy of Alexander Artyukhin) shows the time course of aggregation after $500\,000$ starved L1s were pipetted onto the center of a petri plate. The recording covers $720\,\mathrm{min}$. There is one frame per minute of real time, and the playback rate is $7\,\mathrm{s}^{-1}$. Still images in Figures 4.1A, 4.3A, 5.1C.

neumannBC1d.mov Numerical solution of attractant-only model in one dimension with Neumann boundary conditions (Figure 3.2A. This and all following videos are 200s long at $15\,\mathrm{s}^{-1}$. Time is displayed as "days, H:MM::SS". The first $100\,\mathrm{s}$ (1500 frames) of video cover the interval from 0 to $10\,000$ s (2:46:40) —the remaining $100\,\mathrm{s}$ from $10\,000$ to $200\,000$ s (2 days, 7:33:20). The two numebrs below each panel are the minimum and maximum of the plotted field.

neumann.mov Numerical solution of attractant-only model in two dimensions with Neumann boundary conditions (Figure 3.2B.

periodicBC1d.mov Numerical solution of attractant-only model in one dimension with periodic boundary conditions (Figure 3.3A.

periodic.mov Numerical solution of attractant-only model in two dimensions with periodic boundary conditions (Figure 3.3B.

repellent1d.mov Numerical solution of attractant+repellent model in one dimension with periodic boundary conditions (Figure 3.4A.

repellent.mov Numerical solution of attractant+repellent model in two dimensions with periodic boundary conditions (Figure 3.4B.

cooldown1d.mov Numerical solution of attractant+repellent model with cooldown in one dimension with periodic boundary conditions (Figure 3.8A.

cooldown.mov Numerical solution of attractant+repellent model with cooldown in two dimensions with periodic boundary conditions (Figure 3.8B.